PROCESS DESIGN, OPTIMIZATION AND MATERIAL SCREENING METHODS FOR SMALL-SCALE CHEMICAL MANUFACTURING WITH APPLICATION TO UNCONVENTIONAL NATURAL GAS

A Dissertation

by

AKHIL ARORA

Submitted to the Graduate and Professional School of
Texas A&M University
in partial fulfillment of the requirements for the degree of

DOCTOR OF PHILOSOPHY

Chair of Committee,	M. M. Faruque Hasan
Committee Members,	Efstratios N. Pistikopoulos
	Joseph Sang-II Kwon
	Hae-Kwon Jeong
Head of Department,	Arul Jayaraman

August 2021

Major Subject: Chemical Engineering

ABSTRACT

To meet the increasing global needs for energy, chemicals and commodity products, there is a substantial push for utilizing unconventional feedstocks such as stranded natural gas, shale gas, biogas and landfill gas. However, unconventional feedstocks pose significant challenges for centralized processing due to variabilities in scale and availability. In addition, the geographical sparsity, low feedstock quality and time-varying supply of unconventional natural gas feedstocks render existing chemical facilities inefficient for their utilization. As a result, it is challenging for conventional stick-built plants to keep up with evolving product demands and feedstock availability. An alternative is to develop small-scale, modular and intensified processes which are better suited for handling challenges associated with unconventional feedstocks and can better accommodate dynamic market conditions, process variabilities and geographical sparsity. However, the capital intensity (i.e., cost per unit production) of small-scale plants is much higher compared to their large-scale and centralized counterparts. In this thesis, to counter the diseconomies of scaling, computational frameworks and methodologies are proposed for cost-effective development of small-scale technologies. The proposed methodologies are based on principles rooted in multi-scale process development, dynamic process intensification and equipment standardization where small-scale, modular and intensified equipment modules with optimal materials are designed and operated for distributed chemical manufacturing. The utility of the developed computational frameworks is demonstrated through several midstream and downstream case studies prevalent in unconventional natural gas supply chains.

ACKNOWLEDGMENTS

Above all, I would like to thank Professor M. M. Faruque Hasan for giving me the opportunity to work on my Ph.D. thesis under his supervision, and his constant guidance, support and encouragement throughout the journey. His deep expertise in the field of process systems engineering was instrumental in enhancing the impact, technical contributions and exposition of this thesis. His strong work ethic, discipline, persistence and drive to solve complex chemical engineering problems through rigorous analytical techniques has left a profound impact on me. These factors have helped me in understanding and appreciating the art of identifying challenging problems, and work towards finding creative solutions to them.

I am also very grateful to my thesis committee members Professor Efstratios N. Pistikopoulos, Professor Joseph Sang-II Kwon and Professor Hae-Kwon Jeong. Their multifaceted expertise, diversity of perspectives, valuable insights and advice helped me in defining the research objectives and setting ambitious goals.

Moreover, I would like to thank my research group members who have made my Ph.D. journey very pleasant and enjoyable. Especially, I thank Shachit, Ishan, Emre, Jianping, Spyros, Ahmed, Manali, Akhilesh and Sadaf with whom I share great friendship, experiences and collaborations.

Last but not the least, I would like to express my deepest gratitude to my parents and brother for their continuous support, love and encouragement. They have supported me like a rock every step of the way through this journey, and this thesis would not be possible without their support and sacrifices.

CONTRIBUTORS AND FUNDING SOURCES

This work was supported by a dissertation committee consisting of Professor M. M. Faruque Hasan, Professor Efstratios N. Pistikopoulos, Professor Joseph Sang-II Kwon and Professor Hae-Kwon Jeong of the Department of Chemical Engineering.

The research was sponsored by the U.S. National Science Foundation (NSF CAREER award CBET-1943479 and award CBET-1606027), the DOE RAPID Institute and the American Chemical Society Petroleum Research Fund (ACS PRF 58764-DNI9). Portions of this research were conducted with the advanced computing resources provided by Texas A&M High Performance Research Computing.

TABLE OF CONTENTS

Page

ABSTRACT ii

ACKNOWLEDGMENTS iii

CONTRIBUTORS AND FUNDING SOURCES iv

TABLE OF CONTENTS v

LIST OF FIGURES viii

LIST OF TABLES xii

1. INTRODUCTION 1

1.1 Dynamic process intensification 3
1.2 Equipment design standardization 6
1.3 Literature survey 7
1.4 Research gaps and key challenges 15
1.5 Research objectives 17
1.6 Original contributions 19
1.7 Thesis outline 20

2. GRAMS: A GENERAL PLATFORM FOR ADSORPTION, REACTION AND SORPTION ENHANCED REACTION PROCESSES 22

2.1 GRAMS framework 23
2.1.1 Model development 23
2.1.1.1 Model description 24
2.1.1.2 Numerical scheme 29
2.1.1.3 Model implementation 33
2.1.2 Model validation 35
2.1.2.1 Reactor simulation 35
2.1.2.2 Sorption enhanced reaction process simulation 40
2.1.2.3 Pressure swing adsorption simulation 43
2.2 Optimal synthesis of periodic sorption enhanced reaction processes 50
2.2.1 Periodic SERP: process and cycle configurations 50
2.2.2 SERP Synthesis Model Formulation 53
2.2.2.1 Indices and sets 53
2.2.2.2 Decision variables and their bounds 54

2.2.2.3 Constraints and objective function 56
2.2.2.4 Optimization strategy 63
2.2.3 Case studies 70
2.2.3.1 Sorption enhanced steam methane reforming 70
2.2.3.2 Sorption enhanced water gas shift reaction 84

3. OPTIMAL METHANOL PRODUCTION VIA DYNAMICALLY-INTENSIFIED HYDROGENATION REACTIONS 89

3.1 Motivation 89
3.2 Sorption enhanced methanol synthesis 90
3.3 Process simulation and optimization 92
3.3.1 Model assumptions 92
3.3.2 Decision variables bounds 93
3.3.3 Adsorption kinetics model 95
3.3.4 Reaction kinetics model 96
3.3.5 Process performance metrics 97
3.3.6 Correlations for cost estimation 99
3.3.7 Objective function 103
3.4 Results and discussion 104
3.4.1 Base case: industrial methanol reactor 104
3.4.2 Methanol yield maximization 108
3.4.3 Methanol production cost minimization 116

4. DESIGN STANDARDIZATION OF UNIT OPERATIONS 119

4.1 Functionality-based concurrent design approach 120
4.2 Cost function with both economies of scale and economies of numbers 123
4.3 An MINLP framework for functionality-based design and modular manufacturing 124
4.4 Case studies 127
4.4.1 Concurrent design of methanol and ammonia processes 127
4.4.2 Concurrent design of natural gas liquids fractionation trains 134

5. HIGH-THROUGHPUT MATERIAL SCREENING METHODOLOGY WITH OPTIMAL PROCESS DESIGN, OPERATION AND MATERIAL DESIGN 139

5.1 Methodology 139
5.1.1 Breakthrough time analysis 141
5.1.2 Grand canonical monte carlo simulations 142
5.1.3 Isotherm fitting 143
5.1.4 Artificial neural network model 144
5.2 Results and discussion 148
5.2.1 Effect of material properties on PSA breakthrough dynamics 148
5.2.2 Zeolite screening for post-combustion carbon capture 152
5.2.3 Zeolite screening for natural gas purification 157

6. Conclusions 160

6.1 Summary and thesis contributions 160
6.2 Future work directions 163

REFERENCES 169

APPENDIX A. ADSORPTION MODEL AND ISOTHERM EXPRESSIONS 196

APPENDIX B. BOUNDARY CONDITIONS 197

APPENDIX C. REACTION RATE EXPRESSIONS 200

APPENDIX D. SIMULATION PARAMETERS 202

APPENDIX E. STATE VARIABLES' TRAJECTORIES AT CYCLIC STEADY STATE FOR INTENSIFIED METHANOL REACTOR 204

APPENDIX F. INTENSIFIED METHANOL REACTOR DESIGN WITH VARYING NUMBER OF TUBES 213

APPENDIX G. METHANOL-AMMONIA CASE STUDY 214

APPENDIX H. NGL FRACTIONATION CASE STUDY 229

APPENDIX I. EFFECT OF ADSORBENT PROPERTIES ON BREAKTHROUGH DYNAMICS 235

LIST OF FIGURES

FIGURE Page

1.1 Potential monetization routes for unconventional natural gas feedstocks. 1

1.2 Challenges in utilizing unconventional natural gas feedstocks. 2

1.3 Centralized versus distributed chemical manufacturing routes. 3

1.4 Increase in hydrogen production cost with reducing production capacity scale due to diseconomies of scaling. 3

1.5 Key research questions and proposed multi-scale frameworks for achieving economic and design targets of small-scale processes. 17

1.6 New design targets for small-scale technologies incorporating dynamic process intensification, material screening and equipment standardization. 18

2.1 GRAMS framework for simulation and optimization of NAPDE-based SERP systems and its derivatives. 22

2.2 Graphical depiction of compartmentalized adsorption-reaction systems. 29

2.3 GRAMS implementation and procedure for specific process simulation. 34

2.4 SMR in a tubular reactor on Ni-Al catalyst. 36

2.5 Effect of changing reactor temperature on methane conversion in SMR reactor at steady state. 39

2.6 Effect of changing steam-to-methane feed ratio on methane conversions in SMR reactor at steady state. 39

2.7 SE-WGSR breakthrough simulation. 43

2.8 Graphical depiction of the 4-step VSA cycle for capturing CO_2 from flue gas mixture. 46

2.9 Effluent mole fraction of CO_2 and N_2 for a 4-step VSA cycle. 49

2.10 Possible operation stages of a column with sorption/reaction phenomena. 51

2.11 Different cycle configurations obtained by combining different operation modes. 52

2.12 Pressure profile inside the SERP column for the illustrative 4-step cycle: SR → rDP → rSR → P. 59

2.13 Graphical representation of the working of the two-phase grey-box algorithm with GRAMS framework. 65

2.14 Optimal cycle configuration for SE-SMR. 78

2.15 Pressure change in the SE-SMR column for the 4-step optimal cycle. 79

2.16 Optimal hydrogen productivity with varying S/C ratio. 81

2.17 Optimal cycle configuration for SE-WGSR. 88

2.18 Pressure change in the SE-WGSR column for the 4-step optimal cycle. 88

3.1 Overall flowsheet for CH_3OH production from synthesis gas using periodic SERP concept. 91

3.2 Fitted Langmuir dual-site isotherms representing adsorption of H_2O on NaX zeolite. 97

3.3 Base case industrial methanol reactor case. 104

3.4 Effect of replacing catalyst with adsorbent on CH_3OH yield for a single-step sorption-enhanced methanol synthesis process. 107

3.5 Effect of sorption-enhancement on the CH_3OH yield and production capacity obtained for (i) fixed feed specifications (cases a-c) and (ii) varying feed specifications (cases d-f). 110

3.6 Comparison of performance of optimal SE-MeOH process with base case Lurgi-type industrial reactor. 111

3.7 Dynamic profiles of outlet gas mole fraction and reactor temperature at different bed length relative to the inlet boundary. 112

3.8 Effect of catalyst effectiveness factor on CH_3OH yield and production capacity. 115

4.1 Conventional fixed-design approach and novel common functionality-based design approach for modular chemical processes. 121

4.2 Individually-designed versus commonly-designed process synthesis. 122

4.3 Methanol and ammonia synthesis process flowsheets with three classes of equipment. 122

4.4 Flexible heat exchanger efficiency for different operating heat duties. 128

4.5 Percent reduction in total cost for methanol and ammonia processes due to equipment standardization. 132

4.6 Optimal production capacities and product portfolio of methanol and ammonia processes. 133

4.7 Process flowsheets with different NGL sources. 134

5.1 Framework for high-throughput screening of candidate adsorbents for adsorption process. 140

5.2 Fitted dual site adsorption isotherms for CO_2 adsorption on ABW, ACO, AEI and AEL zeolites. 145

5.3 Mathematical operations occurring at each node within hidden layers of the ANN model. 146

5.4 Adsorption isotherm space for the two gas species using fitting parameters' bounds. 147

5.5 Effects of equilibrium adsorption parameters and material properties on breakthrough dynamics. 151

5.6 Validating predicted breakthrough curves with first principles model for ABW, ACO, AEI and AEL zeolites for CO_2/N_2 separation. 153

5.7 Dynamic loading capacity and selectivity metrics for CO_2/N_2 separation. 155

5.8 Comparing top screened zeolites with results reported in literature. 155

5.9 Performance evaluation metrics reported by Hasan et al. 157

5.10 τ_b, dynamic loading capacity and selectivity metrics for CO_2/CH_4 separation. 159

6.1 Envisioned renewable-integrated distributed and intensified production process for manufacturing blue hydrogen. 164

6.2 Arbitrage opportunities available due to high methanol prices and low natural gas feedstock prices. 165

6.3 Conceptual methanol and ammonia co-production master flowsheet. 166

6.4 Conceptual process for direct production of methanol from natural gas using intensified SMR, RWGSR and MeOH processes. 168

I.1 Effect of (a) heat of adsorption and (b) adsorbent framework density on outlet temperature. 235

I.2 Effect of saturation adsorption capacity of gas species 2 on (a) breakthrough dynamics and (b) equilibrium adsorption isotherms. 235

I.3 Effect of adsorption energy of gas 2 on (a) breakthrough dynamics and (b) equilibrium adsorption isotherms. 236

I.4 Effect of heat of adsorption of gas 2 on outlet (a) concentration and (b) temperature profiles. 236

LIST OF TABLES

TABLE Page

1.1 Indicative list of modeling studies for SERP systems. 11

2.1 Dimensionless groups in the NAPDE model. 30

2.2 Reaction kinetics for SMR. 38

2.3 Parameters used for SMR simulation. 38

2.4 Parameters used for SE-WGSR simulation. 42

2.5 Dual-site Langmuir model parameters for CO_2 adsorption of zeolite 13X-APG. 45

2.6 Parameters used for VSA simulation. 47

2.7 Obtaining the sequence of process operation stages using the pressures in the set P_{all}. 58

2.8 The lower and upper bounds, and parameters used in the SE-SMR and SE-WGSR case studies. 75

2.9 SE-SMR results for both 95% and 98% hydrogen purity cases. 76

2.10 Comparison of the hydrogen productivity obtained of 95% and 98% hydrogen product with the existing data in literature. 80

2.11 SE-SMR synthesis results for cost minimization of hydrogen production for three different purity levels (90%, 92% and 95%), and $Prod_u^{min} = 0.4$ mmol H_2/ (kg solid. s). 82

2.12 SE-WGSR synthesis results for both 95% and 98% hydrogen purity cases. 86

3.1 Bounds on decision variables in the optimization model. 94

3.2 Parameters for H_2O adsorption on NaX zeolite. 96

3.3 Reaction kinetics model of Froment et al. for CH_3OH synthesis. 98

3.4 Cost correlations for computing total installed costs of the unit operations in the CH_3OH synthesis flowsheet. 100

3.5 Design and feed specifications, and process operating conditions for base case industrial methanol reactor. 105

3.6 Optimization results of optimized industrial methanol reactor case with maximum yield for different daily CH_3OH production capacities. 109

3.7 Optimization results with decision variables including feed composition and flow rate. 113

3.8 Optimization results obtained by minimizing CH_3OH production cost with fixed synthesis gas feed specifications. 117

4.1 Sets and indices used for methanol and ammonia case study. 129

4.2 Results for the methanol-ammonia case study. 131

4.3 Input parameters for NGL fractionation case study. 136

4.4 Results for NGL fractionation case study. 137

4.5 Optimal equipment design variables and flexible equipment performance. 138

5.1 Input bounds for training ANN models. 148

5.2 Zeolites for CO_2/N_2 separation ranked based on breakthrough time. 154

5.3 Correlation matrix for material performance metrics. 157

5.4 Top ranked zeolites for CO_2/CH_4 separation. 158

1. INTRODUCTION

Increasing global needs for energy, chemicals and commodity products provide a major impetus for utilizing unconventional feedstocks such as stranded natural gas, shale gas, biogas and landfill gas [1]. By unconventional feedstocks, we refer to those raw material feedstocks which are not typically utilized in chemical industries due to inherent processing challenges. Figure 1.1 shows several different routes for monetizing unconventional natural gas some of which include pipeline transportation, liquified natural gas (LNG) production, or manufacturing intermediate energy carriers such as ammonia, methanol and gasoline. Using unconventional feedstocks, there is a huge interest in manufacturing intermediate energy carriers to meet local chemical demands, and for obtaining easily transportable energy carriers. However, unconventional feedstocks pose significant challenges for centralized processing due to spatial and temporal variabilities in scale and availability, and poor feedstock quality [2] (Figure 1.2). Consequently, traditional stick-built chemical facilities are rendered ineffective for wide-scale monetization of unconventional feedstocks.

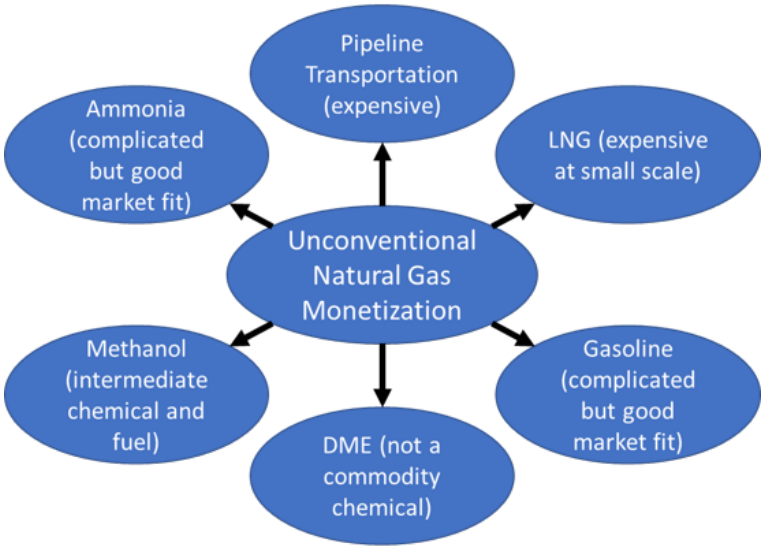

Figure 1.1: Potential monetization routes for unconventional natural gas feedstocks.

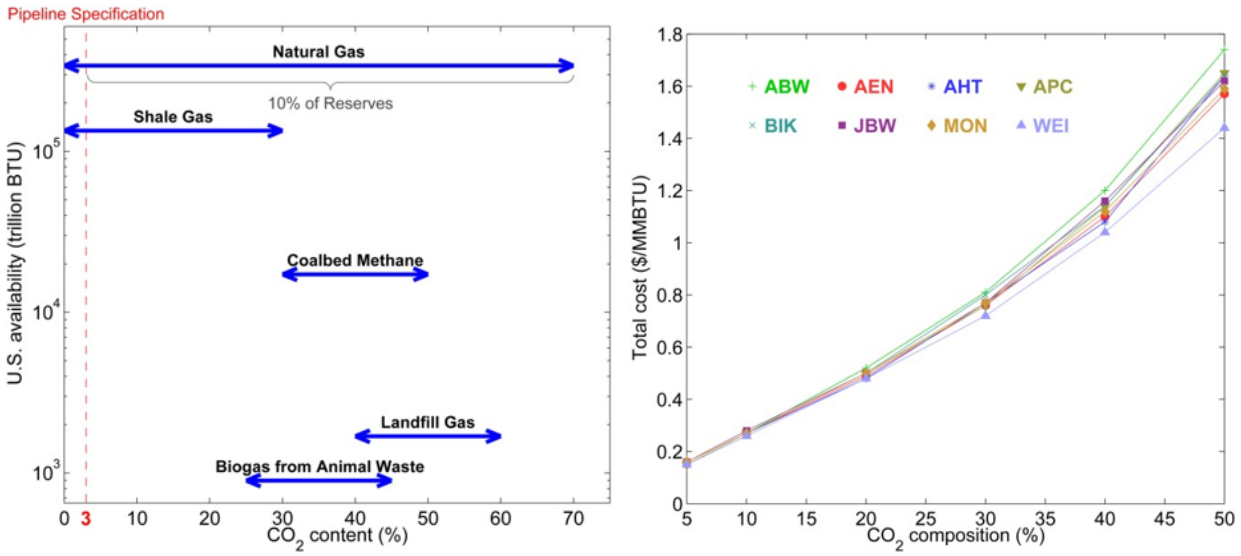

(a) (b)

Figure 1.2: Challenges in utilizing unconventional natural gas feedstocks. (a) High CO_2 contamination in natural gas resources, (b) high adsorption-based separation costs for removing CO_2 to bring natural gas to pipeline specifications. Reproduced in part with permission from First, E. L., Hasan, M. M. F., & Floudas, C. A., "Discovery of novel zeolites for natural gas purification through combined material screening and process optimization." AIChE Journal, Vol 60, Number 5. Copyright 2014 American Institute of Chemical Engineers.

Alternatively, small-scale, modular and intensified processes can be developed which are better suited for handling dynamic processing and market conditions due to inherent mobility, modularity, and feedstock- and market-flexibility. In addition, small-scale and modular chemical processes enable distributed chemical manufacturing which has several advantages including production flexibility, localized chemical manufacturing, lower transportation costs and resilience to supply chain disruptions (Figure 1.3). However, the current small-scale designs suffer from poor economies of scale thereby leading to high capital intensity, i.e., cost per unit production. For instance, reducing the scale of hydrogen production from 1000 ton/day to 0.5 ton/day can increase the per-unit hydrogen production costs by 70% (Figure 1.4).

To counter diseconomies of scaling, in this thesis, we propose new design targets for small-scale technologies that reduces the overall cost intensity by creating new opportunities for modularity, intensification and process optimization. The developed frameworks incorporate the concepts

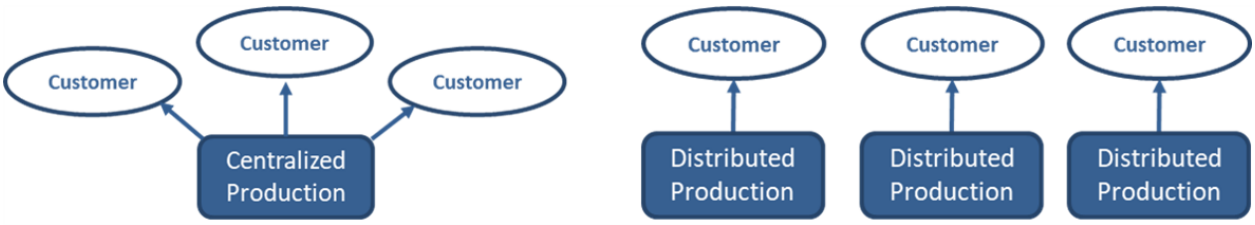

Figure 1.3: Centralized versus distributed chemical manufacturing routes. Distributed manufacturing has several inherent advantages including production capacity flexibility, localized product manufacturing, lower transportation costs and higher resilience to supply chain disruptions.

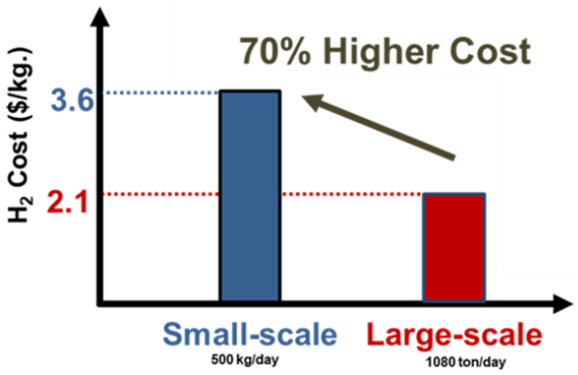

Figure 1.4: Increase in hydrogen production cost with reducing production capacity scale due to diseconomies of scaling.

of process intensification and optimization, and equipment standardization to realize economic benefits. In this section, we begin by introducing the concepts of process intensification and equipment standardization. Next, we describe the state-of-the-art in these fields, and the key research gaps and challenges that need to be addressed before their wide-scale adoption for chemical manufacturing. Finally, we conclude this section by elaborating on the research objectives and thesis outline.

1.1 Dynamic process intensification

Process intensification leads to efficient processes by significantly reducing equipment sizes, number of unit operations, utilities, waste production, and energy consumption [3]. These improvements are achieved by refining the processes at four different scales - spatial, thermodynamic,

functional and temporal [4]. Dynamic process intensification technologies are specially focused on utilizing the process dynamics for achieving intensification. Baldea and Edgar [5] define dynamic process intensification as *"any change to the dynamics, operation strategy and/or control of a conventional or intensified system, that leads to a substantially more efficient processing path"*.

To achieve dynamic process intensification, the processing scheme changes can happen both at the design level or operation level, as well as to both conventional or inherently intensified processes. At design-level intensification, the predominant focus is on developing new process configurations whereas at the operation-level intensification, changes in operational strategies such as manipulating control variables are leveraged. The major differences between steady-state and dynamic process intensification are that the dynamic process intensification systems evolve with time and are therefore more complex to study. Furthermore, they typically achieve periodic steady state due to their cyclic operation as opposed to time-invariant steady states in conventional intensified systems.

The major objective of dynamic process intensification systems is that, on an average, the periodic operation of chemical systems should lead to better process performance compared to steady-state counterparts. This is achieved by operating a dynamically intensified system in discrete steps and/or imposing a periodic forcing signal (e.g., feed conditions) for a more beneficial operational regime. There are several incentives and rationales for developing dynamically intensified processes. These include (i) countering the inherent manufacturing inefficiencies in thermodynamically-limited processes by pushing the thermodynamic barrier, (ii) developing more efficient processes for effective utilization of raw material feedstocks by merging several chemical phenomena or functionalities for developing compact and modular chemical processes, and (iii) improving process operational strategy to bring about process improvements and enhancing process productivity and/or efficiency.

There are several technologies that leverage the principles of dynamic process intensification. Some of these technologies include continuous chemical reactors, cyclic distillation, oscillating baffled reactors, pressure swing adsorption (PSA), sorption enhanced reaction processes (SERP)

and simulated moving bed chromatography. Some of these technologies, such as continuous chemical reactors, utilize time-varying control variables to achieve dynamic process intensification whereas other technologies such as SERP are inherently dynamically intensified by design as they merge multiple chemical phenomena within a single unit operation for achieving dynamic process intensification.

Baldea and Edgar define four major principles that underpin the majority of dynamic process intensification systems [6]. These include parallelization, functionalization, system nonlinearity and mixing or segregation. In this thesis, we focus predominantly on the functionalization principle for developing dynamic process intensification processes. Process improvements can be achieved by improving the system fundamentally using multi-functional reactors, which carry out multiple synergistic phenomena in a single, intensified column. Integrating reaction and separation forms the basis of multi-functional reactors [7,8]. Various applications of process intensification leverage the famous Le Chatelier's principle: removal of a reaction product shifts the equilibrium in favor of product formation. Reactive distillation, membrane reactors and chromatographic reactors are a few examples taking advantage of *in situ* removal of product to obtain higher reaction conversions. A recent technology that leverages such hybrid reaction-separation system is SERP.

SERP technology leverages the principle of functionalization and simultaneously carries out multiple functions, i.e., reaction and separation phenomena, in a single unit operation. SERP has gained considerable attention from researchers since the integrated adsorption-reaction columns offer numerous advantages over conventional reactors. Due to simultaneous reaction, byproduct removal and heat integration, SERP occurs at lower temperatures, requires less equipment and less utilities, and is modular thereby offering more flexibility in deployment and operation. The reaction products obtained via SERP have higher purity, selectivity and productivity along with higher reactant conversion [9]. Therefore, the SERP concept has been successfully demonstrated on several reactions such as steam methane reforming (SMR) [10, 11], water gas shift reaction (WGSR) [12, 13], and steam reforming of glycerol [14].

In SERP operation, the column is packed with an admixture of adsorbent and catalyst to simul-

taneously remove reaction byproduct(s) and promote desired reactions. The adsorbent material is utilized for *in situ* capture of reaction product to shift the equilibrium in the forward direction. These adsorbents can hold a finite amount of adsorbates after which it is necessary to regenerate them to prepare for the next cycle [15]. This regeneration can either be carried out inside the same vessel or in a separate column. Various methods of regeneration for removing adsorbed species exist. The regeneration method employed for SERP is chosen by carefully considering the technical and economic aspects. In the subsequent sections, we highlight the challenges that are encountered during optimal synthesis and design of periodic SERP systems, and the developed computational framework for developing modular and cost-effective SERP technologies.

1.2 Equipment design standardization

In the chemical process industry (CPI), bigger is often considered as better. By leveraging the economies of scale, large and centralized processing plants become more efficient and cost-effective. In traditional chemical process design, the major difference in equipment design for different chemical processes originate from customization. Therefore, the equipment design closely follows the feedstocks, product specifications and overall process throughput.

Although different chemical processes follow different prescribed sequences of unit operations to convert raw feedstock into desired product, similar equipment types are often utilized to perform processing tasks or unit operations. For instance, equipment such as heaters, coolers, separators, mixers, compressors, pumps, turbines, cooling towers, and so forth, are often similar in type, if the fluids that are handled by the processes are the same or similar in nature. For example, the acid gas removal systems are typically of the same type in chemical processes that deal with gases such as natural gas, syngas, hydrogen, carbon monoxide, carbon dioxide, nitrogen, and oxygen. The difference is mostly related to the size and the number of equipment. In some cases, the reactors are also similar if the processes involve similar reactions.

Another example of process-level synergy is the production of methanol and ammonia from syngas and nitrogen-hydrogen feedstocks, respectively. In these two processes, there are significant similarities in unit operations involved. Both the processes are synergistic as both the involved

reactions are exothermic, dictated by mass-transfer limitations and slow reaction kinetics, and favored at moderate temperature and high pressure. These observations highlight the fact that many similarities exist among the designs of different standalone chemical processes.

Even though traditional design methodologies for large-scale chemical manufacturing results in cost savings due to economies of scales, they miss out on the opportunity of furthering cost savings via economies of numbers. The traditional design methods are asynchronous in a sense that they only focus on designing a single process at a time. In this way, the equipment designs and sizes closely follow the given feedstocks, products specifications and the overall throughput. While this leads to optimal process design, it also limits the number of off-the-shelf equipment that can be constructed with standard designs.

In addition, increasing amount of distributed energy sources have rendered traditional large-scale chemical plants inadequate due to limited pipeline transportation. For example, many natural gas reserves are currently stranded because they require long-distance pipelines to be transported to central processing facilities. Therefore, in the context of changing dynamics of resource availability and products demands, and the need for small-scale and modular chemical processes, one needs to reconsider the traditional process design workflow [16]. In the forthcoming sections, we will show our proposed process design methodology to create new opportunities for economies of numbers through standardizing the equipment designs across multiple processes in the CPI.

1.3 Literature survey

Small-scale and distributed chemical manufacturing

Increasing global demands of chemical products indicate that the future CPI will need to utilize both conventional feedstocks (e.g., crude oil) and unconventional feedstocks (e.g., shale gas, stranded natural gas, biogas, coalbed methane, landfill gas, biomass, etc.) [1]. However, significant challenges remain to be overcome before these resources become economically feasible and are widely used in the CPI. Unconventional feedstocks are often small-scale, hard-to-access and geographically distributed with significant seasonal variability in volume availability and chem-

ical compositions. In addition, a significant fraction of available natural gas is inaccessible as they require extensive pipeline infrastructure to be transported to central processing facilities. Furthermore, expensive separation technologies need to be deployed to meet the pipeline specifications [17, 18].

The spatio-temporal distribution and the scale of unconventional resources require that one reconsiders the "bigger is better" argument [16]. Furthermore, there is always a need for developing process technologies that are suitable for utilizing hard-to-access resources. Small plants are advantageous due to their agility and mobility [19]. In addition, they can be designed in a modular fashion which offers the distinct advantages of accommodating time-varying product demands and feedstock availability [2,20–22]. Several past studies have demonstrated the benefits and economic advantages of small-scale and modular chemical processes [23–29].

SERP modeling and simulation

This section presents the literature studies on dynamic process intensification systems with specific focus on SERP systems. The studies highlighted include both computational and experimental efforts to conceptualize and analyze SERP-based intensified chemical processes. As SERP inherently covers both single-functional reaction and adsorption studies, some of the indicative literature studies for such conventional and non-intensified systems have also been covered.

Overall, there have been numerous modeling studies on reactors, adsorbers, and sorption enhanced reactors. Karanth and Hughes [30] considered axial dispersion in packed bed reactors and conducted parametric studies on reactors having a single steady state solution. Bussche et al. [31] neglected axial dispersion to simulate reverse flow operation of fixed-bed methanol synthesis reactors by considering solid and gas phases separately. Winterberg et al. [32] developed an extensively validated two-dimensional pseudo-homogeneous model describing heat and mass transport in tubular columns with and without reactions. Shahrokhi and Baghmisheh (2005) used a one-dimensional, heterogeneous model for investigating dynamics of a methanol-synthesis fluidized bed reactor. Halabi et al. [33] adopted a similar adiabatic model for analyzing the performance of autothermal reforming process in a fluidized bed reactor. Manenti et al. [34] employed an isobaric,

pseudo-homogeneous model for studying the effects of modeling assumptions on the process dynamics of a reactor. They demonstrated that the numerical model becomes increasingly stable by addition of modeling details. Adams and Barton [35] developed a detailed 2-D, heterogeneous model for studying WGSR in packed bed reactors. Ghouse and Adams [36] used a similar model for simulating SMR reaction.

Similarly, there have been several studies on simulation of PSA processes. Gomes et al. [37] used a pseudo-homogeneous, isobaric model for evaluating the feasibility of a PSA process for recovering CO_2 from exhaust gases. Jiang et al. [38] neglected axial dispersion and column-wall heat exchange in their mathematical model and used the model further for devising a novel PSA optimization strategy. Cavenati et al. [39], experimentally and computationally, evaluated a Skarstrom cycle for removing CO_2 from contaminated natural gas using a heterogeneous model. Hasan et al. [40] simulated and optimized different PSA and vacuum swing adsorption (VSA) processes for carbon capture. Casas et al. [41] experimentally studied a 4-step PSA cycle for capturing CO_2 from CO_2 + H_2 mixtures, and validated a detailed mathematical model capturing the crucial phenomena and trends observed in experimental results. Haghpanah et al. [42] comprehensively compared total variation diminishing (TVD), weighted essentially non-oscillatory (WENO) and upwind difference scheme (UDS) for PSA/VSA simulations and carried out genetic algorithm-based optimization.

There have been many modeling efforts to reconcile adsorption and reaction phenomena in a single column for sorption enhanced reactive systems. Table 1.1 presents an indicative list of previous modeling works on SERP, and the numerical schemes considered in these works. The research group of Ding and Alpay has studied the SERP systems both experimentally and computationally. They considered the mass-transfer limited adsorption kinetics and Langmuirian adsorption equilibria while developing a pseudo-homogeneous mathematical model for sorption enhanced steam methane reforming (SE-SMR) [43]. Using the orthogonal collocation method, the simulations were performed for the initial step i.e., adsorption-reaction step of the process. Xiu et al. [44, 45] extended Ding and Alpay's model to accommodate multiple boundary conditions and analyzed a five-step, cyclic SERP. They used the same model for devising a novel SERP with *in situ* adsorbent

reactive regeneration [46]. Lee et al. [47] assumed negligible axial dispersion in their experimentally validated model for simulating carbonation-enhanced SMR. Rusten et al. [48] were the first ones to address the complex gas-pellet interactions involved in sorption enhanced processes by using a heterogeneous 1-particle and 2-particle model. Koumpouras et al. [49] theoretically studied H_2 production at low temperatures via SE-SMR. They employed a separate bed for regeneration to decouple reaction and regeneration steps. Reijers et al. [50] [51] worked on improving the model predictions and included several experimental data sets for model validation. Additionally, they undertook sensitivity studies for isotherm parameters. Jang et al. [13] used a pseudo-homogeneous, isobaric CSTRs-in-series model for evaluating the sorption enhanced water gas shift reaction (SE-WGSR) for H_2 production. Fernandez et al. [52, 53] showed the feasibility of SE-SMR process for large scale H_2 production using CaO-based CO_2 sorbent. Wu et al. [54, 55] developed a detailed two-dimensional and heterogenous SERP model and validated it with experimental data for steam reforming of glycerol. Abbas et al. [56, 57] performed experiments and simulations for studying sorption enhanced steam reforming with chemical looping in a packed bed reactor. Lugo et al. [58] developed a heterogeneous model for studying the effects of different multi-functional catalyst-sorbent pellet designs, namely uniform-distributed and core shell, on the performance of SE-SMR and SE-WGSR reactions. Rodrigues and coworkers [59–63] have extensively investigated development and synthesis of multi-functional materials, both experimentally and computationally, for several applications including SE-SMR and sorption enhanced steam reforming of ethanol.

In addition to modeling and simulation, there have been some studies for optimizing SERP systems. He et al. [14] used thermodynamic analysis for obtaining optimal steam-to-glycerol ratio and temperature for steam reforming of glycerol. It was found that without CO_2 sorption, higher temperatures lead to higher reaction conversions, whereas in presence of CO_2 sorption, lower temperatures are favorable. Additionally, excess steam pushed the equilibrium in favor of hydrogen production thereby improving process performance. Wang et al. [65] used Gibbs energy minimization method for studying sorption enhanced steam reforming of propane. Optimal pressure, temperature and steam-to-propane ratio were obtained for producing $>99\%$ pure hydrogen. Bayat

Table 1.1: Indicative list of modeling studies for SERP systems.

Authors	Year	Model properties	Discretization scheme
Ding et al. [43]	2000	1-D pseudo-homogeneous, Ergun's eqn., axial dispersion	orthogonal collocation
Xiu et al. [44, 45]	2002	1-D pseudo-homogeneous, Ergun's eqn., axial dispersion	orthogonal collocation
Lee et al. [47]	2004	1-D pseudo-homogeneous, Ergun's eqn., no axial dispersion	finite difference
Rusten et al. [48]	2007	1-D heterogeneous, rigorous momentum eqn., axial dispersion	finite volume
Koumpouras et al. [49]	2007	1-D heterogeneous, steady state, isobaric, no axial dispersion	centered finite difference
Reijers et al. [50, 51]	2009	1-D pseudo-homogeneous, Ergun's eqn., axial dispersion	orthogonal collocation
Jang et al. [13, 64]	2012	1-D pseudo-homogeneous, CSTRs in series	_
Fernandez et al. [52, 53]	2012	1-D pseudo-homogeneous, Ergun's eqn., no axial dispersion	backward finite difference
Wu et al. [54, 55]	2014	2-D heterogeneous, Ergun's eqn., axial dispersion	orthogonal collocation
Abbas et al. [56,57]	2016	1-D heterogeneous, Ergun's eqn., axial dispersion	backward finite difference
Lugo et al. [58]	2016	1-D heterogeneous, axial dispersion	finite element method

et al. [66] studied methanol production using a membrane gas-flowing solids-fixed bed reactor with *in situ* CO_2 capture and H_2O removal. In another work, they proposed a novel Fischer-Tropsch reactor cycle with *in situ* H_2O capture for gasoline production [67]. Tzanetis et al. [68] performed an exergy analysis to obtain optimal values of reforming temperature. An increase of hydrogen purity of 17.3% was observed for sorption enhanced reforming in comparison to conventional reforming.

Optimization methods for NAPDE systems

The underlying models that capture the dynamics of SERP systems consist of a set of detailed nonlinear and algebraic partial differential equations (NAPDE), and the optimization of such NAPDE models is a challenging problem. In the literature, there have been several studies to address optimization of such complex systems. Nilchan et al. [69] completely discretized the conservation equations both in space and time, and used sequential quadratic programming (SQP) algorithm to optimize resulting nonlinear equations for dynamic periodic adsorption processes (PAPs). Biegler and co-workers used state-of-the-art nonlinear programming (NLP) solver IPOPT for optimizing adsorption processes [70–72]. Typically, in the works involving fully-discretized modeling equations in space and time, the complexity of the model was reduced by using fewer number of discretizations in both space and time. The accuracy of the model is therefore compromised for reducing the computational load. To this end, simulation-based optimization of NAPDE models is attractive because the accuracy of the model is preserved. Agarwal et al. [73] developed reduced-order surrogate models using proper orthogonal decomposition (POD) method for PSA processes. Hasan et al. [40, 74] used a kriging-based surrogate model for optimization of both PSA and VSA processes. Iyer et al. [75] designed an intensified process for syngas production input-output simulation data from a high-fidelity model was used for grey-box optimization.

Simultaneous material screening and process optimization for NAPDE-based processes

To develop cost-effective and efficient intensified technologies, it is crucial to optimize both the selected materials, and process design and operation. We showcase this with the help of complex PSA processes that are governed by complex NAPDE-based models, and the research efforts to design optimal process and material for gas separation applications.

Microporous materials, such as zeolites and metal organic frameworks (MOFs), can selectively adsorb many small gases of significant industrial and environmental interest [76–84]. For example, they have shown a great promise for PSA-based CO_2 capture because of their high selectivity and high storage capacity for CO_2. More than 235 zeolites and 88,000 MOFs are already found or

synthesized, and the list continues to grow. Their properties can be further tuned and controlled because of the modular synthesis approach wherein different building blocks can be selected for providing desired functionalities [85, 86]. In fact, theoretically, there exists millions of different hypothetical structures for potential discovery and synthesis.

Adsorbent selection is a key decision for the development of a PSA process, which is a widely used technology for molecular separation [87–89]. Although there are numerous candidate materials, not all of them are suitable for a given separation. This makes the adsorbent selection a challenging task. Depending on the atomic composition, geometric structure and chemical functionality, the properties of these candidate materials can be drastically different from each other in terms of adsorption capacity, gas loading as dictated by the equilibrium adsorption isotherms, and selectivity, among others. This in turn affects the PSA performance [90]. Selectivity and storage capacity are predominantly used for evaluating adsorbents at equilibrium conditions [91–95]. When considered separately, these metrics are inadequate in predicting the best adsorbents considering their actual performance in realistic PSA conditions [74, 96–98]. It is also observed that these materials-centric metrics can override the effect of each other [99], and should therefore be combined to gain meaningful insights. Hasan et al. [74, 100] introduced a hierarchical computational screening approach that uses a combination of shape, size, and adsorption selectivities to reduce the number of candidate adsorbents for detailed process optimization to eventually generate a rank-ordered list based on total cost of separation. This approach not only selects the most cost-effective materials, but it also attains the optimal process conditions while satisfying purity, recovery, and other process constraints. However, because of the use of high-fidelity models, the screening is computationally demanding. Another recent example of combining multiple metrics is the general evaluation metric (GEM) [101] that uses information from isotherm data and internal energy of adsorption. Recently, Park et al. [102] used a combination of working capacity and adsorbent performance at a process level is useful in predicting the ranking of materials for CO_2 capture application.

A simple, yet holistic, metric is the breakthrough time based on the transient response of an

adsorption column. It is the time required to saturate an adsorbent-packed column until there is no more adsorption taking place when passing a mixture of gases through the column. At the beginning, most of the gases fed to the column are adsorbed and the outlet composition stays the same. However, as time progresses, the rate of adsorption decreases, and we reach a point when the outlet composition starts to change for the first time. We refer to this as breakthrough initiation time and denote as τ_b. The outlet composition of each gas continues to change with time until it gradually reaches a steady state value which is the same as the feed composition. We refer to this as breakthrough completion time and denote as τ_c.

Breakthrough times capture both the equilibrium and kinetic adsorption behaviors of individual gases passing through the column. They are useful in determining the column size, the regeneration frequency and the design of a PSA cycle. It is, therefore, natural that many studies have considered breakthrough times (both τ_b and τ_c) as a metric for materials screening [103–108]. Britt et al. [109] compared dynamic loading capacities of six different MOFs for selectively adsorbing harmful gases such as SO_2, NH_3 and CO. They further performed breakthrough experiments on NaX zeolite, Mg-MOF-74 and Zn-MOF-74 adsorbents for evaluating their CO_2 separation capacity from CO_2/CH_4 mixtures [106]. Krishna et al. [99] investigated the breakthrough curves of an adsorber column with different zeolites and MOFs for separating CO_2 from a CO_2/N_2 mixture. Duan et al. [110] performed breakthrough simulations for evaluating the practical feasibility of a novel MOF for separating pure CH_4 from CO_2 and C_2-hydrocarbon gas mixtures. Prats et al. [111] leveraged transient breakthrough simulations for screening 10 faujasite structures and extended their analysis to include detailed PSA and VSA simulations for obtaining optimal carbon capture conditions. In their study, breakthrough time was selected as the final criterion for selecting adsorbents.

While breakthrough times have been used for screening a handful of candidate materials in the past, experimental screening based on breakthrough times of a large number of candidate materials is impractical. The increased sophistication and accuracy of mathematical models in capturing detailed dynamics have, therefore, shifted the focus from experimental to computational screening

[100, 112–116]. However, predicting breakthrough times require solving complex NAPDE-based first-principles adsorption models [40] which are increasingly onerous due to high computational demands.

1.4 Research gaps and key challenges

As mentioned previously, dynamic process intensification and equipment standardization are two strategies that can be used effectively for bringing down the high cost of small-scale processes. Intensified units can result in reducing the number and size of equipment used for a processing operation, and standardization of equipment designs can help in leveraging the economies of numbers via experiential learning. However, significant challenges need to be addressed in these technologies before their wide-scale application in practical situations.

In case of achieving dynamic process intensification for small-scale processes via SERP, the interactions between the reaction and sorption phenomena make it difficult to predict the effects of process design parameters on the SERP performance. There are several critical decision variables involved in SERP cycle synthesis and optimization such as sequence of operation modes, number of steps, operating pressures and durations of each step, feed composition, feed flow rate, sorbent-catalyst distribution, bed length, and temperature. Obtaining optimal design and process operating parameters solely through experimentation is time consuming [117]. Additionally, the large number of decision variables and the computational complexities involved in solving detailed NAPDE-based models make the SERP synthesis and optimization immensely challenging. This highlights the need of a systematic and robust simulation and optimization platform for obtaining optimal cycle configurations. The framework should be general enough to be used for desired periodic-SERP applications and other SERP derivatives. The framework should also yield optimal steps present in a process cycle along with cycle step time, and other process operating conditions such as step pressures and feed conditions.

From a modeling perspective, the dynamic nature of adsorption-reaction systems and the complex, coupled interactions between involved physics make their modeling and simulation a complicated task. The difficulties arise due to stiff PDEs, non-isothermal, non-adiabatic and non-isobaric

nature of the process, presence of two phases and axial dispersion, and wall-fluid-pellet interactions. Furthermore, the reactor columns can have many configurations with different operating conditions, material selection, material distribution, cycle steps, cycle times and boundary conditions. This necessitates a fast, robust and adaptive simulation platform which can then be used for rigorous simulation and optimization to obtain optimal design parameters. The model must be sufficiently accurate, validated and must balance the tradeoffs between computational expensiveness and prediction accuracy well.

The previous modeling studies on hybrid adsorption-reaction systems have predominantly focused on just SERP. Even for SERP, there are just a few groups who have compared simulation and experimental results. For SE-SMR, to our best knowledge, only Ding and Alpay [43], Xiu et al. [44], Lee et al. [47], and Reijers et al. [118] have made the comparison. For SE-WGSR, the only group who has performed validation is of Jang et al. [13]. Even in these validated studies, the applicability of the same model for simulating just-reaction and/or just-adsorption cases has not been studied in detail. Most of the works have focused more on simulating large-scale systems without performing rigorous validation. Overall, firstly, only a few previous works have experimentally validated their models, and secondly, none of them have explored the applicability of the same model for sub-cases such as pure adsorption and pure reaction.

In addition, simultaneous design and optimization of materials and process significantly increases the computational complexity of numerical problems. Large number of material properties and process design and operation variables result in a large number of decision variables, and the complex interactions between material properties and process performance make finding an optimal solution difficult. This is specially challenging for systems driven by complex NAPDE models, such as those of SERP and PSA. There only exists limited literature on developing computationally efficient and accurate multiscale models that bridge the gap between material and process scales, and can be tractably applied on numerous potential candidate materials.

On the other hand, for small-scale modular manufacturing, the key challenge that remains unexplored is how can we effectively increase the number of standardized equipment modules for

manufacturing such that small-scale processes become more economically attractive compared to large-scale counterparts. One way to counter the unfavorable economies of scale is to standardize the design for mass-production and reduce the equipment manufacturing costs by exploiting the economies of numbers. To our best knowledge, there does not exist a computational framework that focuses on combining economies of scaling and economies of numbers for designing multiple processes. Additionally, increasing the number of processes that are designed simultaneously exponentially increases the computational complexity of the optimization problem. It is difficult to solve problems of such scale with present state-of-the-art optimization solvers, therefore necessitating the need of developing an efficient solution strategy.

1.5 Research objectives

Based on the aforementioned challenges that exist in the development of small-scale and modular technologies, the overall objectives of the thesis are as follows (Figure 1.5):

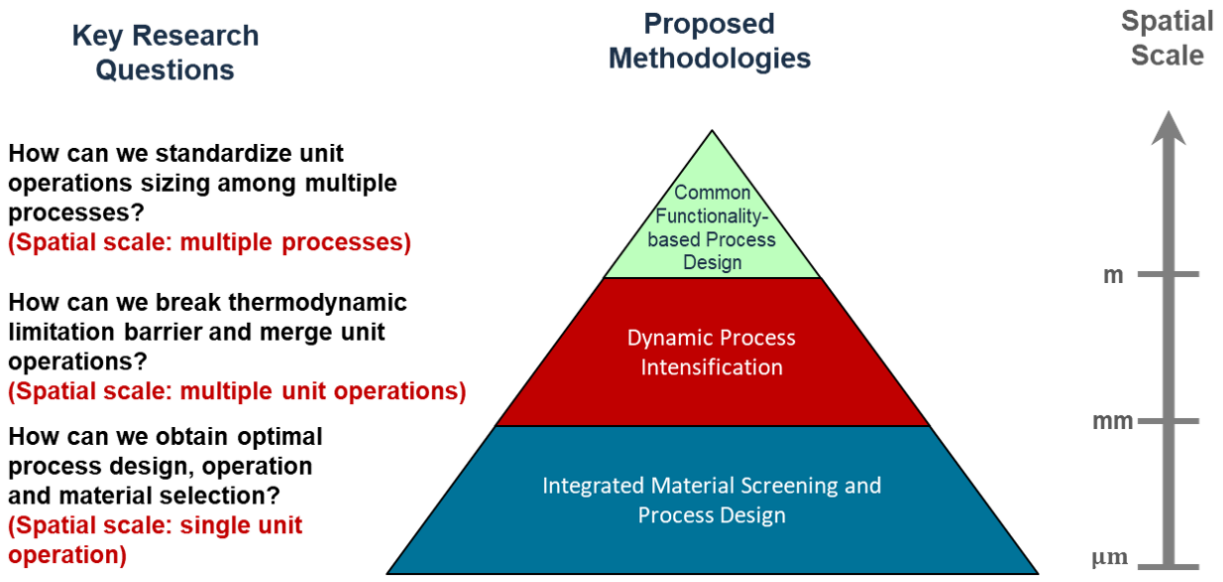

Figure 1.5: Key research questions and proposed multi-scale frameworks for achieving economic and design targets of small-scale processes.

- Objective 1: Developing dynamically-intensified chemical processes for monetizing unconventional natural gas feedstocks
- Objective 2: Developing a functionality-based design approach that creates new opportunities for economies of numbers through standardizing the equipment designs across multiple processes in the CPI
- Objective 3: Developing a multi-scale approach with integrated material screening, process design and optimization

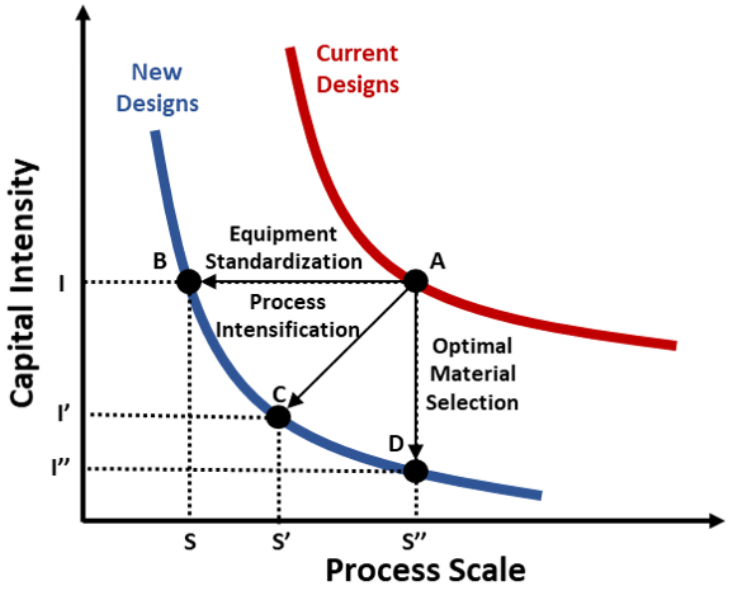

Figure 1.6: New design targets for small-scale technologies incorporating dynamic process intensification, material screening and equipment standardization.

For objective 1, multifunctional chemical processes are proposed that integrate reaction and adsorption phenomena, as in SERP, to utilize unconventional natural gas for reaction, conversion and storage purposes. To investigate such systems, a high-fidelity generalized reaction and adsorption modeling, simulation and optimization (GRAMS) platform is developed for accurately capturing

reaction and adsorption dynamics in SERP systems packed with solid catalysts and porous adsorbents. The developed framework is capable of optimizing periodic SERP cycle configuration, column design specifications and process operating conditions.

For objective 2, we depart from asynchronous design of single-processes and instead adopt a common-functionality-based approach for simultaneous design of multiple processes. This involves exploring synergies between the functionalities of unit operations used within a multitude of chemical processes and synthesize them all concurrently. To leverage economies of numbers, an optimization-based concurrent design framework is developed for standardization of modular units with common functionality. Based on the special structure of the mathematical formulation identified, an augmented Lagrangean-based decomposition algorithm is proposed that is suited for designing a large number of processes simultaneously.

To attain objective 3, a high-throughput screening framework is developed for ranking a large adsorbent database for purifying unconventional natural gas. The concept of breakthrough event times is introduced, and for their accurate prediction, accurate ANN-based surrogate models are developed. Breakthrough time is a unified metric that combines the effects of both selectivity and adsorption capacity, and is therefore used as the final criterion for ranking candidate adsorbents. The developed strategy has very high accuracy compared to the detailed first principles model, and due to lower computational complexity, it can be leveraged for screening millions of potential adsorbents within seconds.

1.6 Original contributions

The original contributions of this thesis are as follows:

- A first-of-its-kind computational framework GRAMS for synthesis, design and optimization of dynamic process intensification systems which integrate multiple materials within a single unit operation thereby leading to cost-effective chemical processes

- A common functionality-based concurrent process design methodology for modular chemical processes that exploits the similarities in the functionality of unit operations among

multiple processes via unified economies of scaling and economies of numbers

- A high-throughput multi-scale computational framework for screening large material databases while preserving high-fidelity nature of first principles-based process simulations with applications to unconventional natural gas purification and carbon capture
- Novel intensified and modular processes for unconventional natural gas monetization to manufacture promising energy vectors including hydrogen, methanol, ammonia and syngas

1.7 Thesis outline

The thesis has been organized in 6 sections. Section 2 introduces the dynamic process intensification framework, GRAMS, for design, synthesis and optimization of SERP systems. Section 2.1 describes the transport equations that are utilized to describe SERP systems. In this section, we also brief upon the finite volume scheme used for discretization, and the resulting spatially discretized dimensionless equations present in the NAPDE model. Several case studies are presented which validate the model predictions with experimental data. Additionally, several technologies and processes including SE-WGSR, PSA and packed bed reactors are analyzed. In Section 2.2, we introduce the NAPDE-based SERP cycle synthesis and optimization model wherein we present a generalized boundary condition formulation that handles all possible SERP cycle steps using continuous pressure variables. The two-phase grey-box optimization strategy used for SERP cycle synthesis and optimization is also described. The applicability of the optimization framework is shown for deriving optimal cycle configuration of SE-SMR and SE-WGSR processes for pure hydrogen production using natural gas as raw material feedstock.

In Section 3, we leverage the GRAMS framework for developing a novel and intensified methanol synthesis process with *in situ* water adsorption. The section presents an overview of the methanol synthesis process flowsheet, and the major distinctions between steady-state and proposed dynamic methanol processes. Next, the section outlines the overall optimization model for optimal design and operation of sorption enhanced methanol (SE-MeOH) processes. This section describes the sets, indices, objective function and constraints employed in the SE-MeOH optimiza-

tion model. Moreoever, the rate expressions used for capturing adsorption and reaction dynamics of SE-MeOH processes are also described along with process cost correlations. The performance of the resultant optimal SE-MeOH processes is compared with that of a base-case industrial reactor. The results are reported for two scenarios which include retrofitting industrial reactor performance using SERP technology, and optimizing the industrial reactor using SERP with variable synthesis gas feed composition and flow rate.

Section 4 describes the functionality-based concurrent process design methodology. We introduce a generalized cost function expression that incorporates both economies of scale and economies of numbers. Next, we describe the mixed integer nonlinear programming (MINLP) model for simultaneous design of multiple processes and equipment module standardization. We illustrate the framework using two case studies. The first case study identifies the common designs for small-scale methanol and ammonia processes whereas the second case study utilizes the proposed framework for the concurrent design of deethanizer–depropanizer distillation trains for producing natural gas liquids (NGLs) using different natural gas sources.

In Section 5, we describe the overall methodology for high-throughput material screening with specific application to adsorption technologies. The section introduces a breakthrough initiation time metric and breakthrough time events for evaluating material performance in gas separation applications. Subsequently, the ANN models are utilized for accurately approximating breakthrough transient dynamics, and high-throughput screening of numerous candidate materials. The section also reports the best zeolites screened from the Structure Commission of the International Zeolite Association (IZA-SC) database comprising of 196 zeolites for post-combustion carbon capture and natural gas purification applications.

Section 6 concludes the thesis by highlighting major contributions of this work, and the future research directions.

2. GRAMS: A GENERAL PLATFORM FOR ADSORPTION, REACTION AND SORPTION ENHANCED REACTION PROCESSES*

Here, we present the overall simulation framework, GRAMS, which is used for performing high-fidelity simulation and optimization of SERP systems and its derivatives [119–121]. GRAMS stands for generalized reaction and adsorption modeling, simulation and optimization framework, and can be used for simulating both non-intensified processes, i.e., reactors and adsorbers, and intensified processes, i.e., layered and composite SERP (Figure 2.1).

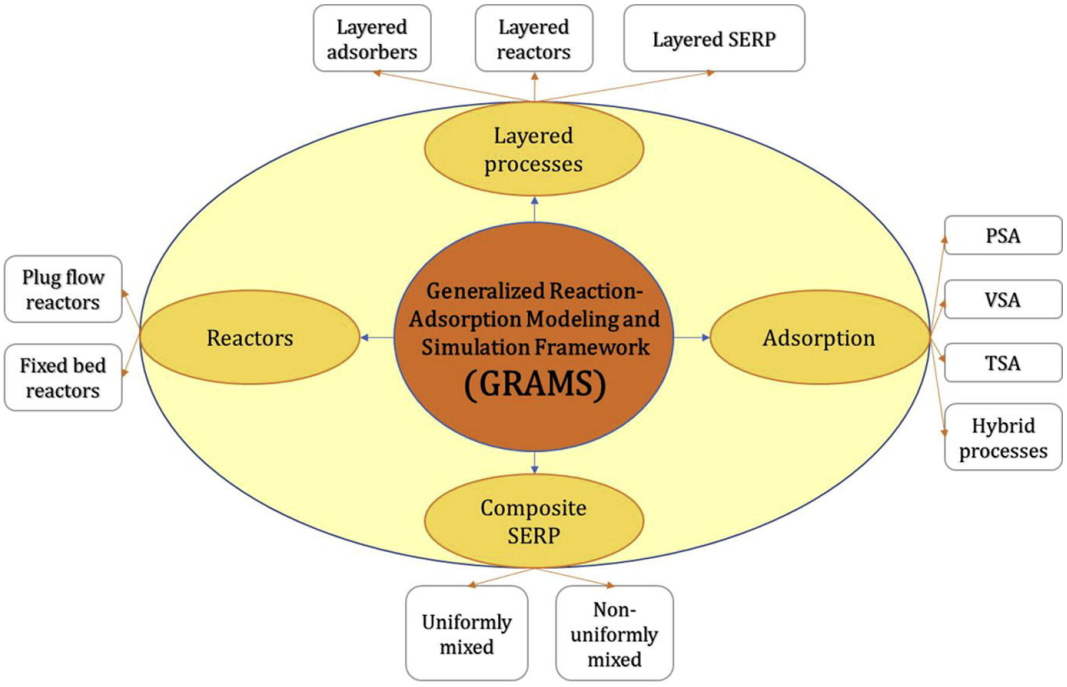

Figure 2.1: GRAMS framework for simulation and optimization of NAPDE-based SERP systems and its derivatives.

*Reproduced in part with permission from Arora, A., Iyer, S. S., & Hasan, M. M. F., "GRAMS: A general framework describing adsorption, reaction and sorption-enhanced reaction processes." Chemical Engineering Science, Vol 192, Pages 335-358. Copyright 2018 Elsevier Ltd. Reproduced in part with permission from Arora, A., Bajaj, I., Iyer, S. S., & Hasan, M. M. F., "Optimal synthesis of periodic sorption enhanced reaction processes with application to hydrogen production." Computers & Chemical Engineering, Vol 115, Pages 89-111. Copyright 2018 Elsevier Ltd.

Using GRAMS, plug flow reactors and fixed bed reactors can be simulated as is the case for only-reaction systems. In case of only-adsorption systems, several process configurations including PSA, VSA and temperature swing adsorption (TSA) can be simulated. Moreover, systems with simultaneous reaction and adsorption phenomena can also be simulated as is the case in SERP which include both layered as well as homogeneously-distributed catalyst and adsorbent material.

GRAMS is versatile and can be used for simulating several chemical engineering systems of interest because the reaction and adsorption terms in the underlying first principles model can be included or discarded from the formulated set of equations depending on the system being simulated. This can be achieved by carefully manipulating the adsorbent and catalyst density values in the model, as well as manipulating the boundary conditions.

In this section, the simulation model within GRAMS is firstly described in detail. Next, the simulation model is coupled with a gray box optimization algorithm for design, synthesis and optimization of hybrid adsorption-reaction systems. Finally, the utility of the GRAMS framework is demonstrated through several different case studies.

2.1 GRAMS framework

2.1.1 Model development

Within GRAMS, the modeling assumptions made to yield a tractable set of PDEs are as follows:

- Temperature, concentration and pressure gradients are negligible in the radial direction. Therefore, the model is one-dimensional.
- The flow is described by an axial-dispersed plug flow model.
- Intra-particle heat and mass transfer limitations are negligible. Therefore, a pseudo-homogeneous adsorption-reaction model is assumed.
- The gas phase obeys the ideal gas law.
- The adsorbent and catalyst properties, and bed voidage are constant throughout the reactor.

- Darcy's law describes the frictional pressure drop along the column.
- A linear driving force (LDF) model accounts for adsorption kinetics.
- The heat transfer coefficient across the wall is assumed to be constant.

2.1.1.1 Model description

By using first principles [122] and aforementioned simplifying assumptions, the relevant transport equations are obtained. These equations involve conservation of mass of species i and overall mass balance, and conservation of heat energy of column and wall elements.

The component mass balance equation for each species $i \in I$ in the gas phase is as follows. It should be noted that species i would be present in bed void volume as well as in the void space in adsorbent and catalyst pores.

$$\varepsilon_t \frac{\partial C_i}{\partial t} = \varepsilon_b \frac{\partial}{\partial z}\left(D_L C \frac{\partial y_i}{\partial z}\right) - \varepsilon_b \frac{\partial \left(v C_i\right)}{\partial z} - \rho_{b,ads} \frac{\partial \overline{q}_i}{\partial t} - \rho_{b,cat} \sum_{k \in R} \nu_{ik} \eta_k (-R_k) \tag{2.1}$$

where C_i is the gas phase concentration of species i, y_i is the gas phase mole fraction of species i, $\overline{q}_i$ is the solid phase concentration, v is the interstitial velocity, $\rho_{b,ads}$ and $\rho_{b,cat}$ are adsorbent and catalyst bulk densities, respectively, ν_{ik} is the stoichiometric coefficient of species i in reaction k, η_k is the effectiveness factor for reaction k, R_k is the rate of reaction k, D_L is the axial dispersion coefficient, C is the total gas phase concentration, z is the bed length coordinate, ε_b, ε_p and ε_t are bed, particle and total porosities, respectively, and t is the time. In the above equation, the four terms on the right hand side take into account the contribution of diffusion, convection, adsorption and reaction terms to the species accumulation term in bed volume element. Note that the sets I and R contain all the species present and reactions occurring in the system, respectively.

We use the ideal gas law, $C_i = \dfrac{y_i P}{RT}$ and $C = \dfrac{P}{RT}$, for converting the gas phase concentrations into mole fractions in the component mass balance (Eq. 2.1). The chain rule is then used to obtain the following equation in terms of gas phase mole fraction (y_i):

$$\frac{\partial y_i}{\partial t} + \frac{y_i}{P}\frac{\partial P}{\partial t} - \frac{y_i}{T}\frac{\partial T}{\partial t} = D_L \frac{\varepsilon_b}{\varepsilon_t}\frac{T}{P}\frac{\partial}{\partial z}\left(\frac{P}{T}\frac{\partial y_i}{\partial z}\right) - \frac{\varepsilon_b}{\varepsilon_t}\frac{T}{P}\frac{\partial}{\partial z}\left(\frac{y_i v P}{T}\right) - \frac{\rho_{b,ads} RT}{\varepsilon_t P}\frac{\partial \overline{q}_i}{\partial t} - \frac{\rho_{b,cat} RT}{\varepsilon_t P}\sum_{k\in R}\nu_{ik}\eta_k(-R_k) \tag{2.2}$$

The above equation is summed over for all species $i \in I$ to obtain the dimensionless overall mass balance equation. Since $\sum_{i\in I} y_i$ = 1, we obtain an explicit equation for the partial derivative of P w.r.t t.

$$\frac{\partial P}{\partial t} = \frac{P}{T}\frac{\partial T}{\partial t} - \frac{\varepsilon_b T}{\varepsilon_t}\frac{\partial}{\partial z}\left(\frac{Pv}{T}\right) - \frac{\rho_{b,ads} RT}{\varepsilon_t}\sum_{i\in I}\frac{\partial \overline{q_i}}{\partial t} - \frac{\rho_{b,cat} RT}{\varepsilon_t}\sum_{i\in I}\sum_{k\in R}\nu_{ik}\eta_k(-R_k) \tag{2.3}$$

We only require $|I| - 1$ component mass balances along with overall mass balance to obtain an independent set of $|I|$ equations necessary to solve for gas phase mole fractions of all the species.

To consider the non-isothermal nature of reaction-adsorption processes, the energy balance equation for a bed volume element is formulated as,

$$\left(\rho_{b,ads}C_{p,ads} + \rho_{b,cat}C_{p,cat} + C_{p,a}\rho_{b,ads}\sum_{i\in I}\overline{q}_i\right)\frac{\partial T}{\partial t} = K_z\frac{\partial^2 T}{\partial z^2} - \frac{C_{pg}\varepsilon_b}{R}\frac{\partial}{\partial z}(vP) - C_{p,a}\rho_{b,ads}T\sum_{i\in I}\frac{\partial \overline{q}_i}{\partial t} + \rho_{b,cat}\sum_{k\in R}\eta_k R_k\left(-\Delta H_{r,k}\right) - \frac{C_{pg}\varepsilon_t}{R}\frac{\partial P}{\partial t} - \frac{2h_{in}}{r_{in}}(T - T_w) \tag{2.4}$$

where T and T_w are respectively the gas phase and wall temperatures, $C_{p,ads}, C_{p,cat}, C_{p,a}$ and C_{pg} are the specific heat capacities of adsorbent, catalyst, adsorbate and gas mixture, respectively, R is the universal gas constant, K_z is the axial gas heat conductivity, $\Delta H_{r,k}$ is the heat of reaction k, h_{in} and r_{in} are respectively the wall-bed heat transfer coefficient and inside bed radius. In the column energy balance equation above, the first two terms on the right hand side are the contributions of heat diffused and convected to the accumulation term. The third and fourth terms represent the heat of adsorption and reaction, respectively. The last term is for the heat transferred between

the column and wall.

The overall energy balance of a wall element, which includes the heat transfer across the wall, is formulated as,

$$\rho_w C_{pw} \frac{\partial T_w}{\partial \tau} = K_w \frac{\partial^2 T_w}{\partial z^2} + \frac{2 r_{in} h_{in}}{(r_{out}^2 - r_{in}^2)} (T - T_w) - \frac{2 r_{out} h_{out}}{(r_{out}^2 - r_{in}^2)} (T_w - T_a) \tag{2.5}$$

where h_{out} and r_{out} are wall-surroundings heat transfer coefficient and outside column radius, and ρ_w, $C_{p,w}$ and K_w are respectively the density, specific heat capacity and thermal conductivity of the wall. In the above equation, the first term on the right describes the heat conducted inside the wall whereas the second and third terms express the bed-to-wall and wall-to-surroundings heat transfer, respectively.

In the developed model, the Darcy's law describes the axial pressure drop along the packed column, and the respective steady-state momentum balance is formulated as follows [123]:

$$-\frac{\partial P}{\partial z} = \frac{150}{4 r_p^2} \left(\frac{1 - \varepsilon_b}{\varepsilon_b} \right)^2 \mu v \tag{2.6}$$

where μ is the viscosity of the gas phase mixture and r_p is the particle radius.

The LDF relation is used to compute the adsorption kinetics of gases into the adsorbent as follows:

$$\frac{\partial \overline{q_i}}{\partial t} = k_i \left(q_i^* - \overline{q_i} \right) \tag{2.7}$$

We adopt single and dual site single-component adsorption isotherms for obtaining the equilibrium loading capacity. Therefore, in the GRAMS framework, we include both single-site and dual-site Langmuir isotherms for computing equilibrium solid loading capacity as follows.

Single-site isotherm:

$$q_i^* = \frac{m_i b_i P_i}{1 + b_i P_i} \tag{2.8}$$

Dual-site isotherm:

$$q_i^* = \frac{m_{i,1} b_{i,1} P_i}{1 + b_{i,1} P_i} + \frac{m_{i,2} b_{i,2} P_i}{1 + b_{i,2} P_i} \tag{2.9}$$

The reaction rate, R_k, is a function of species' partial pressure, composition and temperature.

$$R_k = g_k(y, P, T) \tag{2.10}$$

For each of the case-studies discussed later, the appropriate reaction kinetics relations are reported accordingly.

The following scaled variables and scaling parameters are used for computing the dimensionless form of transport equations.

$$\overline{P} = \frac{P}{P_0}, \overline{T} = \frac{T}{T_0}, \overline{T}_w = \frac{T_w}{T_0}, \overline{T}_a = \frac{T_a}{T_0}, x_i = \frac{\overline{q}_i}{q_{s,0}}, \overline{v} = \frac{v}{v_0}, Z = \frac{z}{L}, \tau = \frac{tv_0}{L}, \overline{R}_k = \frac{R_k}{r_0}, \alpha_i = \frac{k_i L}{v_0} \tag{2.11}$$

where $\overline{P}$ is the dimensionless gas phase pressure, $\overline{T}$, $\overline{T}_w$ and $\overline{T}_a$ are the dimensionless gas phase, wall and ambient temperature, respectively, x_i is the dimensionless solid loading capacity, $\overline{v}$ is the dimensionless interstitial velocity, Z is the dimensionless length coordinate, τ is the dimensionless time, $\overline{R}_k$ is the dimensionless rate of reaction k, and α_i is the dimensionless lumped mass transfer coefficient of species i.

Finally, after applying the ideal gas assumption and scaling the transport equations, we obtain the following dimensionless NAPDE model.

Dimensionless component mass balance:

$$\frac{\partial y_i}{\partial \tau} = \frac{\varepsilon_b}{\varepsilon_t Pe}\frac{\overline{T}}{\overline{P}}\frac{\partial}{\partial Z}\left(\frac{\overline{P}}{\overline{T}}\frac{\partial y_i}{\partial Z}\right) - \frac{\varepsilon_b \overline{T}}{\varepsilon_t \overline{P}}\frac{\partial}{\partial Z}\left(\frac{y_i \overline{P} v}{\overline{T}}\right) - \psi\frac{\overline{T}}{\overline{P}}\frac{\partial x_i}{\partial \tau} - \psi_r \frac{\overline{T}}{\overline{P}}\sum_{k\in R}\nu_{ik}\eta_k(-\overline{R}_k) - \frac{y_i}{\overline{P}}\frac{\partial \overline{P}}{\partial \tau} + \frac{y_i}{\overline{T}}\frac{\partial \overline{T}}{\partial \tau} \tag{2.12}$$

Dimensionless overall mass balance:

$$\frac{\partial \overline{P}}{\partial \tau} = \frac{\overline{P}}{\overline{T}}\frac{\partial \overline{T}}{\partial \tau} - \frac{\varepsilon_b \overline{T}}{\varepsilon_t}\frac{\partial}{\partial \mathrm{Z}}\left(\frac{\overline{P}\overline{v}}{\overline{T}}\right) - \overline{T}\psi\sum_{i\in I}\frac{\partial x_i}{\partial \tau} - \overline{T}\psi_r\sum_{i\in I}\sum_{k\in R}\nu_{ik}\eta_k(-\overline{R}_k) \tag{2.13}$$

Dimensionless column energy balance:

$$\frac{\partial \overline{T}}{\partial \tau}=\Omega_1 \frac{\partial^2 \overline{T}}{\partial Z^2}-\Omega_{2a} \frac{\partial\left(\overline{v}\overline{P}\right)}{\partial \mathrm{Z}}-\Omega_{2\mathrm{b}} \frac{\partial \overline{P}}{\partial \tau}+\sum_{i \in I} \sigma_{a,i} \frac{\partial x_i}{\partial \tau}-\Omega_3 \overline{T} \sum_{i \in I} \frac{\partial x_i}{\partial \tau}-\Omega_4\left(\overline{T}-\overline{T}_w\right)+\sum_{k \in R} \sigma_{r,k} \eta_k(\overline{R}_k) \tag{2.14}$$

Dimensionless wall energy balance:

$$\frac{\partial \overline{T}_w}{\partial \tau}=\pi_1 \frac{\partial^2 \overline{T}_w}{\partial Z^2}+\pi_2\left(\overline{T}-\overline{T}_w\right)-\pi_3\left(\overline{T}_w-\overline{T}_a\right) \tag{2.15}$$

Dimensionless steady-state momentum balance:

$$\overline{v}=\frac{-4}{150 \mu v_0 L} r_p^2 P_0\left(\frac{\varepsilon_b}{1-\varepsilon_b}\right)^2\left(\frac{\partial \overline{P}}{\partial Z}\right) \tag{2.16}$$

Dimensionless LDF expression:

$$\frac{\partial x_i}{\partial \tau}=\alpha_i\left(x_i^*-x_i\right) \tag{2.17}$$

Single-site adsorption isotherm:

$$x_i^*=\frac{\left(\frac{m_i}{q_{s,0}}\right) b_i y_i \overline{P} P_0}{1+b_i y_i \overline{P} P_0} \tag{2.18}$$

Dual-site adsorption isotherm:

$$x_i^*=\frac{\left(\frac{m_{i,1}}{q_{s,0}}\right) b_{i,1} y_i \overline{P} P_0}{1+b_{i,1} y_i \overline{P} P_0}+\frac{\left(\frac{m_{i,2}}{q_{s,0}}\right) b_{i,2} y_i \overline{P} P_0}{1+b_{i,2} y_i \overline{P} P_0} \tag{2.19}$$

Dimensionless reaction rate:

$$\overline{R}_k=g'(y, \overline{P}, \overline{T}) \tag{2.20}$$

The steep gradients present in the adsorption-reaction system often result in difficulties in nu-

merical convergence. Due to scaling, the numerical issues are avoided and the resulting equations converge to the solution faster. Figure 2.2 graphically shows the scaled variables, which are present in the formulated set of equations below. The expressions for the dimensionless parameters present in (Eqs. 2.12-2.20) are reported in Table 2.1. This completes the NAPDE model for GRAMS. The following section presents the discretization scheme used for converting the aforementioned PDEs into ODEs.

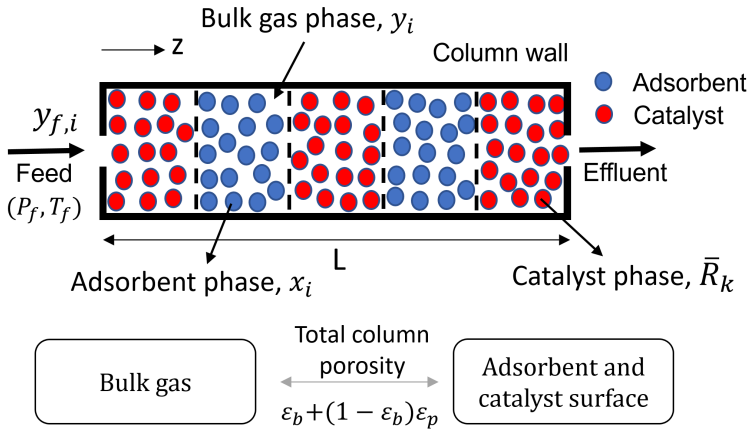

Figure 2.2: Graphical depiction of compartmentalized adsorption-reaction systems.

2.1.1.2 Numerical scheme

The finite volume method is used for spatially discretizing partial differential equations into coupled ordinary differential equations. In this scheme, the column domain is divided into a finite number of sub-domains (cells), and the nodes are defined at the center of each sub-domain. For a cell indexed j, the volume average of any conserved quantity, f, is defined as

$$f_j(t) = \frac{1}{\Delta V} \int_{V_j} f(t) dV. \tag{2.21}$$

The transport equations are formulated in integral form for each cell, and the derivatives present in the equations are approximated by interpolation with nodal values. The upward difference

Table 2.1: Dimensionless groups in the NAPDE model (Eqs. 2.12-2.20).

$$x_i^* = \frac{\left(\frac{m_i}{q_{s,0}}\right) b_i P_i}{1 + b_i P_i}$$

$$\alpha_i = \frac{k_i L}{v_0}$$

$$Pe = \frac{v_0 L}{D_L}$$

$$Pe_h = \frac{\varepsilon v_0 L \rho_g C_{pg}}{K_z}$$

$$\psi = \frac{R T_0 q_{s0} \rho_{b,ads}}{P_0 \varepsilon_t}$$

$$\psi_r = \frac{R T_0 L r_0 \rho_{b,cat}}{P_0 \varepsilon_t v_0}$$

$$\Omega_1 = \frac{\frac{K_z}{v_0 L}}{\left[\rho_{b,ads} C_{p,ads} + \rho_{b,cat} C_{p,cat} + C_{p,a} \rho_{b,ads} q_{s,0} \sum_{i \in I} x_i\right]}$$

$$\Omega_{2a} = \frac{\frac{C_{pg} \varepsilon_b P_0}{R T_0}}{\left[\rho_{b,ads} C_{p,ads} + \rho_{b,cat} C_{p,cat} + C_{p,a} \rho_{b,ads} q_{s,0} \sum_{i \in I} x_i\right]}$$

$$\Omega_{2b} = \frac{\frac{C_{pg} \varepsilon_t P_0}{R T_0}}{\left[\rho_{b,ads} C_{p,ads} + \rho_{b,cat} C_{p,cat} + C_{p,a} \rho_{b,ads} q_{s,0} \sum_{i \in I} x_i\right]}$$

$$\Omega_3 = \frac{C_{p,a} \rho_{b,ads} q_{s,0}}{\left[\rho_{b,ads} C_{p,ads} + \rho_{b,cat} C_{p,cat} + C_{p,a} \rho_{b,ads} q_{s,0} \sum_{i \in I} x_i\right]}$$

$$\Omega_4 = \frac{\frac{2 h_{in} L}{r_{in} v_0}}{\left[\rho_{b,ads} C_{p,ads} + \rho_{b,cat} C_{p,cat} + C_{p,a} \rho_{b,ads} q_{s,0} \sum_{i \in I} x_i\right]}$$

$$\sigma_{r,k} = \frac{\frac{\rho_{b,cat} r_0 L \left(-\Delta H_{R,k}\right)}{v_0 T_0}}{\left[\rho_{b,ads} C_{p,ads} + \rho_{b,cat} C_{p,cat} + C_{p,a} \rho_{b,ads} q_{s,0} \sum_{i \in I} x_i\right]}$$

$$\sigma_{a,i} = \frac{\frac{\rho_{b,ads} q_{s,0} \left(-\Delta H_{a,i}\right)}{T_0}}{\left[\rho_{b,ads} C_{p,ads} + \rho_{b,cat} C_{p,cat} + C_{p,a} \rho_{b,ads} q_{s,0} \sum_{i \in I} x_i\right]}$$

$$\pi_1 = \frac{K_w}{\rho_w C_{pw} v_0 L}$$

$$\pi_2 = \frac{2 r_{in} h_{in} L}{\left(r_{out}^2 - r_{in}^2\right) \rho_w C_{pw} v_0}$$

$$\pi_3 = \frac{2 r_{out} h_{out} L}{\left(r_{out}^2 - r_{in}^2\right) \rho_w C_{pw} v_0}$$

scheme UDS is used for relating the wall values, at boundaries $j+0.5$ and $j-0.5$, to the node values. Consequently, the finite volume scheme reduces to finite difference scheme. However, more accurate schemes such as WENO and TVD schemes can be used to relate wall values with node values [42]. Here, a combination of forward and backward difference approximations is used to discretize second order spatial derivatives. The coupled ordinary differential equations obtained by applying UDS scheme are provided below.

Spatially discretized component mass balance (Eq. 2.12):

$$\frac{\partial y_{i,j}}{\partial \tau} = \frac{\varepsilon_b}{\varepsilon_t Pe}\frac{\overline{T}_j}{\overline{P}_j}\frac{1}{\Delta Z}\left[\left.\frac{\overline{P}}{\overline{T}}\right|_{j+0.5}\left(\frac{y_{i,j+1}-y_{i,j}}{\Delta Z}\right) - \left.\frac{\overline{P}}{\overline{T}}\right|_{j-0.5}\left(\frac{y_{i,j}-y_{i,j-1}}{\Delta Z}\right)\right] - \frac{\varepsilon_b}{\varepsilon_t}\frac{\overline{T}_j}{\overline{P}_j}\frac{1}{\Delta Z}\times \left[\left.\frac{y_i\overline{P}\overline{v}}{\overline{T}}\right|_{j+0.5} - \left.\frac{y_i\overline{P}\overline{v}}{\overline{T}}\right|_{j-0.5}\right] - \psi\frac{\overline{T}_j}{\overline{P}_j}\frac{\partial x_{i,j}}{\partial \tau} - \psi_r\frac{\overline{T}_j}{\overline{P}_j}\sum_{k\in R}\nu_{ik}\eta_k(-\overline{R}_{k,j}) - \frac{y_{i,j}}{\overline{P}_j}\frac{\partial \overline{P}_j}{\partial \tau} + \frac{y_{i,j}}{\overline{T}_j}\frac{\partial \overline{T}_j}{\partial \tau} \tag{2.22}$$

Spatially discretized overall mass balance (Eq. 2.13):

$$\frac{\partial \overline{P}_j}{\partial \tau} = \frac{\overline{P}_j}{\overline{T}_j}\frac{\partial \overline{T}_j}{\partial \tau} - \frac{\varepsilon_b}{\varepsilon_t}\frac{\overline{T}_j}{\Delta Z}\left[\left.\frac{\overline{P}\overline{v}}{\overline{T}}\right|_{j+0.5} - \left.\frac{\overline{P}\overline{v}}{\overline{T}}\right|_{j-0.5}\right] - \overline{T}_j\psi\sum_{i\in I}\frac{\partial x_{i,j}}{\partial \tau} - \overline{T}_j\psi_r\sum_{i\in I}\sum_{k\in R}\nu_{ik}\eta_k(-\overline{R}_{k,j}) \tag{2.23}$$

Spatially discretized column energy balance (Eq. 2.14):

$$\frac{\partial \overline{T}_j}{\partial \tau} = \frac{\Omega_{1,j}}{\Delta Z}\left[\left(\frac{\overline{T}_{j+1}-\overline{T}_j}{\Delta Z}\right) - \left(\frac{\overline{T}_j-\overline{T}_{j-1}}{\Delta Z}\right)\right] - \frac{\Omega_{2a,j}}{\Delta Z}\left[\left.\overline{v}\overline{P}\right|_{j+0.5} - \left.\overline{v}\overline{P}\right|_{j-0.5}\right] - \Omega_{2b,j}\frac{\partial \overline{P}_j}{\partial \tau} + \sum_{i\in I}\sigma_{a,i,j}\frac{\partial x_{i,j}}{\partial \tau} - \Omega_{3,j}\overline{T}_j\sum_{i\in I}\frac{\partial x_{i,j}}{\partial \tau} - \Omega_{4,j}\left(\overline{T}_j - \overline{T}_{w,j}\right) + \sum_{k\in R}\sigma_{r,k,j}\eta_k(\overline{R}_{k,j}) \tag{2.24}$$

Spatially discretized wall energy balance (Eq. 2.15):

$$\frac{\partial \overline{T}_{w,j}}{\partial \tau} = \frac{\pi_1}{\Delta Z}\left[\left(\frac{\overline{T}_{w,j+1}-\overline{T}_{w,j}}{\Delta Z}\right) - \left(\frac{\overline{T}_{w,j}-\overline{T}_{w,j-1}}{\Delta Z}\right)\right] + \pi_2\left(\overline{T}_j - \overline{T}_{w,j}\right) - \pi_3\left(\overline{T}_{w,j} - \overline{T}_{a,j}\right) \tag{2.25}$$

Spatially discretized pressure drop (Eq. 2.16):

$$\overline{v}_{j+0.5} = \frac{-4}{150\mu v_0 L} r_p^2 P_0 \left(\frac{\varepsilon_b}{1-\varepsilon_b}\right)^2 \frac{\left(\overline{P}_{j+1} - \overline{P}_j\right)}{\Delta Z} \tag{2.26}$$

For calculating velocity at left and right walls, the spatial derivatives are approximated using forward and backward difference in the half cells, respectively.

$$\begin{aligned} \overline{v}_{0.5} = \overline{v}|_{Z=0} &= \frac{-8}{150\mu v_0 L} r_p^2 P_0 \left(\frac{\varepsilon_b}{1-\varepsilon_b}\right)^2 \frac{\left(\overline{P}_1 - \overline{P}_{0.5}\right)}{\Delta Z} \\ \overline{v}_{N+0.5} = \overline{v}|_{Z=1} &= \frac{-8}{150\mu v_0 L} r_p^2 P_0 \left(\frac{\varepsilon_b}{1-\varepsilon_b}\right)^2 \frac{\left(\overline{P}_{N+0.5} - \overline{P}_N\right)}{\Delta Z} \end{aligned} \tag{2.27}$$

In cases where the velocity at inlet boundary is given, Eq. 2.27 can be rearranged to obtain an explicit expression for calculating the inlet pressure.

$$\overline{P}_{0.5} = \overline{P}\big|_{Z=0} = \overline{P}_1 - \frac{\overline{v}_{0.5}\Delta Z}{\left[\frac{-8}{150\mu v_0 L} r_p^2 P_0 \left(\frac{\varepsilon_b}{1-\varepsilon_b}\right)^2\right]} \tag{2.28}$$

Spatially discretized LDF relation (Eq. 3.1):

$$\frac{\partial x_{i,j}}{\partial \tau} = \alpha_{i,j}\left(x^*_{i,j} - x_{i,j}\right) \tag{2.29}$$

Single-site langmuir adsorption isotherm:

$$x^*_{i,j} = \frac{\left(\frac{m_i}{q_{s,0}}\right) b_{i,j} y_{i,j} \overline{P}_j P_0}{1 + b_{i,j} y_{i,j} \overline{P}_j P_0} \tag{2.30}$$

Dual-site langmuir adsorption isotherm:

$$x^*_{i,j} = \frac{\left(\frac{m_{i,1}}{q_{s,0}}\right) b_{i,1,j} y_{i,j} \overline{P}_j P_0}{1 + b_{i,1,j} y_{i,j} \overline{P}_j P_0} + \frac{\left(\frac{m_{i,2}}{q_{s,0}}\right) b_{i,2,j} y_{i,j} \overline{P}_j P_0}{1 + b_{i,2,j} y_{i,j} \overline{P}_j P_0} \tag{2.31}$$

Spatially discretized rate equation (Eq. 2.20):

$$\overline{R}_{k,j} = g'(y_j, \overline{P}_j, \overline{T}_j) \tag{2.32}$$

Upwind difference scheme [124]:

$$f_{j+0.5} = \begin{cases} f_j & \text{when } \overline{P}_j > \overline{P}_{j+1} \\ f_{j+1} & \text{otherwise} \end{cases}$$

Using the above discretized set of Eqs. 2.22-2.32, we perform simulations for reactors, adsorbers and SERP. This system of coupled ODEs is solved using ode23s, a stiff ODE solver provided in MATLAB^{TM}. The following section shows how the GRAMS framework is employed to obtain different configurations of a reaction-adsorption column.

2.1.1.3 Model implementation

Figure 2.3 describes the overall GRAMS framework. The input to the framework includes the catalyst and adsorbent databases having appropriate physical and kinetics properties for catalysts, and physical, equilibrium and kinetic properties for adsorbents, respectively. For simulating a process with reaction and/or adsorption phenomena, three steps are required for obtaining system configuration in GRAMS. Firstly, the process which is to be simulated is selected. Here, there are several options to choose from including reactors, adsorbers, composite SERP, and layered processes. Next, materials with which the column is filled are selected. The corresponding material properties are subsequently obtained from the adsorbent and catalyst databases. Finally, the column configuration is decided which includes selecting process steps and appropriate boundary conditions.

In the NAPDE model in GRAMS, the overall set of equations used include Eqs. 2.22-2.32. The conservation equations (mass, momentum and energy balance) incorporate separate terms accounting for adsorption and reaction phenomena. When the column is packed only with adsorbent,

$\rho_{b,cat} = 0$ and therefore, the dimensionless parameters, ψ_r and $\sigma_{r,k}$ would equal zero. As a result, the corresponding reaction terms would be eliminated from the set of transport equations. The resulting model would be applicable for pure adsorption cases when there are no reactions occurring in the system. Similarly, when the column is packed with just catalyst, $\rho_{b,ads} = 0$ and therefore, $\psi = \Omega_3 = \sigma_{a,i} = 0$. Thus, the final set of dimensionless transport equations would not include adsorption terms, and the resulting model would be applicable for pure-reaction cases when none of the species present in gas mixture is adsorbed.

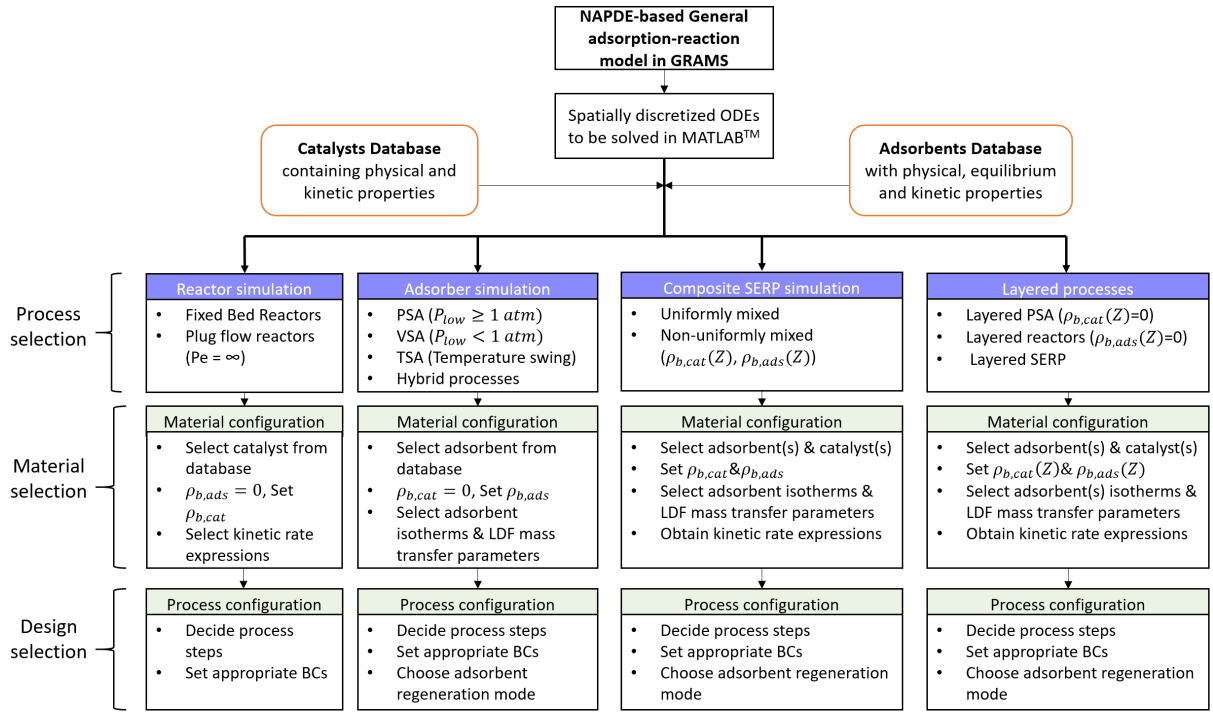

Figure 2.3: GRAMS implementation and procedure for specific process simulation. The developed framework can be used for obtaining different process configurations including reactors (FBR, PFR); adsorbers (PSA, VSA, TSA, hybrid processes); composite SERP (uniformly and non-uniformly mixed); and layered processes (layered adsorbers, layered reactors, layered SERP).

However, packed beds containing both adsorbent and catalyst would have non-zero bulk packing density values of both particles ($\rho_{b,cat} \neq 0$ & $\rho_{b,ads} \neq 0$) inside the bed. Consequently, the final set of transport equations formulated would consist of both reaction and adsorption terms account-

ing for respective phenomena. There are two ways in which adsorbent and catalyst particles can be distributed along the bed - homogeneous and heterogeneous. For homogeneous distributions having uniform mixtures of adsorbent and catalyst, the bulk packing density parameters would have finite values throughout the bed length. On the other hand, heterogeneous particle distributions with compartmentalized sections of catalyst and adsorbent would result in finite density values only for discrete sections of bed length. The catalytic packing density parameter would be equal to zero for sections filled with pure adsorbent, and equivalently, the adsorbent packing density would be equal to zero for bed sections containing pure catalyst. In the following sections, we use the GRAMS framework to simulate different adsorption-reaction processes and compare the results with experimental observations.

2.1.2 Model validation

2.1.2.1 Reactor simulation

A plethora of reactions are used in the industry for chemically converting raw materials into value-added products. One of such vital reactions is SMR [125, 126]. It is the leading low-cost method for producing H_2 - a product immensely useful in chemical, metallurgical, petroleum and electronic industries. SMR is also used in producing methanol which can further be processed to manufacture value-added chemicals such as olefins. SMR consists of three reversible reactions - (I)(II) strongly endothermic methane reforming, and (III) weakly exothermic WGSR. Due to equilibrium-limited nature of the reactions, low conversions of methane are achieved at moderate conditions. Since the reforming reactions involved in SMR are endothermic, higher temperatures are needed for attaining significant reaction conversions. The multi-tubular reactors, typically used for SMR, operate in pressure range of 1.6-4.1 MPa and with H_2O/CH_4 ratios of 2-4 for improving reaction conversions further [127].

$$H_2O + CH_4 \rightleftharpoons CO + 3\,H_2, \quad \Delta H_{298} = \Delta H_{r,I} = 206.2\,\mathrm{kJ/mol} \tag{I}$$

$$2\,H_2O + CH_4 \rightleftharpoons CO_2 + 4\,H_2, \quad \Delta H_{298} = \Delta H_{r,II} = 164.9\,\mathrm{kJ/mol} \tag{II}$$

$$H_2O + CO \rightleftharpoons CO_2 + H_2, \quad \Delta H_{298} = \Delta H_{r,III} = -41.1\,\mathrm{kJ/mol} \tag{III}$$

Here, we use the GRAMS framework for simulating SMR. Figure 2.4 shows a pictorial representation of the SMR tubular reactor considered in the simulations. The feed to the reactor consists of methane and excess steam, and the effluent stream consists of products H_2, CO_2 and CO, and unreacted CH_4 and H_2O. The major factors influencing the reactor performance are temperature and H_2O/CH_4 feed ratios. Therefore, our intention is to observe the effects of different reactor temperatures and feed compositions on methane conversion. We simulate the tubular reactor for (a) varying temperatures in the range 673-773 K and for (b) varying H_2O/CH_4 feed ratios in the range 2-3.5. For measuring reactor performance, we calculate the conversion of the limiting reactant - CH_4. A higher conversion of CH_4 results in higher hydrogen yield, thereby yielding better reactor performance. Thermodynamically, the methane conversion is expected to be higher at higher temperatures and higher H_2O/CH_4 feed ratios.

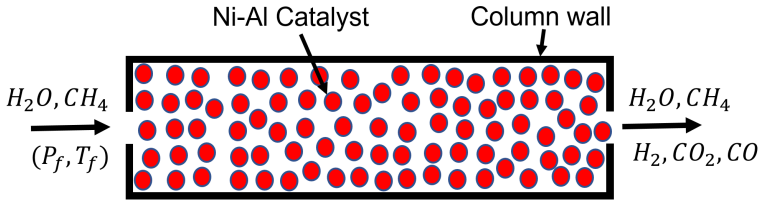

Figure 2.4: SMR in a tubular reactor on Ni-Al catalyst. The feed to the reactor consists of methane and excess steam at P_f and T_f. The products of SMR, i.e., hydrogen, carbon dioxide and carbon monoxide exit the reactor along with unreacted methane and steam.

For case a (different temperatures), a feed composed of H_2O and CH_4 in the ratio 3:1 enters the reactor having a flow rate of 0.0362 mmol/s. The reactor is assumed to be operating at an isobaric

pressure of 110 kPa without any pressure drop. The simulations are performed for three different temperatures - 673, 723, and 773 K. For case b (different feed compositions), a feed flow rate of 3.2475 mmol/s enters the column at constant pressure and temperatures of 136 kPa and 773 K, respectively. Four different H_2O/CH_4 ratios - 2, 2.5, 3 and 3.5 - are considered. The operating conditions of the reaction are tabulated in Table 2.3. Methane conversion is calculated by the ratio of methane consumed by SMR to the amount fed to the reactor as follows:

$$\mathrm{CH_4\ conversion\ (\%)} = \left(\frac{\mathrm{CH_{4,in}} - \mathrm{CH_{4,out}}}{\mathrm{CH_{4,in}}}\right) \times 100 \tag{2.33}$$

For both the cases, the reaction kinetic model of Xu and Froment [128] is used for calculating SMR reaction rates on Ni-Al catalyst. The rate equations are given in Table 2.2. A bed length of 2 m and reaction step time of 200 s are used in the simulations. It was observed that the outgoing concentration profiles had reached steady state values at these conditions. As the reactor is only filled with catalyst, the bulk packing densities of catalyst and adsorbent are set to be 249 (kg cat.)/(m^3 bed) and 0 (kg ads.)/(m^3 bed), respectively. Since there is no adsorbent, the dimensionless parameters ψ, Ω_3 and $\sigma_{a,i}$ (Table 2.1) would be equal to zero. Consequently, the adsorption terms would be eliminated from the set of model equations (Eqs. 2.12-2.14), and the framework is primed for simulating the SMR reactor.

For validating the model predictions, the methane conversion values obtained are compared with the experimental results of Shu et al. [127] and Gallucci et al. [129]. Figure 2.5 shows the dependence of methane conversion on temperature for case (a). The steady state methane conversions, predicted by the simulations, show an excellent agreement with thermodynamic equilibrium conversions and experimentally observed values. Due to the endothermicity of the reforming reactions, an increase in reaction temperature favors the conversion of methane to hydrogen. At 673 K, methane conversion of approximately 16% is observed experimentally which jumps to 36% at 773K. It roughly translates to an enhancement factor of two in reaction conversion due to 100 K increase in temperature. Therefore, significant improvements in SMR conversions can be made by operating the reactor at higher temperatures.

Table 2.2: Reaction kinetics for SMR [128].

$$-R_{I,j} = \frac{1}{(DEN_j)^2}\frac{k_{1,j}}{\left(y_{\mathrm{H_2O},j}\overline{P}_j P_0\right)^{2.5}}\left(\frac{y_{\mathrm{H_2},j}^3\, y_{\mathrm{CO},j}\,\overline{P}_j^4 P_0^4}{K_{I,j}} - y_{\mathrm{CH_4},j}\, y_{\mathrm{H_2O},j}\,\overline{P}_j^2 P_0^2\right)$$

$$-R_{II,j} = \frac{1}{(DEN_j)^2}\frac{k_{2,j}}{\left(y_{\mathrm{H_2O},j}\overline{P}_j P_0\right)^{3.5}}\left(\frac{y_{\mathrm{H_2},j}^4\, y_{\mathrm{CO_2},j}\,\overline{P}_j^5 P_0^5}{K_{II,j}} - y_{\mathrm{CH_4},j}\, y_{\mathrm{H_2O},j}^2\,\overline{P}_j^3 P_0^3\right)$$

$$-R_{III,j} = \frac{1}{(DEN_j)^2}\frac{k_{3,j}}{\left(y_{\mathrm{H_2},j}\overline{P}_j P_0\right)}\left(\frac{y_{\mathrm{H_2},j}\, y_{\mathrm{CO_2},j}\,\overline{P}_j^2 P_0^2}{K_{III,j}} - y_{\mathrm{CO},j}\, y_{\mathrm{H_2O},j}\,\overline{P}_j^2 P_0^2\right)$$

$$DEN_j = 1 + (K_{\mathrm{CO},j}\, y_{\mathrm{CO},j} + K_{\mathrm{H_2},j}\, y_{\mathrm{H_2},j} + K_{\mathrm{CH_4},j}\, y_{\mathrm{CH_4},j})\overline{P}_j P_0 + \frac{K_{\mathrm{H_2O},j}\, y_{\mathrm{H_2O},j}}{y_{\mathrm{H_2},j}}$$

$$K_{I,j} = \frac{1}{\exp(0.2513Z_j^4 - 0.3665Z_j^3 - 0.58101Z_j^2 + 27.1337Z_j - 3.2770)}\ atm^2$$

$$K_{III,j} = \exp\left(-0.29353Z_j^3 + 0.63508Z_j^2 + 4.17782Z_j + 0.31688\right); K_{II,j} = K_{I,j} \times K_{III,j}$$

$$k_{1,j} = 1.842 \times 10^{-4}\ \exp\left[-\frac{240,100}{R}\left(\frac{1}{\overline{T}_j T_0} - \frac{1}{648}\right)\right]\ \frac{kmol.bar^{0.5}}{kg_{cat}.hr}; Z_j = \frac{1000}{\overline{T}_j T_0} - 1$$

$$k_{2,j} = 2.193 \times 10^{-5}\ \exp\left[-\frac{243,900}{R}\left(\frac{1}{\overline{T}_j T_0} - \frac{1}{648}\right)\right]\ \frac{kmol.bar^{0.5}}{kg_{cat}.hr}$$

$$k_{3,j} = 7.558\ \exp\left[-\frac{67,130}{R}\left(\frac{1}{\overline{T}_j T_0} - \frac{1}{648}\right)\right]\ \frac{kmol}{kg_{cat}.hr.bar}$$

$$K_{\mathrm{CO},j} = 40.91\ \exp\left[\frac{70,650}{R}\left(\frac{1}{\overline{T}_j T_0} - \frac{1}{648}\right)\right]\ bar^{-1}; K_{\mathrm{H_2},j} = 0.0296\ \exp\left[\frac{82,900}{R}\left(\frac{1}{\overline{T}_j T_0} - \frac{1}{648}\right)\right]\ bar^{-1}$$

$$K_{\mathrm{CH_4},j} = 0.179\ \exp\left[\frac{38,280}{R}\left(\frac{1}{\overline{T}_j T_0} - \frac{1}{823}\right)\right]\ bar^{-1}; K_{\mathrm{H_2O},j} = 0.4152\ \exp\left[-\frac{88,680}{R}\left(\frac{1}{\overline{T}_j T_0} - \frac{1}{823}\right)\right]$$

Table 2.3: Parameters used for SMR simulation.

Parameter	Unit	Case (a) [127]	Case (b) [129]
Temperature	K	673-773	773
Pressure	kPa	110	136
H_2O/CH_4 feed ratio	–	3	2 - 3.5
Feed flow rate	mmol/s	0.0362	3.2475

The change in methane conversions with steam-to-methane feed ratio is shown in Figure 2.6. In the SMR reaction, methane is the limiting reagent and steam is in excess. As a result, an increase in the amount of steam enhances the consumption of methane. Experimentally, a jump in methane conversion from approximately 27% to 40% is observed by increasing H_2O/CH_4 feed ratio from 2 to 3.5 [127]. Accordingly, it is preferable to operate the SMR reactor with steam in excess. The calculated methane conversions by the model match the experimental results well. The conversions of methane can further be improved if the reaction is coupled with separation. For instance, incorporating a selective permeable membrane or an adsorbent inside the reaction

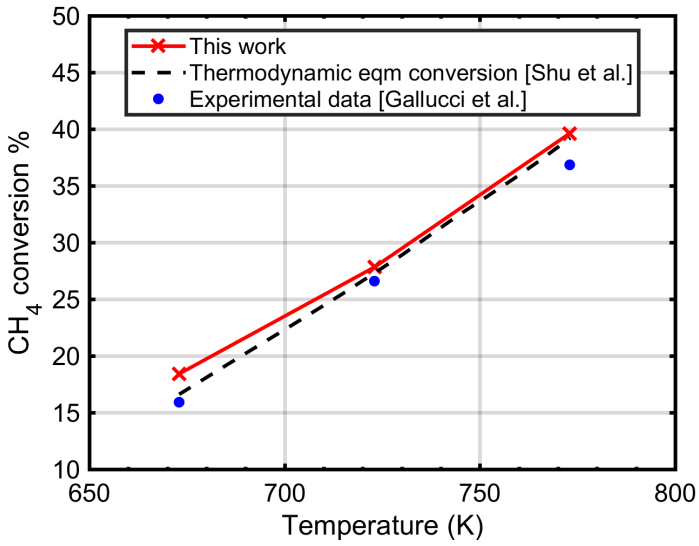

Figure 2.5: Effect of changing reactor temperature on methane conversion in SMR reactor at steady state. Feed pressure, P_f = 110 kPa; H_2O/CH_4 feed ratio = 3; feed flow rate = 0.0362 mmol/s.

column can significantly improve reaction conversions. The inclusion of an adsorbent inside the reactor is studied in the next section.

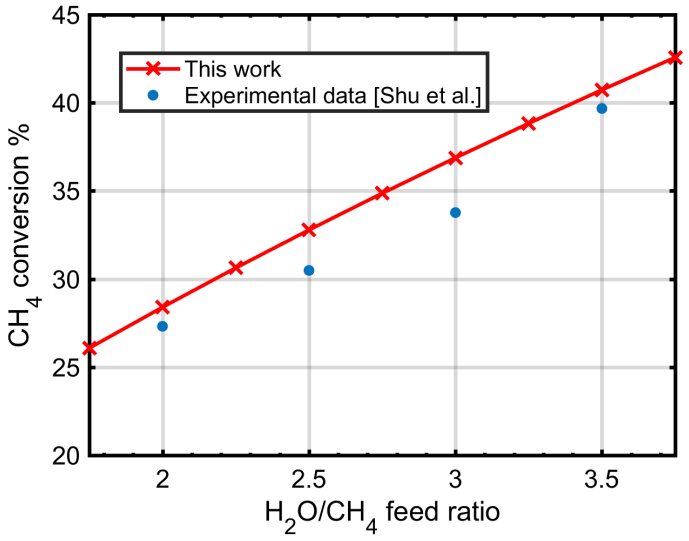

Figure 2.6: Effect of changing steam-to-methane feed ratio on methane conversions in SMR reactor at steady state. Feed temperature, T_f = 773 K; Feed pressure, P_f = 136 kPa; feed flow rate = 3.2475 mmol/s.

2.1.2.2 Sorption enhanced reaction process simulation

For hybrid adsorption-reaction systems, we validate the model predictions using an example of SE-WGSR. A key application of WGSR is for hydrogen production where it occurs along with SMR. During SMR, the feed consists of methane and hydrogen which react to form carbon monoxide byproduct. This carbon monoxide formed further reacts with steam via the WGSR route to produce hydrogen and carbon dioxide. However, WGSR can also happen when only CO and H_2O are present in the feed. This provides an opportunity to convert carbon monoxide, a toxic gas species, to hydrogen via shift reaction. WGSR can also be used in conjunction with fuel cells to produce electric and thermal energy directly from CO and H_2O [130].

$$\mathrm{H_2O + CO \rightleftharpoons CO_2 + H_2},\ \Delta H_{298} = -41.1\,\mathrm{kJ/mol} \tag{IV}$$

In industry, the syngas needed for WGSR is produced by reacting coal with a mixture of H_2O and O_2 at temperatures above 1000 °C. This syngas mixture of CO and H_2 then reacts in the water gas shift reactor for producing the desirable product, H_2, and the undesirable product, CO_2. For achieving significant conversions of syngas to hydrogen, WGSR is carried out in two steps. The first step of the process uses a high-temperature shift catalyst composed of FeO followed by the second step consisting of a low temperature shift catalyst based on a mixture of Cu, ZnO and Al_2O_3. The product stream is then purified using PSA for obtaining high-purity H_2.

WGSR is inherently thermodynamically limited and thus requires a high temperature to result in significant product formation. This limitation can be overcome by introducing the sorption enhancement principle to a water gas shift reactor. In compliance with the Le Chatelier's principle, removing CO_2 from the reaction gas mixture in a water gas shift reactor further pushes H_2 production. The resulting SE-WGSR is capable of producing pure hydrogen at significantly reduced reaction temperatures. As the SE-WGSR now operates at relatively lower temperatures, the requirement of a high temperature shift catalyst is eliminated, and the reactor now only has Cu-ZnO-Al_2O_3 low temperature shift catalyst. Consequently, SE-WGSRs are generally packed

with a uniform mixture of low temperature shift catalyst and K_2CO_3-promoted hydrotalcite (HTC) sorbent wherein the catalyst promotes the WGSR whereas the adsorbent acts as a CO_2 acceptor.

The objective of this section is to draw a comparison between our predicted results for SE-WGSR operation and existing experimental data available in the literature. Jang et al. [13] studied SE-WGSR which simultaneously incorporates WGSR with selective adsorption of carbon dioxide. A study on the effects of operating conditions such as H_2O/CO ratio, catalyst/sorbent ratio, feed and shell side temperature, and reaction pressure on reaction performance was conducted. Furthermore, a novel thermal swing sorption enhanced reaction was also proposed wherein the sorbent is regenerated by pressure and temperature swing. The focus of our work is to demonstrate the validity of our developed model for SE-WGSR. We only compare the model predictions of column breakthrough profiles for SE-WGSR with the experimental results of Jang et al. We replicate the experimental conditions to have a fair comparison. A reactor 0.502 m long with a diameter of 0.0173 m is packed with an admixture of Cu-ZnO-Al_2O_3 catalyst and HTC adsorbent. The weight percent ratio of catalyst to adsorbent is 50%:50% and the bulk packing densities for both particles are 820 kg/(m^3), respectively. A constant bed void fraction of 0.28 is considered for the simulations. Before the start of the process, the SE-WGSR is saturated with steam and argon. A feed mixture of 10.9% CO, 56.4% H_2O, and 32.7% Ar is then introduced to the reactor at 673 K and 1 atm. The volumetric feed flow rate remains constant at 458.6 mL STP/min throughout. A single site Langmuir model is adopted for calculating solid loading capacity, and the respective equations for the model and mass transfer coefficient are given in Appendix A. The fitted dual site parameters are listed in Table D.2. Eq. 2.34 and 2.35 show the kinetics of WGSR over Cu-ZnO-Al_2O_3 catalyst obtained from Choi et al. [131] and the simplified expression of K_{WGS} obtained from Moe et al. [132]. The kinetic and bed parameters used are reported in Table D.2. The wall temperature is kept constant at 673 K and the discretization consists of 100 finite volumes.

Table 2.4: Parameters used for SE-WGSR simulation [13].

Parameter	Unit	Value
Reactor diameter, d_p	m	0.0173
Reactor length, L	m	0.502
Volumetric flow rate	mL STP/min	458.6
Superficial velocity	m/s	0.077
Interstitial velocity, v	m/s	0.275
Feed temperature, T_f	K	673
Feed pressure, P_f	kPa	101.325
Bed porosity, ε_b	–	0.28
Adsorbent bulk density, $\rho_{b,ads}$	kg ads./(m^3 bed)	820
Catalyst bulk density, $\rho_{b,cat}$	kg cat./(m^3 bed)	820
Feed composition		
CO(%)	–	10.9
H_2O(%)	–	56.4
Inert(%)	–	32.7
HTC Adsorbent isotherm parameters		
m_{CO_2}	mol/kg	0.3033
$b_{o,\,CO_2}$	Pa^{-1}	0.000236
ΔU_{CO_2}	J/mol	-31475.6
Reaction kinetics parameters		
Rate constant for WGSR, k_0	mol/(gcat.hr.atm^2)	2.96×10^5
Activation energy, E_{WGS}	J/mol	47400

$$R_{WGS,j} = k_0 \exp\left[\frac{-E_{WGS}}{R\overline{T}_j T_0}\right]\left(y_{\mathrm{CO}} y_{\mathrm{H_2O}} \overline{P}_j^2 P_0^2 - \frac{y_{\mathrm{CO_2}} y_{\mathrm{H_2}} \overline{P}_j^2 P_0^2}{K_{WGS,j}}\right) \times \frac{1}{101325^2}\left(\frac{\mathrm{mol}}{\mathrm{gcat.hr}}\right) \tag{2.34}$$

$$K_{WGS,j} = \exp\left[\frac{4577.8}{\overline{T}_j T_0} - 4.33\right] \tag{2.35}$$

Figure 2.7 shows the H_2O and Ar free effluent gas phase mole fractions exiting the SE-WGSR with time. It is to be noted that two different y-axis scales are used for plotting the effluent gas phase mole fractions to clearly illustrate the breakthrough of CO_2 and unreacted CO. In the beginning of the operation, pure hydrogen is produced. During this phase, the majority of carbon dioxide produced inside the SE-WGSR is captured by the K_2CO_3-promoted HTC adsorbent. This *in situ* removal of CO_2 from the gas mixture pushes the equilibrium forward to favor hydrogen

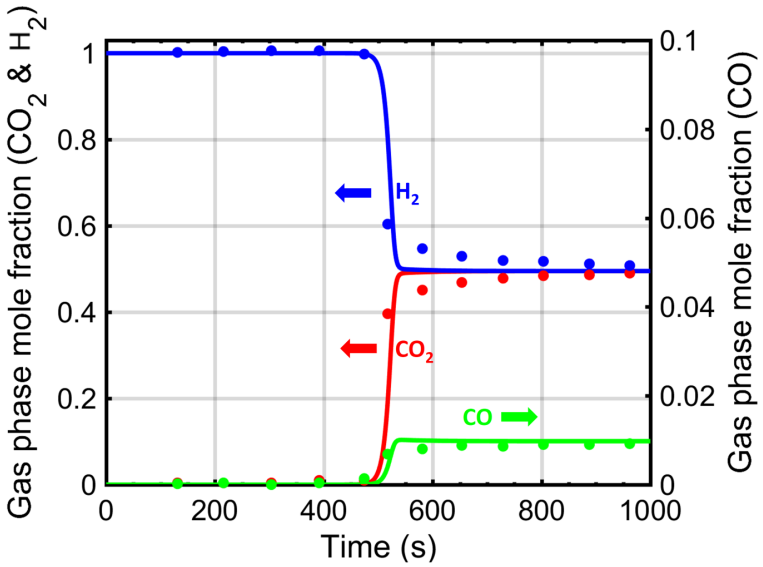

Figure 2.7: SE-WGSR breakthrough simulation. Effluent gas phase (Ar and N_2 free) mole fractions of hydrogen (blue), carbon dioxide (red) and carbon monoxide (green). The solid lines (—) are our model's predictions and dots denote the experimental data of Jang et al. [13].

production. Consequently, the effluent stream is pure hydrogen with insignificant amounts of unreacted CO and unadsorbed CO_2. It shows that WGSR can almost run to completion by removing CO_2 from the reaction mixture. This observation is further supported by the experimental results of Harrison [9]. They analyzed that roughly all of carbon monoxide can be converted to hydrogen if 99-99.5% of CO_2 is captured from the gas phase reaction mixture. The sorbent has a finite capacity for adsorbing CO_2 and as it nears its saturation limit, breakthrough is achieved. From this point, the effluent gas concentration is essentially the thermodynamically governed steady state WGS concentrations which would have occurred in the absence of sorbent. The effluent stream now has CO_2 and H_2 in majority with a small amount of unreacted CO. The comparison with the experimental results shows an excellent agreement with model predictions thereby validating our model for another SERP technology.

2.1.2.3 Pressure swing adsorption simulation

The emission of greenhouse gases by burning fossil fuels is one of the leading reasons of increasing global warming on the planet. Therefore, the need of capturing and sequestering CO_2 is

pressing now more than ever for preventing further damage to the environment. Several technologies for CO_2 capture such as absorption, adsorption, cryogenics, and membrane separation have been extensively studied to discover potential routes for CO_2 capture. Out of all these separation processes, the adsorption technology is particularly attractive due to low operation and equipment costs, automated operation, and re-usability of the adsorbent. It offers an economic and sustainable route for alleviating the effects of greenhouse gases.

PSA, VSA and TSA are some technologies leveraging the same adsorption principles for separating gas mixtures. Fundamentally, an adsorbent with a high selectivity and capacity of CO_2 is chosen for adsorbing carbon dioxide from the feed gas mixture. Once enough CO_2 has been adsorbed, the adsorbent is then regenerated either *in situ* or in a separate column specifically designed for desorption purposes. The regeneration can be done by a swing in pressure, temperature, and/or concentration. An appropriate selection of suitable technique required for regeneration depends on product specifications desired, operation challenges faced and other economic aspects.

There have been numerous studies on CO_2 capture by adsorption. One such study by Wang et al. [133] evaluated the feasibility of the VSA, TSA and hybrid vacuum-temperature swing adsorption (VTSA) processes for capturing CO_2 from flue gas. Their work was based on the premise that just vacuum or temperature swing is not sufficient to capture CO_2 from flue gas with both high purity and recovery. Therefore, they employed a combination of temperature and pressure swing for *in situ* regeneration of adsorbent. Several experiments were performed to compare performance of VSA, TSA and hybrid VTSA for capturing CO_2 from flue gas mixture at near ambient pressure and temperature. The zeolite 13X-APG adsorbent was used due to high working capacity, and high selectivity of capturing CO_2 over N_2. Their results demonstrated the advantages of hybrid VTSA process over both VSA and TSA for capturing carbon from flue gas mixture. The benefits of employing both vacuum and temperature swing for regenerating the adsorption column resulted in significantly higher CO_2 recovery (92.2%) and CO_2 purity (93.6%).

Here, we simulate the 4-step VSA cycle proposed by Wang et al. [133] using GRAMS for capturing CO_2 from flue gas. The aim is to extend the applicability of our developed model for cyclic

adsorption processes. As the adsorber is packed only with an adsorbent, the catalyst bulk density, $\rho_{b,cat}$, would be equal to zero, and therefore, $\psi_r = \sigma_{r,k} = 0$. The corresponding reaction terms would be eliminated from the model equations (Eqs. 2.12-2.14), and the resulting set of formulated equations would be applicable for pure-adsorption cases. The boundary conditions for each step can be found in Appendix B. The process cycle considered in our simulations consist of steps typical to VSA - adsorption, vacuum, purge and pressurization. These process steps are briefly described below with feed specifications and column operating parameters. Figure 2.8 depicts the schematic of the VSA process, and Table 2.6 reports the duration and operating conditions of each of the steps.

- Step 1: Co-current adsorption (open-open): the feed to the VSA column consists of 15% CO_2 and 85% N_2 at P_H and T_f. The effluent stream is almost pure nitrogen with small amounts of CO_2.
- Step 2: Counter-current depressurization (open-closed): The column is then depressurized exponentially from P_H to P_L by regulating the pressure at $z = 0$. The outlet stream contains both CO_2 and N_2 in sufficient amounts.
- Step 3: Counter-current purge (open-open): N_2 is used for purging CO_2 out of the column. The adsorbent is efficiently regenerated at the end of this step.
- Step 4: Co-current pressurization (open-closed): the column is linearly pressurized from P_L to P_H by the flue gas mixture consisting of 15% CO_2 and 85% N_2. The regenerated bed is now ready to undergo another VSA cycle.

Table 2.5: Dual-site Langmuir model parameters for CO_2 adsorption of zeolite 13X-APG.

Gas (i)	$m_{1,i}$(mol/kg)	$m_{2,i}$(mol/kg)	$b_{0,1,i}(\mathrm{Pa}^{-1})$	$b_{0,2,i}(\mathrm{Pa}^{-1})$	$\Delta U_{1,i}$(J/mol)	$\Delta U_{2,i}$(J/mol)
CO_2	3.7854	1.0005	3.92×10^{-10}	5.17×10^{-10}	-30266.91	-38695.35
N_2	1	0.4260	1.16×10^{-9}	0	-20207.66	-25944.05

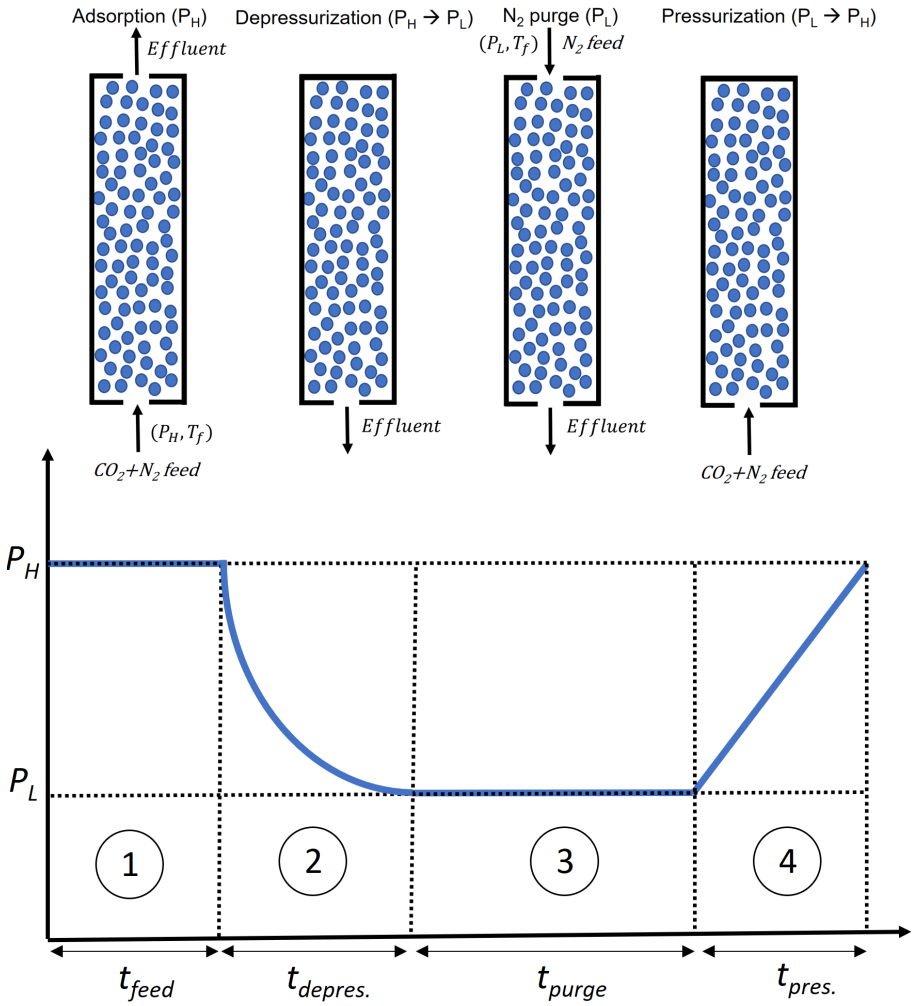

Figure 2.8: Graphical depiction of the 4-step VSA cycle for capturing CO_2 from flue gas mixture. The cycle consists of 4 steps - (a) co-current adsorption at P_H, (b) counter-current exponential depressurization from P_H to P_L, (c) counter-current purge at P_L, and (d) co-current linear pressurization from P_L to P_H.

A bed of length 0.35 m and radius 0.0125 m is packed with zeolite 13X-APG adsorbent. The incoming feed to the bed is composed of 15% CO_2 and 85% N_2, and the flow rate is fixed at 3.318 SLPM. Initially, the pressure and temperature of the column is the same as the feed conditions - 298 K and 1 atm. The zeolite adsorbent is regenerated under a vacuum for which a nitrogen purge (at 298 K and 10 kPa) is used. During pressurization, pressure is linearly increased from P_L to P_H whereas, during depressurization, bed pressure is exponentially decreased from P_H to P_L. The pressure equation at the outlet boundary during the depressurization step and the value of

the exponential parameter λ used are both reported in Table 2.6. A dual site Langmuir isotherm is used for the simulations as it fits the adsorption equilibrium data of CO_2 and N_2 on zeolite 13X-APG well. The fitted dual-site parameters are reported in Table 2.5. The simulations were run for 20 cycles after which cyclic steady state (CSS) is attained resulting in negligible changes in concentration. A constant wall temperature of 298 K is maintained throughout the simulation time.

Table 2.6: Parameters used for VSA simulation [133].

Parameter	Unit	Value
Reactor diameter, d_p	m	0.025
Reactor length, L	m	0.35
Bed porosity, ε_b	–	0.39
Adsorbent bulk density, $\rho_{b,ads}$	kg ads./(m^3 bed)	666.5
Catalyst bulk density, $\rho_{b,cat}$	kg cat./(m^3 bed)	0
Axial dispersion coefficient, D_L	m^2/s	8.33×10^{-4}
Bed-wall heat transfer coefficient, h_{in}	W/(m^2.K)	50
Solid heat capacity, C_{ps}	J/(kg.K)	920
Feed conditions		
CO_2(%)	–	15
N_2(%)	–	85
Volumetric flow rate	SLPM	3.318
Interstitial velocity, v	m/s	0.3154
Feed pressure, P_f	kPa	101.325
Feed temperature, T_f	K	298
Purge conditions		
N_2(%)	–	100
Volumetric flow rate	SLPM	0.15
Interstitial velocity, v	m/s	0.1445
Purge pressure, P_f	kPa	10
Purge temperature, T_f	K	298
Step times		
Adsorption, t_{feed}	s	120
Depressurization, $t_{depres.}$	s	120
N_2 purge, t_{purge}	s	90
Feed pressurization, $t_{pres.}$	s	60
Depressurization	$P = P_L + (P_H - P_L)e^{-\lambda t}$	
λ	s^{-1}	0.063

The predicted adsorber performance is compared with experimental observations. The performance of the VSA process is judged on the basis of CO_2 recovery, purity, and productivity. These parameters are calculated using the following equations wherein the ideal gas law is used for calculating the concentrations at inlet and outlet boundaries.

$$\text{CO}_2 \text{ purity } (\%) = \frac{\int_0^{t_{\text{depres.}}} \left.\frac{y_{\text{CO}_2} Pv}{RT}\right|_{z=0} dt + \int_0^{t_{\text{purge}}} \left.\frac{y_{\text{CO}_2} Pv}{RT}\right|_{z=0} dt}{\int_0^{t_{\text{depres.}}} \left.\frac{Pv}{RT}\right|_{z=0} dt + \int_0^{t_{\text{purge}}} \left.\frac{Pv}{RT}\right|_{z=0} dt} \times 100 \tag{2.36}$$

$$\text{CO}_2 \text{ recovery } (\%) = \frac{\int_0^{t_{\text{depres.}}} \left.\frac{y_{\text{CO}_2} Pv}{RT}\right|_{z=0} dt + \int_0^{t_{\text{purge}}} \left.\frac{y_{\text{CO}_2} Pv}{RT}\right|_{z=0} dt}{\int_0^{t_{\text{feed}}+t_{\text{pres.}}} \left.\frac{y_{\text{CO}_2} Pv}{RT}\right|_{z=0} dt} \times 100 \tag{2.37}$$

$$\text{CO}_2 \text{ productivity } (\text{mol CO}_2/(\text{kg ads. sec})) = \frac{\left(\int_0^{t_{\text{depres.}}} \left.\frac{y_{\text{CO}_2} Pv}{RT}\right|_{z=0} dt + \int_0^{t_{\text{purge}}} \left.\frac{y_{\text{CO}_2} Pv}{RT}\right|_{z=0} dt\right) \varepsilon_b}{t_{\text{total}}\, \rho_{b,ads}\, L} \tag{2.38}$$

where t_{feed}, $t_{depres.}$, $t_{pres.}$ and t_{purge} are feed, depressurization, pressurization and purge step times, respectively.

CO_2 purity is the percentage composition of CO_2 in the effluent streams during depressurization and purge steps. For measuring CO_2 recovery, the ratio of CO_2 captured (during depressurization and purge stages) to CO_2 fed to the adsorber (during feed and pressurization steps) is computed. The productivity of CO_2 is calculated by determining the number of moles of CO_2 exiting the column during depressurization and purge steps for a unit amount of adsorbent per unit time. The higher values of CO_2 purity, recovery and productivity are desirable and lead to better performance of the adsorber.

Figure 2.9 shows the gas phase mole fraction of CO_2 and N_2 at the inlet and outlet ends with time. The inlet and outlet ends would switch after the end of adsorption and purge steps. This switching is due to the change in the flow direction inside and/or to the column. During the

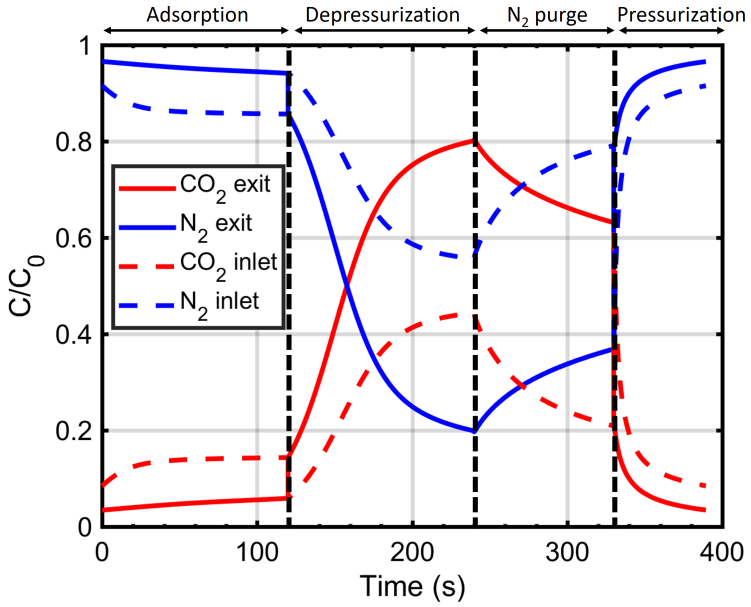

Figure 2.9: Effluent mole fraction of CO_2 and N_2 for a 4-step VSA cycle. These profiles have been computed at CSS (20th cycle). The solid lines (—) and the dashed lines (- -) are the concentrations at the outlet and inlet ends, respectively. The time for each of the constituting steps are (a) adsorption (0-120 s), (b) depressurization (120-240 s), (c) purge (240-330 s), and (d) pressurization (330-390 s).

adsorption step, nearly pure nitrogen ($\sim$95%) comes out in the effluent stream. In the subsequent vacuum step, a decrease in pressure drives the adsorbed CO_2 out of the solid phase. The majority of CO_2 is evacuated by the nitrogen purge. According to simulated results, roughly three times more CO_2 is obtained during the purge step in comparison to the vacuum step.

A comparison between the model predictions and experimental results for CO_2 recovery, purity and productivity is performed. Experimentally, a CO_2 recovery of 57.2%, purity of 64.1% and productivity of 0.101 $kgCO_2$/(kgads.hr) is observed [133]. According to simulation results, a CO_2 recovery of 57.1%, purity of 71.7%, and productivity of 0.099 $kgCO_2$/(kgads.hr) is obtained. The model predictions for recovery and productivity are in agreement with the experimental values. However, the model overestimates the CO_2 purity value. One reason for the deviation could be the assumption of pseudo-homogeneous nature of the process according to which no concentration and temperature gradients exist between the bulk gas and solid particles. In reality, there could be appreciable gradients in concentration and temperature which would necessitate the need of

using a more detailed heterogeneous model. Furthermore, better LDF mass transfer coefficients values for obtaining the adsorption and desorption kinetics of CO_2 and N_2 on zeolite 13X-APG are required for more accurate simulations of the adsorption process.

2.2 Optimal synthesis of periodic sorption enhanced reaction processes

This section discusses the SERP optimization model for a single-bed SERP system with an admixture of catalyst and sorbent. The model consists of an objective function (e.g., maximizing product purity or productivity, or minimizing production cost) and several constraints. The developed optimization framework has been demonstrated by optimizing the design and operation of SE-SMR and SE-WGSR systems.

2.2.1 Periodic SERP: process and cycle configurations

In SERP operation, when the sorbent reaches near its saturation limit, regeneration of the sorption enhanced reactor is performed. Sorbent regeneration can occur either *in situ* or outside the reactor in a separate column. Due to intermediate bed regeneration steps, the product formation via single-bed SERP is discontinuous. This results in a multi-step, multi-cycle process. Some of the steps would be aimed at regenerating the bed whereas other steps would produce the desired products. For continuous product formation, multiple reactors need to be operated in tandem. Typically, an SERP cycle consists of a combination of sorption-reaction, pressurization, depressurization and purging steps. A single-column, periodic SERP process can have at most six unique modes of operation: Sorption-Reaction (SR), Depressurization (DP), Pressurization (P), Reverse Sorption-Reaction (rSR), Reverse Depressurization (rDP), and Reverse Pressurization (rP). Figure 2.10 depicts the SERP column configurations corresponding to these operation modes.

The operation modes majorly differ in boundary conditions used for performing simulations. During the sorption-reaction modes (SR and rSR), both the boundaries of the column are open (Figure 2.10). The pressure at the column-exit is fixed which can then be used for obtaining outlet velocities using the Darcy's law. At the inlet, the feed velocity is fixed, which is used for obtaining inlet pressures. During pressurization modes (P and rP), the column pressure is increased by

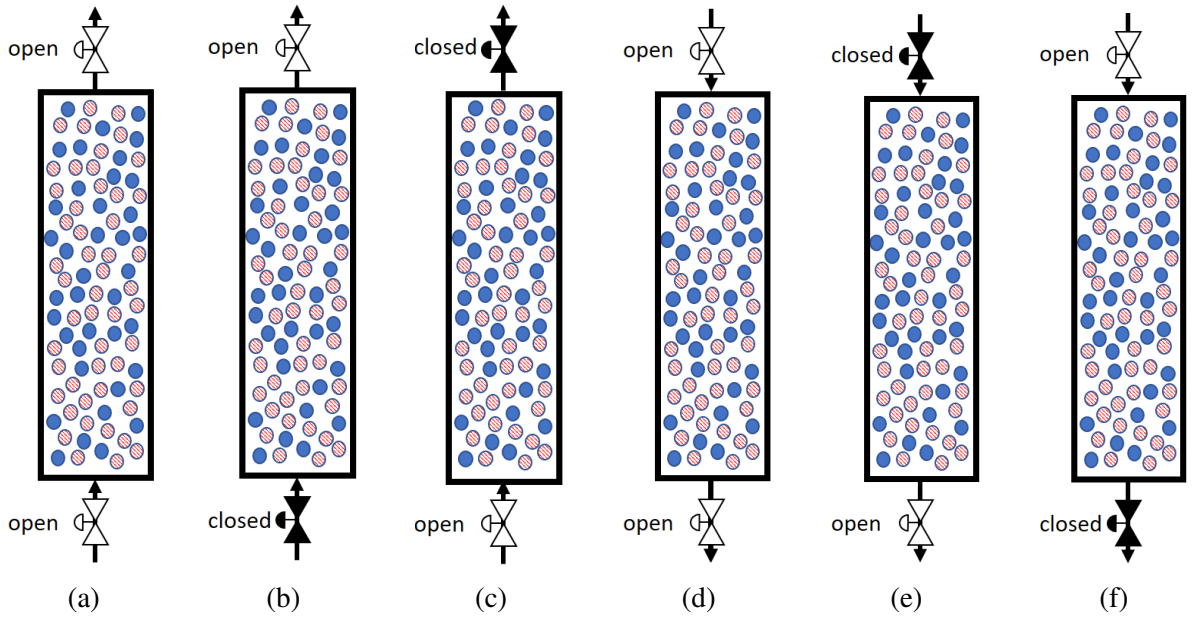

Figure 2.10: Possible operation stages of a column with sorption/reaction phenomena. (a) Sorption-Reaction (SR), (b) Depressurization (Dp), (c) Pressurization (P), (d) Reverse Sorption-Reaction (rSR), (e) Reverse Depressurization (rDP), and (f) Reverse Pressurization (rP).

keeping the inlet boundary open and the exit boundary closed. The pressure at the inlet boundary steadily increases with time during column pressurization. This inlet pressure is then used for obtaining inlet feed velocities. During depressurization stages (DP and rDP), the pressure at the outlet boundary is set, and therefore, outlet velocities can be obtained using the Darcy's law. At the closed end of the column, the velocity is always set to zero.

The operation modes shown in Figure 2.10 can be selectively chosen and arranged in different manners to obtain numerous SERP cycle configurations. For example, SR $\rightarrow$ rDP $\rightarrow$ P denotes a 3-step SERP cycle where the cycle has three modes: SR, rDP, and P. These three operation modes are repeated over and over again in a cyclic manner. In general, when there are no constraints imposed on a process cycle configuration, SERP cycle can be configured in m^n possible ways, where m and n represent the maximum possible number of operation modes and number of steps in a cycle, respectively. A few examples of cycle configurations along with corresponding pressure variations are shown in Figure 2.11. The most basic SERP cycle consists of two steps - sorption-reaction and desorption (Figure 2.11a). It is to be noted that either sorption or desorption phenomena can occur

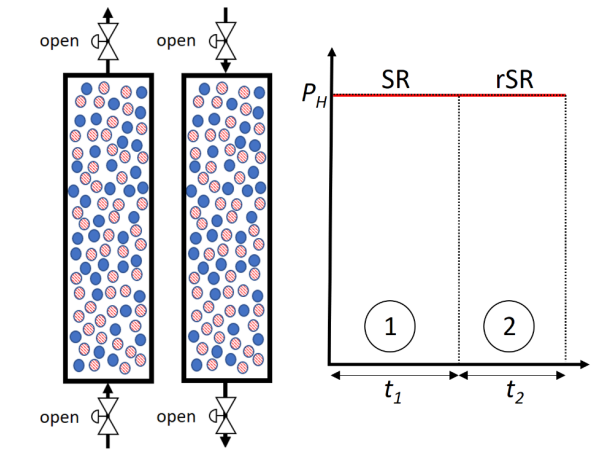

(a) 2-step SERP: SR → rSR

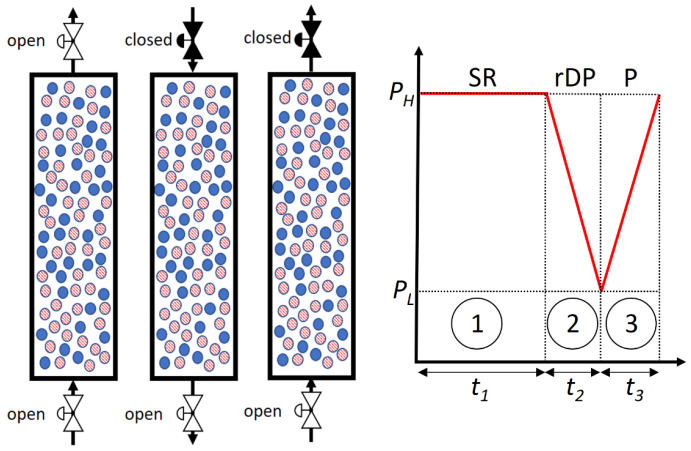

(b) 3-step SERP: SR → rDP → P

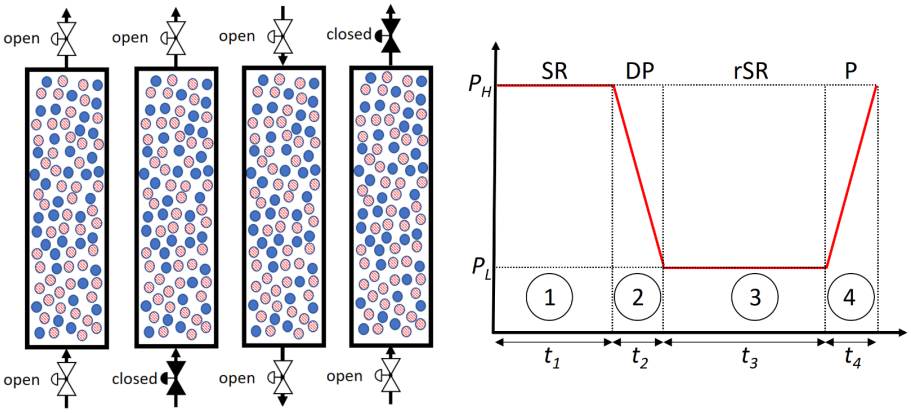

(c) 4-step SERP: SR → DP → rSR → P

Figure 2.11: Different cycle configurations obtained by combining different operation modes. (a) 2-step cycle with SR and rSR, (b) 3-step cycle with SR, rDP and P, (c) 4-step cycle with SR, DP, rSR and P. Using different selection and sequence of operation modes, several other cycle configuration designs can be obtained.

during SR/rSR steps depending on the pressure at which the column is operating. In this cycle, the column is operated at same pressure throughout and purge step (rSR) regenerates the bed for the next cycle. Figure 2.11b shows a 3-step cycle wherein regeneration of the bed is predominantly achieved during depressurization step. In SERP operation, sorption-reaction and purging steps might be favorable at different pressures. For improving process performance, intermediate steps are therefore used to carry out sorption-reaction and desorption at respective favorable pressures. Figure 2.11c shows a 4-step cycle in which bed purge (rSR) occurs at a lower pressure in comparison to the first step.

The sequence of the operation modes in SERP cycle design has cyclic symmetry. For example, the 4-step cycle: SR $\rightarrow$ rDP $\rightarrow$ rSR $\rightarrow$ P is the same as the cycle: rDP $\rightarrow$ rSR $\rightarrow$ P $\rightarrow$ SR (considering same corresponding step durations) due to cyclic symmetry. We break this symmetry by considering the first operation mode of an SERP cycle to be sorption-reaction (SR). This assumption is made so as to simplify the operation mode selection for the first step. Furthermore, this is done as the SERP column is fed with reactant species during the first step of the cycle, and the product species is formed during first step.

The performance of SERP systems depends on several discrete decisions and continuous operating parameters. The discrete decisions include selecting optimal operation modes in an appropriate sequence such that the desired performance from SERP could be obtained. The continuous decision variables affecting SERP performance consist of reactant feed composition, operating pressures and temperatures, step durations, product venting time, SERP column geometry, feeds flow rate, and sorbent-to-catalyst mass ratio. The following section discusses the SERP model formulation used for optimizing these discrete and continuous decision variables.

2.2.2 SERP Synthesis Model Formulation

2.2.2.1 Indices and sets

The indices used in the SERP optimization model are:

i: component

k: reaction

m: operation mode

s: step

s′: alias of index s

fs: feed stream

ads: adsorbent

cat: catalyst

The following sets are also defined.

The set of all components, ***I***, is :

$$i \in I = \{CS_1, CS_2, CS_3, ..\}$$

The set of the reactions, ***R***, is :

$$k \in R = \{R_1, R_2, R_3, ..\}$$

The set of all possible modes of operation, ***M***, is:

$$m \in M = \{\mathrm{SR}, \mathrm{DP}, \mathrm{P}, \mathrm{rSR}, \mathrm{rDP}, \mathrm{rP}\}$$

The set of all steps, ***S***, is as follows:

$$s, s' \in S = \{1, 2, 3, .., NS\}$$

where ***NS*** is the total number of steps.

The set of all feed streams, ***FS***, is:

$$fs \in FS = \{fs_1, fs_2, fs_3, .., fs_{\mathrm{NS}}\}$$

The set of all pressures, P_{all}, is:

$$P_{all} = \{P_0, P_1, P_2, .., P_{\mathrm{NS}}\}$$

where P_0 is the initial pressure.

The set of all catalysts, ***CAT***, is:

$$cat \in CAT = \{Cat_1, Cat_2, Cat_3, ..\}$$

The set of all adsorbents, ***ADS***, is:

$$ads \in ADS = \{Ads_1, Ads_2, Ads_3, ..\}$$

2.2.2.2 Decision variables and their bounds

The following decision variables for the design of a periodic SERP systems are defined:

$y_{i,fs}$: Mole fraction of component ***i*** in feed stream ***fs***

P_s : Pressure at the end of step ***s***

T_{fs} : Temperature of feed stream ***fs***

$t_{prod,start}$: Time at which product withdrawal is started

$t_{prod,dur}$: Time duration for which product withdrawal is continued

t_s : Duration of step ***s***

$v_{fs,sup}$: Superficial velocity of feed stream fs entering the column during step *s*

L : Length of the SERP column

α : Sorbent-to-catalyst mass ratio

The first step is defined as the mode during which hydrogen product is produced. Steam and carbon are the reactants during this step which react to form hydrogen product. The composition of steam and carbon in the reactant feed (y_{i,fs_1}) is controlled by controlling the ratio of steam to carbon, which varies between r_{lb} and r_{ub}. It is further assumed that the composition of other incoming streams used in the process ($fs \in \{fs_2, fs_3, ..., fs_{NS}\}$) are known *a priori*. Since the first step is the hydrogen producing step, the product venting would start and end at the beginning and completion of first step, respectively. Therefore, $t_{prod,start} = 0$ and $t_{prod,dur} =$ step 1 duration = t_1. Other aforementioned continuous decision variables such as step pressures, durations and temperatures, superficial velocity, SERP column length and sorbent-to-catalyst ratio are appropriately bounded. Overall, the bounding constraints on decision variables are as follows:

$$r_{lb} \leq \text{ S/C feed ratio} \leq r_{ub} \tag{2.39}$$

$$P_{s,lb} \leq P_s \leq P_{s,ub} \qquad \forall s \in S \tag{2.40}$$

$$t_{s,lb} \leq t_s \leq t_{s,ub} \qquad \forall s \in S \tag{2.41}$$

$$v_{fs,lb} \leq \mathrm{v}_{fs,sup} \leq v_{fs,ub} \qquad \forall fs \in FS \tag{2.42}$$

$$\alpha_{lb} \leq \alpha(z) \leq \alpha_{ub} \tag{2.43}$$

$$T_{fs,lb} \leq T_{fs} \leq T_{fs,ub} \qquad \forall fs \in FS \tag{2.44}$$

where r_{lb} and r_{ub} are the lower and upper bounds on steam-to-carbon ratio in the reactant feed during the first step (SR), $P_{s,lb}$ and $P_{s,ub}$ are lower and upper bounds on operating pressures of step s, $t_{s,lb}$ and $t_{s,ub}$ are lower and upper bounds on step s duration, $v_{fs,lb}$ and $v_{fs,ub}$ are lower

and upper bounds on superficial velocity of feed fs, α_{lb} and α_{ub} are lower and upper bounds on sorbent/catalyst mass ratio in the SERP column, and $T_{fs,lb}$ and $T_{fs,ub}$ are lower and upper bounds on feed fs temperature.

2.2.2.3 Constraints and objective function

The constraints and objective function used in the model for optimizing SERP systems are described in this section in detail. The constraints include product and process specifications, boundary conditions, and the objective function is to maximize the hydrogen productivity and minimize hydrogen production cost.

Product and process specifications

Eq. 2.45 is the operational constraint which has been included in the SERP optimization model. This constraint ensures that the pressure difference between consecutive process steps s and s' is either equal to zero or is above the tolerance value ΔP_{tol}. By its inclusion in the model, samples are generated with pressure difference between consecutive steps either equal to zero, or with some significant value. This is the key constraint which help us in obtaining discrete cycle configuration decisions using continuous pressure variables.

$$-M^{\zeta_{s,s'}} \leq P_{s'} - P_s \leq M^{\zeta_{s,s'}} \qquad \forall (s,s') \in \{(1,2),(2,3),...,(NS-1,NS),(NS,1)\} \quad (2.45)$$

$$\text{where } \zeta_{s,s'} = \left[\frac{\left(\frac{P_{s'}-P_s}{\Delta P_{tol}}\right)^2 - 1}{\left(\frac{P_{s'}-P_s}{\Delta P_{tol}}\right)^2 + 1} \right]$$

In Eq. 2.45, P_s and $P_{s'}$ are the pressure values of previous and next steps respectively, M is a big number (e.g., 10^{10}), and $\zeta_{s,s'}$ is an exponent value of which depends on pressures $P_{s'}$ and P_s . When $\mid P_{s'} - P_s \mid > \Delta P_{tol}$, $\zeta_{s,s'}$ would be a positive number, thereby relaxing the constraints Eq. 2.45. However, when $\mid P_{s'} - P_s \mid < \Delta P_{tol}$, $\zeta_{s,s'}$ would be a negative number. This would activate the above set of constraints and would ensure that $P_{s'}$ and P_s are approximately equal. Note that

the bigger the value of parameter M, the less soft the above constraints would be.

To bound the step durations of pressure-changing steps so that better objective function values could be obtained by the optimizer, the following constraint is imposed:

$$t_{s+1} \leq t_{s+1,lb} + (t_{s+1,ub} - t_{s+1,lb}) M^{-(P_{s+1}-P_s)^2} \qquad \forall s \in S \tag{2.46}$$

Eq. 2.46 ensures that the duration for the pressure-changing operation modes (P, rP, DP and rDP) for which $P_s \neq P_{s-1}$ have an upper bound of t_{lb}, which is the minimum allowable step duration time. This constraint is automatically relaxed for the steps with constant pressure throughout step operation, which is during SR and rSR operation modes.

To ensure that the purity of hydrogen product obtained is above P_u^{min}, which is the lower bound on the hydrogen product purity obtained from the SERP system, the following constraint is used:

$$\text{H}_2 \text{ purity (dry basis) } \% = \frac{\int_{t_{prod,start}}^{t_{prod,start}+t_{prod,dur}} \left.\frac{y_{\text{H}_2} Pv}{RT}\right|_{z=L} dt}{\int_{t_{prod,start}}^{t_{prod,start}+t_{prod,dur}} \left.\frac{Pv}{RT}\right|_{z=L} dt} \times 100 \geq P_u^{min} \tag{2.47}$$

Without loss of generality, it is always considered that the first step produces hydrogen product while the rest of the steps are primarily for regeneration purposes. Therefore, in Eq. 2.47, $t_{prod,start} = 0$ and $t_{prod,dur} = t_1 =$ duration of the first step.

It is assumed that the first step occurs at the same pressure and the direction of the flow is forward. Furthermore, the final pressure of a process cycle is imposed to be the same as that of the initial pressure at the beginning of the cycle. Consequently, the following constraints are included in the model:

$$P_0 = P_1 = P_{NS} \tag{2.48}$$

where P_0, P_1, and P_{NS} are respectively the pressures at the beginning of SERP cycle, at the end of first process step and at the end of SERP cycle.

Selection of operation modes using pressure variables

For any process consisting of at most *NS* unknown operation modes, a set $P_{all} = \{P_0, P_1, P_2, .., P_{NS}\}$ is defined. Here, P_0 is the pressure at the beginning of the process. The rest of the pressures (P_1, P_2, ..., P_{NS}) are the pressures at the end of steps $1, 2, .., NS$, respectively. For obtaining the mode of operation during any step s, the values of pressures P_{s-1} and P_s are used. These are the pressures at the beginning and end of step s, respectively. If the absolute value of pressure at the end of step s is greater than the initial pressure, i.e., $\mid P_s \mid > \mid P_{s-1} \mid$, the step s is undergoing pressurization. Similarly, when pressure at the end of step s is less than that at the beginning of the step, i.e., $\mid P_s \mid < \mid P_{s-1} \mid$, step s is a depressurization step. During sorption-reaction mode, the pressure of the column at the beginning and end of the step stays the same. Therefore, when $\mid P_s \mid = \mid P_{s-1} \mid$, step s is a sorption-reaction step.

As mentioned above, the absolute values of pressures in the set P_{all} are utilized for obtaining the modes of operation the SERP column is undergoing in each cycle. To take into account the flow direction, an abstract concept of negative pressures is defined. Negative pressures allow the inclusion of reversed-flow cases such as those of rSR, rDP and rP. It should be noted that the sign of the pressures is only used for obtaining flow directions. In the set $P_{all} = \{P_0, P_1, P_2, .., P_{NS}\}$, whenever the sign of successive pressures change, there is a change in direction of the flow. For example, for step s, if P_{s-1} is negative and P_s is positive (or vice versa), flow direction would change when switching from step $s-1$ to step s. However, if both the pressures P_{s-1} and P_s have same signs, the flow direction during step s would be the same as that of step $s-1$.

Table 2.7: Obtaining the sequence of process operation stages using the pressures in the set P_{all}.

Step s	P_{s-1} (atm)	P_s (atm)	$\mid P_s \mid - \mid P_{s-1} \mid$	Sign change from P_{s-1} to P_s?	Mode of Operation
1	4.5	4.5	0	No	SR
2	4.5	-1	-3.5	Yes	rDP
3	-1	-1	0	No	rSR
4	-1	4.5	3.5	Yes	P

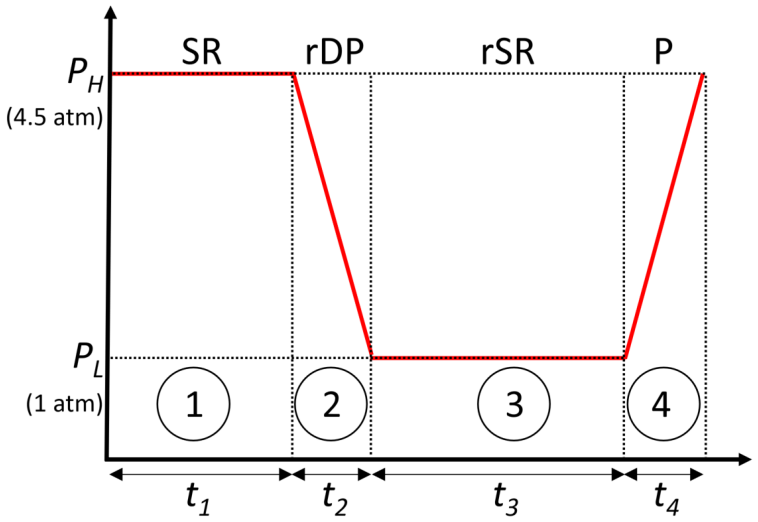

Figure 2.12: Pressure profile inside the SERP column for the illustrative 4-step cycle: SR $\rightarrow$ rDP $\rightarrow$ rSR $\rightarrow$ P. Here, the set P_{all} = {4.5, 4.5, -1, -1, 4.5}. The signs of the pressure elements in the set P_{all} are used for obtaining the flow direction whereas the magnitude of the pressure values is used to obtain the sequence of operation modes of an SERP cycle.

As an illustration of the concept, a 4-step SERP cycle (SR $\rightarrow$ rDP $\rightarrow$ rSR $\rightarrow$ P) is taken as shown in Table 2.7 and Figure 2.12. If the pressure set P_{all} (in atm) = {4.5, 4.5, -1, -1, 4.5}, the sequence of steps in the process cycle would be {SR, rDP, rSR, P}. The absolute value here (4.5 and 1) are used to see which of the sorption-reaction, depressurization or pressurization steps is chosen, and the sign of the variables are utilized to obtain whether flow is reversed or not.

A general boundary condition formulation representing different operation modes

For each of the operation modes shown in Figure 2.10, there is a corresponding set of boundary conditions which is used for simulating the corresponding operation mode. In this section, a single, unified expression containing boundary conditions of six possible operations involved in SERP operation is proposed. The generalized boundary condition expression yields appropriate boundary conditions just by using the pressure variables in the set P_{all}. To this end, a variable c_s is defined such that,

$$c_s = \frac{|\,\mathrm{P}_s\,| - |\,\mathrm{P}_{s-1}\,|}{||\,\mathrm{P}_s\,| - |\,\mathrm{P}_{s-1}\,|| + \epsilon} \qquad \forall s \in S \tag{2.49}$$

where ϵ is an infinitesimally small number used for avoiding numerical instabilities. Depending on the values of P_{s-1} and P_s, c_s would be calculated for step s. There can be three different values of c_s corresponding to sorption-reaction, pressurization and depressurization steps as follows:

$$c_s = \begin{cases} 0 & \text{if } \mid \mathrm{P}_s \mid = \mid \mathrm{P}_{s-1} \mid \qquad \text{(steps SR and rSR)} \\ -1 & \text{if } \mid \mathrm{P}_s \mid < \mid \mathrm{P}_{s-1} \mid \qquad \text{(steps DP and rDP)} \\ 1 & \text{if } \mid \mathrm{P}_s \mid > \mid \mathrm{P}_{s-1} \mid \qquad \text{(steps P and rP)} \end{cases} \tag{2.50}$$

The calculated value of c_s for step s can be used to obtain boundary condition expressions ($BC_{s,b}^{fwd}$ and $BC_{s,b}^{rev}$) for both forward and reverse flow. In the first expression, the variable $BC_{s,b}^{fwd}$ is calculated for the forward-flow stages of operation (SR, DP & P). Here, the index b belongs to a set B which contains values of model variables (velocity, pressure, mole fraction, gas phase temperature, and wall temperature) for which boundary conditions are specified. Therefore, $b \in B = \{\overline{v}_{z=0},\ \overline{v}_{z=L},\ \overline{P}_{z=0},\ \overline{P}_{z=L},\ y_{i,z=0},\ y_{i,z=L},\ \overline{T}_{z=0},\ \overline{T}_{z=L},\ \overline{T}_{w,z=0},\ \overline{T}_{w,z=L}\}$. Another similar expression is used for calculating $BC_{s,b}^{rev}$ that takes into account boundary conditions for reverse flow modes of operation (rSR, rDP & rP). The equations used for obtaining $BC_{s,b}^{fwd}$ and $BC_{s,b}^{rev}$ are as follows:

$$BC_{s,b}^{fwd} = BC_{SR,b}(1- \mid c_s \mid) + \frac{1}{2}\left[\mid c_s \mid (BC_{P,b} + BC_{DP,b}) + c_s(BC_{P,b} - BC_{DP,b})\right] \qquad \forall s \in S, \forall b \in B \tag{2.51}$$

where $BC_{SR,b},\ BC_{P,b}$ and $BC_{DP,b}$ are boundary conditions for sorption-reaction, pressurization and depressurization steps, respectively. Note that the expression of c_s would allow only one of

them to be activated. Similarly,

$$BC_{s,b}^{rev} = BC_{rSR,b}(1- \mid c_s \mid) + \frac{1}{2}\left[\mid c_s \mid (BC_{rP,b} + BC_{rDP,b}) + c_s(BC_{rP,b} - BC_{rDP,b})\right] \quad \forall s \in S, \forall b \in B \tag{2.52}$$

where $BC_{rSR,b},\ BC_{rP,b}$ and $BC_{rDP,b}$ are boundary conditions for reverse sorption-reaction, reverse pressurization and reverse depressurization steps respectively. The above values of $BC_{s,b}^{fwd}$ and $BC_{s,b}^{rev}$, along with the pressure at the end of step s, are used for deriving a single expression for all the six modes of operation as follows:

$$BC_{s,b} = \frac{1}{2}\left[(BC_{s,b}^{fwd} + BC_{s,b}^{rev}) + \frac{\mathrm{P}_s}{\mid \mathrm{P}_s \mid}(BC_{s,b}^{fwd} - BC_{s,b}^{rev})\right] \qquad \forall s \in S, \forall b \in B \tag{2.53}$$

The above expression helps in using the continuous pressure variables for deriving appropriate boundary conditions. Therefore, if the pressure set P_{all} is given, appropriate boundary conditions of all the process steps present in the SERP cycle can be obtained using Eq. 2.53.

For example, for a step s, if $P_{s-1} = 4.5$ atm and $P_s = -1$ atm, the step s would be a reverse depressurization step. As $\mid P_s \mid < \mid P_s - 1 \mid$, c_s would be equal to -1 (Eq. 2.49). By substituting the value of c_s in Eqs. 2.51 and 2.52, the following equations are obtained:

$$BC_{s,b}^{fwd} = BC_{DP,b} \tag{2.54}$$

$$BC_{s,b}^{rev} = BC_{rDP,b} \tag{2.55}$$

By using the values of $BC_{s,b}^{fwd}$ and $BC_{s,b}^{fwd}$ in Eq. 2.53, the boundary conditions of the reverse depressurization step are obtained as follows:

$$BC_{s,b} = BC_{rDP,b} \tag{2.56}$$

where $b \in B = \{\overline{v}_{z=0},\ \overline{v}_{z=L},\ \overline{P}_{z=0},\ \overline{P}_{z=L},\ y_{i,z=0},\ y_{i,z=L},\ \overline{T}_{z=0},\ \overline{T}_{z=L},\ \overline{T}_{w,z=0},\ \overline{T}_{w,z=L}\}$.

Objective function

The optimizations have been performed for producing hydrogen with different purity levels via SE-SMR and SE-WGSR. In case of SE-SMR, the objective of the reported optimization studies are the maximization of hydrogen productivity and minimization of hydrogen production cost. For SE-WGSR, the optimizations have been performed for maximizing hydrogen productivity. The corresponding objective functions for productivity-maximization and cost-minimization are as follows:

Maximizing hydrogen productivity: The objective function for maximizing the productivity of SE-SMR and SE-WGSR systems during the first step, i.e., sorption-reaction step is formulated as follows:

$$\max\ \text{Hydrogen productivity}\ = \frac{\left(\int_{t_{prod,start}}^{t_{prod,start}+t_{prod,dur}} \left.\frac{y_{\mathrm{H_2}} P v}{RT}\right|_{z=L} dt\right) \varepsilon_b}{\int_0^L [\rho_{b,ads}(z) + \rho_{b,cat}(z)] dz\ t_{cycle}} \tag{2.57}$$

where z is the bed length coordinate, $t_{prod,start} = 0$, $t_{prod,dur} = t_1 =$ duration of the first step, $y_{\mathrm{H_2}}$ is the gas phase mole fraction of product stream at the outlet boundary ($z = L$), $P,\ T$ and v are gas phase pressure, temperature and velocity respectively, R is the universal gas constant, $\rho_{b,ads}$ and $\rho_{b,cat}$ are sorbent and catalyst bed apparent density, respectively, and t_{cycle} is the total duration of one cycle.

Minimizing hydrogen production cost: The total cost of hydrogen production (TC) in \$/kg H_2, which needs to be minimized for SE-SMR, is calculated as follows [75]:

$$\min\ \text{Total hydrogen production cost}, TC = \frac{AIC}{P_{\mathrm{H_2}}} + OC \tag{2.58}$$

where AIC is the annualized investment cost for producing hydrogen in \$/year, OC is the operating cost (\$/kg H_2) and $P_{\mathrm{H_2}}$ is the annual hydrogen production of hydrogen in kg/year where 8000 operational hours are assumed in a year. In case of cost minimization, it is ensured that the productivity of hydrogen is above the threshold value $Prod_u^{min}$ [Hydrogen Productivity (Eq. 2.57) $\geq\ Prod_u^{min}$].

The annualized investment cost (AIC) is obtained as follows [75]:

$$AIC = \phi TPC + AMC \tag{2.59}$$

where $\phi = 0.154$ is the capital recovery factor [40], TPC is the total plant cost and AMC is the annual maintenance cost, where AMC is assumed to be 5% of TPC [75]. For obtaining TPC , the following expression is used:

$$TPC = TIC + IDC + BPC \tag{2.60}$$

where TIC is the total installed cost, IDC is the indirect cost and BPC is the balance plant cost. IDC and BPC are taken as 32% and 20% of TIC, respectively [75].

2.2.2.4 Optimization strategy

We employ the grey-box constrained optimization algorithm, developed by Bajaj et al. [134], for optimal SERP design.

Grey-box constrained optimization: overall algorithm

SERP cycle synthesis can be posed as a grey-box constrained problem by considering the objective function and some of the constraints in the NAPDE model as black-box. The key idea here is to recast the NAPDE model as a general grey-box model (i.e., a mixture of black-box objective, black-box constraints and known constraints) as follows:

$$\min_{x} \quad f(x) \tag{2.61}$$

$$s.t. \quad g_u(x) \leq 0 \qquad \forall u \in \{1, ..., p\} \tag{2.62}$$

$$g_v(x) \leq 0 \qquad \forall v \in \{1, ..., q\} \tag{2.63}$$

$$x \in [x^L, x^U] \tag{2.64}$$

where $x \in \mathbb{R}^n$ are the decision variables in the optimization problem. The decisions variables

are $x \in \{\text{S/C feed ratio}, P_s, t_s, v_{fs,sup}, \alpha, T_{fs}\}$ for optimizing SERP systems. The aim of the above problem is to obtain optimal values of x for minimizing the black-box objective $f(x) : \mathbb{R}^n \rightarrow \mathbb{R}$. The objective function $f(x)$ consists of hydrogen productivity maximization for SE-SMR and SE-WGSR (Eq. 2.57), and hydrogen production cost minimization for SE-SMR (Eq. 2.58). $g_u(x) : \mathbb{R}^n \rightarrow \mathbb{R}, \forall u \in \{1, ..., p\}$ are the black-box constraints of which the analytical forms are unknown. For hydrogen productivity maximization, there is only one constraint on hydrogen purity (Eq. 2.47) the analytical form of which is unknown. However, for cost minimization, there would be two black-box constraints on hydrogen purity and productivity. $g_v(x) : \mathbb{R}^n \rightarrow \mathbb{R}, \forall v \in \{1, ..., q\}$ are the known constraints analytical form of which are known. The lower and upper bound on decision variables x are $x^L \in \mathbb{R}^n$ and $x^U \in \mathbb{R}^n$, respectively.

The grey-box constrained algorithm constructs surrogate models using input-output SERP simulation data to approximate both objective function and constraints violation [134]. The *known* constraints are those which are known *a priori* such as bounds on pressure and step duration. Here, those constraints are referred to as *black-box* constraints which are evaluated using the GRAMS simulation. For example, hydrogen purity for an SE-SMR process can only be calculated after the simulation has been performed at the respective decision variables vector. The grey-box algorithm consists of two phases - (i) feasibility phase and (ii) optimization phase, which interacts with the GRAMS framework to generate input-output data. The feasibility phase starts from an infeasible point and seeks a feasible point which satisfies all the known and black-box constraints. Once a feasible point has been obtained, the optimization phase focuses on improving the objective function value while maintaining feasibility.

Before the feasibility and optimization phases are described in more detail, the form of the surrogate model used for fitting input-output data is explained. Both phases require simulation runs for obtaining the values of the objective function and constraint violation for different input data which are then used for obtaining approximately fitted surrogate models. The following cubic radial basis functions (CRBF) are used for approximating objective function $f(x)$, black-box constraints $g_u(x)$ and constraint violation $\theta(x)$ [135]:

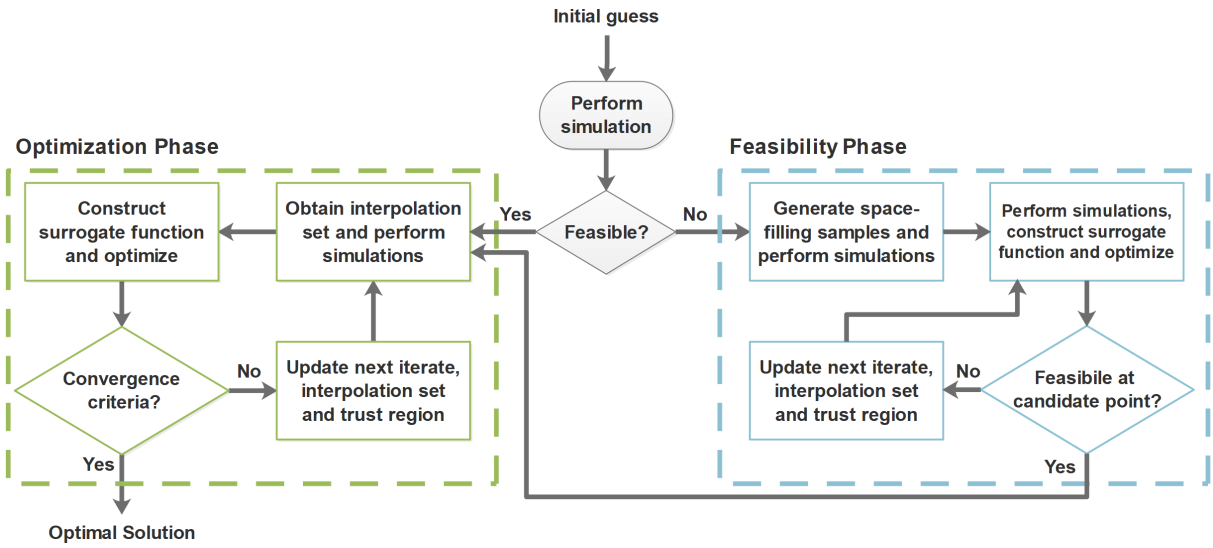

Figure 2.13: Graphical representation of the working of the two-phase grey-box algorithm with GRAMS framework. The grey-box constrained algorithm consists of feasibility and optimization phases. The feasibility phase focuses on finding a feasible point whereas the optimization phase improves the objective function while maintaining feasibility. If the initial guess x_o is feasible, the algorithm straightaway proceeds to the optimization phases. Otherwise, it firstly goes to the feasibility phase and then the optimization phase. At all steps of the algorithm, the optimizer inputs decision variables vector x to the GRAMS framework and obtains the values of black-box objective ($f(x)$) and black-box constraints ($g_u(x)$).

$$s_c^r(x) = \sum_{d=1}^{n_d} b_d x_d + \sum_{l=1}^{n_s} \omega_l \left(\sqrt{\sum_{d=1}^{n_d} (x_d - y_d^l)^2} \right)^3 \tag{2.65}$$

where

$$s_c^r(y^l) = s(y^l) \qquad \forall l \in \{1, ..., n_s\} \tag{2.66}$$

$$\sum_{l=1}^{n_s} \omega_l y_d^l = 0 \qquad \forall d \in \{1, ..., n_d\} \tag{2.67}$$

In the above expressions, $s_c^r(x)$ is the continuous surrogate function, n_d is the dimension of decision variables vector x, n_s is the total number of samples in the interpolating set, y^l is the interpolation sample l, x_d is the component d of decision variable x, y_d^l is the component d of sample l, and b_d and ω_l are $n_d + n_s$ parameters that are calculated by solving an optimization problem. The slack variables SP_d^1, SN_d^1, SP_l^2 and SN_l^2 are introduced to the above set of equations, and

the following linear optimization problem is solved where the objective is to minimize the values of slack variables.

$$\min_{b_d,\omega_l,SP_d^1,SN_d^1,SP_l^2,SN_l^2} \quad \sum_{d=1}^{n_d}(SP_d^1 + SN_d^1) + \sum_{l=1}^{n_s}(SP_l^2 + SN_l^2) \tag{2.68}$$

$$s.t. \quad \sum_{d=1}^{n_d} b_d y_d^l + \sum_{l'=1}^{n_s} \omega_{l'} \left(\sqrt{\sum_{d=1}^{n_d}(y_d^{l'} - y_d^l)^2} \right)^3 = s_l + SP_l^2 - SN_l^2 \qquad \forall l \in \{1, 2, ..., n_s\} \tag{2.69}$$

$$\sum_{l=0}^{n_s} \omega_l y_d^l = SP_d^1 - SN_d^1 \qquad \forall d \in \{1, 2, ..., n_d\} \tag{2.70}$$

$$SP_d^1, SN_d^1, SP_l^2, SN_l^2 \geq 0 \qquad \forall d \in \{1, 2, ..., n_d\}, \forall l \in \{1, 2, ..., n_s\} \tag{2.71}$$

The above linear programming problem is solved to obtain the surrogate model parameters for f^r, g_u^r and θ^r, which are the surrogate-model equivalent of black-box objective function $f(x)$, black-box constraints $g_u(x)$ and constraint violation $\theta(x)$.

In the beginning of the algorithm, a simulation is performed at the user-input initial guess, x_o. If the initial point satisfies all the known and black-box constraints within pre-specified tolerance, the algorithm straightaway proceeds to the optimization phase with $x_o^f = x_o$. Regardless of whether the initial point is feasible or not, the following NLP sub-problem is solved using the global solver ANTIGONE [136] for obtaining n_s space-filling samples which satisfy the known constraints. The n_s samples are used later in feasibility and optimization phases as interpolation points for surrogate-model fitting as follows:

$$\min_{\bar{x}} \quad \left(\frac{4}{3}\right)^{n_d} + \frac{1}{{n_s}^2} \sum_{l=1}^{n_s}\sum_{l'=1}^{n_s}\prod_{d=1}^{n_d}\left[\frac{3}{2} - |\bar{x}^l - \bar{x}_d^{l'}|(1 - |\bar{x}_d^l - \bar{x}_d^{l'}|)\right] \tag{2.72}$$

$$s.t. \quad g_v(\bar{x}) \leq 0 \qquad \forall v \in \{1, ..., q\} \tag{2.73}$$

$$||\bar{x} - \bar{x}_r|| \in \Delta_r \tag{2.74}$$

where $\bar{x}_d$ is the normalized component d of decision variable x_d. It is obtained by using the lower and upper bounds of decision variables x such that $\bar{x}_d = (x_d - x_d^L)/(x_d^U - x_d^L)$. In the above expression, $\bar{x}_d^l$ refers to the scaled component d of sample l, n_d is the dimension of the decision variables x, Δ_r is the size of the trust region, and $\bar{x}_r$ is the trust-region center. The simulations are then performed at these n_s space-filling samples and the output objective function and constraint violations values are obtained. The algorithm then undergoes feasibility and optimization phases described as follows. The interested reader is advised to refer to Bajaj et al. [134] to explore the two-phase algorithm in a greater detail. Here, a brief overview of the working of feasibility and optimization phases of the algorithm is reported.

Feasibility phase

The algorithm enters the feasibility phase when the initial point provided is infeasible. During this phase, the constraint violation of each of n_s samples is defined using a smooth constraint violation function as follows:

$$\theta(x^l) = \sum_{u=1}^{p} (\max(0, g_u(x^l)))^2 \qquad \forall l \in \{1, ..., n_s\} \tag{2.75}$$

The constraint violation is calculated for each sample $x^l,\ \forall l \in \{1, 2, ..., n_s\}$ using the above expression. Note that the constraint violation is zero for a feasible point whereas it is positive for an infeasible point. The values of constraint violation $\theta(x^l)$ are then used as interpolating points to develop a surrogate model $\theta^r(x)$. The following sub-problem is then solved using the global solver ANTIGONE [136] to minimize the approximated constraint violation $\theta^r(x)$ over known constraints to obtain a candidate point x^{fop} at which the value of the constraint violation surrogate model is minimum. The sub-problem aims to minimize the constraint violation of black-box constraints $g_u(x)$ while maintaining feasibility subject to known constraints $g_v(x)$ as follows:

$$\min_{x} \qquad \theta^r(x) \tag{2.76}$$

$$s.t. \qquad g_v(x) \leq 0 \qquad \forall v \in \{1, ..., q\} \tag{2.77}$$

$$||x - x_r|| \in \Delta_r \tag{2.78}$$

After performing a simulation at x^{fop}, the constraint violation $\theta(x^{fop})$ is calculated using Eq. 2.75. If $\theta(x^{fop})$ is less than a pre-specified constraint violation tolerance, x^{fop} is feasible and the algorithm proceeds to the optimization phase with $x_o^f = x^{fop}$. However, if x^{fop} is infeasible, it is accepted as the trust region center if $\theta(x^{fop})$ is less than the constraint violation at current iterate. Thereafter, the interpolation set over which θ^r is fitted is updated by replacing a point, which damages the geometry and poisedness of the interpolation set, with x^{fop} [134]. The updated surrogate model is then minimized to obtain a new candidate point. It is to be noted that sometimes the surrogate model developed would have a low accuracy due to which it would be unable to find a point with lower constraint violation. In such cases, the size of the trust region is reduced to increase the accuracy of the surrogate model. Before decreasing trust-region size, however, the fully-linear property of the surrogate model is ensured. If the model is not fully-linear, a model improvement algorithm [134] is called to construct a fully linear model. The ratio of actual reduction in constraint violation to predicted reduction in constraint violation is calculated. If this ratio is higher than a certain threshold, the model is sufficiently accurate and the trust region size is increased. The feasibility phase eventually obtains a feasible point x_o^f, which is feasible subject to both known and black-box constraints.

Optimization phase

The algorithm enters the optimization phase once a feasible point, x_o^f, has been found. In this phase, the objective is to find a set of non-increasing sequence of feasible iterates which at least converge to a local minima. Here, n_s interpolation points are considered again in the entire space to explore the global features of the objective function and constraints. The feasible point found in the feasibility phase, x_o^f, is also one of the interpolating points to indicate the location of feasible region to the model. The core of the optimization phase is similar to that of the feasibility phase except the strategy for updating trust region center. Using $f(x^l)\text{and } g_u(x^l)$, the surrogate models $f^r(x) \text{ and } g^r(x)$ are developed by fitting cubic radial basis function. The following sub-problem to minimize the surrogate objective function is then solved to global optimality using

ANTIGONE [136] to obtain a candidate point x^{sop}:

$$\min_{x} \quad f^r(x) \tag{2.79}$$

$$s.t. \quad g_u^r(x) \leq 0 \qquad \forall u \in \{1, ..., p\} \tag{2.80}$$

$$g_v(x) \leq 0 \qquad \forall v \in \{1, ..., q\} \tag{2.81}$$

$$||x - x_r|| \in \Delta_r \tag{2.82}$$

where $f^r(x)$ is the objective function's surrogate model, $g_u^r(x), \forall u \in \{1, ..., p\}$ are the black-box constraints' surrogate models, $g_v(x), \forall v \in \{1, ..., q\}$ are the known constraints, x_r is the trust region center and Δ_r is the trust region. Once the sub-problem is solved and the optimal decision point x^{sop} is obtained, a simulation is performed at this candidate point. If the constraint violation at x^{sop} is lower than the pre-specified tolerance, it is examined whether a decrease in objective function has been obtained or not. If a decrease is observed, x^{sop} is set as the trust-region center. Furthermore, x^{sop} replaces the worst point in the interpolating set for improving interpolation set geometry and poisedness. The size of the trust region is also considered before certifying the optimality of the point x^{sop}. The change in the size of the trust region is handled in a similar way as that of the feasibility phase. If the surrogate model is inaccurate due to which the optimizer cannot find a better point, the trust region size is decreased. Before decreasing the size, however, the fully linear property of the surrogate model is ensured. If the model is not fully linear, a model improvement algorithm is initiated to construct a fully linear model. When the accuracy of the surrogate model is sufficiently high and the ratio of actual reduction in objective function to its predicted value is above a pre-specified threshold, the size of the trust region is increased. The optimization phase eventually converges to the optimal point, x^{opt}, and further details regarding the algorithm convergence can found in Bajaj et al [134].

2.2.3 Case studies

2.2.3.1 Sorption enhanced steam methane reforming

The simulation-based SERP optimization model is used for optimizing hydrogen production via SE-SMR. In conventional SMR processes, to produce pure hydrogen, steam is first reformed to form syngas, which consists of hydrogen, carbon monoxide and small quantities of carbon dioxide. Steam reforming is then followed by WGSR, which converts carbon monoxide and steam to form more hydrogen and carbon dioxide. Based on studies and data from industrial producers, the shifted gas stream must contain at least 70 mol% hydrogen before it can be economically purified in a PSA unit [137]. For a hydrogen feed to a PSA having 70 mol% hydrogen, a typical product purity of 99.9% with a recovery of 85% can be obtained [137]. In contrast, more efficient SE-SMR processes have been developed offering better hydrogen purity and selectivity with lowered utility consumption due to lower operating temperature and pressure [43, 47, 48, 138].

The reactants to the SE-SMR column include steam and methane with former in excess. In the column, the SMR reactions are coupled with selective capture of CO_2 for achieving reaction conversions higher than the SMR process. Due to CO_2 capture, the equilibrium is pushed in the forward direction, which enhances the conversion of reactants to form product hydrogen in accordance with the Le Chatelier's principle. Due to enhanced methane conversion, the column can operate at moderate pressures and temperatures for achieving significant amounts of hydrogen product. The column usually contains an admixture of Ni-Al SMR catalyst and HTC CO_2 sorbent [139]. Once the sorbent is saturated with CO_2, the sorption-reaction step is stopped, and regeneration is carried out. The regeneration of HTC sorbent can be achieved in a variety of ways, such as pressure, temperature or concentration swings, and/or reactive regeneration.

The studies on multi-step, multi-cyclic SE-SMR processes typically pre-assign the cycle configuration. The major factors affecting the process performance include steam/carbon (S/C) ratio, reactor temperature and pressure. Li et al. [140] studied multiple cycles for SE-SMR and sorbent regeneration in a fixed bed reactor. The mathematical models were developed for studying the

effects of cycle number on SERP performance during repeating carbonation/calcination cycles. In another work [141], they produced 90% pure hydrogen continuously by periodically operating two parallel SE-SMR reactors in conjunction. Hufton et al. [138] achieved 96% hydrogen purity with a productivity of 0.8 mmol H_2/g solid. The multi-cycle process used was predesignated and each of the cycles consisted of the following steps - (1) sorption-reaction, (2) counter-current depressurization, (3) counter-current purge with 5-10% hydrogen, and (4) counter-current pressurization. Lee et al. [142] conceptualized and simulated a single cycle of a thermal-swing sorption enhanced reaction process with simultaneous SMR reactions and CO_2 byproduct removal. Xiu et al. [143] performed numerical simulations to observe the effects of controlling sub-section wall temperature and packing ratio of catalyst and sorbent on the purity of hydrogen product at CSS. By controlling sub-section wall temperature, the CO concentration in the product gas was reduced to 30 ppm. The model predictions of Beaver et al. [144] showed that hydrogen productivity of SERP is much higher at a reaction temperature of 863 K than at 823 K or 793 K. Methane conversion increases insignificantly ($<$1%) as the reactor temperature increases from 793 K to 863 K.

Due to the endothermic nature of SMR reactions, higher temperatures are favorable for thermodynamic equilibrium and faster kinetics [144]. With an increase in temperature, however, the removal of CO_2 from gas-phase reaction mixture becomes unfavorable [144]. There exists an optimum temperature at which the trade-offs between CO_2 sorption capacity and reaction conversions are well balanced [145]. Another major factor is that sorption of adsorbate species is favored at high pressures, while desorption is easier to achieve at lower pressures due to lower partial pressure. In SERP, sorption and reaction phenomena happen together in a single, intensified column. High pressure values might favor the sorption, but it can also limit the conversion. As a result, optimum pressures and temperatures must be obtained for SE-SMR to balance the trade-off between sorption and reaction phenomena well so as to optimally produce the product while satisfying product specifications. In addition, the types and duration of steps in an SERP cycle must be appropriately selected to achieve superior process performance at CSS. Desired values of hydrogen purity and productivity, and optimal hydrogen production cost, can be obtained during

sorption-reaction step by controlling bed residence time and feed compositions. For example, increasing residence time would improve hydrogen purity levels but would result in lower hydrogen productivity. A higher S/C ratio would also improve purity due to greater methane conversions but would take a toll on productivity. Therefore, the optimizer needs to find optimum pressure values at which both reaction and sorption rates are well-balanced.

To our best knowledge, none of the previous works on SE-SMR used optimization techniques for obtaining the optimal operating conditions for SE-SMR operation. Furthermore, all the studies on single-bed and multi-bed cyclic SE-SMR assign the configuration of the cycle *a priori*. However, pre-assignment of cycle configuration may result in suboptimal configurations with inferior process performance. Here, the objective is to leverage the simulation-based SERP optimization framework presented earlier to obtain optimal cycle configuration and optimal process parameters for maximizing hydrogen productivity, and minimizing hydrogen production cost.

In the SE-SMR process considered, methane and steam enter the column at high pressures during the first step of the process. For bed pressurization, pure steam feed is used whereas hydrogen and steam gas mixture is used during purge steps. As the use of steam is energy-intensive, the optimizer should ideally suggest an optimal cycle with minimum use of steam. The duration of the cycle is implicitly included in the objective function for hydrogen-productivity maximization (Eq. 2.57) and cost minimization (Eq. 2.58). The optimizer would try to minimize the overall cycle time such that the hydrogen productivity can be maximized, and production cost can be minimized, thereby reducing the purging time. A lower purge duration would result in lowered amounts of steam purge needed. For both hydrogen-productivity maximization and cost minimization, different optimizations were performed for obtaining different levels of hydrogen purity on a dry basis. In case of hydrogen productivity maximization, there is only one black-box constraint on product hydrogen purity whereas there are two black-box constraints on hydrogen purity and productivity during cost minimization. Additionally, the following assumptions were made for the optimization studies:

- The duration, direction of flow and type of operation stage have been fixed for the first

step. During this step, the column undergoes SR step in the forward direction with the step duration assumed to be 300 s.

- The temperature of all feed streams ($T_{fs_1}, T_{fs_2}, T_{fs_3}, T_{fs_4}$) is a fixed constant value T_c.
- The column dimensions were fixed (L = 0.223 m and $d_{in} = 0.126$ m [146]).
- 95% H_2O + 5% H_2 feed is used for purging whereas pure steam is used for pressurization purposes [138].
- If an SERP cycle has a purge step, the velocity of the purging gas is 0.20 m/s [44].
- The maximum number of steps in the process cycle allowed is four (i.e., $NS = 4$) [147].
- To reduce the computational complexity, the sorbent and catalyst were assumed to be distributed with the same ratio throughout the SE-SMR column. Therefore, $\alpha_1 = \alpha_2 = ... = \alpha_N = \alpha_c$, where α_c is the constant sorbent-to-catalyst ratio.
- The pressure of a step cannot be less than 100 kPa. If a sample generated by the optimizer has pressure less than this pressure, it is taken care of by the simulation solver. The pressure is appropriately increased to the threshold 100 kPa pressure.
- For all the simulations, 20 finite volume cells were used, and it was assumed that the CSS was obtained after 5 process cycles.
- The pressure changes linearly during pressurization and depressurization steps.
- The wall temperature is assumed to be constant, and is same as that of the incoming feed temperature.

In the cycle synthesis problem for SE-SMR, there are several continuous variables which would affect the process performance as mentioned earlier. These variables include steam-to-methane feed ratio, pressures at which the steps occur, operational modes chosen, steps duration, superficial velocity of the reactants feed, sorbent-to-catalyst ratio and operating temperature. Therefore, $x \in$

$\{\mathrm{S/C\ ratio}, P_1, P_2, P_3, t_2, t_3, t_4, v_{fs_1,sup}, \alpha_c, T_c\}$. Since $NS = 4$, P_{all} = {P_0, P_1, P_2, P_3, P_4}, where P_0, P_1 and P_4 are equal. Several of the steps can merge to synthesize a process with fewer steps compared to maximum allowable steps. As an instance, for the four-step process, if the optimizer finds a configuration in which the first step is the hydrogen generation step, and the rest of the three steps are purge steps, the latter three stages can be merged to form a single purge step resulting in a 2-step process.

The performance of the sorption enhanced reactor for hydrogen production can be computed based on several parameters such as hydrogen productivity and purity, and hydrogen production cost. The hydrogen productivity is computed by obtaining the amount of hydrogen product formed during the sorption-reaction step per unit mass of solid in the reactor per second (Eq. 2.57). The hydrogen purity is the percentage of hydrogen in the effluent stream during the sorption-reaction step of the cycle (Eq. 2.47). The cost for producing hydrogen is computed using operating costs and investment costs (Eq. 2.58). Higher values of both hydrogen productivity and purity, and lower cost for hydrogen production are desired in the process. Therefore, for SE-SMR, the optimization studies in this study consist of (i) maximizing hydrogen productivity and (ii) minimizing hydrogen production cost.

Hydrogen productivity maximization

To this end, firstly, the cost-independent optimization problem is formulated for maximizing hydrogen productivity produced via SE-SMR during the sorption-reaction step. The problem consists of 10 optimization variables and the objective of the SE-SMR optimization model is to maximize the productivity of product hydrogen. The problem consists of several constraints namely conservation constraints, bounds on decision variables, constraints on SERP cycle configuration and hydrogen product specifications, boundary condition constraints and solid material distribution constraints. Table 2.8 reports the bounds and other parameters used in the SE-SMR optimization problem. The incoming steam-to-methane ratio has lower and upper bounds of 3 and 6, respectively [148]. The pressures of SERP cycle steps can vary between -700 and 700 kPa, which is within the conventional SMR reactor pressure range [149], and negative pressure values control

the gas flow direction. The step durations are assumed to range from 20 to 600 s, and the duration of pressure-changing steps (P, rP, DP, and rDP) were constrained to be 20 s using Eq. 2.46. The superficial velocity of the incoming reactants gas feed fs_1 during the first step varies between 0.02-0.20 m/s range within which sufficient reactions conversions are obtained [150]. The sorbent-to-catalyst ratio in the SERP column has bounds of 1 and 10, which gives sufficient flexibility to the optimizer for choosing optimal material distribution. The parameters M and ΔP_{tol} in Eq. 2.45 have values of 10^{10} and 50.66 kPa, respectively, and the solid bed density (ρ_{bed}) is 748 kg solid per m^3 bed volume. The optimization is performed for two different purities of hydrogen product - 95% and 98%. The rest of the parameters (SMR reaction rates, isotherms and process parameters) used for solving the SE-SMR NAPDE model can be found in Appendix C and D.

Table 2.8: The lower and upper bounds, and parameters used in the SE-SMR and SE-WGSR case studies.

Parameter	Units	SE-SMR	SE-WGSR
r_{lb}	-	3	1
r_{ub}	-	6	10
$P_{s,lb}$	kPa	-700	-700
$P_{s,ub}$	kPa	700	700
$t_{s,lb}$	s	20	20
$t_{s,ub}$	s	600	1000
$v_{fs_1,lb}$	m/s	0.02	0.02
$v_{fs_1,ub}$	m/s	0.20	0.20
α_{lb}	-	1	1
α_{ub}	-	10	10
$T_{fs,lb}$	K	673	673
$T_{fs,ub}$	K	773	773
M	-	10^{10}	10^{10}
ΔP_{tol}	kPa	50.66	50.66
P_u^{min}	-	95, 98 %	95, 98 %
ρ_{bed}	kg solid/m^3 bed	748	1640

While solving the above SE-SMR optimization problem, a $10k$ sampling strategy was adopted to generate initial space-filling samples, where $k = 10$ is the total number of decision variables

which need to be optimized. Therefore, 100 initial samples were generated by solving the space-filling optimization problem to explore global features of the decision variables space. The generation of several samples helps the optimizer in exhaustively considering several two-, three- and four-steps process for SE-SMR operation. Once a feasible point has been found, the algorithm then proceeds to the optimization phase as described earlier in Section 2.2.2.4.

For the formulated SE-SMR optimization model, the optimization algorithm converged to a 4-step cycle optimal solution for both 95% and 98% hydrogen purity cases. The optimization was performed with five different initial guesses for improving the chances of obtaining a better objective function value. These initial guesses were heuristically chosen and predominantly differed in the cyclic configuration the process assumed. Table 2.9 reports the initial decision variables value for which the best objective was obtained. At the reported initial guess, a hydrogen purity of 51.87% was obtained. As the product specification constraint (Eq. 2.47) requires hydrogen purity to be greater than 95% and 98%, the initial guess was infeasible. Therefore, the algorithm entered the feasibility phase to find a feasible point and then the optimization phase to obtain a better objective value (Figure 2.13).

Table 2.9: SE-SMR results for both 95% and 98% hydrogen purity cases.

Decision Variable	Units	Initial Guess	Optimum Solution (95% H_2 purity)	Optimum Solution (98% H_2 purity)
Number of steps, NS	-	4	4	4
Steps sequence	-	(i) Sorption-Reaction (ii) Reverse Depres. (iii) Reverse Purge (iv) Pressurization	(i) Sorption-Reaction (ii) Reverse Depres. (iii) Reverse Purge (iv) Pressurization	(i) Sorption-Reaction (ii) Reverse Depres. (iii) Reverse Purge (iv) Pressurization
S/C feed ratio	-	6	6	6
P_1	kPa	233.33	111.14	111.37
P_2	kPa	100	100	100
P_3	kPa	100	100	100
t_2	s	20	20	20
t_3	s	422.45	202.04	253.49
t_4	s	20	20	20
$v_{fs_1,sup}$	m/s	0.05	0.029	0.02
α_c	-	10	2.405	2.445
T_c	K	673	773	773
H_2 purity (dry basis) (%)	-	51.87	95	98
H_2 productivity	$\frac{\text{mmol } H_2}{\text{kg solid. s}}$	0.013	0.534	0.204

The optimal decision variables and cycle configuration obtained for both 95% and 98% pure hydrogen cases are reported in Table 2.9. The optimal solution yielded hydrogen productivity of 0.534 and 0.204 mmol H_2/ (kg solid. s) for 95% and 98% hydrogen purity cases, respectively. The tradeoff between hydrogen purity and productivity could be clearly observed from these solutions. To obtain a higher amount of hydrogen product, the purity of the product would need to be compromised. In total, the grey-box optimization algorithm performed 760 and 909 simulations to find the optimum for obtaining 95% and 98% hydrogen products, respectively. Additionally, it took 34.66 and 38.47 hours to finish the optimization runs for the two cases without any parallelization. It was observed that the optimization phase of the algorithm typically needed more simulation runs in comparison to the feasibility phase. For the two cases, 533 and 552 simulations were performed in the optimization phase of the algorithm, and the time for each of the simulations was in the range 23.5-148.7 seconds depending on the nonlinearity of SERP cyclic configurations.

Figure 2.14 shows the optimal SE-SMR cycle configuration, which is the same for obtaining 95% and 98% hydrogen products. In the figure, $T_c = 773$ K and $P_2 = 100$ kPa for both 95% and 98% hydrogen purity whereas $P_1 = 111.14$ kPa and 111.37 kPa, respectively. The periodic process cycle consists of 4 steps briefly described as follows:

- Step 1: Sorption-reaction: a 6:1 mixture of steam and methane is fed to the reactor filled with an admixture of HTC sorbent and Ni-based SMR catalyst at P_1 and T_c. The effluent stream consists of majority hydrogen during this step, and this stream is withdrawn from the reactor until carbon dioxide concentration reaches threshold values.

- Step 2: Reverse depressurization: the reactor is depressurized to near ambient pressure P_2 by counter-currently withdrawing desorbed CO_2 and void gases.

- Step 3: Reverse steam purge: purging with 95% H_2O + 5% H_2 stream at P_2 and T_c is carried out during this step. The effluent gas predominantly consists of desorbed CO_2, and purge H_2O and H_2.

- Step 4: Pressurization: finally, the reactor is pressurized from pressure, P_2, to initial bed

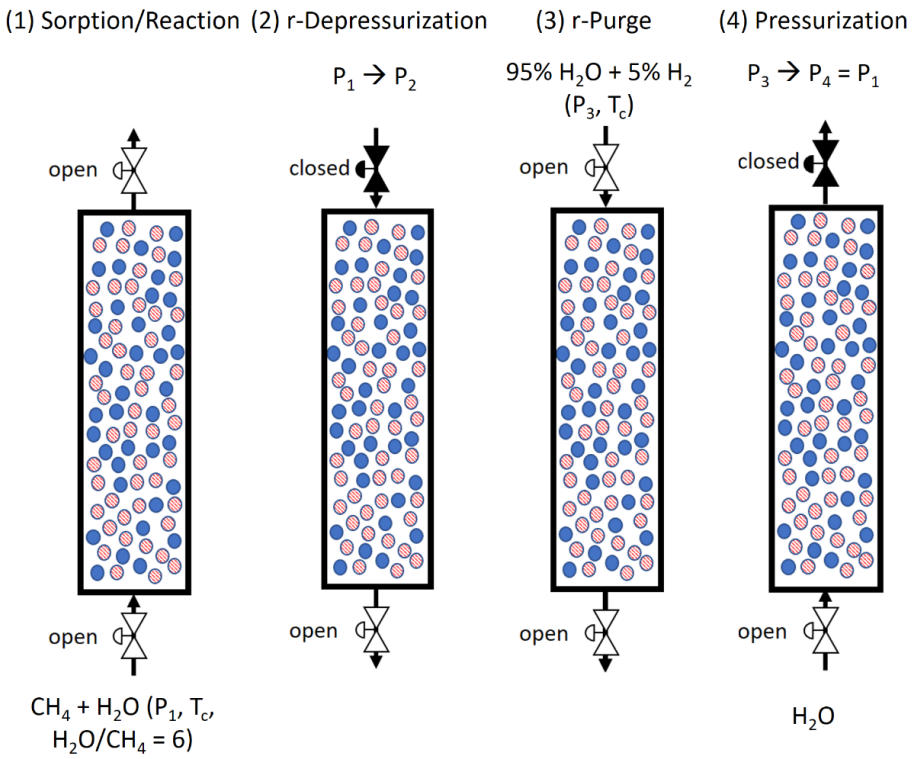

Figure 2.14: Optimal cycle configuration for SE-SMR.

pressure, P_1. The reactor is now primed to undergo another cycle.

Figure 2.15 depicts the pressure profiles inside the SE-SMR column during the 4-step optimal cycle. Higher pressures do not particularly favor SMR reactions although they are favorable for CO_2 sorption on HTC sorbent [151]. Therefore, as can be seen in Table 2.9, the optimizer selected low pressure values of 111.14 kPa and 111.37 kPa for hydrogen purity of 95% and 98% to balance the tradeoffs between SMR reaction rates and CO_2 sorption capacity well. As methane is the limiting reagent, increasing the amount of steam in the input feed enhances the methane conversion. Consequently, the steam-to-carbon feed ratio hits the upper bound of 6 for both hydrogen-purity constraint values. In both the cases, the regeneration step was carried out at the lowest possible pressure (100 kPa). Due to low pressure, much of the adsorbed CO_2 is transferred from the solid sorbent to the gas phase, which is then removed from the SE-SMR column by the purge stream. Low values of purge duration (202.04 and 253.49 seconds) were selected by the optimizer for 95%

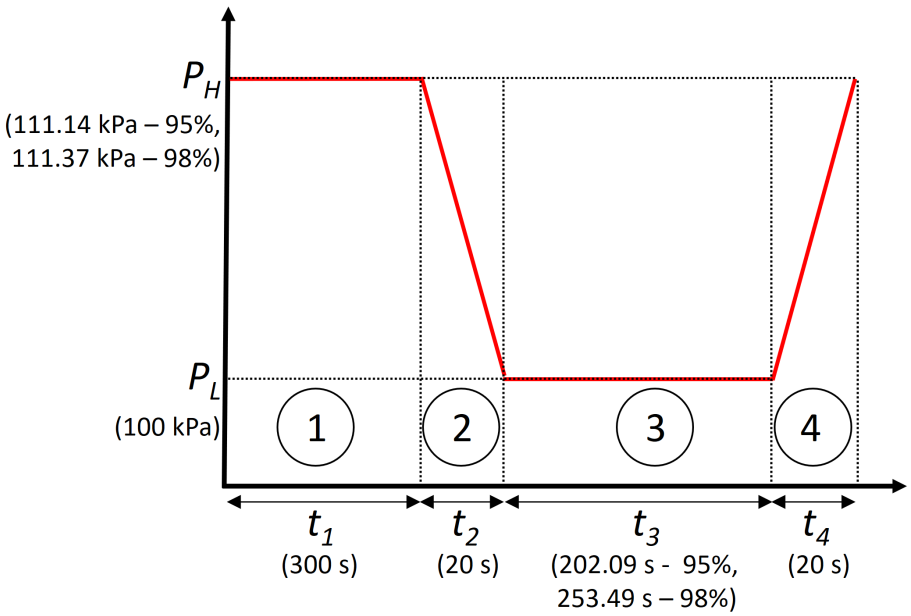

Figure 2.15: Pressure change in the SE-SMR column for the 4-step optimal cycle. The optimal cycle consists of (i) sorption-reaction (P_H), (ii) reverse-depressurization ($P_H \rightarrow P_L$), (iii) reverse-purge (P_L) and (iv) pressurization ($P_L \rightarrow P_H$) steps.

and 98% cases. Minimizing purge duration is favorable for improving objective function as the expression for obtaining hydrogen productivity (Eq. 2.57) has total cycle time in the denominator. In addition, a lower purge time would ensure that lesser amounts of purge stream ($H_2O + H_2$) is used which reduces the amount of utility used. The hydrogen productivity values were also affected by the bed residence time. Higher superficial velocity of steam and methane feed during the hydrogen production step increases the productivity of hydrogen but also reduces hydrogen purity as the product would be contaminated with unreacted methane. Therefore, lower values of superficial velocity had been chosen by the optimizer to have a sufficient bed residence time for converting majority of entering methane. The optimizer yielded maximum possible value of temperature (773 K) for both 95% and 98% hydrogen product cases as higher temperatures are favorable for thermodynamic equilibrium and faster reaction kinetics. The sorbent-to-catalyst ratio in the bed also affects the sorption-enhancement obtained in the process. If the ratio is high, the bed would mostly be packed with the sorbent and there would not be enough catalyst to carry out the SMR reactions. On the other hand, if the ratio is low, lesser amounts of CO_2 would be adsorbed in the column as

not enough HTC sorbent would be present. Consequently, the optimizer chose moderate values of α_c to have optimum amounts of sorbent and catalyst in the bed to carry out both SMR and CO_2 sorption efficiently.

Table 2.10: Comparison of the hydrogen productivity obtained of 95% and 98% hydrogen product with the existing data in literature.

	Waldron et al. [147]	Xiu et al. [152]	This work	
H_2 purity	94.4%	93.8%	95%	98%
H_2 productivity $\left(\frac{\text{mmol } H_2}{\text{kg solid. s}}\right)$	0.221-0.397	0.13	0.534	0.204
Number of steps	4	4	4	4
Steps sequence	(i) Sorption-Reaction (ii) Reverse Depres. (iii) Reverse Purge (iv) Reverse Pres.	(i) Sorption-Reaction (ii) Reverse Depres. (iii) Reverse Purge (iv) Reverse Pres.	(i) Sorption-Reaction (ii) Reverse Depres. (iii) Reverse Purge (iv) Pressurization	(i) Sorption-Reaction (ii) Reverse Depres. (iii) Reverse Purge (iv) Pressurization

Table 2.10 reports the comparison of hydrogen productivity values obtained with those existing in the literature. The experimental studies of Waldron et al. [147] and the computational results of Xiu et al. [152] have been used for drawing the comparison. To obtain 94.4% pure hydrogen product, Waldron et al. [147] used a periodic 4-step cycle consisting of sorption-reaction, reverse depressurization, reverse purge and reverse pressurization steps. The hydrogen productivity observed for such a cycle was 0.221-0.397 mmol H_2/ (kg solid. s). A range of hydrogen productivity is reported as the exact cycle time has not been mentioned in Waldron et al [147]. Xiu et al. [152] used a similar multi-cycle configuration to obtain 93.8% pure hydrogen product with a productivity of 0.13 mmol H_2/ (kg solid. s). For similar hydrogen purity ($\approx$95%), higher hydrogen productivity of 0.534 mmol H_2/(kg solid. s) is obtained, which is 35% higher than the other studies. It should be noted that the improvements in the hydrogen productivity values were observed predominantly due to the optimization of the operating conditions as the process cycle steps and sequence obtained are similar to those of Waldron et al. [147] and Xiu et al. [152].

Additionally, the optimizations were performed for several fixed values of S/C ratio to study the resulting effect of varying S/C ratio on hydrogen productivity. A fixed initial guess was used

as follows: S/C feed ratio = 6, $P_0 = P_1 = P_4 = 233.33$ kPa, $P_2 = P_3 = 100$ kPa, $t_2 = t_4 = 20$ s, $t_3 = 422.45$ s, $v_{fs_1,sup} = 0.05$ m/s, $\alpha_c = 10$, and $T_c = 673$ K, and the initial guess was infeasible subject to the black-box constraints. Figure 2.16 shows the change in hydrogen productivity with S/C feed ratio where the purity of hydrogen product is greater than or equal to 95%. Typically, higher hydrogen productivity levels were observed with increasing S/C ratio due to higher amounts of steam in the gas reaction mixture which improves reaction conversions. The results shown are for S/C feed ratios in the range 4.5-8. Even though better hydrogen productivities were achieved at higher S/C feed ratios, more steam consumption renders the system economically favorable. This is due to high costs incurred for steam generation and recovery. Consequently, modern SMR processes remain economical by using lower values of S/C ratio despite having lower hydrogen productivities. For ratios below 4.5, it was observed that the optimizer could not obtain a feasible point with hydrogen purity greater than 95%. This is because lower hydrogen purity levels are obtained due to decrease in the amount of steam, thereby leading to infeasibility.

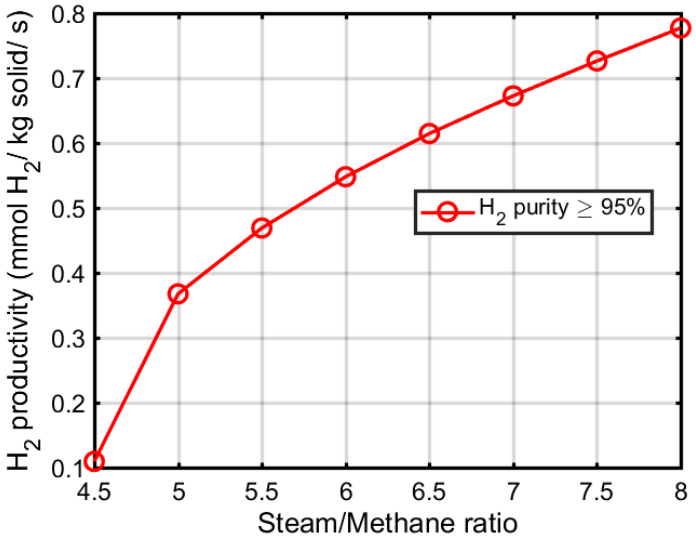

Figure 2.16: Optimal hydrogen productivity with varying S/C ratio.

Hydrogen production cost minimization

In addition to hydrogen productivity maximization, optimization studies were performed for minimization of hydrogen production cost without heat integration. For cost minimization, the black-box and known constraints were similar to those in productivity maximization. An additional constraint on hydrogen productivity was imposed such that it was greater or equal to the lower bound $Prod_u^{min}$. It was assumed that several parallel reactors were operated independently with common compressor, heating and cooling sources, and high-temperature piping and valve network [146]. Enough reactors were operated in parallel for obtaining an approximate hydrogen production capacity of 500 kg hydrogen per day, which is the typical production capacity of small-scale, distributed plants [153].

Table 2.11: SE-SMR synthesis results for cost minimization of hydrogen production for three different purity levels (90%, 92% and 95%), and $Prod_u^{min} = 0.4$ mmol H_2/ (kg solid. s).

Decision Variable	Units	Initial Guess	Optimum Solution (90% H_2 purity)	Optimum Solution (92% H_2 purity)	Optimum Solution (95% H_2 purity)
Number of steps, NS	-	4	4	4	4
Steps sequence	-	(i) Sorption-Reaction (ii) Reverse Depres. (iii) Reverse Purge (iv) Pressurization	(i) Sorption-Reaction (ii) Reverse Depres. (iii) Reverse Purge (iv) Pressurization	(i) Sorption-Reaction (ii) Reverse Depres. (iii) Reverse Purge (iv) Pressurization	(i) Sorption-Reaction (ii) Reverse Depres. iii) Reverse Purge (iv) Pressurization
S/C feed ratio	-	6	6	6	6
P_1	kPa	111.14	191.54	164.97	132.98
P_2	kPa	100	100	100	100
P_3	kPa	100	100	100	100
t_2	s	20	20	20	20
t_3	s	202.05	106.82	112.08	175.39
t_4	s	20	20	20	20
$v_{fs_1,sup}$	m/s	0.029	0.02	0.02	0.023
α_c	-	2.405	2.356	3.365	3.068
T_c	K	773	773	773	773
H_2 purity (dry basis) (%)	-	95	90	92	95
H_2 productivity	$\frac{\text{mmol } H_2}{\text{kg solid. s}}$	0.534	0.829	0.725	0.534
H_2 production cost, TC	$\frac{\$}{\text{kg } H_2}$	3.41	2.13	2.31	3.12
Operating cost, OC	$\frac{\$}{\text{kg } H_2}$	2.23	1.20	1.34	1.93
Investment cost, $\frac{AIC}{P_{H_2}}$	$\frac{\$}{\text{kg } H_2}$	1.18	0.93	0.97	1.19
Number of parallel reactors	-	2851	1835	2099	2853
Overall H_2 production	$\frac{\text{kg } H_2}{\text{day}}$	500.04	500	500.1	500.14

The optimizations were performed for three different purities of hydrogen product - 90%, 92% and 95%, and the minimum productivity ($Prod_u^{min}$) was fixed at 0.4 mmol H_2/(kg solid. s), which is approximately the maximum productivity obtained by Waldron et al. [147] for 95% hydrogen

product. The optimal solution obtained during productivity-maximization for 95% hydrogen (Table 2.9) was used as the initial guess for all the optimizations. Table 2.11 reports the initial guess used and the optimal solutions obtained by using the SERP optimization framework. The grey-box algorithm directly entered the optimization phase as the initial guess was feasible subject to the black-box constraints on hydrogen productivity and purity.

Table 2.11 reports the values of the decision variables at the optimum solutions. Additionally, the breakdown of total hydrogen production cost into investment and operating costs, the number of parallel SE-SMR reactors used for producing approximately 500 kg hydrogen per day, and the corresponding hydrogen purity and productivity obtained are also reported. For each case (90%, 92% and 95% hydrogen purity), the optimal cycle configuration consisted of the same operation modes as earlier in hydrogen-productivity maximization: (i) sorption-reaction, (ii) reverse depressurization, (iii) reverse purge and (iv) pressurization. It was observed that the cost of hydrogen production was predominantly dependent on the purity of hydrogen product, and not on the hydrogen productivity. For instance, the hydrogen productivities obtained for all the three cases were greater than the lower bound on hydrogen productivity, $Prod_u^{min}$. Therefore, decreasing the productivity obtained from the corresponding SE-SMR processes did not lower the cost of hydrogen production. However, the production costs significantly depended on the hydrogen purity desired.

The production cost of hydrogen rose from \$2.13 to \$3.12 per kg hydrogen when the purity requirement was increased from 90% to 95%. With an increase in desired hydrogen purity, it was observed that the optimizer selected lower pressure values during step 1 (P_1) as higher pressures are not favorable for methane conversion [151]. Furthermore, the duration of reverse purge operation mode (t_3) increased with an increase in hydrogen purity for improving the regeneration of the SE-SMR reactor column. The hydrogen cost for small-scale, distributed systems is approximately \$3.5 per kg of hydrogen without considering the carbon imputed cost [153]. Therefore, the cost obtained is 10.86% lower, and the productivity is 35% higher than the currently existing technologies.

2.2.3.2 *Sorption enhanced water gas shift reaction*

Generally, syngas is used for hydrogen production via WGSR. The syngas required is produced through coal gasification where coal reacts with steam to form syngas in a coal gasifier. The product syngas is then purified and sent to water gas shift reactor. In these reactors, the effluent streams consist of considerable concentrations of CO and CO_2. To remove the impurities, the hydrogen is passed through multi-column, multi-step PSA units for purification. This complex, sequential process could instead be replaced by using a single column containing a mixture of both catalyst and sorbent. The thermodynamic limitations can be overcome by using SE-WGSR where WGSR is combined with selective sorption of CO_2. According to Le Chatelier's principle, removal of one of the reaction byproducts drives the reaction in the forward direction thereby resulting in higher reaction conversions. The intensified process then directly produces pure hydrogen in a single step.

Typically, the process is favored by high H_2O/CO ratio and lower temperatures. A higher H_2O/CO ratio decreases the amount of CO present in effluent stream due to higher reaction conversions. Lower temperatures were observed to be favorable as both WGSR and CO_2 sorption are exothermic. According to Le Chatelier, low temperature is favorable, and there is no effect of pressure. However, rate of reaction decreases with a decrease in pressure and temperature [154].

There have been numerous studies on hydrogen production through SE-WGSR. Harrison et al. [9] experimentally used a fixed-bed reactor for carrying out single-step SE-WGSR. The reactor was packed with an admixture of CaO and MgO which respectively act as CO_2 sorbent and WGS catalyst. They studied the characteristics of the process as a function of temperature, pressure, synthesis gas feed composition, residence time and sorbent properties. Lee et al. [155] proposed a thermal swing sorption enhanced reaction with simultaneous hydrogen production and CO_2 capture. The periodic process was shown to produce high-purity hydrogen with high CO conversion, enhanced forward reaction rate and high temperature operation. The proposed 5-step cycle had (1) sorption enhanced reaction, (2) co-current CO_2 purge, (3) heating, (4) regeneration by high pressure counter-current steam purge and (5) multi-tasking regeneration steps. Jang et al. [13] studied the effects of H_2O/CO feed ratio, sorbent-to-catalyst ratio, operating temperature and reaction

pressure on a single-step SE-WGSR process performance. Several parametric studies were performed for observing the effects of aforementioned parameters on hydrogen production. In a later work [64], they studied SE-WGSR wherein a two-section sorption enhanced reactor was utilized. The resulting process had a higher hydrogen productivity, CO conversion and overall improved performance. In the compartmentalized, reactor, the first section was packed with more catalyst to promote WGS and had a shorter length. The second section, on the other hand, had more sorbent for promoting SE-SMR and longer length. The effects of other crucial operating parameters such as pressure and temperature, and feed conditions were not included in the study.

None of the earlier studies on SE-WGSR has optimized the performance of the process. Furthermore, in all the works on cyclic SE-WGSR, the cycle configuration of the process has been preassigned. In our analysis, the cycle configuration is not fixed beforehand, and the optimization framework is instead used for optimizing process performance.

The optimization problem formulation for maximizing hydrogen productivity produced via SE-WGSR is similar to that of SE-SMR. In the formulation, only the parameters and variables bounds were updated for SE-WGSR as reported in Table 2.8. The upper bound of step durations $t_{s,ub}$ and solid bed density ρ_{bed} have been updated to 1000 s and 1640 kg solid/ m^3 bed [13], respectively.

The SERP optimization model was utilized to obtain optimal operating conditions and cycle configuration for carrying out SE-WGSR. Similar to the SE-SMR case-study, the optimization was performed for two different purity constraints on hydrogen product - 95% and 98%, and five different initial guesses were selected to run the optimization algorithm. For all the initial guesses, the hydrogen purity constraint was violated thereby leading the algorithm to enter the feasibility phase. Table 2.12 shows the best initial guess which was used for both 95% and 98% hydrogen purity cases. The initial guess was infeasible as the hydrogen purity obtained was just 74.93%. After a feasible point was found in the feasibility phase, the algorithm initiated the optimization phase to improve the objective function value while maintaining feasibility. The grey-box optimization algorithm took 78.44 and 63.69 hours for 95% and 98% H_2 purity cases respectively, and it took the algorithm 1192 and 1033 SE-WGSR simulations for obtaining optimal decision variables values.

A majority of the time was spent in the optimization phase of the algorithm, which needed 999 and 837 simulation runs, respectively, for the two different hydrogen products. The time needed per simulation was dependent on the nonlinearity of obtained process cycle configurations, and ranged from 32.72-230.93 s.

Table 2.12: SE-WGSR synthesis results for both 95% and 98% hydrogen purity cases.

Decision Variable	Units	Initial Guess	Optimum Solution (95% H_2 purity)	Optimum Solution (98% H_2 purity)
Number of steps, NS	-	4	4	4
Steps sequence	-	(i) Sorption-Reaction (ii) Reverse Depres. (iii) Reverse Purge (iv) Pressurization	(i) Sorption-Reaction (ii) Reverse Depres. (iii) Reverse Purge (iv) Pressurization	(i) Sorption-Reaction (ii) Reverse Depres. (iii) Reverse Purge (iv) Pressurization
S/C feed ratio	-	8	4.02	4.36
P_1	kPa	700	700	700
P_2	kPa	100	100	100
P_3	kPa	100	100	100
t_2	s	20	20	20
t_3	s	700	196.9	199.8
t_4	s	20	20	20
$v_{fs_1,sup}$	m/s	0.08	0.02	0.02
α_c	-	5	10	10
T_c	K	773	773	773
H_2 purity (dry basis) (%)	-	74.93	95	98
H_2 productivity	$\frac{\text{mmol } H_2}{\text{kg solid. s}}$	0.247	0.204	0.188

Table 2.12 shows the optimal process operating parameters for both 95% and 98% hydrogen purity optimization cases. The optimizer obtains hydrogen productivity of 0.204 and 0.188 mmol H_2/(kg solid. s) for 95 and 98% H_2 product, respectively. A very high H_2O/CO ratio would increase the purity of hydrogen product but would also lead to lower productivity values as there would not be enough CO to convert H_2O into H_2 product. Therefore, the optimizer yields moderate values of H_2O/CO feed ratio - 4.02 and 4.36 for 95% and 98% hydrogen product specification cases, respectively. For these values of H_2O/CO ratio, the tradeoff between CO conversion values and H_2 productivity were balanced well. The optimizer selects highest and lowest possible pressure values (700 kPa and 100 kPa) for sorption-reaction and purge steps, respectively. A high pressure

is selected for sorption-reaction step so as to obtain high CO_2 sorption capacity. According to Le Chatelier's principle, WGSR is not affected by pressure as the number of moles of gases are the same on both reactants and products side. Therefore, while selecting an optimum pressure value for carrying out SE-WGSR for hydrogen production, the optimizer just focuses on enhancing CO_2 sorption as the reaction is unaffected by pressure. The optimum solution consists of lowest pressure possible to carry out purge step so that CO_2 desorption could be promoted for efficiently regenerating the bed. During purge, another objective is to use as less of purging stream (H_2O + H_2) as possible. This could be achieved by reducing the purging time which is implicitly handled in the hydrogen productivity objective defined for SE-WGSR formulation. Therefore, the optimizer selects lower values of purging time (196.9 s and 199.8 s) which regenerate the bed enough to maintain respective hydrogen purity constraints at CSS. At optimum, the superficial velocity of the feed gas during hydrogen production step hits the lower bound 0.02 m/s. This is done to increase the bed residence time to achieve high CO conversion thereby leading to higher hydrogen productivity and purity values. The upper bound of sorbent-to-catalyst ratio was selected by the optimizer for both 95% and 98% hydrogen product cases. Therefore, even at such a high sorbent-to-catalyst ratio, enough catalyst is present to facilitate WGSR. Increased sorption enhancement offered by higher amounts of sorbent present in the column improved the performance of SE-WGSR process.

Figure 2.17 shows the optimal cyclic sequence of process steps for SE-WGSR obtained from grey-box optimizer, which is the same for both 95% and 98% hydrogen purity cases. The optimal cycle obtained consisted of 4 operation modes as described earlier for SE-SMR cases. Figure 2.18 shows the variation in pressure profiles inside the SE-WGSR column during the 4-step optimal cycle. Except the purge step 3 duration, all the other cycle configuration parameters were the same for both 95% and 98% H_2 purity cases. In the optimal SE-WGSR cycles for 95% and 98% hydrogen purity cases, $P_1 = 700$ kPa whereas P_2 and P_3 both equal 100 kPa.

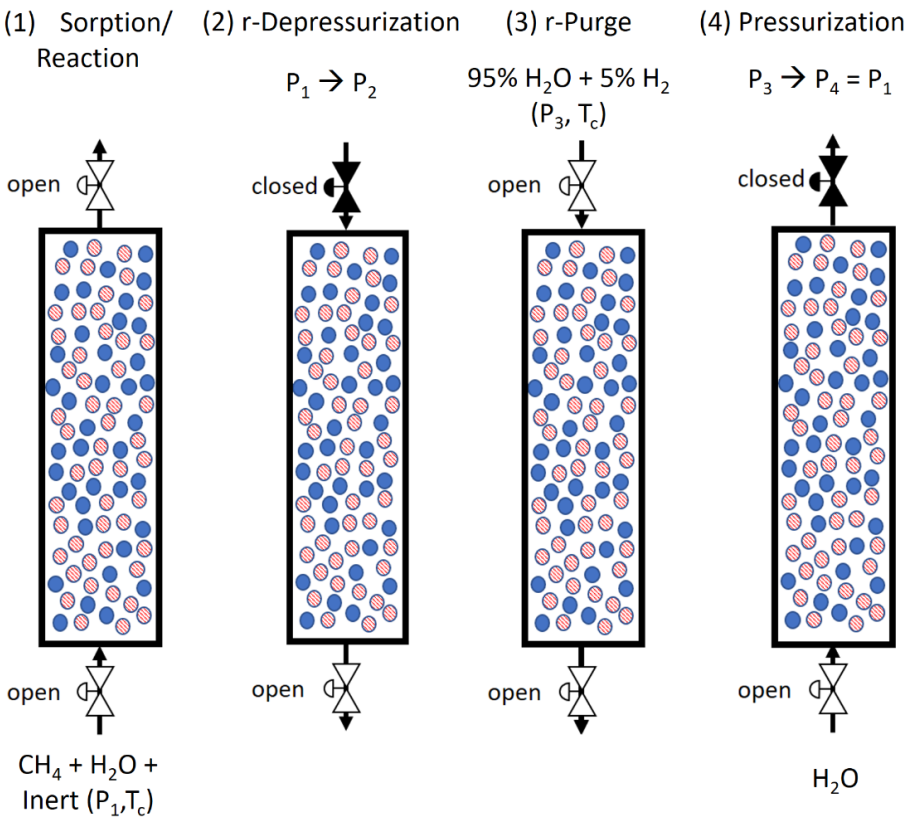

Figure 2.17: Optimal cycle configuration for SE-WGSR.

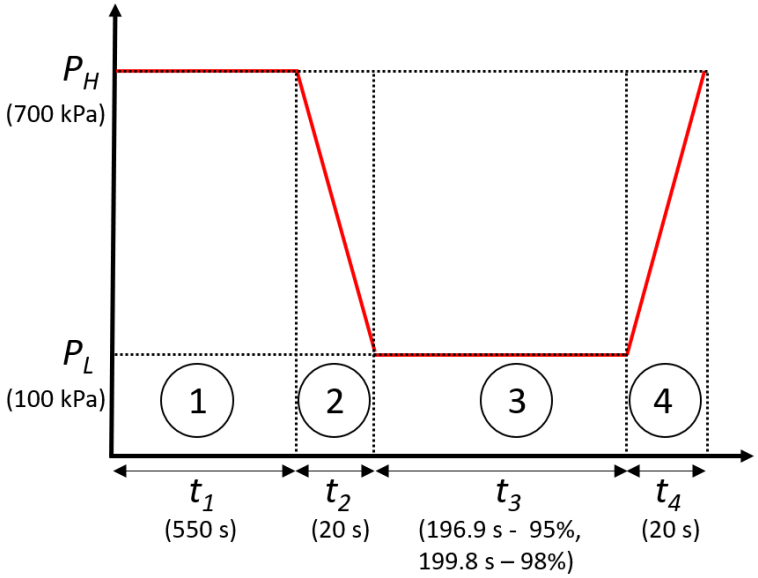

Figure 2.18: Pressure change in the SE-WGSR column for the 4-step optimal cycle.

3. OPTIMAL METHANOL PRODUCTION VIA DYNAMICALLY-INTENSIFIED HYDROGENATION REACTIONS*

3.1 Motivation

Methanol is one of the largest commodity chemicals produced in the chemical industry [156] and is a promising alternate fuel to rapidly depleting fossil fuels reserves [157, 158]. For the past five years, the demand of methanol has been steadily increasing at an average annual rate of 5%, and the global annual demand is expected to reach 100 million tons by 2020 [159]. The soaring demand of methanol is due to its varied potential uses as a clean-burning liquid fuel, as an energy carrier, as a precursor for several vital chemicals including olefins, formaldehyde, methyl tert-butyl ether, dimethyl ether, acetic acid and biodiesel, and as a way for utilizing CO_2 [160–162].

Currently, for producing methanol, two reactor designs dominate the industry – (i) adiabatic ICI Kellogg reactor with cold gas injections for cooling, and (ii) shell and heat exchanger-type multi-tubular Lurgi reactor. Both reactor configurations use Cu-ZnO-Al_2O_3 as the methanol synthesis catalyst [163]. In industrial methanol reactors, the per-pass reactor conversions are significantly lower than equilibrium conversions due to inherent thermodynamic limitations [164].

The role of Cu in the Cu-ZnO-Al_2O_3 catalyst is widely debated in the literature. However, the consensus is that metallic copper clusters provide the active sites for methanol synthesis [165]. Overall, the following three reactions are mainly involved in methanol production from synthesis gas mixtures consisting of H_2, CO and CO_2 [166]:

$$\mathrm{CO\,(g) + 2\,H_2(g) \rightleftharpoons CH_3OH(g),\ \ \Delta H_{298} = \Delta H_{r,I} = -90.70\,kJ/mol} \quad \text{(I)}$$

$$\mathrm{CO_2(g) + 3\,H_2(g) \rightleftharpoons CH_3OH\,(g) + H_2O(g),\ \Delta H_{298} = \Delta H_{r,II} = -49.51\,kJ/mol} \quad \text{(II)}$$

$$\mathrm{CO\,(g) + H_2O\,(g) \rightleftharpoons CO_2(g) + H_2(g),\ \Delta H_{298} = \Delta H_{r,III} = -41.19\,kJ/mol} \quad \text{(III)}$$

*Reproduced in part with permission from Arora, A., Iyer, S. S., Bajaj, I., & Hasan, M. M. F., "Optimal methanol production via sorption-enhanced reaction process." Industrial & Engineering Chemistry Research, Vol 57, Number 42, Pages 14143-14161. Copyright 2018 American Chemical Society.

The reactions (I) and (II) are hydrogenation of CO and CO_2 to form CH_3OH, and reaction (III) is WGSR. The mechanism of methanol formation is convoluted and finding the exact reaction mechanism remains an unresolved challenge. However, most of the earlier studies agree with CO_2 being the source of carbon for methanol synthesis [167].

For SE-MeOH process, the sorption-enhanced reactor consists of an admixture of methanol synthesis catalyst (Cu-ZnO-Al_2O_3) and H_2O adsorbent (NaX zeolite). Due to limited sorption capacity of the adsorbent, the reactor bed is periodically regenerated thereby resulting in multi-step, multi-cycle periodic process. Consequently, a single-column SE-MeOH system discontinuously produces the methanol product as compared to conventional industrial reactors which operate continuously. Investigating the tradeoff between production capacity and process performance, therefore, becomes crucial for optimal SE-MeOH performance.

To this end, an industrial methanol-reactor case study is first adopted from Rezaie et al [168] as the base case and the accuracy of our process simulation model is validated with their published industrial data. Following this, the advantages of replacing some catalyst (present in their reactor) with H_2O adsorbent are demonstrated which results in higher CH_3OH yields at comparable production capacity levels. Two different optimization studies are performed for (i) optimizing base case industrial reactor using SERP technology with fixed synthesis gas feed specifications and reactor design specifications, and (ii) designing a novel SE-MeOH process with optimized process operating conditions, reactor design and feed specifications. For both cases, the objective function consists of methanol-yield maximization and methanol production cost minimization.

3.2 Sorption enhanced methanol synthesis

The SERP concept is applied for promoting CH_3OH synthesis via *in situ* H_2O removal. As shown in Figure 3.1, the resulting periodic SE-MeOH process for producing CH_3OH from synthesis gas is integrated in the overall process flowsheet. During the first step of the cyclic process, synthesis gas consisting of a mixture of H_2, CO_2, CO, CH_4, inerts, and small amounts of CH_3OH and H_2O enter the compressor at 51.2 bar and 323 K [169]. The compressor increases the synthesis gas pressure to the desired levels required in the downstream methanol reactor. The compressed

synthesis gas is then passed through the heat exchanger where it takes up excess heat from the product stream produced during first step. The remainder of the heat is provided by the heater upstream of the reactor so that the temperature can be raised to desired levels.

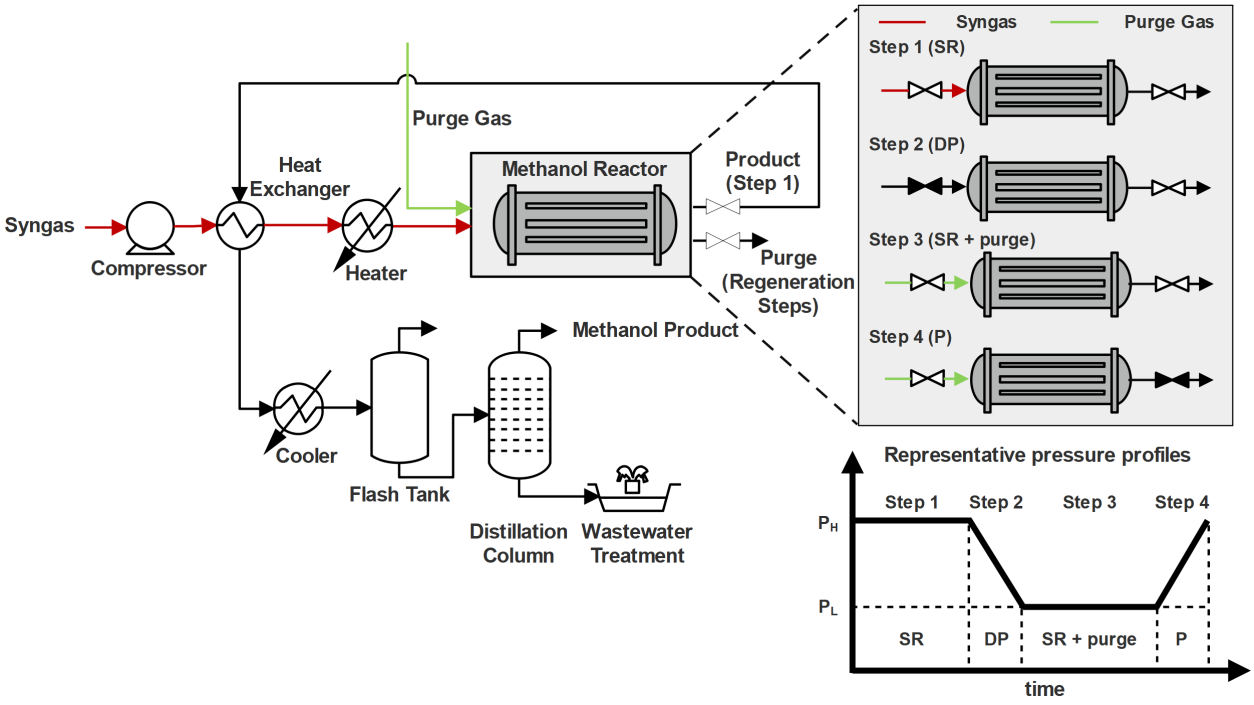

Figure 3.1: Overall flowsheet for CH_3OH production from synthesis gas using periodic SERP concept. During first step of the periodic process, compressed synthesis gas is fed to the reactor for producing CH_3OH. For the rest of the stages, the reactor is regenerated via depressurization and/or purging operation modes.

The fixed-bed, multi-tubular methanol reactor consists of a sorbent-catalyst mixture and converts synthesis gas to CH_3OH with *in situ* removal of H_2O from the gas mixture via adsorption. For recovering the produced CH_3OH, the product stream is firstly cooled to 311 K by using a sequence of heat exchanger and cooler units. The cooled stream is then sent to a flash tank to remove most of the light key components from the liquid mixture. The vapor stream from the flash tank can be recompressed and recycled back to the reactor to obtain higher overall reaction conversions. However, the recycling stream is not considered in the process flowsheet for simplification purposes.

If recycle stream were considered, significant computational resources would need to be spent for achieving CSS, which is beyond the current scope. The liquid stream from the flash stage predominantly consists of CH_3OH and H_2O, and it is processed in a multi-stage distillation column for achieving CH_3OH-H_2O separation. The composition specifications of the column are assumed to be bottom products with 0.01 mol % CH_3OH, and distillate with 0.1 mol % H_2O [169]. During the regeneration stages of the periodic SERP systems, a purge gas consisting of nitrogen is used for desorbing and purging H_2O out of the reactor. Figure 3.1 also shows an illustrative 4-step SE-MeOH cycle which can be used for achieving periodic CH_3OH production and bed regeneration. The sequence of the operation modes in the period cycle is as follows: (i) SR, (ii) DP, (iii) purge and (iv) P.

3.3 Process simulation and optimization

To simulate SE-MeOH systems for generating input-output data, the GRAMS framework is used. In this section, the appropriate adsorption and reaction rate expressions, simplifying modeling assumptions and process performance metrics and cost relations are described which are used for simulations.

3.3.1 Model assumptions

The following assumptions have been taken to simplify the modeling, simulation and optimization of SE-MeOH processes:

- There is no recycling of the unconverted CO and CO_2 reactants [168, 170].
- The methanol synthesis catalyst does not undergo catalyst deactivation, and the effectiveness factor of methanol synthesis reactions is one [171].
- The ideal gas law is followed [172–175].
- The CH_3OH synthesis reactions occur in the gas phase, and there are no side reactions [34].
- The boiling water on shell side of the Lurgi reactor which is used for cooling is not modeled,

and it is assumed that it maintains the wall of the tubes at a constant temperature which is the same as of feed temperature.

- The synthesis gas feed to the methanol reactor is free of sulphur.
- Only H_2O is adsorbed on the NaX zeolite adsorbent [176].
- In periodic SE-MeOH processes, the first process step is fixed as an open-open step (i.e., SR or rSR) during which synthesis gas mixture is fed to the reactor and methanol product is produced.
- If a process cycle has a purge operation mode, nitrogen is used as the purging gas. Furthermore, the superficial velocity of purging stream is four times that of first step (i.e., sorption-reaction step) to achieve significant bed regeneration.
- For computational efficiency, the simulations are performed for 10 spatial volumes and 20 process cycles. It was observed that an increase in either of the two values did not show any change in the process performance metrics' values.
- The pressure changes linearly during pressure-changing steps (i.e., P, DP, rP and rDP).
- The temperature of the reactor outlet stream is reduced to 448 K after passing through heat exchanger [169].
- The cooler reduces the product feed temperature from 448 to 311 K, and the corresponding pressure drop is 3.4 bar [169].

3.3.2 Decision variables bounds

There are twelve decision variables in the optimization model, since the maximum number of process steps in the SE-MeOH cycle is considered to be four. The considered decision variables include the compositions of CO_2 and CO in synthesis gas feed, three pressure values which describe the cyclic configuration and operating pressures, four step duration variables, two variables

for feed flow rate and temperature, and adsorbent-to-catalyst mass ratio. Note that the first process cycle step is fixed as a sorption-reaction step to break the problem symmetry. These variables have been appropriately bounded with lower and upper bounds, which can be found in Table 3.1. For bounding chemical species' composition in synthesis gas feed, four different industrial reactor conditions were considered to obtain the typical synthesis gas compositions in methanol synthesis plants [166]. The minimum and maximum values of compositions (among the four synthesis gas feed specifications) were set as lower and upper bounds, respectively (Table 3.1). Furthermore, it is assumed that feed consists of 2.47% inerts and the remainder of the feed is composed of H_2. The upper bound on the column pressure is taken as 76.98 bar, which is the operating pressure of an industrial methanol reactor [168], and the lower bound on pressure is kept as 1 bar. The step duration is assumed to be in the range 30-1000 s, and the steps during which column pressure changes (P, DP, rP, rDP) are constrained to be 30 s long to reduce overall cycle time. The synthesis gas feed flow rate is assumed to vary between 0.3-1.0 mol s^{-1}, which is the typical range of industrial feed specification [31]. The feed temperature variable has a narrow range of operation between 493 and 543 K [177], and the adsorbent-to-catalyst ratio is assumed to vary between 0-0.5.

Table 3.1: Bounds on decision variables in the optimization model.

Parameter	Unit	Lower bound	Upper bound
y_{CO_2}	-	0.0295	0.4136
y_{CO}	-	0.0476	0.285
P^*	bar	-76.98	76.98
t	s	30	1000
$\dot{n}$	mol s^{-1}	0.30	1
T	K	493	543
α	-	0	0.5

*Negative pressure values indicate reverse flow direction in sorption-enhanced reactor

3.3.3 Adsorption kinetics model

In published literature, several adsorbents have been used for capturing H_2O which include zeolites, silica gel, hygroscopic salts, activated carbon, aluminophosphates and polymeric desiccants [178]. Among them, hydrophilic zeolites are suitable for H_2O adsorption in SE-MeOH processes due to high adsorption capacity and thermal stability at moderately high temperatures. In fixed-bed SE-MeOH systems, the H_2O adsorbent must be suitably selected such that the affinity towards H_2O is not too high which may result in difficult regeneration. Therefore, NaX zeolite is preferred over zeolite 4A or 5A as it has moderate affinity towards H_2O adsorption [179].

In the LDF model used for capturing the adsorption dynamics of H_2O on NaX zeolite, the dimensionless mass transfer coefficient (α_i) is calculated using the following equation [145]:

$$\alpha_i = \frac{15L}{r_p^2 v_0} \frac{\varepsilon_p D_{p,i}}{\varepsilon_p + \frac{\rho_{p,ads} R \overline{T} T_0 q_{s,0}}{P_0} \left(\frac{\partial x_i^*}{\partial (y_i \overline{P})} \right)} \tag{3.1}$$

where L is the bed length. r_p, $\rho_{p,ads}$ and ε_p are the adsorbent particle radius, density and porosity, respectively. $\overline{P}$ and $\overline{T}$ are dimensionless pressure and temperature, and P_0 and T_0 are the corresponding scaling parameters. $q_{s,0}$ and v_0 are the scaling parameters for solid loading capacity and interstitial velocity, respectively. A dual-site Langmuir adsorption isotherm model is used for fitting the experimentally obtained adsorption capacities of H_2O on NaX zeolite. $b_{i,1}$ and $b_{i,2}$ are the dual-site isotherm parameters and are dependent on temperature in an Arrhenius-type manner as follows:

$$b_{i,1} = b_{o,i,1}.\ \exp\left[-\frac{\Delta U_{i,1}}{R.\overline{T}.T_0} \right] \tag{3.2}$$

$$b_{i,2} = b_{o,i,2}.\ \exp\left[-\frac{\Delta U_{i,2}}{R.\overline{T}.T_0} \right] \tag{3.3}$$

where, ΔU_1 and ΔU_2 are the heat of adsorption of sites 1 and 2, and $b_{o,i,1}$ and $b_{o,i,2}$ are the dual-site isotherm's fitting parameters.

For obtaining dual-site fitted parameters, the experimental data for adsorption of H_2O on NaX

zeolite at 373 K and 548 K are obtained from Chuikina et al. [180] and Carvill et al. [179], respectively. The obtained equilibrium adsorption capacities $\left(q^*_{\mathrm{H_2O}} = \dfrac{x^*_{\mathrm{H_2O}}}{x_0}\right)$ is fitted as a function of temperature and partial pressure of H_2O. An optimization problem, based on least-squares fitting, is formulated and solved using the nonlinear programming solver ANTIGONE [136] in the GAMS environment. The experimental data and the fitted dual-site Langmuir isotherms are shown in Figure 3.2, and the respective fitting parameters and other required parameters for simulating adsorption dynamics are reported in Table 3.2.

Table 3.2: Parameters for H_2O adsorption on NaX zeolite.

Parameter	Unit	Value	Reference
$D_{p,i}$	$m^2\ s^{-1}$	3×10^{-5}	[181]
$\rho_{p,ads}$	kg ads. m^{-3} ads.	590	[182]
ΔH_i	J mol^{-1}	-75312	[179]
$m_{i,1}$	mol kg^{-1}	16.875	fitted
$m_{i,2}$	mol kg^{-1}	1.379	fitted
$b_{o,i,1}$	Pa^{-1}	10^{-9}	fitted
$b_{o,i,2}$	Pa^{-1}	$10^{-}9$	fitted
$\Delta U_{i,1}$	J mol^{-1}	-39934.04	fitted
$\Delta U_{i,2}$	J mol^{-1}	-66541.76	fitted
$q_{s,0}$	mol kg^{-1}	16.875	max($m_{i,1}$,$m_{i,2}$)

3.3.4 Reaction kinetics model

Several kinetic models for CH_3OH synthesis over commercial Cu-ZnO-Al_2O_3 catalyst exist for both gas-phase and liquid-phase reactions [183–189]. The models predominantly differ in pressure and temperature ranges considered, and the composition of Cu, Zn and Al in the catalyst. The kinetic models of Bussche and Froment [183] and Graaf et al. [187] are the most popular for simulating CH_3OH-synthesis reactions physics. The model of Bussche and Froment is adopted as it addresses some of the limitations of other kinetic models [190]. In this model, it is assumed that CO_2 is the primary source of carbon for CH_3OH synthesis. As the three reactions involved in CH_3OH synthesis are linearly dependent, only CO_2 hydrogenation and water gas shift reactions

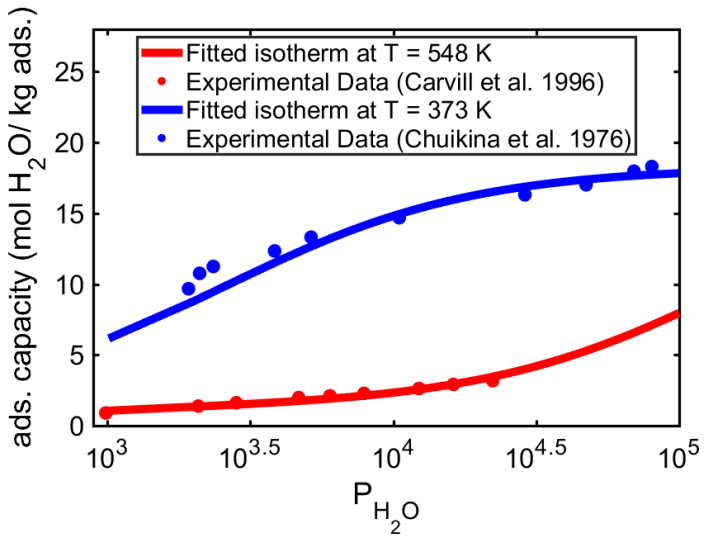

Figure 3.2: Fitted Langmuir dual-site isotherms representing adsorption of H_2O on NaX zeolite. The experimental data have been used for least-squares fitting, and P_{H_2O} is the partial pressure of water in pascals.

(reactions II and III) are considered in their study. The corresponding rate expressions, obtained from their study, are reported in Table G.4. $\overline{R}_{II}$ and $\overline{R}_{III}$ are the dimensionless reaction rates of CO_2 hydrogenation and WGSR, and these parameters have been appropriately scaled using a scaling parameter r_0. r_0 has been primarily used for maintaining the dimensionless nature of the model and is set equal to one in the process simulations.

3.3.5 Process performance metrics

The performance of SE-MeOH systems is gauged by computing values of single-pass CO_2 conversion, CO conversion, CH_3OH yield and CH_3OH production cost [177]. Higher values of reaction conversion and yield, and lower CH_3OH production cost are desirable to obtain an efficient process, which in turn would result in lower recycle ratios and significant capital and operating costs savings. The metrics are calculated for the first step duration when synthesis gas is fed to the reactor, and the product CH_3OH is obtained from the periodic or continuous process.

Table 3.3: Reaction kinetics model of Froment et al. for CH_3OH synthesis.

$$\overline{R}_{II} = \frac{K'_9.K'_{10}}{r_0.(K'_8)^3} \ ; \text{ unit of } r_0 = \text{mol kg cat.}^{-1}\ \text{s}^{-1}$$

$$\overline{R}_{III} = \frac{K'_2}{r_0.K'_8}\left[\frac{y_{\text{CO}_2}.\overline{P}.P_0}{10^5} - \frac{K'_7.y_{\text{H}_2\text{O}}.y_{\text{CO}}.\overline{P}.P_0}{y_{\text{H}_2}.10^5}\right]$$

where,

$$K'_1 = 1.07 \exp\left(\frac{36696}{R.T_0.\overline{T}}\right) \text{mol kg cat.}^{-1}\ \text{s}^{-1}\ \text{bar}^{-2}$$

$$K'_2 = 1.22 \times 10^{10} \exp\left(\frac{-94765}{R.T_0.\overline{T}}\right) \text{mol kg cat.}^{-1}\ \text{s}^{-1}\ \text{bar}^{-1}$$

$$K'_3 = 3453.38$$

$$K'_4 = 6.62 \times 10^{-11} \exp\left(\frac{124119}{R.T_0.\overline{T}}\right)\ \text{bar}^{-1}$$

$$K'_5 = 0.499 \exp\left(\frac{17197}{R.T_0.\overline{T}}\right)\ \text{bar}^{-0.5}$$

$$K'_6 = \exp\left(\frac{3066}{T_0.\overline{T}} - 10.592\right)\ \text{bar}^{-2}$$

$$K'_7 = \exp\left(\frac{2073}{T_0.\overline{T}} - 2.029\right)$$

$$K'_8 = 1 + \frac{K'_3.y_{\text{H}_2\text{O}}}{y_{\text{H}_2}} + \frac{K'_4.y_{\text{H}_2\text{O}}.\overline{P}.P_0}{10^5} + K'_5\sqrt{\frac{y_{\text{H}_2}.\overline{P}.P_0}{10^5}}$$

$$K'_9 = \frac{K'_1.y_{\text{H}_2}.\overline{P}.P_0}{10^5}\text{mol kg cat.}^{-1}\ \text{s}^{-1}\ \text{bar}^{-1}$$

$$K'_{10} = \frac{y_{\text{CO}_2}.\overline{P}.P_0}{10^5} - \frac{y_{\text{H}_2\text{O}}.y_{\text{CH}_3\text{OH}}.10^5}{K'_6.y^3_{\text{H}_2}.\overline{P}.P_0}\text{bar}$$

CO_2 conversion is calculated by obtaining the percentage of CO_2, present in the inlet synthesis gas feed, which converts to form CH_3OH [177]:

$$\text{CO}_2 \text{ conversion } (\%) \ = \frac{n_{\text{CO}_2,in} - n_{\text{CO}_2,out}}{n_{\text{CO}_2,in}} \times 100 \tag{3.4}$$

CO conversion is computed by calculating the percentage of CO converting into CH_3OH [177]:

$$\text{CO conversion } (\%) \ = \frac{n_{\text{CO},in} - n_{\text{CO},out}}{n_{\text{CO},in}} \times 100 \tag{3.5}$$

CH_3OH yield metric helps us in realizing the actual amount of CH_3OH formed in comparison to the highest possible amount of CH_3OH which would have formed if all of entering CO_2 and CO had converted to CH_3OH. Therefore, CH_3OH yield is defined as the number of moles of CH_3OH formed per mole of carbon entering in synthesis gas feed (in form of either CO or CO_2), and is computed as follows [190]:

$$\text{CH}_3\text{OH yield } (\%) = \frac{n_{\text{CH}_3\text{OH},out} - n_{\text{CH}_3\text{OH},in}}{n_{\text{CO},in} + n_{\text{CO}_2,in}} \times 100 \tag{3.6}$$

The following metric, consisting of total cost incurred for producing a kilogram of CH_3OH (TC), is defined to evaluate the economic feasibility of CH_3OH synthesis process:

$$TC\left(\frac{\$}{\text{kg CH}_3\text{OH}}\right) = \frac{AIC}{PC_{\text{CH}_3\text{OH}}} + OC \tag{3.7}$$

where AIC is the annualized investment cost incurred for CH_3OH synthesis in \$ per year, $PC_{\text{CH}_3\text{OH}}$ is the annual CH_3OH production capacity in kilograms, and OC is the overall operating cost of the process in \$ per kg CH_3OH.

3.3.6 Correlations for cost estimation

The following expression is used to obtain annualized investment cost (AIC) [191]:

$$AIC = \frac{I_t IR}{1 - \frac{1}{(1+IR)^{t_e}}} \times \left[1 - \frac{t_t - t_e}{t_t(1+IR)^{t_e}}\right] \tag{3.8}$$

where IR = 10% is the interest rate, t_e = 15 years and t_t = 25 years are the economic and technical lifetimes, and I_t is the total investment cost. The CH_3OH production process from synthesis gas consists of the following production units - methanol reactor, flash tank, distillation unit, heat exchanger, compressor, heater, cooler and wastewater treatment. The total investment cost (I_t) is

the sum of all equipment costs, and is computed as follows:

$$I_t = \sum_{e \in E} TIC_e \tag{3.9}$$

where the individual equipment costs can be found in Table 3.4.

Table 3.4: Cost correlations for computing total installment costs of the unit operations in the CH_3OH synthesis flowsheet [192].

Equipment (e)	Total Installed Cost in M\$ (TIC_e)	Scaling Factor (S_e)
Methanol reactor ($reac$)	$19.225 \left(\frac{S_{reac}}{87.5}\right)^{0.6}$	maximum feed flow rate in kg hr^{-1}
Flash tank ($flash$)	$2.891 \times 10^{-3} \left(S_{flash}\right)^{0.8}$	feed gas in kg s^{-1}
Distillation column ($dist$)	$30.002 \left(\frac{S_{dist}}{6.75}\right)^{0.7}$	CH_3OH flow rate in tons per hr
Heat exchanger (he)	$69.640 \left(\frac{S_{he}}{355}\right)$	heat exchanger duty in MW
Compressor (com)	$24.735 \left(\frac{S_{com}}{10}\right)^{0.67}$	compressor power in MW
Heater ($heat$)	$1.410 \times 10^{-9} \left(S_{heat}\right)^{0.8}$	heat duty in MW
Cooler ($cool$)	$87.981 \left(\frac{S_{cool}}{470}\right)^{0.67}$	cooling duty in MW
Wastewater treatment (ww)	$59.848 \left(\frac{S_{ww}}{393100}\right)^{1.05}$	water feed flow rate in kg hr^{-1}

For calculating the operating cost (OC) of the process, the sum of the operating costs of compressor, heater, cooler, and distillation column is obtained. Therefore, the overall expression for computing operating costs of CH_3OH synthesis process is as follows:

$$OC \left(\frac{\$}{\text{kg } CH_3OH}\right) = OC_{com} + OC_{heat} + OC_{cool} + OC_{dist} \tag{3.10}$$

where OC_{com}, OC_{heat}, OC_{cool} and OC_{dist} are respectively the operating costs of compressor, heater, cooler and reboiler stage of distillation column in \$ per kg CH_3OH.

The power consumed by compressor is denoted by S_{com}, and is calculated as follows [75]:

$$S_{com}\,(\mathrm{W}) = \frac{1}{\eta_m \eta_c} F_{SG,in} R T_{fs_1} \left(\frac{\gamma}{\gamma - 1}\right) \left[\left(\frac{P_{high}}{P_{low}}\right)^{\frac{\gamma-1}{\gamma}} - 1\right] \tag{3.11}$$

where η_m and η_c are the compressor and motor efficiency which are equal to 95% and 75%, respectively. $F_{SG,in}$ and T_{fs_1} are the incoming synthesis gas molar flow rate in kmol s^{-1} and feed temperature in K, P_{high} and P_{low} are respectively the exiting and incoming synthesis gas feed pressures, and γ is the heat capacity ratio and is assumed to be equal to 1.40. The overall compressor power consumed is the sum of power consumed for compressing synthesis gas during the first process step and during the bed pressurization stages. The electricity consumed by the compressor (MWh per cycle) can be computed as follows:

$$E_{com} = \frac{S_{com} t_1}{3600} \tag{3.12}$$

The price of the electricity is assumed to be \$70 per MWh [75]. Therefore, the operating cost of compressor is:

$$OC_{com} = \frac{70 E_{com}}{\mathrm{CH_3OH\ produced\ in\ kg\ per\ cycle}} \tag{3.13}$$

Due to compressor work, the temperature of the exiting synthesis gas feed is higher and is computed using the following relation [193]:

$$T_{o,com} = T_{i,com} + \frac{T_{i,com}}{\eta_c} \left[\left(\frac{P_{high}}{P_{low}}\right)^{\frac{\gamma-1}{\gamma}} - 1\right] \tag{3.14}$$

where $T_{o,com}$ and $T_{i,com}$ are respectively the outgoing and incoming synthesis gas feed temperatures. The temperature of synthesis gas is further raised from $T_{o,com}$ to $T_{o,he}$ with the use of a heat exchanger which transfers the excess heat from methanol reactor outlet stream to synthesis gas reactant feed. The remaining heat duty to raise synthesis gas temperature from $T_{o,he}$ to the desired

reactor temperature (T_{reac}) is provided by a heater, and the required heating duty is computed as follows:

$$S_{heat}\ (\mathrm{MW}) = \frac{\sum_{i \in I} F_{i,in} \int_{T_{o,he}}^{T_{reac}} C_{p,i} dT}{\eta_h} \tag{3.15}$$

where $F_{i,in}$ is the molar flow rate of species i to the heater in kmol s^{-1}, $C_{p,i}$ is the molar heat capacity of species i in kJ mol^{-1} K^{-1}, and $\eta_h = 0.8$ is the heater efficiency [194]. As the purge gas is assumed to be available at desired reactor conditions during regeneration stages, the heater is only used for heating the reactant synthesis gas and not the nitrogen purge. Medium-pressure steam is used for heating purposes which has an operating cost (OC_{steam}) of \$29.59 per MWh (\$8.22 per GJ) [169]. Therefore, the overall operating cost of the heater (OC_{heat}) is calculated using:

$$OC_{heat} = \frac{OC_{steam} \left(\frac{S_{heat} t_1}{3600} \right)}{\mathrm{CH_3OH\ produced\ in\ kg\ per\ cycle}} \tag{3.16}$$

For obtaining the amount of heat rejected to the cooler, the amount of heat transferred due to latent heat of condensation of CH_3OH and H_2O, and the sensible heat required for reducing the temperature to 311 K is calculated. The heat of condensation is assumed to be 12 kJ mol^{-1} and 34 kJ mol^{-1} for CH_3OH and H_2O, respectively. The heat capacities of the species involved are obtained using the Shomate equation [195]. In the cooler, cooler water is used and the change in its temperature is fixed to be 10 K. The overall amount of cooling water required (in kg per cycle) is calculated as follows:

$$M_{CW} = \frac{t_1 Q_C}{C_{p,CW} \Delta T} \tag{3.17}$$

where, $C_{p,CW}$ is the heat capacity of cooling water, ΔT is the drop in cooling water temperature and is assumed to be 10 K, Q_c is the overall sensible and latent heat rejected to the cooler in kW, and t_1 is the duration of first process step in seconds. It is assumed that the amount of electricity being used is 0.528 W per kg cooling water [74]. Therefore, the overall operating costs of the

cooling unit is as follows:

$$OC_{cool} = \frac{C_c \, M_{CW}}{\mathrm{CH_3OH\ produced\ in\ kg\ per\ cycle}} \tag{3.18}$$

where, C_c is the cost of cooling water in \$ per kg. The amount of reboiler heat in the distillation column is assumed to be 0.0215 kW which is obtained by linearly scaling the reboiler duties w.r.t production typical capacities in this study and in the work of Luyben [169]. This heat is provided by low-pressure steam which has a cost of \$7.78 per GJ [169]. Therefore, the operating cost of distillation column is as follows:

$$OC_{dist} = \frac{R_c \, t_1}{\mathrm{CH_3OH\ produced\ in\ kg\ per\ cycle}} \tag{3.19}$$

where, $R_c = 1.673 \times 10^{-7}$ is the reboiler cost in \$ per second.

3.3.7 Objective function

Maximizing CH_3OH yield: The objective function for maximizing the average CH_3OH yield produced via SE-MeOH during the first process step (i.e., sorption-reaction) is as follows:

$$\begin{aligned}&\max \text{methanol yield } (\%) \ = \\ &\frac{\left(\int_0^{t_1} \left.\frac{y_{\mathrm{CH_3OH}} \overline{P} P_0 \overline{v} v_0}{R \overline{T} T_0}\right|_{Z=1} dt\right) \varepsilon_b \pi r_{in}^2 - \left(\left.\frac{y_{\mathrm{CH_3OH}} \overline{P} P_0 \overline{v} v_0}{R \overline{T} T_0}\right|_{Z=0}\right) t_1 \varepsilon_b \pi r_{in}^2}{\left(\left.\frac{\left(y_{\mathrm{CO}} + y_{\mathrm{CO_2}}\right) \overline{P} P_0 \overline{v} v_0}{R \overline{T} T_0}\right|_{Z=0}\right) t_1 \varepsilon_b \pi r_{in}^2} \times 100\end{aligned} \tag{3.20}$$

where $y_{\mathrm{CH_3OH}}$, y_{CO} and $y_{\mathrm{CO_2}}$ are respectively the gas phase mole fraction of CH_3OH, CO and CO_2. $\overline{P}$, $\overline{v}$ and $\overline{T}$ are the dimensionless gas phase pressure, interstitial velocity and temperature, respectively, and P_0, T_0 and v_0 are their respective scaling parameters. $Z = 0$ and $Z = 1$ denote the reactor's inlet and outlet boundaries, and L is the bed length. ε_b and r_{in} are respectively the bed void fraction and tube inside radius. t_1 is the step one duration in SE-MeOH process cycle. The

numerator denotes the overall number of moles produced from synthesis gas conversion, and the denominator computes the total number of moles of CO and CO_2 fed to the reactor.

Minimizing CH_3OH production cost: The second objective function, considered in the optimization studies, consists of minimizing the overall production costs of CH_3OH as follows:

$$\min TC \left(\frac{\$}{\text{kg } CH_3OH} \right) = \frac{AIC}{PC_{CH_3OH}} + OC \tag{3.21}$$

where the cost relations for computing the annualized investment costs (AIC) and operating costs (OC) are reported in Section 3.3.6.

3.4 Results and discussion

This section reports the optimized SE-MeOH process results for both with and without variable synthesis gas feed specification cases. For each of the cases, the optimized results for both CH_3OH yield maximization and cost minimization are presented.

3.4.1 Base case: industrial methanol reactor

Before delving into the optimization studies, a base case is used which consists of a Lurgi-type methanol industrial reactor adopted from Rezaie et al [168]. The objective here is to study the effect of partial replacement of Cu-ZnO-Al_2O_3 catalyst with NaX zeolite on CH_3OH yield, which eventually dictates the performance of the CH_3OH synthesis process.

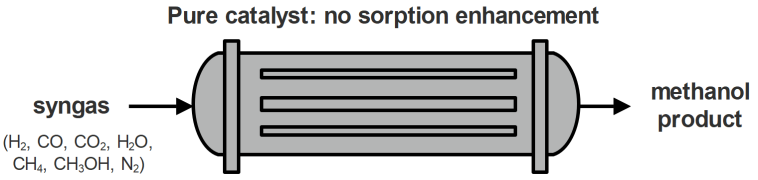

Figure 3.3: Base case industrial methanol reactor.

Base case without sorption-enhancement: To this end, firstly, the methanol reactor is simulated in absence of adsorption using the exact process operating conditions, feed specifications and

design parameters as that of the industrial reactor (see Figure 3.3). Even though the reactor performance data are available for the entire 1200 days of operation of the industrial methanol reactor in Rezaie et al [168], only the data point for the first day of operation is used when the catalyst is fully activated. This is done to have a fair comparison with our model predictions as catalyst deactivation is not considered in our process model. As a few of the parameters are missing in the original study, other sources in literature are referred to for obtaining typical values of those missing parameters in industrial methanol reactors. Overall, the parameters used for performing the simulations have been reported in Table 3.5.

Table 3.5: Design and feed specifications, and process operating conditions for base case industrial methanol reactor.

Parameter	Unit	Value
feed composition [168]:		
CH_4	%	10.26
CO_2	%	9.4
CO	%	4.6
H_2O	%	0.04
H_2	%	65.90
CH_3OH	%	0.50
N_2	%	9.30
feed flow rate [168]	mol s^{-1} $tube^{-1}$	0.64
feed pressure [168]	bar	76.98
feed temperature [168]	K	503
number of tubes [168]	-	2962
tube length [168]	m	7.022
particle diameter [168]	mm	5.47
particle porosity [168]	-	0.37
tube diameter [169]	cm	3.675
heat transfer coefficient [169]	W m^{-2} K^{-1}	283.58
packing density [190]	kg solid m^{-3} bed	1100
bed void fraction [190]	-	0.38

For simulating the industrial reactor system, 100 spatial volumes are used for accurate depiction of the actual process. Furthermore, each of the tubes in the multi-tubular reactor is assumed to be

operated independently. The predicted CH_3OH production capacity by the simulation model is 276.2 tons per day, which is 6.37% lower than the actual plant capacity of 295 tons per day. The kinetics of synthesis gas conversion to CH_3OH are equilibrium-limited. According to simulated results, the CH_3OH yield is 34.02% with 20.61% CO_2 and 60.95% CO single-pass conversions. There are several factors which could contribute to the deviation of predicted CH_3OH production capacity from the plant data. These factors include underestimation of reaction kinetics considered in the base case; inexact overall heat transfer coefficient; neglecting shell-side fluid modeling; and difference in industrial catalyst composition.

Base case with sorption-enhancement: Once the validation of model predictions has been performed at industrial reactor conditions, the effect of sorption-enhancement on process performance is studied. The performance of the SE-MeOH process is compared with the base industrial reactor case to observe the advantages provided by selective H_2O by-product removal over the conventional reactor. Before studying the cyclic processes, the benefits of SERP technology for a single-step process are explored. In the simulations performed, the effect of two parameters, adsorbent-to-catalyst ratio and process step duration, are observed on CH_3OH yield. The catalyst present in the reactor is gradually replaced with adsorbent (with fixed solid packing density) to promote more adsorption of H_2O, and CH_3OH yield is compared for different adsorbent-to-catalyst ratios. Furthermore, different values of step duration are used to observe the effect of varying levels of bed saturation on product yield. The product yield is compared with the base case for which the model predicted a CH_3OH yield of 34.02%. For a fair comparison, all the operating parameters and process specifications, except the material distribution, are kept the same as that of the base industrial reactor case (Table 3.5). The initial bed pressure and temperature are the same as that of feed conditions, and the bed is filled with 6.4% H_2 and 93.6% N_2 mixture, which is within the typical feed composition range used for Cu-ZnO-Al_2O_3 catalyst regeneration [196].

Figure 3.4 shows the variation in CH_3OH yields from the base case for different adsorbent-to-catalyst ratios and step duration. It should be noted that as the SE-MeOH reactor is fully regenerated at the start of the single-step process, the reported yields are the highest possible for given

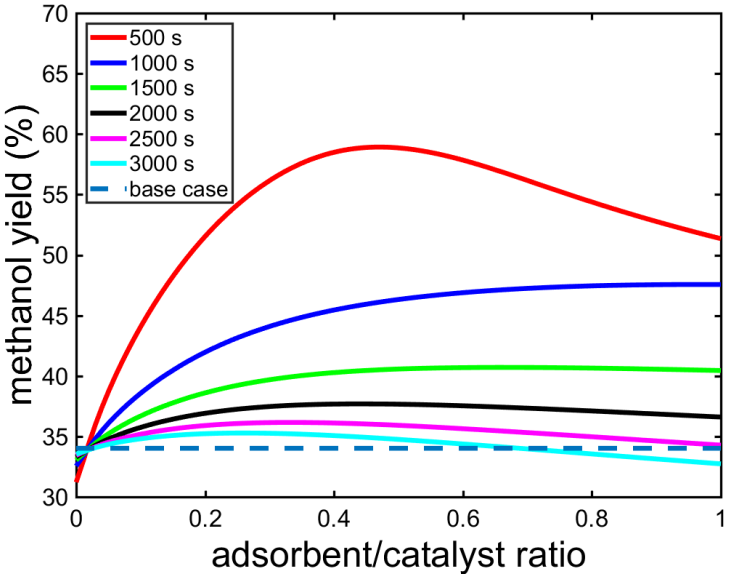

Figure 3.4: Effect of replacing catalyst with adsorbent on CH_3OH yield for a single-step sorption-enhanced methanol synthesis process.

mass ratio and step duration. Lower CH_3OH yields should be expected for periodic processes as they would have lower working capacities than the fully-regenerated single-step process case presented here. For comparison purposes, Figure 3.4 also presents the yield for base industrial case without any sorption-enhancement (34.02%). It can be clearly observed that by replacing catalyst with adsorbent, a significantly higher CH_3OH yield can be obtained when compared to the predicted base case values. This is due to the *in situ* adsorption of H_2O, which in turn pushes the equilibrium towards higher CH_3OH synthesis. Typically, at higher ratios, an inferior process performance and CH_3OH yield is observed due to lesser amounts of catalyst. The slow reaction kinetics of the process, along with lower catalyst amount, offsets the enhancement provided by H_2O adsorption thereby leading to lower CH_3OH yields. Due to sorption-enhancement in the process, CH_3OH yields as high as 59.92% are obtained for 500 s case, which is approximately 76.13% higher than the predicted base case values. Even higher CH_3OH yields would be obtained for process step duration less than 500 s due to further enhancement in removal of H_2O by the adsorbent. For an adsorbent-to-catalyst ratio of zero, when the reactor only contains catalyst, different values

of CH_3OH yield are obtained for different step duration. This is due to the initial conditions, and the deviation from base case is higher for smaller step duration. As the duration of the process step increases, the CH_3OH yield converges to that of the base case, where initial conditions have insignificant effect on CH_3OH yield.

3.4.2 Methanol yield maximization

After observing the promising effects of replacing CH_3OH catalyst with H_2O adsorbent on product yield, optimization studies are performed to improve the performance of the existing industrial reactor with SERP technology. For having a fair comparison with the base case industrial reactor, the same reactor design specifications (column geometry and number of tubes) and feed conditions (composition and flow rate) are used as of the industrial reactor. The optimization studies are performed for optimizing several decision variables including periodic cycle design, operating pressure and temperature, steps duration and material distribution. The objective, here, is to maximize the yield of product CH_3OH while producing at least $PC^{min}_{\mathrm{CH_3OH}}$ amount of CH_3OH.

It was observed that for fixed feed conditions and design specifications as that of the industrial reactor, the optimizer could not find a feasible solution with the production capacity at least as much as of the industrial plant (295 tons per day). This could be due to underestimated model predictions of production capacity in comparison to actual results. Furthermore, another possibility is the inclusion of process regeneration stages, which, in fact, are not present in the real plant. A significant amount of process time is spent on reactor regeneration thereby reducing the duration for which the reactor produces CH_3OH product. Therefore, it becomes difficult for the reactor to match the production capacity of the industrial reactor. To counter this, the constraints on CH_3OH production capacity are relaxed and optimizations are performed for three different relaxed values of $PC^{min}_{\mathrm{CH_3OH}}$: 150 (case a), 200 (case b), and 250 (case c) tons per day.

The obtained optimal decision variables and cyclic configurations are reported in Table 3.6. With a decrease in the minimum production capacity amounts, an increase in CH_3OH yield obtained from the process is observed. For a production capacity of 250 tons per day, a yield of 52.8% is observed, which is almost 55% higher than the predicted base case industrial reactor

Table 3.6: Optimization results of optimized industrial methanol reactor case with maximum yield for different daily CH_3OH production capacities. The results have been compared with predicted yield and production capacity of the base case industrial reactor (yield = 34.02%, production capacity = 276.20 tons per day).

Parameter	Unit	Productivity, $PC^{min}_{CH_3OH}$		
		case a (150 tons per day)	case b (200 tons per day)	case c (250 tons per day)
CH_3OH yield	%	63.62	60.90	52.78
CH_3OH production capacity	tons per day	150.02	200.16	250.02
CO conversion	%	21.70	33.28	46.31
CO_2 conversion	%	87.92	81.94	61.98
cycle configuration	-	(i) sorption-reaction (ii) reverse depres. (iii) reverse purge (iv) pressurization	(i) sorption-reaction (ii) reverse depres. (iii) reverse purge (iv) pressurization	(i) sorption-reaction (ii) depressurization (iii) purge (iv) pressurization
yield improvement	%	(+) 87.01	(+) 79.01	(+) 55.14
production capacity decrease	%	(-) 45.68	(-) 27.53	(-) 9.48
y_{CO_2,fs_1}	-	0.094	0.094	0.094
y_{CO,fs_1}	-	0.046	0.046	0.046
P_1	bar	76.98	76.98	76.98
P_2	bar	1	1	1
P_3	bar	1	1	1
t_1	s	289	202	279
t_2	s	30	30	30
t_3	s	602	216	123
t_4	s	30	30	30
$\dot{n}_{fs_1}$	mol s^{-1}	0.64	0.64	0.64
T_c	K	499.24	501.83	506.92
α_c	-	0.475	0.340	0.391

conditions. In case of higher production capacities, the periodic reactor must spend majority of the cycle time on producing CH_3OH to match desired capacity levels. Therefore, significant bed regeneration cannot be achieved which adversely affects the product yield. However, for lower desirable production capacities as in 150 tons per day case, the bed regeneration can be enhanced as the reactor can operate for longer duration in the regeneration stages. This results in a significantly higher CH_3OH yield of 63.6%. Figure 3.5 shows this tradeoff between CH_3OH production capacity levels and the corresponding CH_3OH yields obtained.

In all the three cases, the optimal cycle configurations consist of the following four operation modes - sorption-reaction, depressurization, nitrogen purge and pressurization. The obtained configurations slightly differ in the feed flow direction (see Table 3.6). The CH_3OH-producing step of

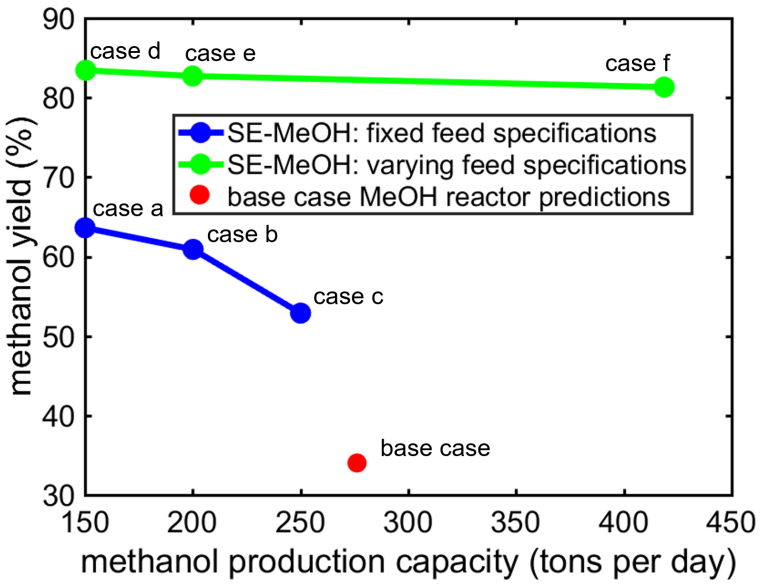

Figure 3.5: Effect of sorption-enhancement on the CH_3OH yield and production capacity obtained for (i) fixed feed specifications (cases a-c) and (ii) varying feed specifications (cases d-f). For cases a-c, the obtained results have the same feed composition and flow rate as of the industrial reactor. In cases d-f, the feed composition and flow rates are also optimized thereby leading to significant process performance improvement.

the process (i.e., step 1) operates at the highest possible pressure of 77 bar. This step is followed by a depressurization of the reactor to 1 bar at which purging occurs for regenerating the bed. The optimal adsorbent-to-catalyst ratios typically increase with decreasing desired production capacity levels. This observation is in alignment with the earlier-reported results for single-step process (Figure 3.4). Higher values of adsorbent-to-catalyst mass ratio positively affect the CH_3OH yield when the desired production capacity ($PC^{min}_{CH_3OH}$) is low. This is due to higher percentage of cycle time which can be spent on bed regeneration, which eventually enhances the sorption-enhancement produced and product yield. However, for higher desirable production capacities, it is preferable to have lower amounts of adsorbent inside the reactor as sufficient regeneration could not be achieved.

Figure 3.6 indicates the overall performance of the optimal SE-MeOH process compared to the base case industrial methanol reactor. The observed CH_3OH yields were significantly higher than the predicted base case values for all the cases considered. Due to the periodic nature of SE-MeOH systems, these processes consumed lower amounts of synthesis gas reactant in comparison to base

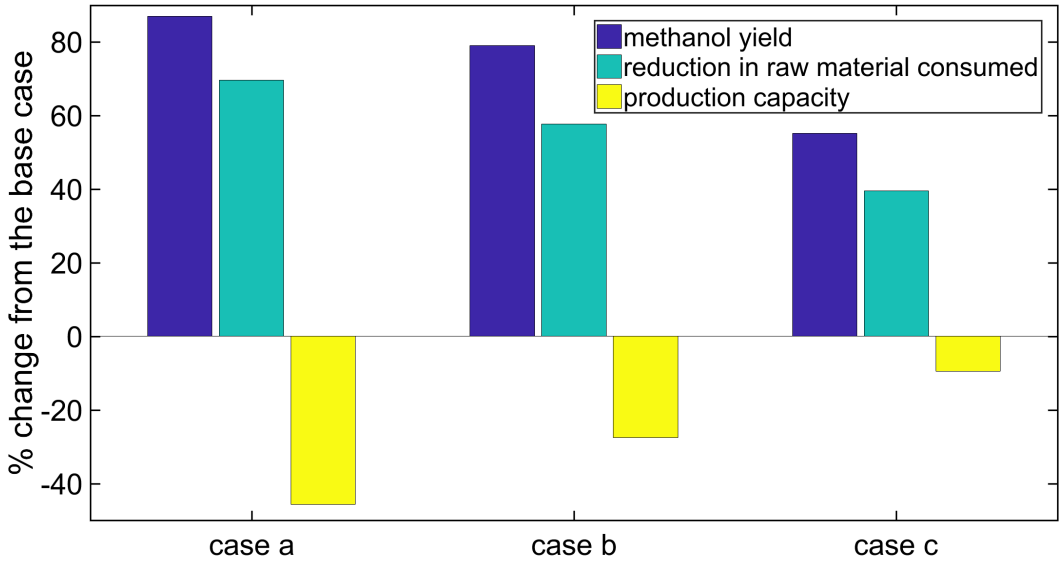

Figure 3.6: Comparison of performance of optimal SE-MeOH process with base case industrial reactor.

case methanol reactor which consumes synthesis gas continuously. This leads to a significant reduction in amount of synthesis gas consumption, as can be seen in Figure 3.6. The reduction should favorably affect the process economics as synthesis gas generation is the most expensive step of CH_3OH synthesis from natural gas [197]. Figure 3.6 also reports the compromise on the production capacity which has to be done due to periodicity of SE-MeOH processes as opposed to continuous industrial reactors. This trend denotes a tradeoff between process performance and overall amount of CH_3OH produced.

For demonstration purposes, the state variables' trajectories for case c at CSS has been reported here in Figure 3.7. The figure indicates the variation in outlet gas-phase mole fraction profiles and reactor bed temperature with time. The temperature is measured at spatial distances relative to the inlet boundary. It can be observed that most of the water adsorbed during the first step is purged out of the reactor bed during the purging step, i.e., third step. In addition, the temperature of the reactor bed does not exceed 543 K thereby preventing catalyst deactivation. For the rest of the cases a and b, the dynamic profiles can be found in Appendix E.

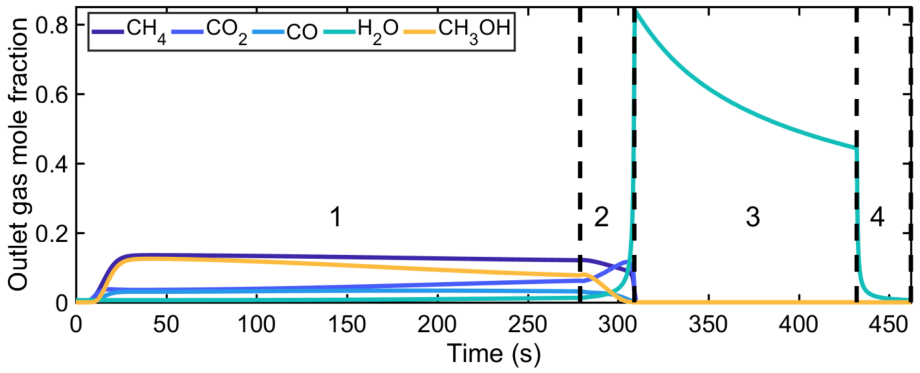

(a) Outlet gas mole fraction except the inert purge vs time

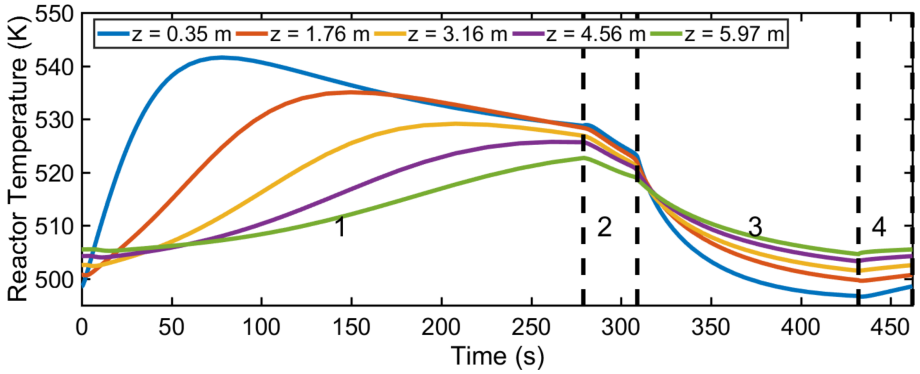

(b) Bed temperature vs time

Figure 3.7: Dynamic profiles of outlet gas mole fraction and reactor temperature at different bed length relative to the inlet boundary.

Effect of synthesis gas feed composition and flow rate: Even though the synthesis gas feed specifications in an industrial methanol reactor are constrained by the upstream SMR unit, the objective is to observe the effects of varying feed compositions and flow rates on product yield and production capacity. To achieve it, a separate set of optimization studies are performed with varying CO_2 and CO synthesis gas feed composition, and feed flow rates. In these studies, the synthesis gas feed is assumed to consist only of the reactants (CO, CO_2 and H_2) with low levels of inert nitrogen ($\approx 2.5\%$). The bounds on synthesis gas composition and flow rates can be found in Table 3.1 (Section 3.3.2). Three different cases are again considered which differ in the amount of minimum CH_3OH production capacity, i.e., $PC^{min}_{CH_3OH} = 150$ (case d), 200 (case e) and 250 (case f) tons per day.

For all the cases, the obtained results from the optimizations have been reported in Table 3.7.

Table 3.7: Optimization results with decision variables including feed composition and flow rate.

Parameter	Unit	Productivity, $PC^{min}_{\mathrm{CH_3OH}}$		
		case d (150 tons per day)	case e (200 tons per day)	case f (250 tons per day)
CH_3OH yield	%	83.44	82.72	81.33
CH_3OH production capacity	tons per day	150.37	199.98	418.73
CO conversion	%	84.95	88.00	90.54
CO_2 conversion	%	89.22	73.29	11.62
cycle configuration	-	(i) sorption-reaction (ii) reverse depres. (iii) reverse purge (iv) pressurization	(i) sorption-reaction (ii) depressurization (iii) reverse purge (iv) pressurization	(i) sorption-reaction (ii) reverse depres. (iii) depressurization (iv) pressurization
$y_{\mathrm{CO_2},fs_1}$	-	0.0295	0.0295	0.0295
y_{CO,fs_1}	-	0.1177	0.1358	0.2033
stoichiometric number (S. N.)	-	5.42	4.72	3.06
P_1	bar	76.98	76.98	76.98
P_2	bar	1	1	76.19
P_3	bar	1	1	75.32
t_1	s	973	1000	800
t_2	s	30	30	30
t_3	s	922	622	30
t_4	s	30	30	30
$\dot{n}_{fs_1}$	mol s^{-1}	0.30	0.30	0.30
T_c	K	502.01	500.41	493
α_c	-	0.220	0.206	0.040

The benefits of manipulating synthesis gas feed composition can be clearly seen in these results. The CH_3OH yields are in the range of 81.3%-83.4%, which are significantly higher compared to the earlier fixed-feed-specification cases. The typical trend is that the CH_3OH yield has a higher dependence on synthesis gas feed composition and flow rate in comparison to adsorbent-to-catalyst ratio. For all the cases, synthesis gas flow rate hits the lower bound of 0.30 mol s^{-1} in order to increase the bed residence time. The optimizer selects the composition of CO_2 in synthesis gas raw material feed as 2.95%, which is also the lower bound on the feed CO_2 composition. Such concentrations of CO_2 in the feed are sufficient to keep the catalyst in the intermediate oxidation state (thereby preserving catalyst activity) and not retard the CH_3OH synthesis reactions due to strong chemisorption of CO_2 on the catalyst [184]. Furthermore, the hydrogenation of CO is much faster than that of CO_2. This leads to a preference of the optimizer to select higher CO/CO_2 ratios while maintaining a sufficiently high concentration of excess reactant, H_2, in the feed. The

stoichiometric number (SN) has also been reported for the obtained results in Table 3.7, which is computed as follows:

$$\text{SN} = \frac{\text{H}_2 - \text{CO}}{\text{CO} + \text{CO}_2} \tag{3.22}$$

If SN ratios are higher than two, it denotes that H_2 is in excess in comparison to CO and CO_2. For SN ratios less than two, carbon species is in excess. Therefore, in our obtained results, a higher SN ratio typically results in higher reaction yields due to higher amount of excess H_2, and lower CH_3OH production capacity (due to lower amounts of carbon available for CH_3OH production). Even though an SN ratio of two has been long considered to be ideal, industries typically operate at SN values much higher than two for obtaining sufficiently high driving force for CH_3OH synthesis. Iyer et al [166] compiled four different industrial synthesis gas feed compositions and reported the range of SN ratio to vary in the range 2.9-10. Our obtained SN ratios, therefore, are within the typical range of industrial SN values. Nevertheless, it should be noted that significant separation, recompression and reheating costs are incurred due to higher recycling loads at higher SN ratios. Further investigation is therefore required for obtaining optimal values of SN ratios which would balance the tradeoffs between reaction yield and recycling ratios appropriately.

Table 3.7 shows that with increasing $PC^{min}_{\text{CH}_3\text{OH}}$ values, the presence of higher amounts of adsorbent in the reactor does not necessarily benefit the reaction yields. In higher $PC^{min}_{\text{CH}_3\text{OH}}$ cases, the obtained results show a preference of packing more catalyst in the reactor over adsorbent. This is because due to higher amounts of required CH_3OH production, the amount of H_2O byproduct produced is also higher. It leads to a faster rate of adsorbent saturation, which quickly renders the adsorbent ineffective. Furthermore, for higher percentage duration of bed operation in the first step of the cycle compared to overall cycle time $\left(\frac{t_1}{t_{cycle}}\right)$, lower values of adsorbent-to-catalyst are selected due to ineffectiveness of adsorbent. The variations in key state variables (outlet gas phase mole fraction and reactor temperature) for optimized results presented in Table 3.7 can be found in Appendix E.

The results reported in Figures 3.5 and 3.6 assume a constant catalyst effectiveness factor of one. However, as the size of methanol catalyst is large (≈ 0.5 cm), there may be appreciable

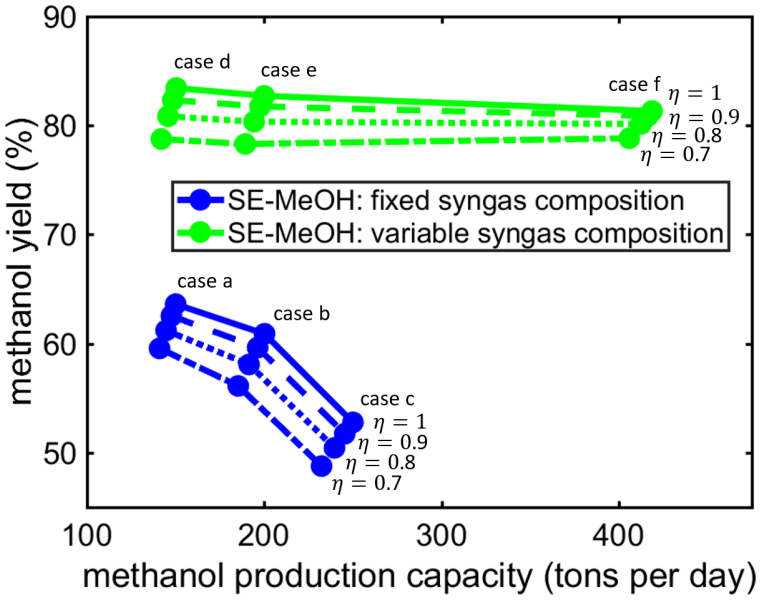

Figure 3.8: Effect of catalyst effectiveness factor on CH_3OH yield and production capacity.

mass transfer limitations which would reduce the effectiveness of CH_3OH catalyst. Furthermore, the kinetic model of Froment et al. has been developed for a steady-state reactor with negligible transport limitations. However, due to the periodic nature of SE-MeOH systems, diffusion might play a major role in methanol synthesis kinetics. To our best knowledge, there is no previous study on catalyst effectiveness for dynamic SERP-type systems. Therefore, to investigate the effects of catalyst effectiveness values, four different values of η are selected ($\eta = 0.7, 0.8, 0.9$ and 1) and it is assumed that the value of η is same for both methanol synthesis reactions considered. With the chosen values of η, the results reported in Figure 3.5 are simulated again. Figure 3.8 reports the variation in CH_3OH yield and daily production capacities with catalyst effectiveness. The results predict a moderate decrease in CH_3OH yield and production capacity in the range 6-12% when catalyst effectiveness factor is reduced from 1 to 0.7.

It should be noted that the CH_3OH yield improvements reported in Tables 3.6-3.7 are due to high levels of regeneration obtained due to extreme pressure swings (typically between 1 and 77 bar). However, such periodic pressure swings require significant compression work and, in most cases, would be uneconomical. Our model predictions showed high bed recompression costs ($>$

$50 per kg of CH_3OH). This motivates further research into more cost-effective and efficient adsorbent regeneration schemes. Possible alternatives include reactive regeneration, temperature swing and alternate recompression strategies.

3.4.3 Methanol production cost minimization

In addition to CH_3OH yield maximization, optimization studies are performed for minimizing CH_3OH production cost. This helps us in evaluating the performance of the proposed SE-MeOH processes from a techno-economic standpoint. Here, the objective is to minimize the total CH_3OH production cost. The respective objective function has been mentioned in Eq. 3.21. For computing the annualized investment cost and total cost, appropriate equipment cost and operating cost relations reported in Section 3.3.6 are used. Additionally, the synthesis gas feed composition and flow rate are fixed as in Rezaie et al. [168]. In alignment with previous optimization studies, the optimizations are performed for three different values of minimum CH_3OH production capacity ($PC^{min}_{\mathrm{CH_3OH}}$): (i) 150 (case g), (ii) 200 (case h) and (iii) 250 (case i) tons per day.

For cost optimizations, the final solution of optimal industrial reactor cases (reported in Table 3.6, Section 3.4.2) are used as initial guess. This ensures that the initial guess is feasible, and therefore, the optimization algorithm straightaway enters the optimization phase. Table 3.8 reports the results obtained for the three cost-minimization cases. The observed values of CH_3OH production cost from synthesis gas is about $96 per ton CH_3OH, and these values do not include the cost of synthesis gas production from natural gas. Typically, 60-70% of the overall natural gas to CH_3OH process cost is incurred on synthesis gas production. By assuming that 70% of overall process cost is for synthesis gas production, the obtained CH_3OH production cost is approximately $0.32 per kg CH_3OH ($0.96 per gallon), which is competitive with traditional CH_3OH production processes [198]. For all the cases, the obtained CH_3OH yield varies in the range 36.55-36.80%, which is at least 7.43% higher than predicted base case yield of 34.02%. Higher values of production capacities, in the range 270.4–272.1 tons per day, were favored to reduce the overall CH_3OH production costs. This shows the preference of the SE-MeOH process to have a balance between CH_3OH yield and production capacity in order to reduce per unit CH_3OH production cost.

Table 3.8: Optimization results obtained by minimizing CH_3OH production cost with fixed synthesis gas feed specifications.

Parameter	Unit	Productivity, $PC^{min}_{CH_3OH}$		
		case g (150 tons per day)	case h (200 tons per day)	case i (250 tons per day)
CH_3OH production cost	\$ per ton CH_3OH	96	96.2	96
CH_3OH production capacity	tons per day	272.10	270.44	272.08
CH_3OH yield	%	36.80	36.55	36.80
CO conversion	%	62.36	61.28	61.41
CO_2 conversion	%	23.90	26.04	26.34
cycle configuration	-	(i) sorption-reaction (ii) reverse depres. (iii) reverse depres. (iv) pressurization	(i) sorption-reaction (ii) reverse depres. (iii) reverse purge (iv) pressurization	(i) sorption-reaction (ii) depressurization (iii) purge (iv) pressurization
y_{CO_2,fs_1}	-	0.094	0.094	0.094
y_{CO,fs_1}	-	0.046	0.046	0.046
P_1	bar	76.98	76.98	76.98
P_2	bar	76.20	58.29	56.49
P_3	bar	72.07	58.29	56.49
t_1	s	1000	1000	1000
t_2	s	30	30	30
t_3	s	30	30	30
t_4	s	30	30	30
$\dot{n}_{fs_1}$	mol s^{-1}	0.64	0.64	0.64
T_c	K	518.71	514.27	514.2
α_c	-	0.048	0.040	0.060

By comparing optimal decision variables of yield-maximization (cases a-c) and cost-minimization (cases g-i) case studies, the major differences were observed in SE-MeOH process operating conditions. In case of yield-maximization, as shown in Table 3.6, SE-MeOH process cycles predominantly operated at 77 bar (highest pressure) during CH_3OH production and 1 bar (lowest pressure) for bed regeneration. However, pressurizing the reactor from 1 bar to 77 bar requires significant compressor work, which results in high compressor operating costs. Therefore, during cost-minimization optimizations, the optimizer selects pressure values of SE-MeOH which do not require high levels. For instance, when $PC^{min}_{CH_3OH}$ = 250 tons per day (case i), bed purging occurs at 56.49 bar. Sufficient bed regeneration occurs to enhance the CH_3OH yield from 34.02% to 36.8% (7.55% higher) compared to base case. This exhibits the need of an economical and effective bed regeneration strategy for further improving the CH_3OH yield, and thereby, the SE-MeOH process performance. The evolving trajectories of crucial state variables (outlet gas phase mole fraction

and reactor temperature) for the cases reported in Table 3.8 can be found in Appendix E.

It should be noted that the optimization results presented in Tables 3.6-3.8 have an upper bound of 543 K on gas phase boundary temperature. However, inside the sorption-enhanced reactor, the temperature may increase well beyond 543 K which would deactivate the catalyst. This situation can be addressed either by (i) postulating a constraint on temperature for each of the spatial nodes, i.e., $T(z) \leq 543$ K; or by (ii) formulating a single constraint, i.e., $\max\ T(z) \leq 543$. However, the former approach is computationally expensive due to addition of black-box constraints, and the latter approach makes the constraints non-smooth which is undesirable to obtain a good solution. Therefore, to retain the computational tractability of the problem and smoothness of the problem, such constraints were not included. Furthermore, the rise in temperature can be preempted to appropriately adjust the upper bound on temperature of the boundary (e.g., lowering it from 543 K to 513-523 K). For the results presented in Tables 3.6-3.8, the reactor temperature typically varies in the range of 495-540 K at which no catalyst deactivation would occur. Therefore, the validity of the results reported in Tables 3.6-3.8 are preserved.

Further economic analysis was performed with the number of parallel reactor tubes as a decision variable. The analysis showed that with an increase in tubes from 2962 to 4000, the CH_3OH production cost from synthesis gas can be further reduced to \$87.9 per ton. Furthermore, the daily CH_3OH production capacity can be increased to 371 tons per day. Further details regarding the optimized results can be found in Appendix F.

4. DESIGN STANDARDIZATION OF UNIT OPERATIONS*

In developing small-scale and distributed chemical processes, a major challenge is the high capital intensity which is primarily due to the unfavorable economies of scale. *Capital intensity* refers to the amount of capital investment that is required to produce a unit amount of product. The overall cost, on the other hand, consists of both the capital investment and the operating costs. One way to counter the unfavorable economies of scale is to standardize the design for mass-production and reduce the equipment manufacturing costs by exploiting the economies of numbers. The key question is: how can we effectively increase the number of standardized equipment modules for manufacturing such that small-scale processes become more economically attractive compared to large-scale counterparts?

To this end, we propose to create new opportunities for economies of numbers through standardizing the equipment designs across multiple processes in the CPI. This allows one to mass-produce equipment with the same design specifications in large numbers which can then be deployed in a variety of processes. The common design of the mass-produced equipment is obtained by investigating the similarities among different processes in terms of the design and the type of equipment used, the process performances expected and the operating conditions employed. As the commonly-designed equipment has the flexibility of being used in a multitude of processes, more of such units are manufactured leading to a significant decrease in per-unit cost. This argument also leads us to systematically incorporate the manufacturing of equipment modules at the conceptual design stage while reaping the benefits of both the economies of scale and the economies of numbers simultaneously. In terms of methodology, the above requires that we depart from the traditional *asynchronous* design of single-processes and adopt a *common-functionality* based simultaneous design of multiple processes that use similar unit operations. The combination of common functionality-based equipment design and economies of numbers allows us to address

*Reproduced in part with permission from Arora, A., Li, J., Zantye, M. S., & Hasan, M. M. F., "Design standardization of unit operations for reducing the capital intensity and cost of small-scale chemical processes." AIChE Journal, Vol 66, Number 2. Copyright 2019 American Institute of Chemical Engineers.

the roadblock associated with unfavorable scaling effects.

Here, we introduce the functionality-based concurrent design approach and discuss the development of a computational framework for the simultaneous synthesis of both standard and standalone designs of equipment and process flowsheets for multiple given chemical processes. The framework is based on a MINLP model that is used to find optimal common designs while minimizing the total equipment and operating costs for all participating processes.

4.1 Functionality-based concurrent design approach

Figure 4.1 highlights the benefits of the functionality-based common design approach and draws a comparison with the conventional small-scale design approach which only factors in economies of numbers. During equipment scale-down, the negative consequences of economies of scale increases the capital intensity. To counter the diseconomies of scale and preserve the advantages offered by economies of numbers, our approach relies on functionality-based common design of modular process equipment. Considering a process P_1 which utilizes an equipment with size V_1, a similar process P_2 is identified. Now, two equipment for both processes are designed with a common size V leading to lower costs per equipment due to a combination of favorable economies of scale and numbers.

Figure 4.2 shows the comparisons between the individually-designed and commonly-designed processes P_1 and P_2 along with the associated tradeoffs in terms of capital cost and operational efficiency. In the former, the two equipment are independently designed leading to the designs D_1 and D_2. As the equipment are designed independently, they have the highest operational efficiencies. In the latter approach, the two equipment have the same design D. This triggers the economies of numbers to play a role in reducing the per-unit equipment cost. The performance efficiencies of the commonly-designed equipment, however, depend on the operating conditions of the processes in which they are eventually used. The deviation of the actual operating conditions from the original design dictate their performance efficiencies. Therefore, the tradeoff between the savings in investment due to economies of numbers and the loss in equipment process performance becomes critical. An optimization-based framework can be used to consider these tradeoffs.

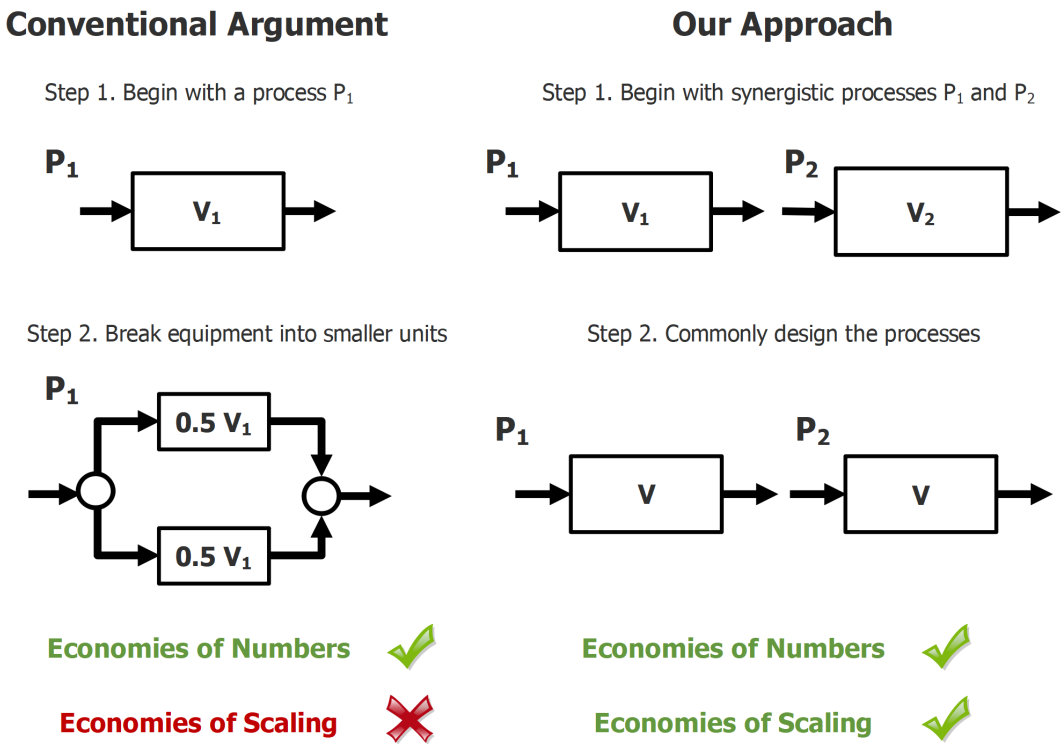

Figure 4.1: Conventional fixed-design approach and novel common functionality-based design approach for small-scale, modular chemical processes.

The applicability of the functionality-based design approach can be illustrated using the methanol and ammonia processes. Methanol and ammonia have vital importance as they are both liquid energy carriers which can be produced using unconventional or renewable sources [22, 28, 121, 160, 199–201]. The manufacturing industries for these chemicals are highly competitive and face fierce competition. Any improvements in process performance can lead to potential savings worth millions of dollars [202, 203]. The methanol and ammonia syntheses processes are synergistic in the sense that both the reactions are exothermic wherein the reaction kinetics are determined by mass-transfer limitations [204, 205]. The processes have favorable reaction conversions at moderate temperature and high pressure. As a result, methanol and ammonia industries use similar type of equipment [202, 206, 207].

Figure 4.3 shows the simplified process flowsheets considered. For methanol process, we consider synthesis gas as the raw material. For the ammonia process, we consider nitrogen and hydro-

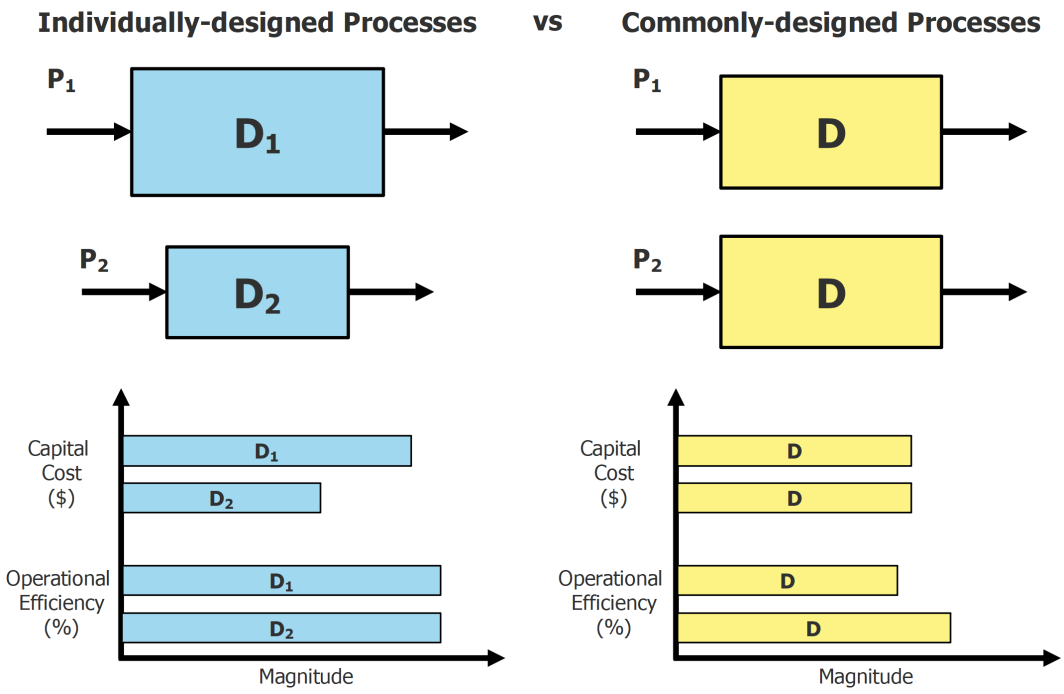

Figure 4.2: Individually-designed versus commonly-designed process synthesis. Effect of economies of numbers and operational performance efficiency of flexible equipment on design decision-making.

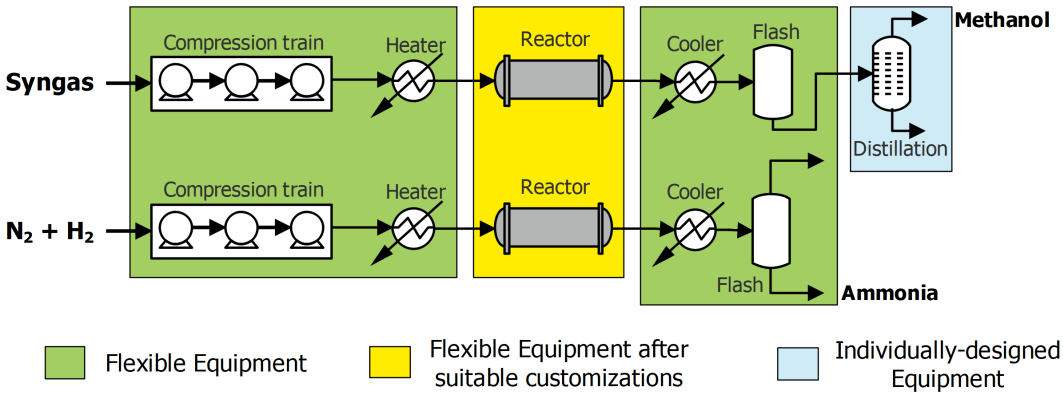

Figure 4.3: Methanol and ammonia synthesis process flowsheets with three classes of equipment.

gen as the feed. The two processes have several similarities including high pressure and moderate temperature requirements in the two packed bed reactors, low single-pass reactor conversions, and similar requirements for thermal management. These lead to similar processing trains for the two processes that consist of reactant feed compression, heating, conversion, and product separa-

tion [202]. As a result, several equipment can be interchangeably used among the two processes with minor or no customization. Here, the equipment are assumed to be classified in three major categories - (i) common equipment which can be interchangeably used among the two processes, (ii) flexible equipment which require minor customization to be used interchangeably, and (iii) independently-designed equipment not required by or designed for the two processes. Later, we return to this case study to suggest whether the equipment falling in the first two categories should have a common design for economic benefits.

4.2 Cost function with both economies of scale and economies of numbers

The term *economies of scale* refers to the reduction in the cost per unit of product produced with an increase in the size of the manufacturing facility. Often a concave power law of the following form is used to capture the effect of economies of scale on the cost:

$$AIC_{eos} = AIC_o \left(\frac{d}{D_o} \right)^{\alpha} \tag{4.1}$$

where, AIC_{eos} is the annualized investment cost of an equipment of capacity d, AIC_o is the base annualized investment cost which includes the indirect cost, capital recovery factor and balance plant cost for the base capacity of D_o. α is the scaling exponent parameter, which is typically less than one.

The term *economies of numbers* refers to the cost reduction of equipment by producing a large number of units of the same design, which is realized due to experiential learning economics [208]. The cost reductions arise due to higher labor efficiency, standardization, and efficient resource allocation. The annualized per-unit investment cost, AIC_{eon}, while considering economies of numbers can be estimated using the following expression:

$$AIC_{eon} = AIC_o \left(\frac{n}{n_o} \right)^{\beta} \frac{1}{n} \tag{4.2}$$

where, n_o and n are the base number and the actual number of equipment units produced,

respectively, and β is the exponent parameter describing the effect of economies of numbers.

The combination of the two relations shown in Eqs. 4.1 and 4.2 gives a generalized expression for capital intensity while considering both economies of scale and numbers:

$$AIC = AIC_o \left(\frac{d}{D_o}\right)^{\alpha} \left(\frac{n}{n_o}\right)^{\beta} \frac{1}{n} \tag{4.3}$$

Accordingly, we can calculate the capital intensity, CI, as follows:

$$CI = \frac{AIC_o}{PC} \left(\frac{d}{D_o}\right)^{\alpha} \left(\frac{n}{n_o}\right)^{\beta} \frac{1}{n} \tag{4.4}$$

where, PC is the annual throughput or capacity. According to the above expression, the capital intensity of a process can be reduced by (i) increasing the total number of equipment units manufactured with a common design and/or (ii) increasing the size of the equipment.

While the above expressions can be used for any number of base equipment (n_0), here we consider this to be one as it corresponds to the case when the processes will be designed individually without sharing any common equipment design, and therefore, without leveraging any economies of numbers. The proposed optimization-based formulation computes the optimal value of n, and for cases with $n \geq 1$, multiple equipment modules with common design are manufactured thereby leading to cost savings due to favorable learning rates. Even though the n_0 values are not in the public domain, this study only focuses on evaluating the benefits of incorporating concurrent process design as opposed to individual process design. To this end, n_0 = 1 is the only deterministic value which helps us in performing this study.

4.3 An MINLP framework for functionality-based design and modular manufacturing

This section outlines an MINLP model for the concurrent design of multiple processes while considering equipment capital and operating costs. Let NP be the set of processes that would be included in the concurrent design. Let $p \in P = \{1, 2, ..., NP\}$ represent a process in this set. Furthermore, let $i \in I = \{1, 2, ..., NE\}$ represent the various types of equipment that are present

in all of the processes considered. Similarly, we use $j \in J = \{1, 2, ..., NJ\}$ for the streams and $s \in S = \{1, 2, ..., NS\}$ for the state variables. NE, NJ, and NS are the number of elements in set I, J and S respectively.

We assume that the following parameters are known for the design problem:

α_i = economies of scale factor for equipment i

β_i = economies of numbers factor for equipment i

$AIC_{o,i}$ = base annualized investment cost for equipment i

$D_{o,i}$ = base design capacity for equipment i

D_i^L = lower bound on the design of equipment i

D_i^U = upper bound on the design of equipment i

$n_{o,i}$ = number of copies of equipment i manufactured for the base case

NU_p = number of copies of process p which need to be manufactured

$\hat{z}_{p,i}$ = 0-1 parameter denoting the presence of equipment i in process p

The variables include the following:

$d_{p,i}$ = design variable for equipment i in process p

D_i = design variable for equipment i manufactured in large numbers

$f_{p,i}$ = economies of numbers factor for equipment i in process p

n_i = number of equipment i produced in large numbers with common design

$OC_{p,i}$ = annualized operating cost for equipment i in process p

$x_{p,j,s}$ = state variable s for process stream j in process p

$z_{p,i}$ = binary variable indicating whether equipment i in process p is produced in numbers or not

The overall MINLP model is formulated as follows:

$$\min \sum_{p \in P} \sum_{i \in I} AIC_{o,i} \left(\frac{d_{p,i}}{D_{o,i}} \right)^{\alpha_i} f_{p,i} + \sum_{p \in P} \sum_{i \in I} OC_{p,i} \tag{4.5}$$

$$\text{s.t. } f_{p,i} = \left(\frac{n_i}{n_{o,i}} \right)^{\beta_i} \frac{z_{p,i}}{n_i} + (1 - z_{p,i}) \forall p, i \tag{4.6}$$

$$n_i = \sum_{p \in P} z_{p,i} NU_p \forall i \tag{4.7}$$

$$D_i - D_i^U(1 - z_{p,i}) \leq d_{p,i} \leq D_i + D_i^U(1 - z_{p,i}) \forall p, i \tag{4.8}$$

$$z_{p,i} \leq \hat{z}_{p,i} \forall p, i \tag{4.9}$$

$$f^{spec}(x_{p,j,s}) \leq 0 \tag{4.10}$$

$$f^{ss}(d_{p,i}, x_{p,j,s}) = 0 \tag{4.11}$$

$$OC_{p,i} = f^{oc}(d_{p,i}, x_{p,j,s}) \tag{4.12}$$

$$f^{design}(d_{p,i}, x_{p,j,s}, n_i) = 0 \tag{4.13}$$

$$f^{op}(d_{p,i}, x_{p,j,s}, z_{p,i}) \leq 0 \tag{4.14}$$

$$f_{p,i} \in \mathbb{R}^{NP \times NE}; d_{p,i} \in \mathbb{R}^{NP \times NE}; z_{p,i} \in [0,1]^{NP \times NE};$$

$$x_{p,j,s} \in \mathbb{R}^{NP \times NJ \times NS}; OC_{p,i} \in \mathbb{R}^{NP \times NE}; n_i \in \mathbb{R}^{NE}; D_i \in \mathbb{R}^{NE}$$

We denote the above formulation (Eqs. 4.5-4.14) as P0. Eq. 4.5 is the cost-minimization objective function which includes the sum of the annualized investment and operating costs for all processes considered. In this expression, the first term denotes the total annualized investment cost of all equipment i manufactured in each process p. It considers the cost of both equipment with common design manufactured in large numbers ($z_{p,i} = 1$) and individually designed equipment ($z_{p,i} = 0$). The second term accounts for the operational cost of all equipment units present in processes p, which is calculated using Eq. 4.12. Note that the objective of P0 is to minimize the overall costs rather than the capital intensity such that the trade-offs between investment and operating costs are considered. However, once the model is solved, capital intensity is determined through Eq. 4.4.

There are several constraints imposed in the overall optimization model for appropriately computing state variables, process operating costs and equipment operating efficiency. The economies of numbers factor $f_{p,i}$ is calculated using Eq. 4.6. The computed value of $f_{p,i}$ depends on whether equipment i in process p is produced in large numbers or not. Eq. 4.7 is used for obtaining the

total number of equipment i manufactured with a common design variable D_i.

If an equipment i in process p is commonly-designed, the corresponding design variables $d_{p,i}$ are constrained to be equal to common design variable D_i using Eq. 4.8. We define separate decision variables $d_{p,i}$ to allow the flexibility of the equipment design to be either commonly- or individually-designed. If an equipment i is not present in process p, the corresponding binary variable $z_{p,i}$ is constrained to be zero with the use of Eq. 4.9.

For the processes considered, the product specifications are taken into consideration through Eq. 4.10. These specifications include minimum demands and purity constraints for the products. All of the processes are assumed to operate at steady state. Therefore, the functional form of steady state equation is imposed using Eq. 4.11. The expressions for computing operating costs incurred by the involved processes are captured by Eq. 4.12. The additional equipment design constraints, if any, can be further imposed in the optimization model and are represented through Eq. 4.13. Eq. 4.14 encapsulates the constraints which calculate the operational efficiency of flexible equipment at different operating conditions.

4.4 Case studies

4.4.1 Concurrent design of methanol and ammonia processes

We apply the MINLP framework for identifying the concurrent design of methanol and ammonia processes. More details regarding the process flowsheets considered for methanol and ammonia production can be found in Appendix G.

Although equipment standardization is done to reduce the capital intensity, it may also require that equipment are operated at different efficiency levels for different applications. For example, the heat exchangers are designed for a specific heating or cooling duty at which they operate efficiently. However, keeping the design of heat exchanger fixed (i.e., heat transfer surface area), different levels of heating or cooling duties can be obtained by controlling the hot or cold utility streams. In such cases, the heat exchanger performs suboptimally as the operating duty deviates from the original design duty. For modeling purposes, we assume that if the operating duty is not

the same as original design duty, the heat exchanger performance efficiency would be lower than the maximum value and the efficiency decreases linearly with increasing deviations.

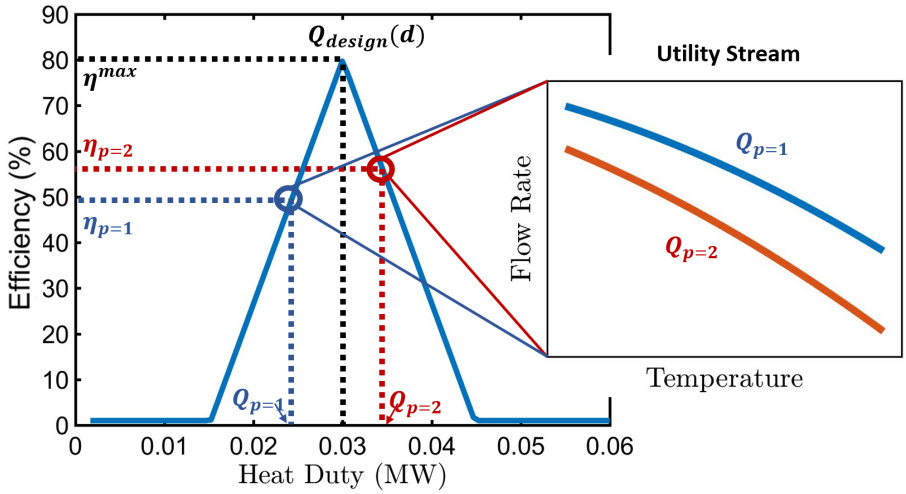

Figure 4.4: Flexible heat exchanger efficiency for different operating heat duties.

As shown in Figure 4.4, the efficiency of both heaters and coolers is modeled using a hat function wherein the maximum equipment efficiency is obtained at design duty d. If two different processes require varying levels of heating or cooling duties $Q_{p=1}$ and $Q_{p=2}$, lower heat exchanger efficiencies $\eta_{p=1}$ and $\eta_{p=2}$ are obtained. It should be noted that to provide the desired heating or cooling duties for both processes, several different combinations of utility flow rate and temperature can be utilized.

The indices, sets and set elements used in this case study are provided in Table 4.1. In Appendix G, we report the variables utilized in the case study, the values of the parameters used during the optimization studies, and the parameters used in cost correlations along with lower and upper bounds on equipment design variables. In continuation with the generalized model presented earlier, the additional constraints used for the case study have also been included in Appendix G. The constraints added consist of the production capacity specifications for methanol and ammonia product, input-output equipment relationships at steady state, equipment design constraints and

operational efficiency constraints for flexible equipment.

Table 4.1: Sets and indices used for methanol and ammonia case study.

Index	Set	Set elements	Description
i	I	$\{1, 2, ..., 6\}$	equipment: 1 - compressor, 2 - heater, 3 - reactor, 4 - cooler, 5 - flash, 6 - distillation
p	P	$\{1, 2\}$	process: 1 - methanol synthesis, 2 - ammonia synthesis
j	J	$\{1, 2, ..., 7\}$	process streams
s	S	$\{1, 2, ..., 10\}$	state variables*: 1 - F_{CO}, 2 - $F_{\mathrm{H_2}}$, 3 - $F_{\mathrm{CO_2}}$, 4 - $F_{\mathrm{CH_3OH}}$ 5 - $F_{\mathrm{H_2O}}$, 6 - $F_{\mathrm{N_2}}$, 7 - $F_{\mathrm{NH_3}}$, 8 - $F_{\mathrm{CH_4}}$, 9 - T, 10 - P
cs	CS	$\{1, 2, ..., 8\}$	subset of set S containing only chemical species

* $F_s \forall s \in \{1, 2, ..., 8\}$: feed flow rate in ton per day

It should be noted that the model has been formulated in such a way that two separate processing trains would be manufactured and operated wherein each of them will produce methanol and ammonia independently. The desired production capacity of ammonia is denoted by PC and the methanol demand is assumed to be 60% that of ammonia. Optimization studies have been performed for 5 different levels of PC (1, 5, 10, 50 and 100 ton per day) and four different experience curve parameter values ($\beta = 0.7, 0.8, 0.9$ and 1). This is done to investigate the effects of scale of the process and experiential improvements on total cost of the process. The β values chosen correspond to the learning rates in the range 0-18.78%, which are well within the values reported in the literature for the energy sector [209, 210]. For the processes considered, the equipment standardization can occur for compressors, heaters, reactors, coolers and flash columns.

The optimization results are presented in Table 4.2 for different combinations of production capacity PC and economies of numbers exponent β. It is observed that with the increase of daily production capacity of methanol and ammonia, the total cost of the process increases as well. For instance, when $\beta = 1$, the total cost increases from \$3.5MM/yr to \$10.6MM/yr when production capacity of ammonia increases from 10 to 100 ton per day. This is because with higher production capacity, the scale of the process increases thereby leading to higher capital and operating cost of operation.

More unfavorable economies of numbers is observed at higher β values, and therefore, the number of commonly-designed equipment reduces with increasing β values. When $\beta = 1$, none of the equipment selected share a common design for either of the methanol or ammonia processes. Therefore, it is taken as the base case when no improvements due to experiential learning occurs. The cases with $\beta < 1$ have cost savings due to increasing number of commonly-designed equipment.

The capital intensity of both methanol and ammonia production processes can be also found in Table 4.2. It can be observed that the capital intensity decreases with the increase of production capacity due to the favorable economies of scale. For instance, for β=0.7, when production capacity of ammonia increases from 1 to 100 ton per day, the capital intensity of methanol process decreases from \$5710.13/ton to \$210.22/ton. Similarly, the capital intensity of ammonia process decreases from \$3286.95/ton to \$59.24/ton. Besides, capital intensity of concurrent design ($\beta < 1$) is smaller than that of individual design ($\beta = 1$) due to the favorable economies of number. For instance, for production capacity PC=10, the capital intensities of methanol and ammonia processes obtained for β = 0.7, 0.8 and 0.9 are all smaller than those of the base case with β=1.

For the cases with $\beta \leq 0.9$, the reactors are commonly-designed to reduce capital intensity of methanol and ammonia processes. The shell and tube-type reactors are observed to be the major contributor to the total cost of methanol and ammonia process operation. Therefore, their production with a common design and in large numbers proves to be more economically feasible. For higher values of β, most of the equipment including reactors are individually designed.

Figure 4.5 shows the percent reduction in total cost compared to the base case. The economies of numbers are more favorable for lower values of β. Therefore, the percent cost reduction obtained is much higher for $\beta = 0.7$ and $\beta = 0.8$ when compared to $\beta = 0.9$ and $\beta = 1$. For instance, when PC = 10 ton per day, no cost savings are observed for $\beta \geq 0.9$. It indicates that the cost for over-designing equipment outweighs the benefits offered by economies of numbers. Reducing the value of β to 0.7, however, reduces the total investment and operating cost by 8%. This indicates that some of the equipment in methanol and ammonia process flowsheets have a common design, and

Table 4.2: Results for the methanol-ammonia case study.

PC (ton per day)		$\beta = 0.7$	$\beta = 0.8$	$\beta = 0.9$	$\beta = 1$
1	Total cost ($MM/yr)	2.46	2.61	2.75	2.88
	Capital Intensity ($/ton)				
	Methanol process ($p = 1$)	5710.13	6085.39	6468.61	6851.54
	Ammonia process ($p = 2$)	3286.95	3512.00	3699.20	3963.55
	Commonly-designed equipment	2 reactors, 2 compressors, 2 flash	2 reactors 2 compressors	2 reactors, 2 flash	-
5	Total cost ($MM/yr)	2.78	2.92	3.07	3.16
	Capital Intensity ($/ton)				
	Methanol process ($p = 1$)	1393.98	1462.24	1535.41	1601.86
	Ammonia process ($p = 2$)	667.05	708.01	751.70	789.70
	Commonly-designed equipment	2 reactors	2 reactors	2 reactors	-
10	Total cost ($MM/yr)	3.24	3.37	3.52	3.52
	Capital Intensity ($/ton)				
	Methanol process ($p = 1$)	818.90	851.90	888.63	929.79
	Ammonia process ($p = 2$)	346.69	368.08	389.28	398.56
	Commonly-designed equipment	2 reactors	2 reactors	2 reactors	-
50	Total cost ($MM/yr)	6.64	6.78	6.92	6.96
	Capital Intensity ($/ton)				
	Methanol process ($p = 1$)	297.95	304.20	311.63	330.51
	Ammonia process ($p = 2$)	96.18	100.46	104.85	105.55
	Commonly-designed equipment	2 reactors	2 reactors	2 reactors	-
100	Total cost ($MM/yr)	10.32	10.45	10.60	10.60
	Capital Intensity ($/ton)				
	Methanol process ($p = 1$)	210.22	213.59	217.03	227.43
	Ammonia process ($p = 2$)	59.24	61.30	63.56	63.70
	Commonly-designed equipment	2 reactors	2 reactors	2 reactors	-

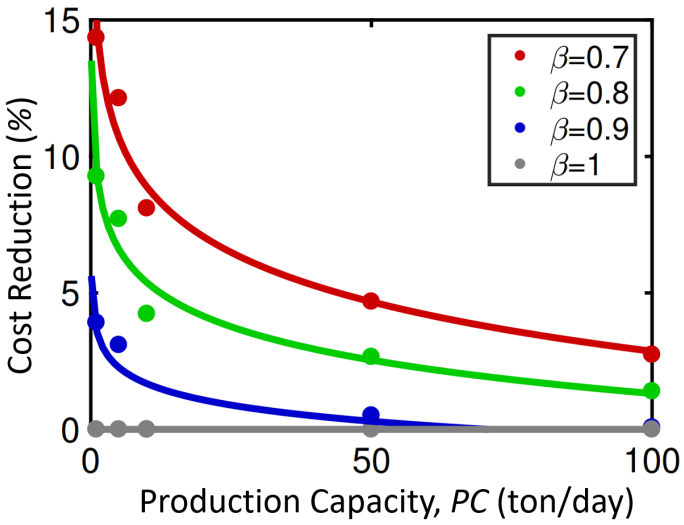

Figure 4.5: Percent reduction in total cost for methanol and ammonia processes due to equipment standardization.

the total cost incurred decreases with more favorable economies of numbers. Another observation is the predominance of economies of numbers for cost reduction at lower production capacities. For PC = 1, 5 and 10 ton per day and $\beta = 1$, the methanol-ammonia processes are expensive due to diseconomies of scale. However, significant savings in cost can be obtained when economies of numbers are leveraged and the equipment are commonly-designed. When $\beta = 0.7$, cost savings of the order of 8-15 % can be obtained for small-scale production.

Next, to obtain an optimal production capacity distribution of methanol and ammonia, we slightly modify the optimization problem. The objective of the modified optimization model is to maximize the total production capacity of methanol and ammonia while keeping the total investment and operating cost lower than a threshold value. Five different values of total cost are considered which vary from \$4MM/yr to \$12MM/yr in increments of \$2MM/yr. The economies of numbers exponent β is considered as 0.8. These studies help us in understanding given the total budget of operation and the fact that two processing trains are being designed for producing methanol and ammonia, what should be the ideal amounts of ammonia and methanol that need to be produced to maximize overall production capacity of the two processes.

Figure 4.6a shows the optimized production capacities of methanol and ammonia for five dif-

ferent total cost values. Higher reaction conversions of ammonia results in its higher production capacities when compared to methanol. It also indicates that it is more expensive to produce methanol than ammonia and this observation agrees well with reported findings in the literature [202]. For lower values of total cost, the ammonia-to-methanol production ratio is much higher. For example, when $TC = \$4$MM/yr, amount of ammonia produced is 10.6 times that of methanol. However, with an increase in the budget available for design and operation of two processes, this gap is closed and a significant portion of product portfolio consists of methanol. When $TC = \$12$MM/yr, the ratio of ammonia-to-methanol product reduces to 2.07. The typical trend observed through the results is that overall production capacity increases and ammonia-to-methanol product ratio decreases with increasing total cost values. Figure 4.6b also highlights this observation by showing the effect of total cost on percent distribution of methanol and ammonia products. For a total cost of \$4M, only 8.6% of the product formed is methanol. However, with increasing total budget available, the percent share of methanol keeps on increasing and it reaches 32.5% for a total budget cost of \$12M.

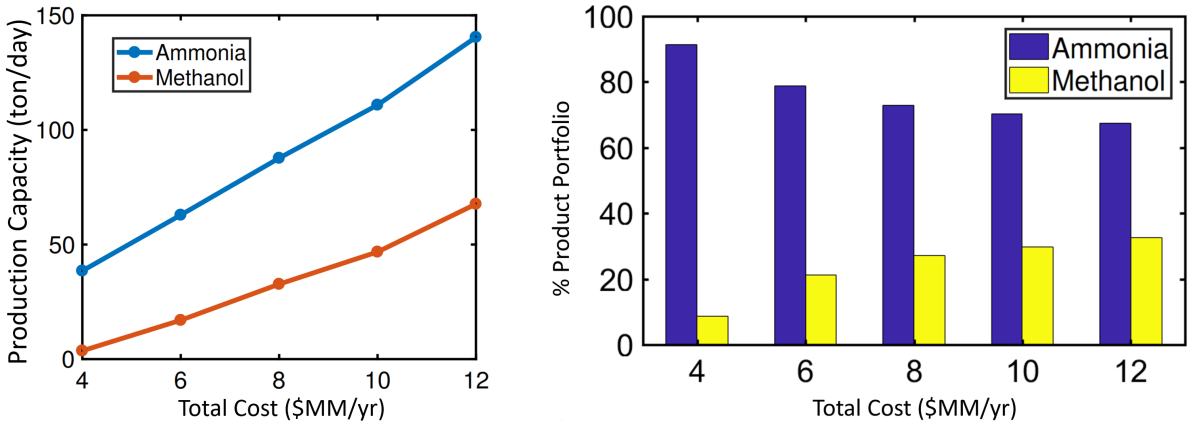

(a) Optimal distribution of ammonia and methanol products for $\beta = 0.8$.

(b) Percent contribution of methanol and ammonia products to overall production capacity.

Figure 4.6: Optimal production capacities and product portfolio of methanol and ammonia processes.

4.4.2 Concurrent design of natural gas liquids fractionation trains

Before transporting the natural gas sourced from wellheads, the heavier hydrocarbons including ethane, propane, butane and pentane are removed from natural gas. These associated hydrocarbons are called NGLs and can be very valuable if separated and sold individually. They have a variety of applications in petrochemical industry and as an energy carrier. Before separating the constituents of NGL, they are first removed from natural gas which predominantly consists of methane. Subsequently, the NGLs are processed through a sequence of distillation columns to obtain purified individual components. Depending on the natural gas source, different compositions of NGLs are obtained which provides opportunities for manufacturing standardized distillation columns and auxiliary units for their upstream processing.

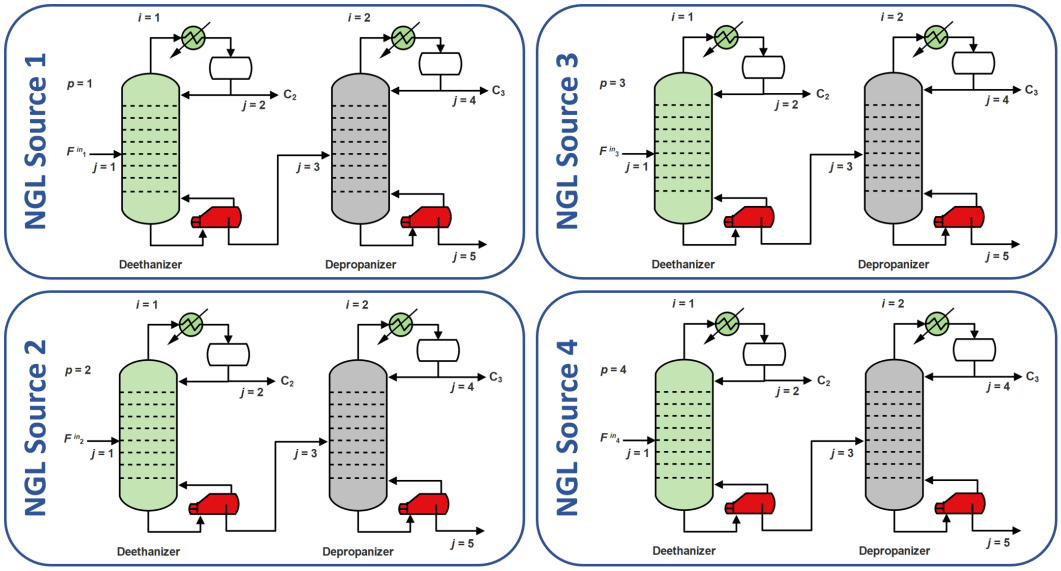

Figure 4.7: Process flowsheets with different NGL sources.

To this end, we apply the proposed functionality-based design framework to explore opportunities for cost reduction via equipment standardization and economies of numbers. In the natural gas fractionation case study considered, four parallel distillation trains are concurrently designed to recover ethane and propane from different NGL sources. Figure 4.7 depicts the processes which

utilize the following unique equipment types - deethanizer, depropanizer, condenser and reboiler. As the configuration and type of equipment used in these processes are the same, each of the unique equipment type can be commonly designed. The four processes primarily differ in the flow rate and composition of inlet feed. Overall, the optimization problem is formulated as follows: given the (i) equipment requirement for each process, (ii) desired product recovery and (iii) inlet NGL feed specifications, the objective is to minimize total annualized investment and operating cost by leveraging both economies of scale and numbers during equipment design and process operation.

We consider the major components of NGLs, i.e., ethane, propane, isobutane and n-butane. For separating ethane and propane out of the NGL feed, a sequence of deethanizer and depropanizer distillation columns are used. For design of multicomponent distillation, several shortcut methods can be used. These methods estimate the minimum and actual number of distillation stages, and the minimum reflux ratio. In this study, we use the widely-used shortcut method called Fenske-Underwood-Gilliland (FUG) [211]. Additionally, for improving the computational tractability of the optimization model, we use the Underwood solutions obtained by Glinos et al [212]. To compute the vapor-liquid equilibrium ratios, we use the DePriester chart and obtain linearized dependence of K values on temperature [213].

The information regarding the optimization model, decision variables and parameters are reported in Appendix H. For fixing the inlet feed composition for the four processes, we refer to four different natural gas compositions [214–216] (Table 4.3). In addition, the pressure of the deethanizer and depropanizer columns are fixed to 450 psia and 250 psia, respectively [216, 217]. The economies of numbers exponential parameter β is chosen as 0.7, which corresponds to a learning rate of 18.78%. It is further assumed that all of the equipment have the same β value. To study the effects of scale of the process, we select two different sets of inlet flowrates for the four parallel processes - 100, 105, 100 and 95 (case a), and 50, 52.25, 50 and 47.5 kmol per hr (case b), respectively.

Table 4.4 reports the optimized total cost and capital intensity obtained for the two cases. The optimization runs are also performed for $\beta = 1$ for which all of the equipment are individually

Table 4.3: Input parameters for NGL fractionation case study.

	Source 1	Source 2	Source 3	Source 4
Feed composition (mol %)				
Ethane	64.6	61.3	66.9	43.5
Propane	24.6	26	22.7	30.6
Isobutane	6.2	7.9	4	8.5
n-butane	4.6	4.8	6.4	17.4
	Process 1	Process 2	Process 3	Process 4
Feed flow rate (kmol per hr)				
case a	100	105	100	95
case b	50	52.5	50	47.5

designed as there are no potential advantages offered by economies of numbers. It is considered as the base case with a total cost of \$1.509MM/yr and \$0.812MM/yr, respectively. Lower β values indicate the potential cost savings due to production of standardized equipment units in large numbers. Therefore, when $\beta = 0.7$, the total overall cost reduces to \$1.429MM/yr and \$0.765MM/yr. For the two cases considered, it translates to an overall cost reduction 5.29% and 5.79% due to mass production of standardized equipment units for the four processes. Besides, the capital intensities of all processes decrease compared to the base case. For instance, for Process 1, the capital intensity decreases to \$0.108/kmol (case a) and \$0.139/kmol (case b) from \$0.1361/kmol and \$0.1712/kmol, respectively. Additionally, capital intensity increases with the decrease of scale of the process. It can be observed that for $\beta = 0.7$, capital intensity increases from \$0.104/kmol (case a) to \$0.134/kmol (case b) in Process 2.

The number of standardized equipment modules manufactured, along with the common design parameters, are also reported in Table 4.4. The optimal equipment design variables and operation efficiency can be found in Table 4.5. It is observed that three deethanizers, seven condensers and four reboilers share a common design. A plausible reason for obtaining more commonly-designed condensers as compared to reboilers is the high utility cost for reboilers. Any loss in the performance, which may arise due to suboptimal reboiler design, can significantly increase its operating cost. Additionally, a higher percentage cost savings is observed for case b where the inlet

Table 4.4: Results for NGL fractionation case study.

	unit	case a	case b
Total cost ($\beta = 0.7$)	\$MM/yr	1.429	0.765
Base cost ($\beta = 1$)	\$MM/yr	1.509	0.812
Cost savings (%)	-	5.29	5.79
Capital intensity ($\beta = 0.7$)	\$/kmol		
Process 1		0.108	0.139
Process 2		0.104	0.134
Process 3		0.104	0.134
Process 4		0.128	0.164
Capital intensity ($\beta = 1$)	\$/kmol		
Process 1		0.1361	0.1712
Process 2		0.1355	0.1708
Process 3		0.1345	0.1691
Process 4		0.1489	0.1876
Commonly-designed equipment	-	3 deethanizers,	3 deethanizers,
	-	7 condensers,	7 condensers,
	-	4 reboilers,	4 reboilers,
Deethanizer common design ($N_{i=1}^{com}$)	-	24.83	24.83
Deethanizer common design ($D_{i=1}$)	ft	1.39	0.983
Condenser common design (D^c)	MW	0.3015	0.1507
Reboiler common design (D^r)	MW	0.3015	0.1507

feed flowrates are half of that of case a. Similar to the previous methanol-ammonia case study, it indicates that common equipment design is better suited to reduce capital intensity of small-scale processes as compared to large-scale processes. With a reduction in process scale, the operating cost reduces linearly whereas the equipment capital cost does not because of diseconomies of scale.

With the use of these case studies, the usefulness of the developed framework is established where the framework serves as an aiding tool for designing equipment for inherently synergistic processes. Further reductions in manufacturing cost of equipment can be obtained if a multitude of processes with flexible equipment are included in the overall framework.

However, to leverage standardization of equipment during multiple process design, the manufacturer/vendor must have the licensing for respective chemical processing technologies. The lack of licenses for similar technologies may limit the practicality of the proposed approach. Additionally, the scale of synergistic chemical processes must be of similar magnitudes to leverage the

Table 4.5: Optimal equipment design variables and flexible equipment performance.

Decision Variable	case a		case b	
	$i = 1$	$i = 2$	$i = 1$	$i = 2$
Number of stages	24.83	25.48	24.83	24.81
	24.83	22.67	24.83	22.67
	24.83	21.89	24.83	21.89
	22.75	24.64	22.22	24.64
Column diameter (ft)	1.39	1.196	0.983	0.847
	1.39	1.273	0.983	0.9
	1.39	1.16	0.983	0.82
	1.224	1.412	0.867	0.998
Condenser design duty (MW)	0.3015	0.3015	0.1507	0.1507
	0.3015	0.3015	0.1507	0.1507
	0.3015	0.3015	0.1507	0.1507
	0.2152	0.3015	0.10	0.1507
Reboiler design duty (MW)	0.3015	0.202	0.1507	0.094
	0.3015	0.231	0.1507	0.107
	0.3015	0.187	0.1507	0.086
	0.2152	0.3015	0.10	0.1507
Condenser performance efficiency (%)	99.8	73.13	99.81	74.35
	99.66	82.21	99.68	82.9
	100	68.1	100	69.14
	100	99.88	100	99.17
Reboiler performance efficiency (%)	99.8	100	99.8	100
	99.66	100	99.67	100
	100	100	100	100
	100	99.8	100	99.77

similarities in equipment sizing during standardization.

For an equipment module, the material of construction is also a crucial component in determining whether the module can be deployed in a variety of processing technologies. In cases when the materials of construction are different, the current methodology assumes that the respective equipment will not offer any advantages due to economies of numbers as their respective manufacturing processes may be entirely different. Such constraints may limit the potential for leveraging economic benefits of equipment standardization.

5. HIGH-THROUGHPUT MATERIAL SCREENING METHODOLOGY WITH OPTIMAL PROCESS DESIGN, OPERATION AND MATERIAL SELECTION*

We develop and employ ANN-based efficient input-output models to approximate transient adsorption behavior and breakthrough times for screening large material databases. The ANN model drastically reduces the computational time while tapping on the predictive capability of a high-fidelity process model.

A key novelty of our ANN-based approach is that it not only predicts the breakthrough times, but it is also able to predict the entire dynamic breakthrough profiles and transient adsorption behavior of different gases adsorbed on different materials. This is done via introducing the concept of breakthrough time events. Each of these events are associated with a specific gas composition and the corresponding time at which that composition is encountered at the column outlet. Another advantage of our approach is that the ANN model is generic and we do not need to develop separate ANN models for separate gas molecules. Using the framework, we screen 196 pure-silica zeolites available in the IZA-SC database [218]. Specifically, we present our results on screening zeolites for CO_2/N_2 separation for carbon capture and CH_4/CO_2 separation for natural gas purification. The same protocol can be followed for other applications involving binary gas mixtures using zeolites or other porous materials (e.g., MOFs) and molecular sieves. It is worth noting that the framework is best applied as an initial screening strategy, and further investigations with detailed dynamics of a multi-step PSA cycle are warranted to capture the regeneration aspects of candidate materials.

5.1 Methodology

The overall material screening framework for adsorption processes is shown in Figure 5.1. For a given database of existing materials, we first computationally obtain the equilibrium gas adsorption isotherms for each gas species adsorbed on these materials using Grand Canonical Monte

*Reproduced in part with permission from Arora, A., Iyer, S. S., & Hasan, M. M. F., "Computational material screening using artificial neural networks for adsorption gas separation." The Journal of Physical Chemistry C, Vol 124, Number 39, Pages 21446-21460. Copyright 2020 American Chemical Society.

Carlo (GCMC)-based molecular simulation. Adsorption parameters are obtained by fitting the isotherm data. Based on these parameters, a trained ANN model is used to efficiently predict the breakthrough times at the process level. These breakthrough times are then ranked in a decreasing order to obtain a list of top candidate materials as adsorbents for a given application. Prior to using the ANN model, it is extensively trained, optimized and validated using simulated breakthrough data. The data are generated by repeatedly solving a high-fidelity NAPDE model for numerous hypothetical adsorbents. These data sampling procedure is designed by systematically varying the isotherm parameters using latin hypercube sampling. Once the development of the ANN model is complete, it is used to predict the breakthrough times for screening purposes. To capture the complex physics typical in adsorption processes within the ANN model, the NAPDE-based GRAMS model [119] is utilized.

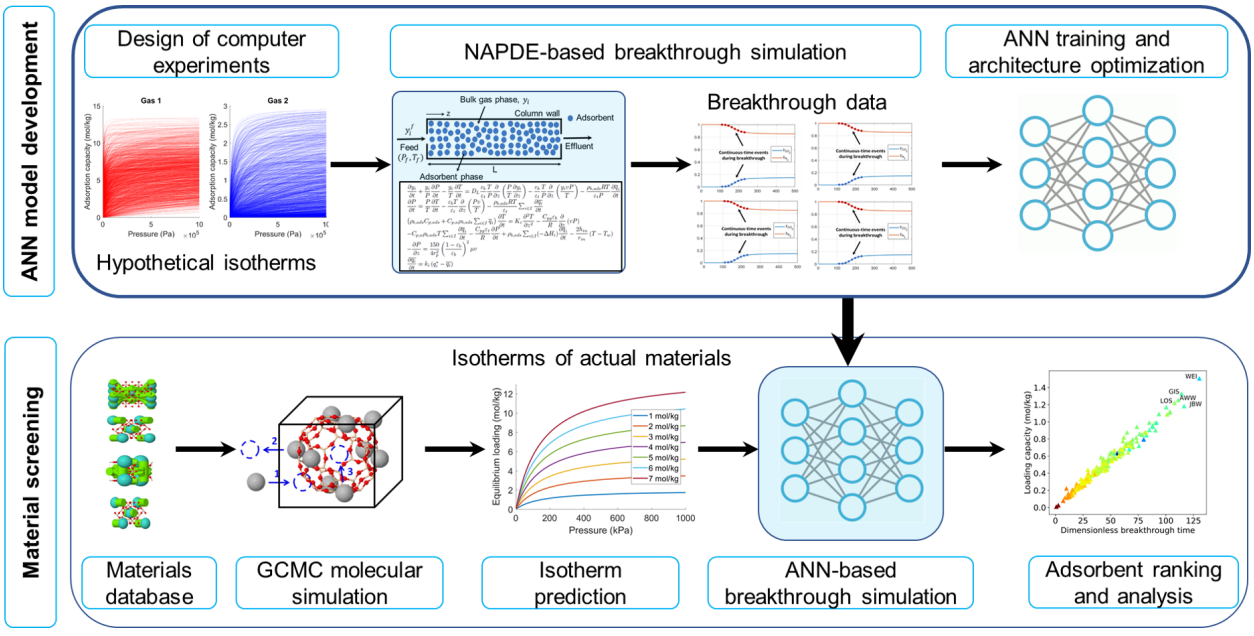

Figure 5.1: Framework for high-throughput screening of candidate adsorbents for adsorption processes.

5.1.1 Breakthrough time analysis

Breakthrough studies capture the complex dynamics of adsorption processes and can therefore be used as an effective tool for evaluating separation performance of an adsorbent. Such an analysis is helpful in analyzing the transient response of an adsorber column and adsorbent material to a step unit gas input. Based on the breakthrough response curves, a threshold time point called breakthrough time (τ_b) is defined at which the percent purity of outlet product reaches below the threshold value. At this stage, during a PSA cycle, the adsorption step is cut off and adsorbent regeneration occurs. Breakthrough time is an effective metric for providing a realistic ranking of adsorbent performance as it combines the effect of both selectivity and adsorption capacity metrics, thereby resulting in a unified metric for evaluating separation performance [103, 219].

Additionally, the dynamic loading capacity is defined as the amount of gas adsorbed before breakthrough occurs. It has been reported in the literature that breakthrough times, when combined with the dynamic adsorption capacity, can provide some of the most useful metrics for adsorbent screening [103]. As a result, there have been several studies utilizing the breakthrough time and dynamic loading capacity metrics for evaluating the separation performance of candidate adsorbents.

To approximate the breakthrough response, we discretize the outlet composition dynamics non-uniformly and introduce a set of continuous time events where breakthrough, i.e., composition transition occurs. This is motivated from continuous time scheduling formulations in process systems engineering wherein time events are postulated within the time horizon where scheduling changes occur. The timing of occurrence of these events are then predicted using ANN. Accurate prediction of the occurrence of these events can result in accurately predicting the entire breakthrough composition profiles. In the next section, we describe the first principles model used for simulating adsorption step, and the ANN models used for capturing input-output relationships.

Given a dynamic composition profile, the equivalent vertical breakthrough dimensionless time can be computed using the following expression assuming equal feed and outlet flowrates and

pressures:

$$\tau_v = \frac{v_f}{L}\int_0^{t_\infty}\left(1 - \frac{y_i}{y_{f,i}}\right)dt \tag{5.1}$$

where, y_i and $y_{f,i}$ are the outlet and feed compositions of gas species i, respectively, L is the column length, and v_f is the feed velocity. While this definition is useful for simplified breakthrough analysis and relatively accurate for sharp breakthrough profiles without tailing behavior, in an actual PSA setting, the duration of the adsorption step (τ_a) is shorter than the equivalent vertical breakthrough time ($\tau_a < \tau_v < \tau_c$), especially for nonisothermal systems with considerable heat effects. Otherwise, depending on the adsorption dynamics, the process may lose significant amount of the product if it is the more adsorbed species, thereby reducing the product recovery. Similarly, if the product is the less adsorbed species, then its purity will be less. Therefore, one should not use the complete or equivalent vertical breakthrough time as a metric, but rather consider the time when the composition starts changing for the first time. For the case of more adsorbed species, it is the time when its outlet composition starts increasing for the first time. The importance of using τ_b instead of τ_c in adsorbent screening will be further highlighted when we describe the effects of adsorption properties on breakthrough dynamics.

5.1.2 Grand canonical monte carlo simulations

In the IZA-SC database, there is a lack of available data for a set of uniform adsorption conditions in case of gases such as CO_2, CH_4 and N_2 on the pure silica zeolite frameworks. Therefore, we leverage GCMC simulations for obtaining equilibrium adsorption capacity data. Specifically, the simulations are used for computing pure component equilibrium adsorption capacity data for different adsorbate-adsorbent pairs. The molecular simulation software RASPA is used for performing the GCMC simulations [220]. For each adsorbate-adsorbent pair, the GCMC simulations are performed for a combination of 3 different temperatures (298, 323 and 373 K) and 11 different pressures (1.3, 5.3, 10.7, 21.3, 42.7, 85.3, 101.3, 266.6, 580, 3500 and 6500 kPa). This leads to a total of 33 simulations per adsorbate-adsorbent pair.

The simulations are performed in a grand canonical ensemble where a fixed volume of ad-

sorbent framework is considered which can exchange energy and molecules with the bulk gas. Bulk gas molecules are inserted into and deleted from the adsorbent framework. Furthermore, gas molecules transition and rotation moves are performed within the ensemble. Subsequently, the net energy of the configuration after performing these moves are computed and their acceptance probability is calculated. Coulombic and van der walls forces determine the interaction energies between the adsorbate and the adsorbent. When the gas molecules in bulk have the same chemical potential as that of gas molecules in adsorbent framework, equilibrium is attained. At equilibrium, the number of gas molecules in adsorbent framework is used for computing the equilibrium adsorption capacity at the pressure and temperature conditions considered. The Leonard-jones interaction parameters used for describing the van der walls interaction are obtained from Garcia-Perez force field for pure-silica zeolites [221]. For obtaining statistically significant results, 50000 equilibration and 50000 production cycles are simulated. More information regarding the GCMC simulations with respect to the interactions between adsorbent framework and bulk gas reservoir, probability distribution of different GCMC moves and the adsorption equilibrium conditions can be found in Iyer et al [115].

5.1.3 Isotherm fitting

The obtained equilibrium adsorption capacity data from GCMC simulations is fitted as a non-linear function of temperature and pressure. Based on least squares fitting, the following NLP-based optimization problem is formulated that minimizes the normalized deviation of predicted adsorption capacity of gas species i, $q^*_{p,i,n}$, from the true equilibrium adsorption capacity data, $q^*_{d,i,n}$. Here, $n \in N$ is the overall set of available data points.

$$\min_{m_{i,s}, b_{o,i,s}, \Delta U_{i,s}} \quad \left(\frac{q^*_{p,i,n} - q^*_{d,i,n}}{q^*_{d,i,n}} \right)^2 \tag{5.2}$$

$$\text{s.t.} \quad q^*_{p,i,n} = \sum_s \left(\frac{m_{i,s} b_{i,n,s} P_{i,n}}{1 + b_{i,n,s} P_{i,n}} \right) \tag{5.3}$$

$$b_{i,n,s} = b_{o,i,s} \exp\left(-\frac{\Delta U_{i,s}}{RT_n}\right) \tag{5.4}$$

$$m_{i,s}^L \leq m_{i,s} \leq m_{i,s}^U, \;\; b_{o,i,s}^L \leq b_{o,i,s} \leq b_{o,i,s}^U, \;\; \Delta U_{i,s}^L \leq \Delta U_{i,s} \leq \Delta U_{i,s}^U$$

The above optimization problem is programmed in the GAMS environment and solved using the global NLP solver BARON [222]. Solving the problem results in the fitted adsorption isotherm parameters $m_{i,s}, b_{o,i,s}$ and $\Delta U_{i,s}$ that best capture the true equilibrium adsorption data. It should be noted that this optimization problem is solved iteratively for each separate pair of adsorbate and adsorbent. As an illustration, Figure 5.2 shows fitted adsorption isotherm curves for CO_2 adsorption on 4 different zeolites.

5.1.4 Artificial neural network model

With enough neurons and training parameters, a feedforward ANN can universally approximate any smooth function with an arbitrarily high level of accuracy [223]. The major advantages of ANNs include low mathematical complexity, capability of learning complex system nonlinearities, and architecture flexibility. Due to their versatility, ANNs have been widely used in a variety of fields in chemical engineering with major applications in response surface modeling, regression and classification where they can be used either for their prediction capabilities or for developing low-complexity surrogate models for optimization [224–226].

In ANNs, the first layer is an imaginary layer with inputs to the network, and the last layer consists of the model outputs. In a fully-connected feedforward ANN, the neurons in a given layer receives inputs from all the neurons in the previous layer. Hence, the information is fed forward and there is no transmission of information backwards. One of the major challenges faced during ANN-model development is deciding the architecture (i.e., number of layers and neurons) and activation function. Therefore, different combinations of ANN architecture are tested on training and cross-validation data for preventing model overfitting and underfitting.

We select rectified linear unit (ReLU) as the activation function which results in piecewise-linear neural networks. Figure 5.3 demonstrates the mathematical operations performed at each neuron inside hidden layers. The node values of the previous neurons (I_n) are multiplied with

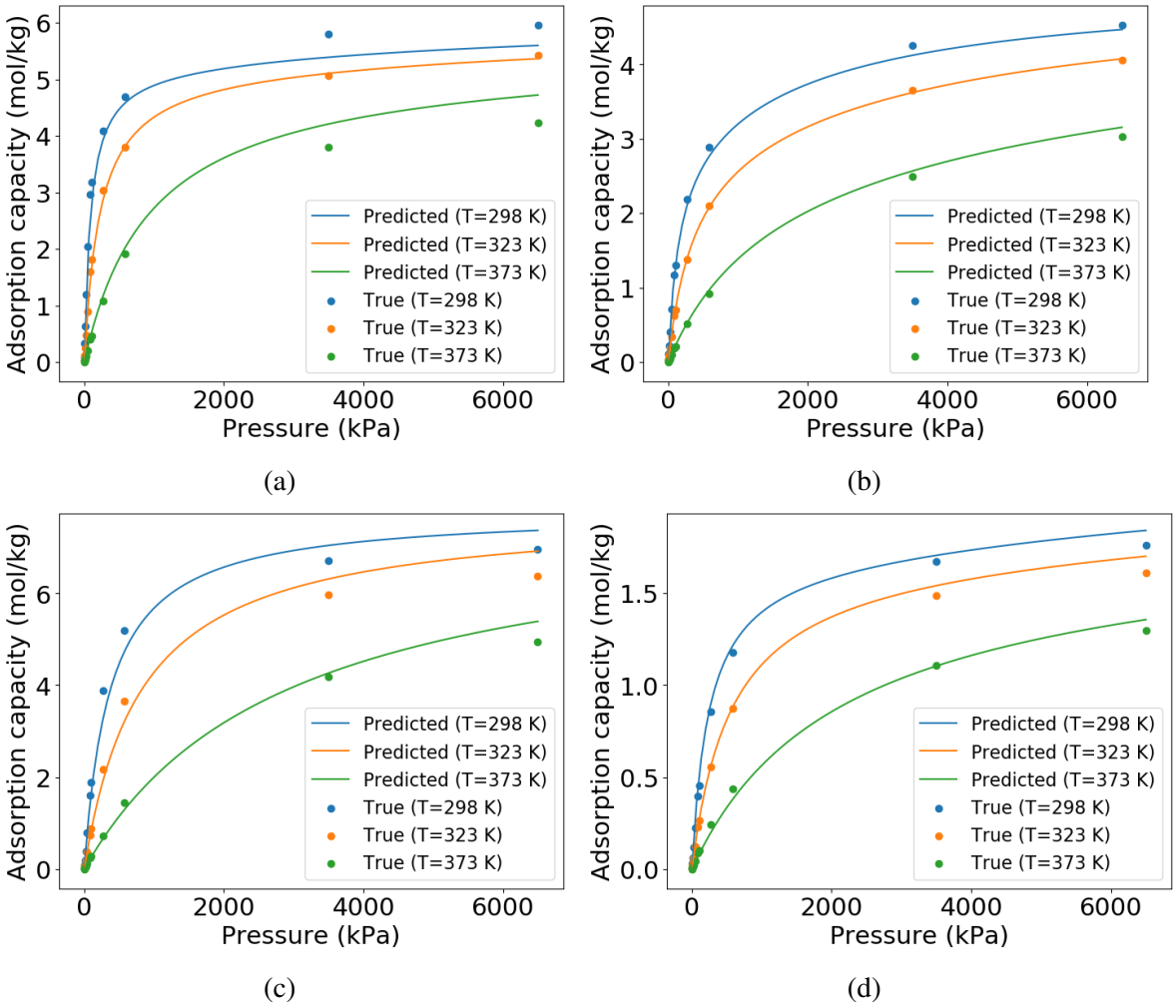

Figure 5.2: Fitted dual site adsorption isotherms for CO_2 adsorption on ABW, ACO, AEI and AEL zeolites.

weights (w_n) and the resulting sum is then added to the neuron bias (b). The overall sum of the weighted inputs and bias (x) is then passed through the ReLU activation function with overall neuron output as $\max\{0, x\}$. These computations are performed for each neuron except the ones in the output layer where only a weighted sum of inputs and bias results in the final output values without any activation function operation.

In the context of learning breakthrough dynamics, we leverage multi-layered feedforward ANNs for predicting the continuous-time events occurring at the time of adsorption breakthrough. The ANN models developed are comprehensive and are used for predicting the effects of col-

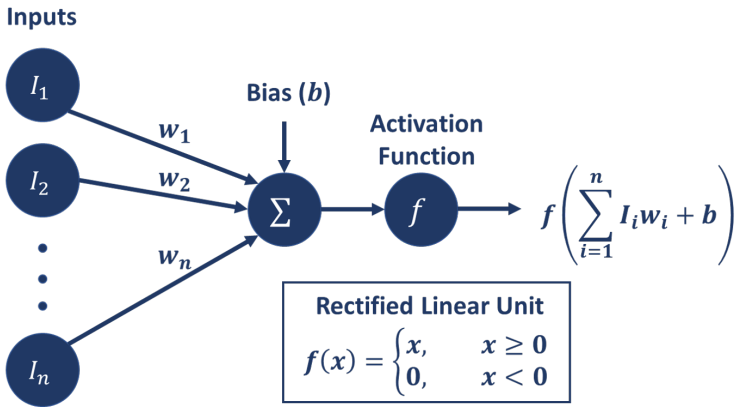

Figure 5.3: Mathematical operations occurring at each node within hidden layers of the ANN model.

umn design, process operating conditions and adsorbent properties on dimensionless breakthrough time. To this end, the inputs to the model consist of bed length, void fraction, feed composition, feed velocity, pressure, isotherm parameters, isosteric heat of adsorption and adsorbent framework density, which results in a total of 17 model inputs. While training the network, these inputs are rescaled between -1 and 1 for normalization purposes. The model outputs consist of breakthrough time events, and we postulate 8 of such events linearly spaced between 0 and y_1^f feed composition.

To generate the training data, we perform 10000 simulations by solving the first principles GRAMS model to obtain breakthrough output times. Different combinations of input variables are generated using latin hypercube sampling in MATLAB to cover the entire input space. Additionally, 5000 separate simulations are performed to generate input-output data for cross-validation. This data is not shown to the network during the training phase and is strictly used for evaluating model performance. Once the training and cross-validation data are generated, ANN models are then trained in Python environment using the keras deep learning package [227]. Keras provides a user-friendly abstraction over the tensorflow open source library, which helps us in quick testing and deployment of ANN models.

It is crucial to perform hyperparameter optimization as model performance depends significantly on hyperparameter values. Therefore, we perform model training and testing for different

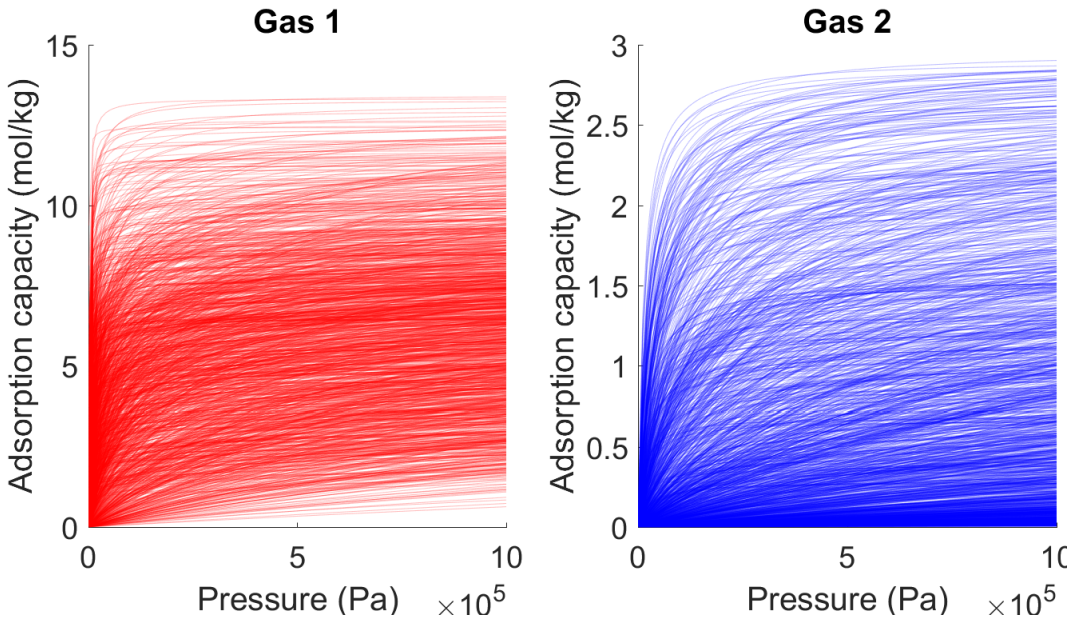

Figure 5.4: Adsorption isotherm space for the two gas species using fitting parameters' bounds.

ANN architectures. Different number of neurons are tested, and the model with the highest cross validation R^2 value is then selected for material screening. The adam optimizer [228] with default parameters is used for model training and minimizing the mean square error is the training loss function. The training is performed for 3000 epochs to give sufficient iterations for learning input-output relationships, and for preventing underfitting and overfitting.

The input bounds on which the ANN models are trained are reported in Table 5.1. The gas with higher equilibrium adsorption capacity (gas 1) is fitted using a dual-site adsorption isotherm, whereas the gas with lower equilibrium adsorption capacity (gas 2) is fitted using a single-site adsorption isotherm. As shown in the case studies later, this combination works efficiently for accurately representing the GCMC data and leads to fewer input variables for model training. Based on input bounds on adsorption isotherm fitting parameters in Table 5.1, Figure 5.4 shows the adsorption isotherm space for the two gases in the pressure range 1-10 bar at 298 K. For the input space, it is observed that breakthrough times are typically less than 6000 s. Therefore, to scale the outputs between 0-100, output times are divided by 60 for normalization. It should further be noted that for gaining higher model accuracy, the isotherm fitting parameters are later readjusted

depending on the adsorption data for each of the two case studies presented.

Table 5.1: Input bounds for training ANN models.

Input variable	Unit	Lower bound	Upper bound
Feed pressure, P_f	bar	1	10
Interstitial velocity, v_f	m s^{-1}	0.2	0.4
Bed length, L	m	0.3	0.5
Gas 1 fitting parameters			
$b_{1,1}$, $b_{1,2}$	Pa^{-1}	10^{-10}	5×10^{-10}
$m_{1,1}$, $m_{1,2}$	mol kg^{-1}	1	7
$\Delta U_{1,1}$, $\Delta U_{1,2}$	kJ mol^{-1}	-40	-15
Gas 2 fitting parameter			
$b_{2,1}$	Pa^{-1}	10^{-10}	5×10^{-10}
$m_{2,1}$	mol kg^{-1}	0.25	3
$\Delta U_{2,1}$	kJ mol^{-1}	-30	-10
Gas 1 heat of adsorption, ΔH_1	kJ mol^{-1}	-45	-10
Gas 2 heat of adsorption, ΔH_2	kJ mol^{-1}	-30	-5
Bed void fraction, ε_b	-	0.3	0.5
Gas 1 feed composition, y_1^f	-	0.15	0.25
Adsorbent bulk density, ρ_b	kg ads. m^{-3} bed	750	2000

5.2 Results and discussion

5.2.1 Effect of material properties on PSA breakthrough dynamics

Before investigating adsorbent materials for specific applications, we examine how the material properties, such as the equilibrium saturation capacity, adsorption energy, heat of adsorption and adsorbent density, affect the breakthrough times and the shape of gas composition profiles at the column outlet. This theoretical analysis is useful for understanding the process dynamics at different conditions and can be further used to predict desirable material properties for any given gas separation application. While different conditions can be analyzed, for this study, we consider passing a 20%/80% (gas 1/2) binary mixture through an adsorbent-packed PSA column at a velocity of 0.3 m s^{-1}. This hypothetical column is 0.4 m long and operates at 5.5 bar with a bed void fraction of 40%. The column is assumed to be initially saturated with the gas species having low

adsorption affinity (gas 2). To establish a nominal case, we consider a hypothetical adsorbent with the following equilibrium adsorption isotherm parameters for the two gases: $m_{1,1} = m_{1,2}$ = 4 mol kg^{-1}, $m_{2,1}$ = 1.2 mol kg^{-1}, $b_{1,1} = b_{1,2} = b_{2,1} = 10^{-10}$ Pa^{-1}, $\Delta U_{1,1} = \Delta U_{1,2} = \Delta H_1 = -27.5$ kJ mol^{-1}, $\Delta U_{2,1} = \Delta H_2 = -17.5$ kJ mol^{-1}. Also, the nominal material density (ρ_b) is 1375 kg ads. m^{-3}. We study the individual effects of these properties by varying these properties from their nominal values.

We first investigate the effect of saturation capacity of gas 1 ($m_{1,1}$ and $m_{1,2}$) between 1 and 7 mol/kg, while keeping the other parameters to their nominal values. The resultant isotherms of gas 1 are shown in Figure 5.5a. As expected, the isotherms are shifted upwards with higher equilibrium loading with increasing capacity. We observe that a material with higher adsorption capacity exhibits delayed onset of breakthrough curves, thus delaying the breakthrough initiation times τ_b as shown in Figure 5.5b. Furthermore, the outlet compositions of gas 1 increase more gradually with time following a long tail before reaching the steady state. This confirms that higher saturation capacities lead to significantly larger breakthrough completion times τ_c. The tailing behavior of the breakthrough profiles are due to heat effect-induced slow adsorption dynamics. For materials with low adsorption capacities, breakthrough times are short, and the adsorption-induced temperature front typically moves slower than the concentration front along the PSA column. Therefore, we do not see the heat effects on the compositions at the column outlet until the gases completely breakthrough. On the other hand, a significant amount of heat is released during adsorption for materials with high capacities. This increases the column temperature and reduces the dynamic loading of the gases on the adsorbent pores. Following the initial breakthrough, the amount of gas adsorbed inside the column reduces, which leads to prolonged breakthrough transition. This observation is further confirmed by performing an isothermal simulation where the heat effects are neglected (Figure 5.5c). The tailing behavior of the outlet gas compositions is not desirable in an actual PSA operation because it reduces the separation performance in terms of product recovery and/or purity. It is likely that the duration of the adsorption step of a PSA process would be constrained by the breakthrough initiation time, but not the breakthrough completion time. Therefore,

τ_b is a better indicator of adsorbent performance than τ_c, and we select to use τ_b as the measure of breakthrough time in subsequent materials screening purposes.

These observations point to an important trade-off in adsorption-based gas separation. A material with large adsorption capacity leads to smaller columns and reduced investment cost for PSA. However, the slow dynamics induced by the prolonged breakthrough transition reduces the purity and recovery of the product. One needs to be aware of this trade-off when selecting an adsorbent material that impacts the overall feasibility and economics of a PSA process.

To investigate the effects of ΔU parameters of gas 1 on the overall breakthrough dynamics, we perform a parametric study by varying them between -40 to -15 kJ mol^{-1}. As shown in Figure 5.5d, higher magnitudes of ΔU result in higher values of equilibrium loading at low pressures. This increases the adsorption selectivity of gas 1 over gas 2. The increased nonlinearity or the steep rise in adsorption loading also delays the breakthrough initiation time (τ_b), but shortens the breakthrough completion time (τ_c), as shown in Figure 5.5e. This again emphasizes the importance of selecting τ_b as a screening criterion over τ_c. The changes in the composition profiles as we change the ΔU parameters are again primarily due to heat effects. The effects are shown in Figure 5.5f, where we observe that, after an initial spike, the temperature gradually reduces leading to a slower transition of outlet compositions with time towards the steady state. The case that corresponds to the sharpest isotherm also sees the largest temperature rise due to the intense adsorption for a relatively short period of time. From a gas adsorption and storage perspective, materials with highly nonlinear isotherms are advantageous for adsorbing gases from dilute mixtures due to high equilibrium adsorption loading at low partial pressures. However, they are not optimal in terms of PSA applications that also involve gas desorption for regeneration purposes. Desorption needs to occur at significant low pressures (preferably at deep vacuum) to effectively regenerate the column, thereby increasing the overall energy consumption and cost.

Next, we study the effects of heat of adsorption on breakthrough dynamics. Specifically, we vary the heat of adsorption of gas 1 (ΔH_1) in the range of -45 to -10 kJ mol^{-1}. Figure 5.5g shows the variations in breakthrough times and outlet gas compositions for different ΔH_1 values.

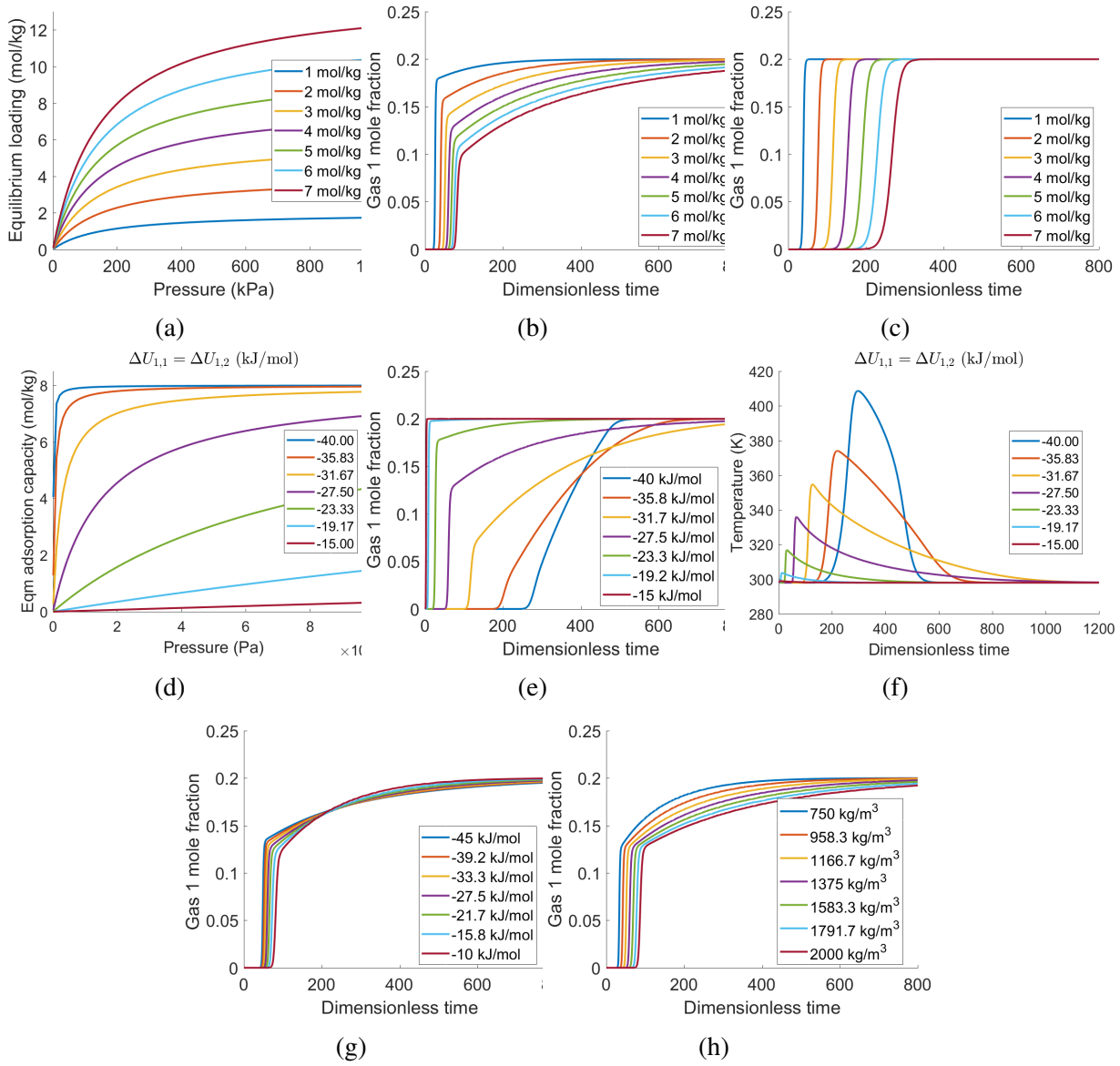

Figure 5.5: Effects of equilibrium adsorption parameters and material properties on breakthrough dynamics: (a-c) show the effects of saturation adsorption capacity on equilibrium adsorption isotherms (a), outlet gas compositions at nonisothermal condition (b), and outlet gas compositions at an isothermal condition of T_f = 298 K (c); (d-f) show the effects of ΔU of gas 1 on equilibrium adsorption isotherms (d), outlet gas compositions (e), and temperature at the column outlet (f); lastly, (g) and (h) show the effects of heat of adsorption and adsorbent framework density on outlet gas compositions, respectively.

Interestingly, the onset of breakthrough curves is achieved earlier for higher values of ΔH_1. This is because a higher heat of adsorption causes a higher rise in bed temperature, thereby reducing

the equilibrium adsorption capacity. Additionally, for higher ΔH_1, the transition to steady state is more gradual as it takes longer for the temperature front to reach the steady state (see Appendix I). Lastly, Figure 5.5h indicates the effect of varying ρ_b on outlet breakthrough profiles. Materials with higher densities also delay the breakthrough times due to higher amount of adsorbent present in the column. Similar parametric studies are performed for material properties with respect to gas 2. However, it is observed that changing the properties of less adsorbed gas species do not significantly change the breakthrough dynamics (see Appendix I).

Typically, it is desirable to have an adsorbent with high saturation capacity, high ΔU, high heat of adsorption, and high density for effective gas separation. Our above parametric study suggests that the effects of these different materials-centric metrics are well captured by breakthrough time analysis at the process scale, and an adsorbent with large τ_b value may be preferable. Therefore, breakthrough time analysis provides a scale-bridging measure towards a unified multiscale framework for materials screening with process insights.

5.2.2 Zeolite screening for post-combustion carbon capture

Adsorption-based CO_2/N_2 separation is a promising technology for post-combustion carbon capture [100, 229–233]. One can design this technology using different operational modes that include PSA, TSA, and concentration swing adsorption (CSA). Adsorbent selection is a key decision in designing an adsorption-based CO_2 capture process. Using the ANN-based screening framework, we guide this selection by predicting the breakthrough times and subsequently evaluating the CO_2 separation performance of pure-silica zeolites available in the IZA-SC database. CO_2 is more adsorbed than N_2 on zeolites. The equilibrium adsorption data obtained from GCMC simulations are fitted using a dual-site Langmuir model for CO_2 and a single-site Langmuir model for N_2. We have tested different ANN architectures and selected to use a 35-35-35 network as it has an average cross-validation R^2 score of 0.9957.

As the ANN model is trained on a range of input values, it can be used for screening numerous materials if the material properties are within the trained input space. To specifically screen zeolites for CO_2/N_2 separation, the isotherm parameters, bulk densities and isosteric heats of adsorption are

computed and scaled between -1 and 1. Next, the design and operating conditions of the adsorbent-filled column are chosen: P_f = 5.5 bar, v_f = 0.3 m s^{-1}, L = 0.4 m, ε_b = 0.4, and y_1^f = 0.15. It is worth noting that different values of adsorber conditions can be used. Using the trained ANN model, τ_b values are predicted for all zeolites. Breakthrough is assumed to be reached when the CO_2 composition in the outlet reaches within 0.05% of steady state [103]. Figure 5.6 compares the ANN-predicted breakthrough curves with the ones obtained using first principles model for several zeolites. Once τ_b values are obtained, dynamic CO_2 loading capacities are computed by integrating the amount of CO_2 fed to the adsorber column. Furthermore, the CO_2/N_2 selectivity values at equilibrium conditions are determined for all zeolites as follows:

$$S_{CO_2/N_2} = \frac{q^*_{CO_2}/q^*_{N_2}}{P_{CO_2}/P_{N_2}} \tag{5.5}$$

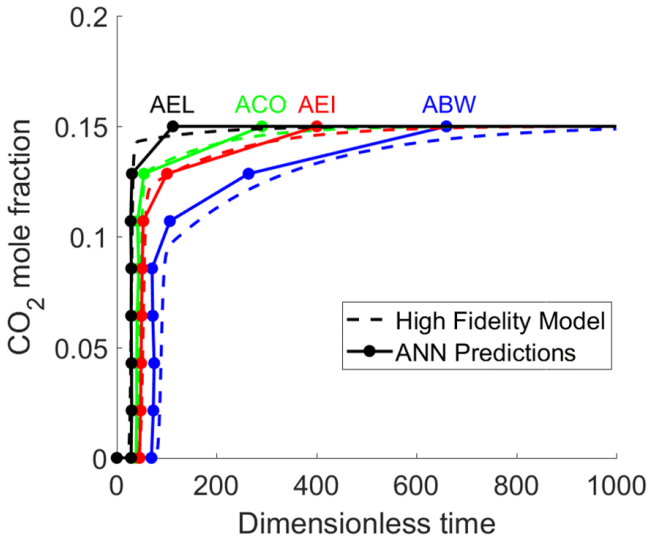

Figure 5.6: Validating predicted breakthrough curves with first principles model for ABW, ACO, AEI and AEL zeolites for CO_2/N_2 separation.

For material screening, the three metrics, i.e., τ_b, dynamic loading capacity and selectivity, are plotted in Figure 5.7. Longer τ_b values are desirable for material screening as it indicates lower

regeneration frequency in a PSA cycle. Therefore, the materials in top-right corner perform the best for CO_2/N_2 separation and are ranked as the best adsorbents. As expected, τ_b and dynamic loading capacity show a strong positive correlation as higher capacity values result in longer τ_b. Table 5.2 reports the 10 zeolites with largest τ_b. These zeolites are WEI, JBW, GIS, AWW, LOS, DFT, ATN, MAR, SIV, and PHI. WEI has the largest τ_b due to a combination of its high CO_2 saturation adsorption capacity, high adsorption selectivity, and a high magnitude of adsorption energy. Even though there are other materials, such as GIS and SIV with higher CO_2 saturation capacities, their low CO_2 adsorption energies lead to lower τ_b values. JBW has low adsorption capacity, but it has a high τ_b due to its high ΔU magnitude values for CO_2. It may seem non-intuitive that JBW has a higher τ_b than GIS or AWW despite lower CO_2 loading capacity. The answer lies in the fact that JBW has a higher bulk density compared to GIS or AWW, which leads to higher amounts of CO_2 adsorbed per unit volume of the column. This in turn results in higher τ_b values for JBW.

Table 5.2: Zeolites for CO_2/N_2 separation ranked based on breakthrough time.

Rank	Zeolite	τ_b	CO_2 loading mol/kg	Selectivity	$m_{1,1}$ mol/kg	$m_{1,2}$ mol/kg	$\Delta U_{1,1}$ kJ/mol	$\Delta U_{1,2}$ kJ/mol	ρ_b kg ads./m^3	ΔH_1 kJ/mol
1	WEI	130.37	1.51	98.92	1.00	6.63	-30.67	-30.67	1646.71	-33.15
2	JBW	116.52	1.18	51.64	1.00	1.79	-33.24	-33.24	1873.75	-35.72
3	GIS	114.19	1.33	43.74	4.94	3.99	-31.60	-17.50	1635.99	-34.04
4	AWW	111.34	1.25	32.89	4.11	1.62	-26.21	-37.58	1688.97	-39.77
5	LOS	107.92	1.22	24.16	2.83	1.74	-26.14	-36.23	1682.47	-38.44
6	DFT	103.81	1.12	28.84	1.00	3.99	-15.00	-30.67	1767.24	-33.14
7	ATN	103.47	1.11	29.09	1.84	2.51	-26.04	-32.67	1777.69	-34.83
8	MAR	101.15	1.09	21.45	1.26	2.29	-36.32	-27.71	1772.85	-38.34
9	SIV	100.37	1.17	40.38	5.00	3.01	-30.72	-18.06	1632.79	-33.15
10	PHI	93.68	1.09	36.24	1.89	5.34	-17.79	-29.40	1634.19	-31.84

Several adsorbents, including MVY, ABW and MON, have high CO_2 selectivity but do not have large τ_b values. Both high selectivity and high CO_2 loading are needed for delayed breakthrough. For instance, MVY zeolite has a CO_2/N_2 selectivity of 3166, but when used in a breakthrough column, it has a low CO_2 loading of 0.63 mol per kg of MVY. It results in a low τ_b value of 56, thus placing MVY at 57th position out of the 196 zeolites that are ranked.

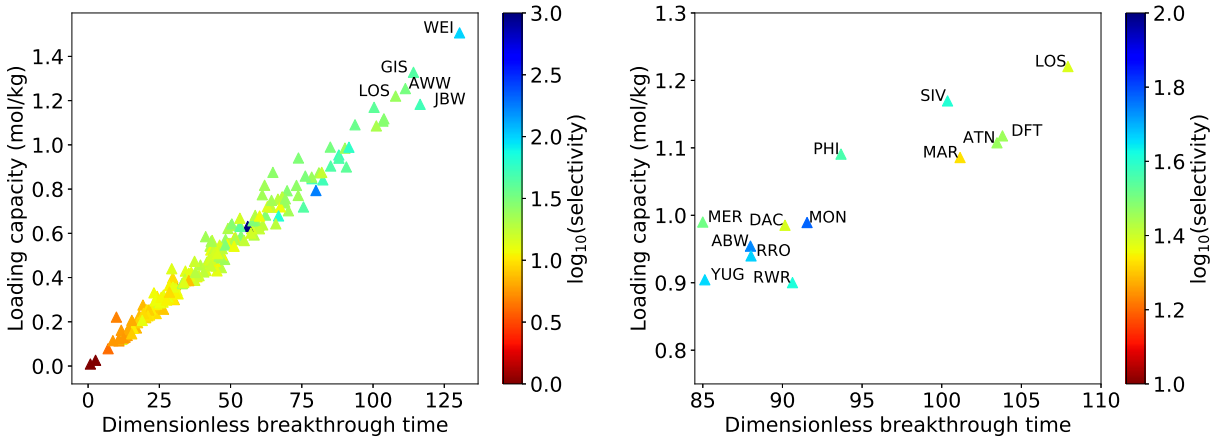

(a) (b)

Figure 5.7: Dynamic loading capacity and selectivity metrics for CO_2/N_2 separation for (a) entire τ_b range and (b) τ_b between 85-110.

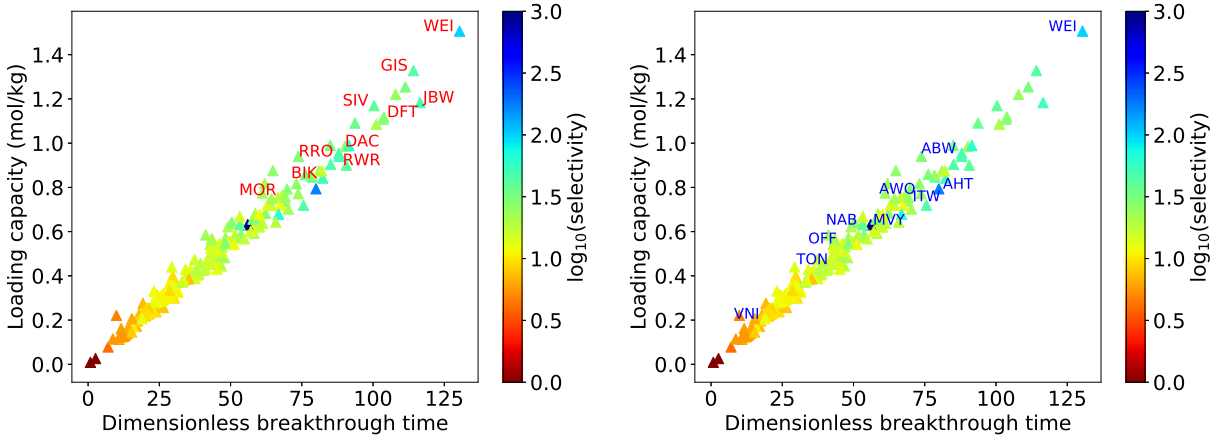

(a) (b)

Figure 5.8: Comparing top screened zeolites with results reported in literature. Top zeolites identified by (a) Lin et al. [234] with minimum parasitic energy and (b) Hasan et al. [100] with minimum total cost and energy penalty.

We have compared the list of candidate zeolites with previously reported screening results. Even though these studies used different metrics than what is used in the current study, this analysis is performed to investigate any indicative correlations among these metrics that can help in bridging

the gap between initial material screening and detailed process development. For example, Lin et al. [234] screened zeolites with minimum parasitic energy and obtained zeolites WEI, JBW, GIS, SIV, DAC, RRO, DFT, BIK, RWR, and MOR as the top 10 candidates for CO_2 capture. A majority of the zeolites suggested by their study have large τ_b values (Figure 5.8a). Similar to their study, we also obtain WEI, JBW and GIS as the top three adsorbents for post-combustion carbon capture. Furthermore, 9 out of the top 10 zeolites identified by Lin et al. [234] are among the top 18 zeolites identified by our screening method. This suggests that theoretical parasitic energies and breakthrough times of these zeolites are well-correlated in the context of CO_2 separation.

Hasan et al. [100] performed a comprehensive study with detailed techno-economic analysis and PSA cycle development to screen best zeolites for CO_2/N_2 separation. They reported the separation cost ($ per ton of CO_2 captured) and the energy penalty (kWh per ton of CO_2 captured) for 56 zeolites considering a 4-step PSA process. We use these values to check if there is any significant correlation between cost, energy penalty and τ_b. The top 10 zeolites obtained in their work are AHT, NAB, MVY, ABW, AWO, WEI, VNI, TON, OFF, and ITW. These zeolites are shown to be capable of capturing CO_2 with more than 90% purity and 90% recovery. However, not all of them attain large breakthrough times, as indicated in Figure 5.8b. In fact, we do not observe a strong correlation between breakthrough times and costs that are obtained based on feasible process operation, as shown in Figure 5.9 and Table 5.3. The correlation values of τ_b are -0.32 and -0.34 for the total cost and the energy penalty, respectively. Another interesting observation is the weak correlation value of 0.034 between τ_b and adsorption selectivity. This is also reflected in Figure 5.7 where the loading capacity values obey an almost linear relationship with τ_b without being significantly affected by selectivity variations. To that end, the methodology proposed by Hasan et al. [100] provides rigorous screening with an end-to-end material characterization and process optimization. However, due to high computational demands, such a detailed analysis is not practical for applications where the material database consists of thousands of prospective materials. To balance these tradeoffs, the ANN model provides a more efficient framework while keeping the essence of the complex dynamics of a PSA process. This analysis further motivates the need

Table 5.3: Correlation matrix for material performance metrics.

	τ_b	Dynamic loading capacity	Selectivity	Total cost	Energy penalty
τ_b	1				
Dynamic loading capacity	0.992	1			
Selectivity	0.034	0.036	1		
Total cost	-0.323	-0.317	-0.118	1	
Energy penalty	-0.341	-0.348	-0.082	0.943	1

of extending the proposed methodology to incorporate adsorbent regenerability characteristics to predict the performance of a candidate adsorbent more accurately when deployed in a realistic multi-step PSA process.

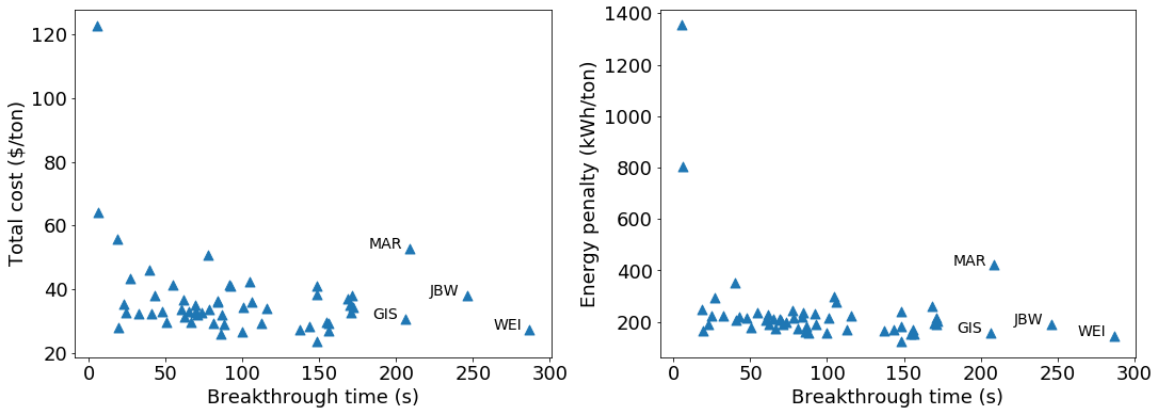

(a) (b)

Figure 5.9: Performance evaluation metrics reported by Hasan et al. [100]. (a) τ_b versus CO_2 capture cost and (b) τ_b versus energy penalty.

5.2.3 Zeolite screening for natural gas purification

The CO_2 concentration in pipeline-ready natural gas must be less than 3% [90]. However, approximately 10% of the U.S. gas reserves have higher CO_2 concentrations than 3% and require expensive purification [74]. PSA offers an attractive route for purifying natural gas contaminated with CO_2 [91, 104, 105, 231].

Here, we apply the ANN-based methodology to identify potential zeolites for CO_2/CH_4 sepa-

ration. Several ANN architectures with different number of nodes and layers are trained, and their prediction accuracies on both training and cross-validation data are obtained. Finally, we select the model with size 35-35-35 for material screening due to its highest cross-validation score of 0.9915. The network is trained for predicting CO_2 and CH_4 breakthrough times and gas loading values for given adsorption isotherm parameters and adsorbent bulk densities of the zeolites listed in the IZA-SC database. We use the same dual-site adsorption isotherm parameters for representing CO_2 adsorption on zeolites. For CH_4, a new set of least-squares fitting problems are solved for obtaining the single-site adsorption isotherm parameters to fit the GCMC simulation data. CO_2 is more adsorbed than CH_4 on zeolites, and hence, is considered to be the gas species 1. The nominal bed design and processing conditions are: P_f = 5.5 bar, v_f = 0.3 m s^{-1}, L = 0.4 m, ε_b = 0.4, and y_1^f = 0.2. The predicted τ_b, dynamic loading capacity and selectivity values are plotted in Figure 5.10 for the zeolites in the database. Based on these values, only the top ranked zeolites for CO_2/CH_4 separation are listed in Table 5.4.

Table 5.4: Top ranked zeolites for CO_2/CH_4 separation.

Rank	Zeolite	τ_b	CO_2 loading mol/kg	Selectivity	$m_{1,1}$ mol/kg	$m_{1,2}$ mol/kg	$\Delta U_{1,1}$ kJ/mol	$\Delta U_{1,2}$ kJ/mol	ρ_b kg ads./m^3	ΔH_1 kJ/mol
1	GIS	114.20	1.77	12.06	4.94	3.99	-31.60	-17.50	1635.99	-34.04
2	SIV	99.22	1.54	10.37	5.00	3.01	-30.72	-18.06	1632.79	-33.15
3	DFT	94.39	1.36	5.91	1.00	3.99	-15.00	-30.67	1767.24	-33.14
4	WEI	92.63	1.43	323.81	1.00	6.63	-30.67	-30.67	1646.71	-33.15
5	MAR	88.28	1.26	4.97	1.26	2.29	-36.32	-27.71	1772.85	-38.34
6	ATN	88.06	1.26	6.89	1.84	2.51	-26.04	-32.67	1777.69	-34.83
7	PAU	87.86	1.32	7.01	2.72	2.72	-28.69	-28.69	1688.76	-31.17
8	DAC	85.93	1.25	5.33	1.99	2.58	-33.02	-26.44	1741.29	-34.95
9	AWW	85.25	1.28	8.34	4.11	1.62	-26.21	-37.58	1688.97	-39.77
10	PHI	84.46	1.31	9.46	1.89	5.34	-17.79	-29.40	1634.19	-31.84

The top screened zeolites for CO_2/CH_4 separation are GIS, SIV, DFT, WEI, MAR, ATN, PAU, DAC, AWW, and PHI. Due to high CO_2 saturation capacity and moderately high magnitude of activation energy, GIS and SIV are selected as the most promising adsorbents. Several zeolites with high selectivity, including WEI and JBW, are ranked lower than GIS, SIV and DFT. In case of

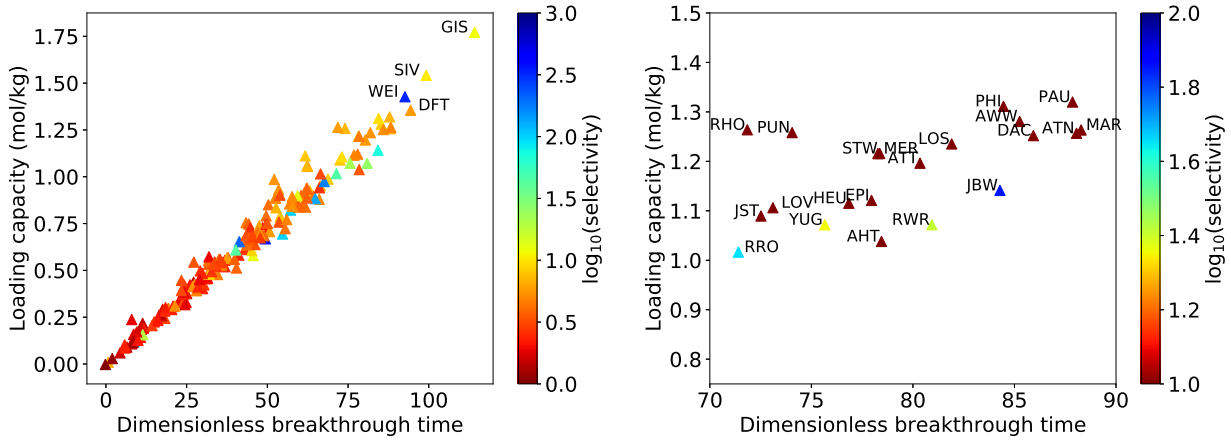

(a) (b)

Figure 5.10: τ_b, dynamic loading capacity and selectivity metrics for CO_2/CH_4 separation for (i) entire τ_b range and (ii) τ_b between 70-90.

WEI, this is due to a low adsorbent packing density. For JBW, it is due to low saturation capacity. For zeolites MAR, ATN and DAC, high adsorption energy values counter the negative effects of low saturation capacities, thus resulting in larger breakthrough times and higher rankings.

An interesting observation is that a majority of the top ranked zeolites have moderate to low selectivity ($<$10) but high τ_b values. This may contradict the norm of only selecting adsorbents with highest adsorption selectivity and not considering non-intuitive materials. However, similar to the case of CO_2/N_2 separation, it points to the important fact that pre-screening strategies need to extensively consider both material properties and process conditions for overall screening.

6. CONCLUSIONS

6.1 Summary and thesis contributions

In this thesis, we develop small-scale, modular and cost-effective chemical processes by leveraging the principles of dynamic process intensification, economies of scales and numbers, and optimal process and material design. To this end, computational methodologies and frameworks are developed that can be worked in tandem or separately to achieve proposed economic advantages during process development stage. To demonstrate the utility of the developed computational methodologies and frameworks, several case studies are considered which are relevant for midstream and downstream processing of natural gas resources. Specifically, in midstream applications, we design cost-effective processes for natural gas purification and natural gas liquids (NGL) fractionation. In downstream applications, the specific applications of interest include the production of intermediate and end-use chemicals such as methanol, ammonia and hydrogen using natural gas as the raw material feedstock.

GRAMS Framework for Dynamic Process Intensification

We develop a single framework, GRAMS, to describe and simulate different processes including fixed bed reactors, pressure/vacuum swing adsorption, sorption enhanced reaction processes (SERP), pressure and/or temperature swing reactors and/or adsorbers, and multi-material processes with layered or composite arrangement of materials. These processes are characterized by the use of packed columns filled with solid and porous adsorbents, catalysts or both. Validations are performed by comparing model predictions for pure-catalyst, pure-sorbent, and sorption enhanced reactors with existing experimental and computational data in the literature. The generalized model is the first step towards developing a high-fidelity model-based computational framework for the design, intensification and optimization of novel, multi-functional and modular technologies.

The framework has been extended for optimal cycle design and optimization of periodic SERP. The earlier studies on cyclic SERP pre-assign the process cycle configuration by utilizing the sys-

tem knowledge. The proposed method does not require the system knowledge for deriving an optimal sequence of process steps and instead relies on optimizing a rigorous model postulated for periodic SERP systems. Several decision variables which are optimized include reactant feed composition, cycle operating pressures, steps duration, bed residence time, sorbent-to-catalyst ratio, and operating temperature. Besides SERP, the optimization framework can be utilized for designing and optimizing the operation of fixed bed reactors, pressure/vacuum/temperature swing adsorption and multi-material intensified column operation.

To optimally solve the complex NAPDE-based SERP optimization problem, a two-phase grey-box algorithm consisting of feasibility and optimization phases is applied. The applicability of the optimization framework is demonstrated by synthesizing optimal cycle configuration and optimal process operation conditions for two different case studies: (i) sorption enhanced steam methane reforming (SE-SMR) and (ii) sorption enhanced water gas shift reaction (SE-WGSR). In the case of SE-SMR, hydrogen productivities of 0.534 and 0.204 (mmol H2/ kg. solid/ s) are obtained for 95% and 98% pure H_2, respectively. The obtained cost of hydrogen production is in the range \$2.13-3.12 per kg of hydrogen depending on the desired hydrogen purity, which varies between 90–95%. For 95% pure hydrogen product, the observed productivity values are 35% higher, and the hydrogen production costs are 10.86% lower in comparison to the currently-existing values in the literature. In this work, the SERP cycle design and optimization framework is primarily used for hydrogen production. The framework can also be used for optimal process synthesis and intensification of other multi-functional, multi-step, periodic systems with combined reaction and sorption phenomena.

Common Functionality-based Process Design Methodology

We have proposed a concurrent process design strategy to reduce the capital intensity and the overall cost of multiple small-scale and modular chemical processes in tandem through a combination of economies of numbers and equipment standardization. A mixed integer nonlinear programming (MINLP)-based computational framework has been developed for exploring the synergies among different chemical processes and for identifying the commonly designed equipment. Due

to experiential learning effects, the manufacturing cost of standardized equipment has lower capital costs in comparison to individually designed customized equipment. The functionality-based concurrent design framework has been demonstrated through two case studies on methanol-ammonia production and NGL fractionation. Both the individually designed and commonly designed equipment have been optimally identified and optimized for two cases. For the methanol–ammonia case study, it is observed that the percent reduction in total cost significantly depends on the production capacity and economies of numbers exponent parameter β. For a learning rate of 18%, cost savings in the range 8–15% is realized through equipment standardization. The methanol and ammonia reactors dominate the overall costs, and therefore, they are commonly designed for reducing capital intensity. In case of NGL fractionation, cost savings in the range 5.3–5.8% is observed through standardization of deethanizers, condensers, and reboilers.

The traditional design practices consider designing one process at a time. In doing so, they are not able to benefit from the economies of equipment numbers. Through proposing a cost function that incorporates both economies of scale and economies of numbers, we have argued that it would be economically favorable if we consider the modular equipment manufacturing in a holistic manner concurrently for a multitude of chemical processes. This way, we can justify the modular design approaches which currently suffer from poor economies of scale.

High-throughput Material Screening Framework

In this thesis, we also develop a multi-scale computational framework for screening the separation performance of a multitude of adsorbents for binary gas separation. The framework developed is comprehensive and can be utilized to rank candidate materials for different process designs (i.e., bed length and void fraction) and operating conditions (i.e, operating pressure, feed velocity and feed composition). A unified metric, called breakthrough initiation time, is leveraged for evaluating material performance as it combines the trade-offs between adsorption capacity and selectivity. For highly spread breakthrough profiles resulting from slow dynamics and considerable heat effects, we selected the breakthrough initiation time, instead of the breakthrough completion time, as the criterion for material selection. The developed framework integrates high-fidelity process mod-

eling and artificial neural network (ANN)-based surrogate models for high-throughput screening of candidate materials. We observed that the effects of different materials-centric metrics are captured well by the column breakthrough times at the process scale, thus providing a scale-bridging measure toward a multiscale framework for materials screening with process insights.

6.2 Future work directions

Renewable-integrated intensified technologies for sustainable chemical processes

Process intensification offers several avenues to dramatically improve the performance of chemical processes in terms of efficiency, productivity and carbon emissions. In order to further curb carbon emissions, renewable sources of energy such as solar and wind energy can be incorporated with intensified technologies to result in more green and sustainable processes. Especially at small scales, electrification of process equipment and their integration with renewables could pave way for sustainable distributed chemical manufacturing. However, several challenges need to be addressed before such technologies could be deployed at commercial scale. First and foremost, both the dynamics of intensified chemical processes and the intermittency of renewable availability need to be appropriately considered. To handle the renewable intermittency challenge, batteries also need to be included in the overall analysis to investigate if it leads to more economic and sustainable processes.

We highlight this concept with the help of an envisioned renewable-integrated distributed and intensified production process for manufacturing blue hydrogen from unconventional natural gas (Figure 6.1). Here, the raw material feedstock consists of a mixture of natural gas and steam which reacts in the SE-SMR reactor to produce hydrogen product. As a byproduct of the SMR reactions, carbon dioxide is also formed that is compressed to a high pressure for sequestration purposes. The hydrogen product could then be used in a variety of applications such as vehicle fueling. The SE-SMR reactor is electrified and the heating requirements are met through the electricity produced from renewables. In addition, renewable energy is utilized for steam generation (via electric boiler), compression and heating purposes. Due to intermittent nature of renewable availability,

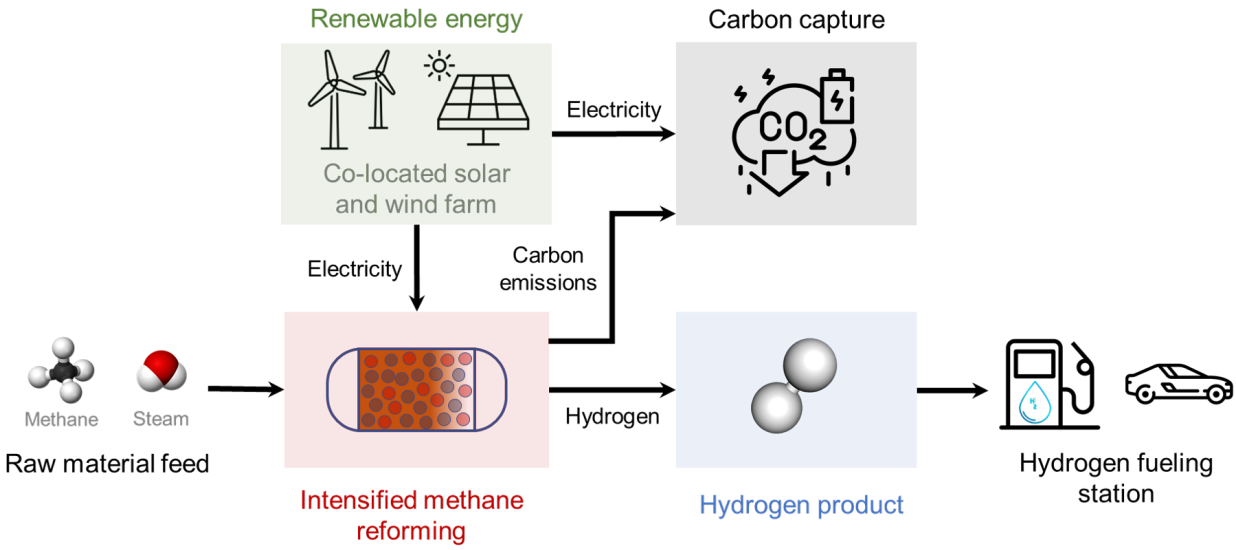

Figure 6.1: Envisioned renewable-integrated distributed and intensified production process for manufacturing blue hydrogen.

either a battery could be installed so that the process could also be operated during time of low renewable availability (e.g., night) or where the process is not connected to the grid. Otherwise, a mix of energy from renewables and grid can satisfy the process energy requirements. PI-enabled SE-SMR reactor is especially suited for such a renewable-integrated hydrogen production process due to its low energy requirements that can be adequately met by incorporating renewables. However, such a highly-integrated process flowsheet with dynamic variabilities in renewable availability and SE-SMR reactor outlet, along with different time scales of these variabilities, make the problem challenging to solve. Research efforts are therefore needed to develop accurate and computationally efficient models for such complex systems.

Leveraging economies of numbers and economies of scaling for multi-product chemical manufacturing: application to methanol and ammonia co-production

Methanol and ammonia have vital importance as they are both liquid energy carriers and are two promising candidate chemicals for monetizing unconventional natural gas. The manufacturing industries for these chemicals are highly competitive and face fierce competition. Any improve-

ments in process performance can lead to potential savings worth millions of dollars.

The markets for methanol and ammonia have high volatility due to large fluctuations in product price and consumer demand. For instance, the price of methanol is highly correlated with that of oil prices as both of them are energy sources. As a result, any price variability in oil prices affects methanol prices as well. If the price of natural gas is low, as if often the case with abundant supply, it presents a significant arbitrage opportunity as low-priced natural gas can be converted to methanol and sold at high prices (Fig. 6.2). On the other hand, ammonia prices are correlated with fertilizer prices, and therefore, any demand variability in fertilizers affect ammonia prices. At small scales, it is much more profitable to manufacture ammonia, as compared to other chemicals such as hydrogen, due to low transportation costs and high localized demands [235].

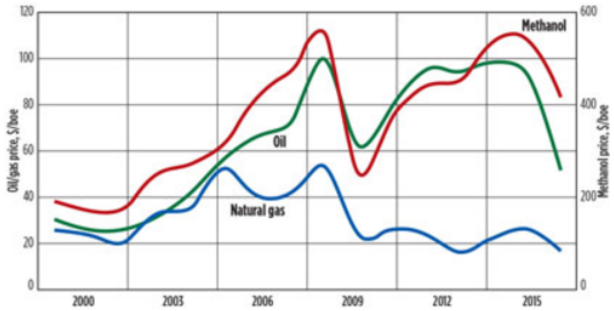

Figure 6.2: Arbitrage opportunities available due to high methanol prices and low natural gas feedstock prices (Source: ADI Analytics, LLC).

Due to high profitability of manufacturing ammonia and methanol from natural gas, and a large variation in their market prices, there is a high interest in developing multi-product processing units that can manufacture both the chemicals in response to market needs [236–240]. For instance, in Woodward, Western Oklahoma, a single-functional ammonia plant had been retrofitted with distillation and reaction sections for adding methanol production functionality. Additionally, EPA has also published a report on converting existing methanol plants to ammonia plants [206]. Such multi-product processing trains improve overall operational profitability by leveraging changes in raw material and product prices, and supply shocks.

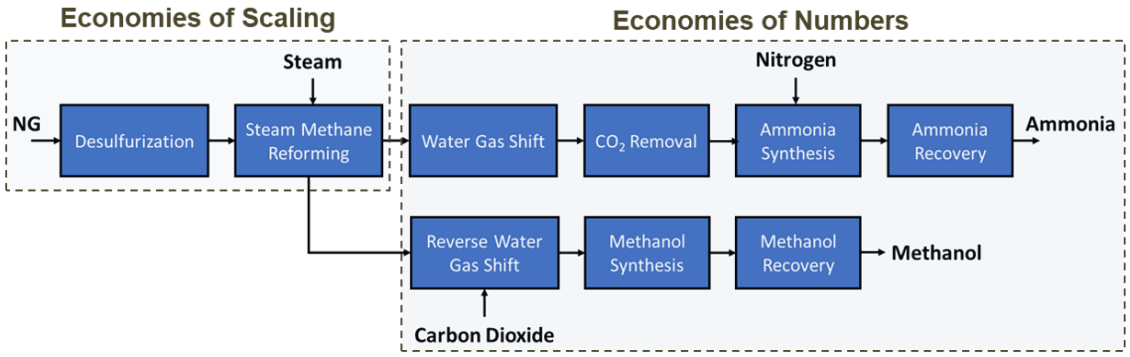

Figure 6.3: Conceptual methanol and ammonia co-production master flowsheet.

However, imparting processing flexibility comes at a cost as additional equipment costs need to be incurred. The existing work on methanol and ammonia co-production only considers the economic opportunities offered by equipment design standardization and economies of numbers. To reduce the cost of multi-product processing train, the combination of both economies of scaling and economies of numbers can be leveraged. To this end, the master flowsheet presented in Figure 6.3 could be utilized. The flowsheet takes advantage of economies of scaling in syngas generation stage and economies of numbers for downstream processing methanol and ammonia trains.

Specifically, there are common desulfurization and SMR stages where large equipment sizing can be made less expensive through economies of scaling. For ammonia production, the SMR outlet stream is sent to the WGS reactor for further conversion of CO to H_2. The CO_2 produced is removed in the CO_2 removal stage, and N_2 is then added to purified H_2 for ammonia production. In case of methanol production, the SMR outlet is sent through reverse water gas shift reactor (RWGSR) and make-up CO_2 is added for attaining an optimal stoichiometric number of resulting syngas for methanol production. Next, the syngas is passed through the methanol reactor where CO, CO_2 and H_2O react, and the methanol product formed is separated from unconverted syngas mixture in downstream purification stages.

The specific research questions that could be investigated include: (i) when is the co-production of methanol and ammonia more profitable than individual production of methanol and ammonia, (ii) how do the variations in methanol and ammonia prices affect the distribution of common syngas

generated, (iii) how much cost-savings are obtained by combining the advantages of economies of scaling and economies of numbers, and (iv) whether the co-production scheme offers any distinct advantages at small-scales where there is more volatility in both feedstock availability and market demand as compared to large-scale production.

Periodic cycle synchronization for multiple dynamic process intensification systems: application to direct natural gas to methanol production

In this thesis, we have developed separate intensified processes for syngas to methanol and natural gas to hydrogen production. However, for deployment of intensified, small-scale technologies for converting unconventional natural gas feedstocks to methanol, a single intensified process would be more economical, modular and easier to deploy. The intensified process needs to combine several phenomena within few unit operations to bring down the size and number of equipment required in the processing train. Therefore, future research efforts could focus on combining the upstream SMR and RWGSR units with the downstream methanol reactor. A conceptual process flowsheet to achieve direct natural gas to methanol process is shown in Figure 6.4. In such a flowsheet, the incoming natural gas is converted to H_2 with little amounts of CO and CO_2 in the SMR reactor. The SMR product outlet is fed to the RWGSR unit for converting some of the hydrogen to CO and CO_2. Consequently, an optimum syngas composition is obtained in the RWGSR outlet, which is further used for methanol production.

In addition, a combined process with intensified SMR and RWGSR can be evaluated for syngas production. In this combined process, the reactor bed would consist of sections of a mixture of Ni-Al catalyst and K-promoted HTC sorbent for enabling SE-SMR, and $Cu/ZnO/Al_2O_3$ catalyst for facilitating RWGSR. SE-SMR is selected, instead of conventional SMR, as it has similar operating temperature range as of RWGSR. The advantages of this conceptual process include direct natural-gas-to-syngas conversion in a single, intensified reactor without the use of capital intensive SMR and RWGR processes separately, and simultaneous SE-SMR sorbent regeneration and syngas production by converting adsorbed CO_2 into syngas. The use of this process, along with the intensified methanol process, can therefore be evaluated for direct natural gas to methanol

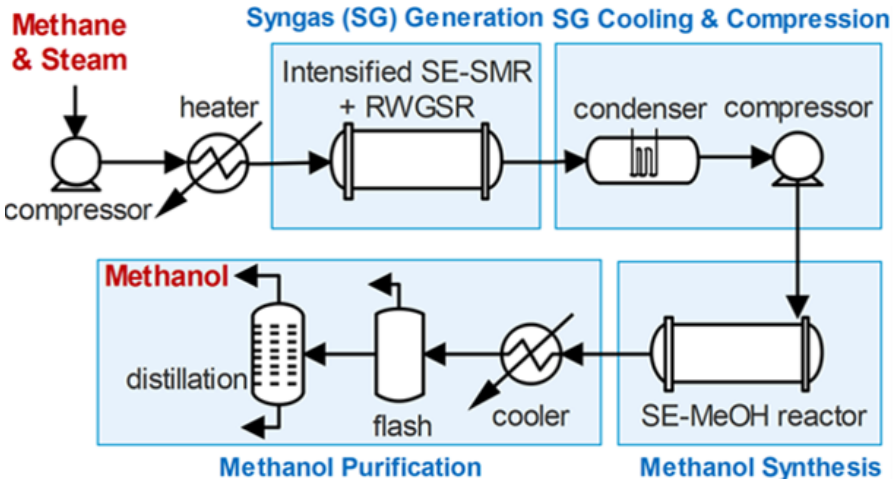

Figure 6.4: Conceptual process for direct production of methanol from natural gas using intensified SMR, RWGSR and MeOH processes.

production.

The combination of the two periodic intensified columns raise the major challenge of synchronizing the respective cycle configurations. Each of the cycles have their own optimal step duration and configurations. However, combining the two beds increases both the computational and operational complexity as the reaction-adsorption steps and the regenerations steps for both the beds have to be synchronized. To address this, efficient computational strategies are therefore required to address large-scale flowsheet design with multiple dynamic unit operations. A potential solution could be development of several surrogate models for different unit operations with each of the model having its own temporal resolution such that multiple surrogate models can be coupled together.

REFERENCES

[1] A. Mitsos, N. Asprion, C. A. Floudas, M. Bortz, M. Baldea, D. Bonvin, A. Caspari, and P. Schäfer, "Challenges in process optimization for new feedstocks and energy sources," *Computers & Chemical Engineering*, vol. 113, pp. 209–221, 2018.

[2] S. H. Tan and P. I. Barton, "Optimal dynamic allocation of mobile plants to monetize associated or stranded natural gas, part i: Bakken shale play case study," *Energy*, vol. 93, pp. 1581–1594, 2015.

[3] A. I. Stankiewicz, J. A. Moulijn, *et al.*, "Process intensification: transforming chemical engineering," *Chemical Engineering Progress*, vol. 96, no. 1, pp. 22–34, 2000.

[4] T. Van Gerven and A. Stankiewicz, "Structure, energy, synergy, time - the fundamentals of process intensification," *Industrial & Engineering Chemistry Research*, vol. 48, no. 5, pp. 2465–2474, 2009.

[5] L. Yan, T. F. Edgar, and M. Baldea, "Dynamic process intensification of binary distillation via periodic operation," *Industrial & Engineering Chemistry Research*, vol. 58, no. 15, pp. 5830–5837, 2018.

[6] M. Baldea and T. F. Edgar, "Dynamic process intensification," *Current opinion in chemical engineering*, vol. 22, pp. 48–53, 2018.

[7] A. Brun-Tsekhovoi, A. Zadorin, Y. R. Katsobashvili, and S. Kourdyumov, "The process of catalytic steam-reforming of hydrocarbons in the presence of carbon dioxide acceptor," in *Hydrogen Energy Progress VII, Proceedings of the 7th World Hydrogen Energy Conference*, vol. 2, pp. 885–900, 1988.

[8] A. Stankiewicz, "Reactive separations for process intensification: an industrial perspective," *Chemical Engineering and Processing: Process Intensification*, vol. 42, no. 3, pp. 137–144, 2003.

[9] C. Han and D. P. Harrison, "Simultaneous shift reaction and carbon dioxide separation for the direct production of hydrogen," *Chemical Engineering Science*, vol. 49, no. 24, pp. 5875–5883, 1994.

[10] A. Lopez Ortiz and D. P. Harrison, "Hydrogen production using sorption-enhanced reaction," *Industrial & Engineering Chemistry Research*, vol. 40, no. 23, pp. 5102–5109, 2001.

[11] E. Ochoa-Fernández, H. K. Rusten, H. A. Jakobsen, M. Rønning, A. Holmen, and D. Chen, "Sorption enhanced hydrogen production by steam methane reforming using Li_2ZrO_3 as sorbent: sorption kinetics and reactor simulation," *Catalysis Today*, vol. 106, no. 1-4, pp. 41–46, 2005.

[12] R. J. Allam, R. Chiang, J. R. Hufton, P. Middleton, E. L. Weist, and V. White, "Development of the sorption enhanced water gas shift process," *Carbon Dioxide Capture for Storage in Deep Geologic Formations*, vol. 1, pp. 227–256, 2005.

[13] H. M. Jang, K. B. Lee, H. S. Caram, and S. Sircar, "High-purity hydrogen production through sorption enhanced water gas shift reaction using K_2CO_3-promoted hydrotalcite," *Chemical Engineering Science*, vol. 73, pp. 431–438, 2012.

[14] L. He, J. M. S. Parra, E. A. Blekkan, and D. Chen, "Towards efficient hydrogen production from glycerol by sorption enhanced steam reforming," *Energy & Environmental Science*, vol. 3, no. 8, pp. 1046–1056, 2010.

[15] Z. Lu and A. Rodrigues, "Pressure swing adsorption reactors: Simulation of three-step one-bed process," *AIChE Journal*, vol. 40, no. 7, pp. 1118–1137, 1994.

[16] A. K. Stark, "Manufactured chemistry: Rethinking unit operation design in the age of additive manufacturing," *AIChE Journal*, vol. 64, no. 4, 2018.

[17] M. Yang and F. You, "Modular methanol manufacturing from shale gas: Techno-economic and environmental analyses of conventional large-scale production versus small-scale distributed, modular processing," *AIChE Journal*, vol. 64, no. 2, pp. 495–510, 2018.

[18] R. C. Allen, D. Allaire, and M. M. El-Halwagi, "Capacity planning for modular and transportable infrastructure for shale gas production and processing," *Industrial & Engineering Chemistry Research*, vol. 58, no. 15, pp. 5887–5897, 2018.

[19] A. Sánchez and M. Martín, "Scale up and scale down issues of renewable ammonia plants: Towards modular design," *Sustainable Production and Consumption*, vol. 16, pp. 176–192, 2018.

[20] L. C. Brée, K. Perrey, A. Bulan, and A. Mitsos, "Demand side management and operational mode switching in chlorine production," *AIChE Journal*, 2018.

[21] X. Peng, T. W. Root, and C. T. Maravelias, "Optimization-based process synthesis under seasonal and daily variability: Application to concentrating solar power," *AIChE Journal*, vol. 65, no. 7, p. e16458, 2019.

[22] M. J. Palys, A. Allman, and P. Daoutidis, "Exploring the benefits of modular renewable-powered ammonia production: A supply chain optimization study," *Industrial & Engineering Chemistry Research*, vol. 58, no. 15, pp. 5898–5908, 2018.

[23] T. Seifert, S. Sievers, C. Bramsiepe, and G. Schembecker, "Small scale, modular and continuous: A new approach in plant design," *Chemical Engineering and Processing: Process Intensification*, vol. 52, pp. 140–150, 2012.

[24] T. Bieringer, S. Buchholz, and N. Kockmann, "Future production concepts in the chemical industry: modular–small-scale–continuous," *Chemical Engineering & Technology*, vol. 36, no. 6, pp. 900–910, 2013.

[25] A. Patil, L. Laumans, and H. Vrijenhoef, "Solar to ammonia–via proton's nfuel units," *Procedia Engineering*, vol. 83, pp. 322–327, 2014.

[26] M. Reese, C. Marquart, M. Malmali, K. Wagner, E. Buchanan, A. McCormick, and E. L. Cussler, "Performance of a small-scale haber process," *Industrial & Engineering Chemistry Research*, vol. 55, no. 13, pp. 3742–3750, 2016.

[27] M. Baldea, T. F. Edgar, B. L. Stanley, and A. A. Kiss, "Modular manufacturing processes: Status, challenges, and opportunities," *AIChE Journal*, vol. 63, no. 10, pp. 4262–4272, 2017.

[28] A. Allman, P. Daoutidis, D. Tiffany, and S. Kelley, "A framework for ammonia supply chain optimization incorporating conventional and renewable generation," *AIChE Journal*, vol. 63, no. 10, pp. 4390–4402, 2017.

[29] Q. Chen and I. E. Grossmann, "Effective generalized disjunctive programming models for modular process synthesis," *Industrial & Engineering Chemistry Research*, vol. 58, no. 15, pp. 5873–5886, 2019.

[30] N. Karanth and R. Hughes, "Simulation of an adiabatic packed bed reactor," *Chemical Engineering Science*, vol. 29, no. 1, pp. 197–205, 1974.

[31] K. V. Bussche, S. Neophytides, I. Zolotarskii, and G. Froment, "Modelling and simulation of the reversed flow operation of a fixed-bed reactor for methanol synthesis," *Chemical Engineering Science*, vol. 48, no. 19, pp. 3335–3345, 1993.

[32] M. Winterberg, E. Tsotsas, A. Krischke, and D. Vortmeyer, "A simple and coherent set of coefficients for modelling of heat and mass transport with and without chemical reaction in tubes filled with spheres," *Chemical Engineering Science*, vol. 55, no. 5, pp. 967–979, 2000.

[33] M. Halabi, M. De Croon, J. Van der Schaaf, P. Cobden, and J. Schouten, "Modeling and analysis of autothermal reforming of methane to hydrogen in a fixed bed reformer," *Chemical Engineering Journal*, vol. 137, no. 3, pp. 568–578, 2008.

[34] F. Manenti, S. Cieri, M. Restelli, and G. Bozzano, "Dynamic modeling of the methanol synthesis fixed-bed reactor," *Computers & Chemical Engineering*, vol. 48, pp. 325–334, 2013.

[35] T. A. Adams and P. I. Barton, "A dynamic two-dimensional heterogeneous model for water gas shift reactors," *International Journal of Hydrogen Energy*, vol. 34, no. 21, pp. 8877–8891, 2009.

[36] J. H. Ghouse and T. A. Adams, "A multi-scale dynamic two-dimensional heterogeneous model for catalytic steam methane reforming reactors," *International Journal of Hydrogen Energy*, vol. 38, no. 24, pp. 9984–9999, 2013.

[37] V. G. Gomes and K. W. Yee, "Pressure swing adsorption for carbon dioxide sequestration from exhaust gases," *Separation and Purification Technology*, vol. 28, no. 2, pp. 161–171, 2002.

[38] L. Jiang, L. T. Biegler, and V. G. Fox, "Simulation and optimization of pressure-swing adsorption systems for air separation," *AIChE Journal*, vol. 49, no. 5, pp. 1140–1157, 2003.

[39] S. Cavenati, C. A. Grande, and A. E. Rodrigues, "Removal of carbon dioxide from natural gas by vacuum pressure swing adsorption," *Energy & Fuels*, vol. 20, no. 6, pp. 2648–2659, 2006.

[40] M. M. F. Hasan, R. C. Baliban, J. A. Elia, and C. A. Floudas, "Modeling, simulation, and optimization of postcombustion CO_2 capture for variable feed concentration and flow rate. 2. pressure swing adsorption and vacuum swing adsorption processes," *Industrial & Engineering Chemistry Research*, vol. 51, no. 48, pp. 15665–15682, 2012.

[41] N. Casas, J. Schell, R. Pini, and M. Mazzotti, "Fixed bed adsorption of CO_2/H_2 mixtures on activated carbon: experiments and modeling," *Adsorption*, vol. 18, no. 2, pp. 143–161, 2012.

[42] R. Haghpanah, A. Majumder, R. Nilam, A. Rajendran, S. Farooq, I. A. Karimi, and M. Amanullah, "Multiobjective optimization of a four-step adsorption process for postcombustion CO_2 capture via finite volume simulation," *Industrial & Engineering Chemistry Research*, vol. 52, no. 11, pp. 4249–4265, 2013.

[43] Y. Ding and E. Alpay, "Adsorption-enhanced steam–methane reforming," *Chemical Engineering Science*, vol. 55, no. 18, pp. 3929–3940, 2000.

[44] G.-h. Xiu, J. L. Soares, P. Li, and A. E. Rodrigues, "Simulation of five-step one-bed sorption-enhanced reaction process," *AIChE Journal*, vol. 48, no. 12, pp. 2817–2832, 2002.

[45] G. Xiu, P. Li, and A. E. Rodrigues, "Adsorption-enhanced steam-methane reforming with intraparticle-diffusion limitations," *Chemical Engineering Journal*, vol. 95, no. 1, pp. 83–93, 2003.

[46] G.-h. Xiu, P. Li, and A. E. Rodrigues, "Sorption-enhanced reaction process with reactive regeneration," *Chemical Engineering Science*, vol. 57, no. 18, pp. 3893–3908, 2002.

[47] D. K. Lee, I. H. Baek, and W. L. Yoon, "Modeling and simulation for the methane steam reforming enhanced by in situ CO_2 removal utilizing the CaO carbonation for H_2 production," *Chemical Engineering Science*, vol. 59, no. 4, pp. 931–942, 2004.

[48] H. K. Rusten, E. Ochoa-Fernández, D. Chen, and H. A. Jakobsen, "Numerical investigation of sorption enhanced steam methane reforming using Li_2ZrO_3 as CO_2-acceptor," *Industrial & Engineering Chemistry Research*, vol. 46, no. 13, pp. 4435–4443, 2007.

[49] G. C. Koumpouras, E. Alpay, and F. Stepanek, "Mathematical modelling of low-temperature hydrogen production with in situ CO_2 capture," *Chemical Engineering Science*, vol. 62, no. 10, pp. 2833–2841, 2007.

[50] H. T. J. Reijers, J. Boon, G. D. Elzinga, P. D. Cobden, W. G. Haije, and R. W. van den Brink, "Modeling study of the sorption-enhanced reaction process for CO_2 capture: 1. model development and validation," *Industrial & Engineering Chemistry Research*, vol. 48, no. 15, pp. 6966–6974, 2009.

[51] H. T. J. Reijers, J. Boon, G. D. Elzinga, P. D. Cobden, W. G. Haije, and R. W. v. d. Brink, "Modeling study of the sorption-enhanced reaction process for CO_2 capture: 2. application to steam-methane reforming," *Industrial & Engineering Chemistry Research*, vol. 48, no. 15, pp. 6975–6982, 2009.

[52] J. Fernandez, J. Abanades, and R. Murillo, "Modeling of sorption enhanced steam methane reforming in an adiabatic fixed bed reactor," *Chemical Engineering Science*, vol. 84, pp. 1–11, 2012.

[53] J. Fernandez, J. Abanades, and G. Grasa, "Modeling of sorption enhanced steam methane reforming—part ii: Simulation within a novel Ca/Cu chemical loop process for hydrogen production," *Chemical Engineering Science*, vol. 84, pp. 12–20, 2012.

[54] Y.-J. Wu, P. Li, J.-G. Yu, A. F. Cunha, and A. E. Rodrigues, "Sorption-enhanced steam reforming of ethanol for continuous high-purity hydrogen production: 2D adsorptive reactor dynamics and process design," *Chemical Engineering Science*, vol. 118, pp. 83–93, 2014.

[55] Y.-J. Wu, P. Li, J.-G. Yu, A. F. Cunha, and A. E. Rodrigues, "High-purity hydrogen production by sorption-enhanced steam reforming of ethanol: a cyclic operation simulation study," *Industrial & Engineering Chemistry Research*, vol. 53, no. 20, pp. 8515–8527, 2014.

[56] S. Z. Abbas, *Modelling of Sorption Enhanced Chemical Looping Steam Reforming (SE-CLSR) of Methane in a Packed Bed Reactor*. PhD thesis, University of Leeds, 2016.

[57] S. Abbas, V. Dupont, and T. Mahmud, "Modelling of high purity H_2 production via sorption enhanced chemical looping steam reforming of methane in a packed bed reactor," *Fuel*, vol. 202, pp. 271–286, 2017.

[58] E. L. Lugo and B. A. Wilhite, "A theoretical comparison of multifunctional catalyst for sorption-enhanced reforming process," *Chemical Engineering Science*, vol. 150, pp. 1–15, 2016.

[59] N. Chanburanasiri, A. M. Ribeiro, A. E. Rodrigues, A. Arpornwichanop, N. Laosiripojana, P. Praserthdam, and S. Assabumrungrat, "Hydrogen production via sorption enhanced steam methane reforming process using Ni/CaO multifunctional catalyst," *Industrial & Engineering Chemistry Research*, vol. 50, no. 24, pp. 13662–13671, 2011.

[60] A. Cunha, Y. Wu, J. Santos, and A. Rodrigues, "Steam reforming of ethanol on copper catalysts derived from hydrotalcite-like materials," *Industrial & Engineering Chemistry Research*, vol. 51, no. 40, pp. 13132–13143, 2012.

[61] Y.-J. Wu, P. Li, J.-G. Yu, A. Cunha, and A. Rodrigues, "Sorption-enhanced steam reforming of ethanol on NiMgAl multifunctional materials: experimental and numerical investigation," *Chemical Engineering Journal*, vol. 231, pp. 36–48, 2013.

[62] A. Cunha, Y.-J. Wu, J. Santos, and A. Rodrigues, "Sorption enhanced steam reforming of ethanol on hydrotalcite-like compounds impregnated with active copper," *Chemical Engineering Research and Design*, vol. 91, no. 3, pp. 581–592, 2013.

[63] A. F. Cunha, Y.-J. Wu, P. Li, J.-G. Yu, and A. E. Rodrigues, "Sorption-enhanced steam reforming of ethanol on a novel K–Ni–Cu–hydrotalcite hybrid material," *Industrial & Engineering Chemistry Research*, vol. 53, no. 10, pp. 3842–3853, 2014.

[64] H. M. Jang, W. R. Kang, and K. B. Lee, "Sorption-enhanced water gas shift reaction using multi-section column for high-purity hydrogen production," *International Journal of Hydrogen Energy*, vol. 38, no. 14, pp. 6065–6071, 2013.

[65] X. Wang, N. Wang, and L. Wang, "Hydrogen production by sorption enhanced steam reforming of propane: a thermodynamic investigation," *International Journal of Hydrogen Energy*, vol. 36, no. 1, pp. 466–472, 2011.

[66] M. Bayat, Z. Dehghani, and M. Rahimpour, "Membrane/sorption-enhanced methanol synthesis process: Dynamic simulation and optimization," *Journal of Industrial and Engineering Chemistry*, vol. 20, no. 5, pp. 3256–3269, 2014.

[67] M. Bayat, M. Hamidi, Z. Dehghani, and M. Rahimpour, "Sorption-enhanced fischer–tropsch synthesis with continuous adsorbent regeneration in GTL technology: Modeling and optimization," *Journal of Industrial and Engineering Chemistry*, vol. 20, no. 3, pp. 858–869, 2014.

[68] K. Tzanetis, C. Martavaltzi, and A. Lemonidou, "Comparative exergy analysis of sorption enhanced and conventional methane steam reforming," *International Journal of Hydrogen Energy*, vol. 37, no. 21, pp. 16308–16320, 2012.

[69] S. Nilchan and C. Pantelides, "On the optimisation of periodic adsorption processes," *Adsorption*, vol. 4, no. 2, pp. 113–147, 1998.

[70] A. Agarwal, L. T. Biegler, and S. E. Zitney, "A superstructure-based optimal synthesis of psa cycles for post-combustion CO_2 capture," *AIChE Journal*, vol. 56, no. 7, pp. 1813–1828, 2010.

[71] A. Agarwal, L. T. Biegler, and S. E. Zitney, "Superstructure-based optimal synthesis of pressure swing adsorption cycles for precombustion CO_2 capture," *Industrial & Engineering Chemistry Research*, vol. 49, no. 11, pp. 5066–5079, 2009.

[72] A. Wächter and L. T. Biegler, "On the implementation of an interior-point filter line-search algorithm for large-scale nonlinear programming," *Mathematical Programming*, vol. 106, no. 1, pp. 25–57, 2006.

[73] A. Agarwal, L. T. Biegler, and S. E. Zitney, "Simulation and optimization of pressure swing adsorption systems using reduced-order modeling," *Industrial & Engineering Chemistry Research*, vol. 48, no. 5, pp. 2327–2343, 2008.

[74] E. L. First, M. F. Hasan, and C. A. Floudas, "Discovery of novel zeolites for natural gas purification through combined material screening and process optimization," *AIChE Journal*, vol. 60, no. 5, pp. 1767–1785, 2014.

[75] S. S. Iyer, I. Bajaj, P. Balasubramanian, and M. M. F. Hasan, "Integrated carbon capture and conversion to produce syngas: Novel process design, intensification, and optimization," *Industrial & Engineering Chemistry Research*, vol. 56, no. 30, pp. 8622–8648, 2017.

[76] L. J. Murray, M. Dincă, and J. R. Long, "Hydrogen storage in metal–organic frameworks," *Chemical Society Reviews*, vol. 38, no. 5, pp. 1294–1314, 2009.

[77] D. Farrusseng, *Metal-organic frameworks: applications from catalysis to gas storage*. John Wiley & Sons, 2011.

[78] A. U. Czaja, N. Trukhan, and U. Müller, "Industrial applications of metal–organic frameworks," *Chemical Society Reviews*, vol. 38, no. 5, pp. 1284–1293, 2009.

[79] J.-R. Li, R. J. Kuppler, and H.-C. Zhou, "Selective gas adsorption and separation in metal–organic frameworks," *Chemical Society Reviews*, vol. 38, no. 5, pp. 1477–1504, 2009.

[80] T. Düren, Y.-S. Bae, and R. Q. Snurr, "Using molecular simulation to characterise metal–organic frameworks for adsorption applications," *Chemical Society Reviews*, vol. 38, no. 5, pp. 1237–1247, 2009.

[81] D. M. D'Alessandro, B. Smit, and J. R. Long, "Carbon dioxide capture: prospects for new materials," *Angewandte Chemie International Edition*, vol. 49, no. 35, pp. 6058–6082, 2010.

[82] S. T. Meek, J. A. Greathouse, and M. D. Allendorf, "Metal-organic frameworks: A rapidly growing class of versatile nanoporous materials," *Advanced Materials*, vol. 23, no. 2, pp. 249–267, 2011.

[83] S. Wang and Y. Peng, "Natural zeolites as effective adsorbents in water and wastewater treatment," *Chemical Engineering Journal*, vol. 156, no. 1, pp. 11–24, 2010.

[84] J. Park, R. P. Lively, and D. S. Sholl, "Establishing upper bounds on co 2 swing capacity in sub-ambient pressure swing adsorption via molecular simulation of metal–organic frameworks," *Journal of Materials Chemistry A*, vol. 5, no. 24, pp. 12258–12265, 2017.

[85] A. N. Dickey, A. Ö. Yazaydın, R. R. Willis, and R. Q. Snurr, "Screening CO_2/N_2 selectivity in metal-organic frameworks using monte carlo simulations and ideal adsorbed solution theory," *The Canadian Journal of Chemical Engineering*, vol. 90, no. 4, pp. 825–832, 2012.

[86] K. Sumida, D. L. Rogow, J. A. Mason, T. M. McDonald, E. D. Bloch, Z. R. Herm, T.-H. Bae, and J. R. Long, "Carbon dioxide capture in metal–organic frameworks," *Chemical Reviews*, vol. 112, no. 2, pp. 724–781, 2012.

[87] D. Ruthven, S. Farooq, and K. S. Knaebel, "Pressure swing adsorption," *New York: VCH Publishers*, vol. 1, no. 994, p. 235, 1994.

[88] S. Sircar, "Pressure swing adsorption," *Industrial & Engineering Chemistry Research*, vol. 41, no. 6, pp. 1389–1392, 2002.

[89] K. S. Knaebel, "For your next separation consider adsorption," *Chemical Engineering*, vol. 102, no. 11, p. 92, 1995.

[90] M. Tagliabue, D. Farrusseng, S. Valencia, S. Aguado, U. Ravon, C. Rizzo, A. Corma, and C. Mirodatos, "Natural gas treating by selective adsorption: Material science and chemical engineering interplay," *Chemical Engineering Journal*, vol. 155, no. 3, pp. 553–566, 2009.

[91] G. D. Pirngruber, L. Hamon, S. Bourrelly, P. L. Llewellyn, E. Lenoir, V. Guillerm, C. Serre, and T. Devic, "A method for screening the potential of mofs as CO_2 adsorbents in pressure swing adsorption processes," *ChemSusChem*, vol. 5, no. 4, pp. 762–776, 2012.

[92] S. U. Rege and R. T. Yang, "A simple parameter for selecting an adsorbent for gas separation by pressure swing adsorption," *Separation Science and Technology*, vol. 36, no. 15, pp. 3355–3365, 2001.

[93] A. D. Wiersum, J.-S. Chang, C. Serre, and P. L. Llewellyn, "An adsorbent performance indicator as a first step evaluation of novel sorbents for gas separations: application to metal–organic frameworks," *Langmuir*, vol. 29, no. 10, pp. 3301–3309, 2013.

[94] M. W. Ackley, J. Smolarek, and F. W. Leavitt, "Pressure swing adsorption gas separation method, using adsorbents with high intrinsic diffusivity and low pressure ratios," Jan. 14 2003. US Patent 6,506,234.

[95] J. M. Huck, L.-C. Lin, A. H. Berger, M. N. Shahrak, R. L. Martin, A. S. Bhown, M. Haranczyk, K. Reuter, and B. Smit, "Evaluating different classes of porous materials for carbon capture," *Energy & Environmental Science*, vol. 7, no. 12, pp. 4132–4146, 2014.

[96] A. K. Rajagopalan, A. M. Avila, and A. Rajendran, "Do adsorbent screening metrics predict process performance? a process optimisation based study for post-combustion capture of CO_2," *International Journal of Greenhouse Gas Control*, vol. 46, pp. 76–85, 2016.

[97] M. Khurana and S. Farooq, "Adsorbent screening for postcombustion CO_2 capture: a method relating equilibrium isotherm characteristics to an optimum vacuum swing adsorp-

tion process performance," *Industrial & Engineering Chemistry Research*, vol. 55, no. 8, pp. 2447–2460, 2016.

[98] R. Kumar, "Pressure swing adsorption process: performance optimum and adsorbent selection," *Industrial & Engineering Chemistry Research*, vol. 33, no. 6, pp. 1600–1605, 1994.

[99] R. Krishna and J. M. van Baten, "A comparison of the co2 capture characteristics of zeolites and metal–organic frameworks," *Separation and Purification Technology*, vol. 87, pp. 120–126, 2012.

[100] M. F. Hasan, E. L. First, and C. A. Floudas, "Cost-effective CO_2 capture based on in silico screening of zeolites and process optimization," *Physical Chemistry Chemical Physics*, vol. 15, no. 40, pp. 17601–17618, 2013.

[101] K. T. Leperi, Y. G. Chung, F. You, and R. Q. Snurr, "Development of a general evaluation metric for rapid screening of adsorbent materials for postcombustion CO_2 capture," *ACS Sustainable Chemistry & Engineering*, vol. 7, no. 13, pp. 11529–11539, 2019.

[102] J. Park, H. O. R. Landa, Y. Kawajiri, M. J. Realff, R. P. Lively, and D. S. Sholl, "How well do approximate models of adsorption-based CO_2 capture processes predict results of detailed process models?," *Industrial & Engineering Chemistry Research*, vol. 59, no. 15, pp. 7097–7108, 2019.

[103] R. Krishna and J. R. Long, "Screening metal–organic frameworks by analysis of transient breakthrough of gas mixtures in a fixed bed adsorber," *The Journal of Physical Chemistry C*, vol. 115, no. 26, pp. 12941–12950, 2011.

[104] L. Bastin, P. S. Bárcia, E. J. Hurtado, J. A. Silva, A. E. Rodrigues, and B. Chen, "A microporous metal- organic framework for separation of CO_2/N_2 and CO_2/CH_4 by fixed-bed adsorption," *The Journal of Physical Chemistry C*, vol. 112, no. 5, pp. 1575–1581, 2008.

[105] S. Couck, J. F. Denayer, G. V. Baron, T. Rémy, J. Gascon, and F. Kapteijn, "An amine-functionalized MIL-53 metal-organic framework with large separation power for CO_2 and CH_4," *Journal of the American Chemical Society*, vol. 131, no. 18, pp. 6326–6327, 2009.

[106] D. Britt, H. Furukawa, B. Wang, T. G. Glover, and O. M. Yaghi, "Highly efficient separation of carbon dioxide by a metal-organic framework replete with open metal sites," *Proceedings of the National Academy of Sciences*, vol. 106, no. 49, pp. 20637–20640, 2009.

[107] Y.-S. Bae and R. Q. Snurr, "Development and evaluation of porous materials for carbon dioxide separation and capture," *Angewandte Chemie International Edition*, vol. 50, no. 49, pp. 11586–11596, 2011.

[108] S. Xiang, Y. He, Z. Zhang, H. Wu, W. Zhou, R. Krishna, and B. Chen, "Microporous metal-organic framework with potential for carbon dioxide capture at ambient conditions," *Nature Communications*, vol. 3, no. 1, pp. 1–9, 2012.

[109] D. Britt, D. Tranchemontagne, and O. M. Yaghi, "Metal-organic frameworks with high capacity and selectivity for harmful gases," *Proceedings of the National Academy of Sciences*, vol. 105, no. 33, pp. 11623–11627, 2008.

[110] X. Duan, Q. Zhang, J. Cai, Y. Yang, Y. Cui, Y. He, C. Wu, R. Krishna, B. Chen, and G. Qian, "A new metal–organic framework with potential for adsorptive separation of methane from carbon dioxide, acetylene, ethylene, and ethane established by simulated breakthrough experiments," *Journal of Materials Chemistry A*, vol. 2, no. 8, pp. 2628–2633, 2014.

[111] H. Prats, D. Bahamon, G. Alonso, X. Giménez, P. Gamallo, and R. Sayós, "Optimal faujasite structures for post combustion CO_2 capture and separation in different swing adsorption processes," *Journal of CO_2 Utilization*, vol. 19, pp. 100–111, 2017.

[112] R. Krishna and J. M. van Baten, "In silico screening of metal–organic frameworks in separation applications," *Physical Chemistry Chemical Physics*, vol. 13, no. 22, pp. 10593–10616, 2011.

[113] Y. J. Colón and R. Q. Snurr, "High-throughput computational screening of metal–organic frameworks," *Chemical Society Reviews*, vol. 43, no. 16, pp. 5735–5749, 2014.

[114] D. Wu, C. Wang, B. Liu, D. Liu, Q. Yang, and C. Zhong, "Large-scale computational screening of metal-organic frameworks for CH_4/H_2 separation," *AIChE Journal*, vol. 58, no. 7, pp. 2078–2084, 2012.

[115] S. S. Iyer, S. E. Demirel, and M. F. Hasan, "Combined natural gas separation and storage based on in silico material screening and process optimization," *Industrial & Engineering Chemistry Research*, vol. 57, no. 49, pp. 16727–16750, 2018.

[116] S. S. Iyer and M. F. Hasan, "Mapping the material-property space for feasible process operation: Application to combined natural-gas separation and storage," *Industrial & Engineering Chemistry Research*, vol. 58, no. 24, pp. 10455–10465, 2019.

[117] P. Xiao, J. Zhang, P. Webley, G. Li, R. Singh, and R. Todd, "Capture of CO_2 from flue gas streams with zeolite 13X by vacuum-pressure swing adsorption," *Adsorption*, vol. 14, no. 4-5, pp. 575–582, 2008.

[118] H. T. J. Reijers, J. Boon, G. D. Elzinga, P. D. Cobden, W. G. Haije, and R. W. van den Brink, "Modeling study of the sorption-enhanced reaction process for CO_2 capture. i. model development and validation," *Industrial & Engineering Chemistry Research*, vol. 48, no. 15, pp. 6966–6974, 2009.

[119] A. Arora, S. S. Iyer, and M. F. Hasan, "GRAMS: A general framework describing adsorption, reaction and sorption-enhanced reaction processes," *Chemical Engineering Science*, vol. 192, pp. 335–358, 2018.

[120] A. Arora, I. Bajaj, S. S. Iyer, and M. F. Hasan, "Optimal synthesis of periodic sorption enhanced reaction processes with application to hydrogen production," *Computers & Chemical Engineering*, vol. 115, pp. 89–111, 2018.

[121] A. Arora, S. S. Iyer, I. Bajaj, and M. F. Hasan, "Optimal methanol production via sorption-enhanced reaction process," *Industrial & Engineering Chemistry Research*, vol. 57, no. 42, pp. 14143–14161, 2018.

[122] R. B. Bird, "Transport phenomena," *Appl. Mech. Rev.*, vol. 55, no. 1, pp. R1–R4, 2002.

[123] C. Sereno and A. Rodrigues, "Can steady-state momentum equations be used in modelling pressurization of adsorption beds?," *Gas Separation & Purification*, vol. 7, no. 3, pp. 167–174, 1993.

[124] R. J. LeVeque *et al.*, *Finite volume methods for hyperbolic problems*, vol. 31. Cambridge university press, 2002.

[125] W. Roger, "Hydrogen production," Dec 1933. US Patent 1,938,202.

[126] J. R. Rostrup-Nielsen, "Catalytic steam reforming," in *Catalysis*, pp. 1–117, Springer, 1984.

[127] J. Shu, B. P. Grandjean, and S. Kaliaguine, "Methane steam reforming in asymmetric Pd- and Pd-ag/porous SS membrane reactors," *Applied Catalysis A: General*, vol. 119, no. 2, pp. 305–325, 1994.

[128] J. Xu and G. F. Froment, "Methane steam reforming, methanation and water-gas shift: I. intrinsic kinetics," *AIChE Journal*, vol. 35, no. 1, pp. 88–96, 1989.

[129] F. Gallucci, L. Paturzo, A. Famà, and A. Basile, "Experimental study of the methane steam reforming reaction in a dense Pd/Ag membrane reactor," *Industrial & Engineering Chemistry Research*, vol. 43, no. 4, pp. 928–933, 2004.

[130] Y. Li, Q. Fu, and M. Flytzani-Stephanopoulos, "Low-temperature water-gas shift reaction over Cu-and Ni-loaded cerium oxide catalysts," *Applied Catalysis B: Environmental*, vol. 27, no. 3, pp. 179–191, 2000.

[131] Y. Choi and H. G. Stenger, "Water gas shift reaction kinetics and reactor modeling for fuel cell grade hydrogen," *Journal of Power Sources*, vol. 124, no. 2, pp. 432–439, 2003.

[132] J. M. Moe, "Design of water-gas shift reactors," *Chem. Eng. Prog.*, vol. 58, pp. 33–36, 1962.

[133] L. Wang, Z. Liu, P. Li, J. Yu, and A. E. Rodrigues, "Experimental and modeling investigation on post-combustion carbon dioxide capture using zeolite 13X-APG by hybrid vtsa process," *Chemical Engineering Journal*, vol. 197, pp. 151–161, 2012.

[134] I. Bajaj, S. S. Iyer, and M. M. F. Hasan, "A trust region-based two phase algorithm for constrained black-box and grey-box optimization with infeasible initial point," *Computers & Chemical Engineering*, 2017.

[135] H.-M. Gutmann, "A radial basis function method for global optimization," *Journal of Global Optimization*, vol. 19, no. 3, pp. 201–227, 2001.

[136] R. Misener and C. A. Floudas, "ANTIGONE: algorithms for continuous/integer global optimization of nonlinear equations," *Journal of Global Optimization*, vol. 59, no. 2-3, pp. 503–526, 2014.

[137] M. Cohce, I. Dincer, and M. Rosen, "Thermodynamic analysis of hydrogen production from biomass gasification," *International Journal of Hydrogen Energy*, vol. 35, no. 10, pp. 4970–4980, 2010.

[138] S. Mayorga, J. Hufton, S. Sircar, and T. Gaffney, *Sorption enhanced reaction process for production of hydrogen. Phase 1 final report.* No. DOE/GO/10059–T1.Jul 1997.

[139] H. T. J. Reijers, S. E. Valster-Schiermeier, P. D. Cobden, and R. W. Van Den Brink, "Hydrotalcite as CO_2 sorbent for sorption-enhanced steam reforming of methane," *Industrial & Engineering Chemistry Research*, vol. 45, no. 8, pp. 2522–2530, 2006.

[140] Z.-s. Li and N.-s. Cai, "Modeling of multiple cycles for sorption-enhanced steam methane reforming and sorbent regeneration in fixed bed reactor," *Energy & Fuels*, vol. 21, no. 5, pp. 2909–2918, 2007.

[141] Z.-s. Li, N.-s. Cai, and J.-b. Yang, "Continuous production of hydrogen from sorption-enhanced steam methane reforming in two parallel fixed-bed reactors operated in a cyclic manner," *Industrial & Engineering Chemistry Research*, vol. 45, no. 26, pp. 8788–8793, 2006.

[142] K. B. Lee, M. G. Beaver, H. S. Caram, and S. Sircar, "Novel thermal-swing sorption-enhanced reaction process concept for hydrogen production by low-temperature steam

methane reforming," *Industrial & Engineering Chemistry Research*, vol. 46, no. 14, pp. 5003–5014, 2007.

[143] G. Xiu, P. Li, and A. Rodrigues, "Subsection-controlling strategy for improving sorption-enhanced reaction process," *Chemical Engineering Research and Design*, vol. 82, no. 2, pp. 192–202, 2004.

[144] M. G. Beaver, H. S. Caram, and S. Sircar, "Sorption enhanced reaction process for direct production of fuel-cell grade hydrogen by low temperature catalytic steam–methane reforming," *Journal of Power Sources*, vol. 195, no. 7, pp. 1998–2002, 2010.

[145] Y. Ding and E. Alpay, "Equilibria and kinetics of CO_2 adsorption on hydrotalcite adsorbent," *Chemical Engineering Science*, vol. 55, no. 17, pp. 3461–3474, 2000.

[146] A. Aguirre, *Computational Fluid Dynamics Modeling and Simulation of Steam Methane Reforming Reactors and Furnaces*. PhD thesis, UCLA, 2017.

[147] W. E. Waldron, J. Hufton, and S. Sircar, "Production of hydrogen by cyclic sorption enhanced reaction process," *American Institute of Chemical Engineers. AIChE Journal*, vol. 47, no. 6, p. 1477, 2001.

[148] D. M. Anderson, P. A. Kottke, and A. G. Fedorov, "Thermodynamic analysis of hydrogen production via sorption-enhanced steam methane reforming in a new class of variable volume batch-membrane reactor," *International Journal of Hydrogen Energy*, vol. 39, no. 31, pp. 17985–17997, 2014.

[149] T. Numaguchi and K. Kikuchi, "Intrinsic kinetics and design simulation in a complex reaction network; steam-methane reforming," in *Tenth International Symposium on Chemical Reaction Engineering*, pp. 2295–2301, Elsevier, 1988.

[150] K. Johnsen, H. Ryu, J. Grace, and C. Lim, "Sorption-enhanced steam reforming of methane in a fluidized bed reactor with dolomite as CO_2-acceptor," *Chemical Engineering Science*, vol. 61, no. 4, pp. 1195–1202, 2006.

[151] K. Hou and R. Hughes, "The kinetics of methane steam reforming over a Ni/α-Al_2Ocatalyst," *Chemical Engineering Journal*, vol. 82, no. 1, pp. 311–328, 2001.

[152] G.-h. Xiu, P. Li, and A. E. Rodrigues, "New generalized strategy for improving sorption-enhanced reaction process," *Chemical Engineering Science*, vol. 58, no. 15, pp. 3425–3437, 2003.

[153] N. R. Council *et al.*, *The hydrogen economy: opportunities, costs, barriers, and R&D needs*. National Academies Press, 2004.

[154] H. F. Rase, *Chemical reactor design for process plants*, vol. 2. Wiley New York, 1977.

[155] K. Lee, M. Beaver, H. Caram, and S. Sircar, "Reversible chemisorption of carbon dioxide: simultaneous production of fuel-cell grade H_2 and compressed CO_2 from synthesis gas," *Adsorption*, vol. 13, no. 3, pp. 385–397, 2007.

[156] W.-H. Cheng, *Methanol production and use*. CRC Press, 1994.

[157] M. Blug, J. Leker, L. Plass, and A. Günther, "Methanol generation economics," in *Methanol: The Basic Chemical and Energy Feedstock of the Future*, pp. 603–618, Springer, 2014.

[158] G. A. Olah, "Beyond oil and gas: the methanol economy," *Angewandte Chemie International Edition*, vol. 44, no. 18, pp. 2636–2639, 2005.

[159] M. Alvarado, "The changing face of the global methanol industry," *IHS Chemical Bulletin*, no. 3, pp. 10–11, 2016.

[160] V. M. Ehlinger, K. J. Gabriel, M. M. Noureldin, and M. M. El-Halwagi, "Process design and integration of shale gas to methanol," *ACS Sustainable Chemistry & Engineering*, vol. 2, no. 1, pp. 30–37, 2013.

[161] B. A. Santos, J. M. Loureiro, A. M. Ribeiro, A. E. Rodrigues, and A. F. Cunha, "Methanol production by bi-reforming," *The Canadian Journal of Chemical Engineering*, vol. 93, no. 3, pp. 510–526, 2015.

[162] M. Martín, "Methodology for solar and wind energy chemical storage facilities design under uncertainty: Methanol production from CO_2 and hydrogen," *Computers & Chemical Engineering*, vol. 92, pp. 43–54, 2016.

[163] A. Cybulski, "Liquid-phase methanol synthesis: catalysts, mechanism, kinetics, chemical equilibria, vapor-liquid equilibria, and modeling — A Review," *Catalysis Reviews – Science and Engineering*, vol. 36, no. 4, pp. 557–615, 1994.

[164] K. R. Westerterp, M. Kuczynski, and C. H. Kamphuis, "The synthesis of methanol in a reactor system with interstage product removal," *Industrial & Engineering Chemistry Research*, vol. 28, no. 6, pp. 763–771, 1989.

[165] L. Wang, L. Yang, Y. Zhang, W. Ding, S. Chen, W. Fang, and Y. Yang, "Promoting effect of an aluminum emulsion on catalytic performance of Cu-based catalysts for methanol synthesis from syngas," *Fuel Processing Technology*, vol. 91, no. 7, pp. 723–728, 2010.

[166] S. S. Iyer, T. Renganathan, S. Pushpavanam, M. V. Kumar, and N. Kaisare, "Generalized thermodynamic analysis of methanol synthesis: Effect of feed composition," *Journal of CO_2 Utilization*, vol. 10, pp. 95–104, 2015.

[167] Y. Yang, C. A. Mims, D. Mei, C. H. Peden, and C. T. Campbell, "Mechanistic studies of methanol synthesis over Cu from $CO/CO_2/H_2/H_2O$ mixtures: The source of C in methanol and the role of water," *Journal of Catalysis*, vol. 298, pp. 10–17, 2013.

[168] N. Rezaie, A. Jahanmiri, B. Moghtaderi, and M. Rahimpour, "A comparison of homogeneous and heterogeneous dynamic models for industrial methanol reactors in the presence of catalyst deactivation," *Chemical Engineering and Processing: Process Intensification*, vol. 44, no. 8, pp. 911–921, 2005.

[169] W. L. Luyben, "Design and control of a methanol reactor/column process," *Industrial & Engineering Chemistry Research*, vol. 49, no. 13, pp. 6150–6163, 2010.

[170] L. Chen, Q. Jiang, Z. Song, and D. Posarac, "Optimization of methanol yield from a lurgi reactor," *Chemical Engineering & Technology*, vol. 34, no. 5, pp. 817–822, 2011.

[171] R. De María, I. Díaz, M. Rodríguez, and A. Sáiz, "Industrial methanol from syngas: kinetic study and process simulation," *International Journal of Chemical Reactor Engineering*, vol. 11, no. 1, pp. 469–477, 2013.

[172] S. A. Velardi and A. A. Barresi, "Methanol synthesis in a forced unsteady-state reactor network," *Chemical Engineering Science*, vol. 57, no. 15, pp. 2995–3004, 2002.

[173] S. Yusup, N. P. Anh, and H. Zabiri, "A simulation study of an industrial methanol reactor based on simplified steady-state model," *International Journal of Recent Research and Applied Studies*, vol. 5, no. 3, pp. 213–222, 2010.

[174] J. Solsvik and H. A. Jakobsen, "Modeling of multicomponent mass diffusion in porous spherical pellets: Application to steam methane reforming and methanol synthesis," *Chemical Engineering Science*, vol. 66, no. 9, pp. 1986–2000, 2011.

[175] S. Arab, J.-M. Commenge, J.-F. Portha, and L. Falk, "Methanol synthesis from CO_2 and H_2 in multi-tubular fixed-bed reactor and multi-tubular reactor filled with monoliths," *Chemical Engineering Research and Design*, vol. 92, no. 11, pp. 2598–2608, 2014.

[176] F. Meunier, P. Gray, J. Kqrger, Z. Xu, and D. Ruthven, "Diffusion of methanol in NaX crystals: Comparison of IR, ZLC, and PFG-NMR measurements," *Zeolites*, vol. 14, no. 4, pp. 242–249, 1994.

[177] A. Zachopoulos and E. Heracleous, "Overcoming the equilibrium barriers of CO_2 hydrogenation to methanol via water sorption: A thermodynamic analysis," *Journal of CO_2 Utilization*, vol. 21, pp. 360–367, 2017.

[178] M. Ghodhbene, F. Bougie, P. Fongarland, and M. C. Iliuta, "Hydrophilic zeolite sorbents for in-situ water removal in high temperature processes," *The Canadian Journal of Chemical Engineering*, vol. 95, no. 10, pp. 1842–1849, 2017.

[179] B. Carvill, J. Hufton, M. Anand, and S. Sircar, "Sorption-enhanced reaction process," *AIChE Journal*, vol. 42, no. 10, pp. 2765–2772, 1996.

[180] V. Chuikina, A. Kiselev, L. Mineyeva, and G. Muttik, "Heats of adsorption of water vapour on NaX and KNaX zeolites at different temperatures," *Journal of the Chemical Society, Faraday Transactions 1: Physical Chemistry in Condensed Phases*, vol. 72, pp. 1345–1354, 1976.

[181] K. Abdallah, P. Grenier, L. Sun, and F. Meunier, "Nonisothermal adsorption of water by synthetic NaX zeolite pellets," *Chemical Engineering Science*, vol. 43, no. 10, pp. 2633–2643, 1988.

[182] N. B. Amar, L. Sun, and F. Meunier, "Numerical analysis of adsorptive temperature wave regenerative heat pump," *Applied Thermal Engineering*, vol. 16, no. 5, pp. 405–418, 1996.

[183] K. V. Bussche and G. Froment, "A steady-state kinetic model for methanol synthesis and the water gas shift reaction on a commercial $Cu/ZnO/Al_2O_3$ catalyst," *Journal of Catalysis*, vol. 161, no. 1, pp. 1–10, 1996.

[184] K. Klier, V. Chatikavanij, R. Herman, and G. Simmons, "Catalytic synthesis of methanol from $CO\text{-}H_2$: Iv. The effects of carbon dioxide," *Journal of Catalysis*, vol. 74, no. 2, pp. 343–360, 1982.

[185] R. Weimer, D. Terry, and P. Stepanoff, "Laboratory kinetics and mass transfer in the liquid phase methanol process," in *Proceedings of the AIChE National Meeting, New York*, 1987.

[186] W. Von Wedel, S. Ledakowicz, and W.-D. Deckwer, "Kinetics of methanol synthesis in the slurry phase," in *Tenth International Symposium on Chemical Reaction Engineering*, pp. 2169–2174, Elsevier, 1988.

[187] G. Graaf, J. Winkelman, E. Stamhuis, and A. Beenackers, "Kinetics of the three phase methanol synthesis," in *Tenth International Symposium on Chemical Reaction Engineering*, pp. 2161–2168, Elsevier, 1988.

[188] C. Krishnan, J. R. Elliott Jr, and J. M. Berty, "Continuous operation of the Berty reactor for the solvent methanol process," *Industrial & Engineering Chemistry Research*, vol. 30, no. 7, pp. 1413–1418, 1991.

[189] S. Ledakowicz, M. Stelmachowski, A. Chacuk, and W.-D. Deckwer, "Methanol synthesis in bubble column slurry reactors," *Chemical Engineering and Processing: Process Intensification*, vol. 31, no. 4, pp. 213–219, 1992.

[190] S. Abrol and C. M. Hilton, "Modeling, simulation and advanced control of methanol production from variable synthesis gas feed," *Computers & Chemical Engineering*, vol. 40, pp. 117–131, 2012.

[191] D. C. Cardenas Barrañon, "Methanol and hydrogen production: energy and cost analysis," 2006.

[192] K. Atsonios, K. D. Panopoulos, and E. Kakaras, "Investigation of technical and economic aspects for methanol production through CO_2 hydrogenation," *International Journal of Hydrogen Energy*, vol. 41, no. 4, pp. 2202–2214, 2016.

[193] J. Seader, W. D. Seider, and D. R. Lewin, *Product and Process Design Principles: Synthesis, Analysis and Evaluation*. Wiley, 2004.

[194] A. Arora, I. Bajaj, S. S. Iyer, and M. M. F. Hasan, "Optimal synthesis of periodic sorption enhanced reaction processes with application to hydrogen production," *Computers & Chemical Engineering*, vol. 115, pp. 89–111, 2018b.

[195] P. J. Linstrom and W. Mallard, "NIST Chemistry webbook; NIST standard reference," p. Database No 69, 2001.

[196] M. Kuczynski, M. Oyevaar, R. Pieters, and K. Westerterp, "Methanol synthesis in a countercurrent gas-solid-solid trickle flow reactor. An experimental study," *Chemical Engineering Science*, vol. 42, no. 8, pp. 1887–1898, 1987.

[197] A. Riaz, G. Zahedi, and J. J. Klemeš, "A review of cleaner production methods for the manufacture of methanol," *Journal of Cleaner Production*, vol. 57, pp. 19–37, 2013.

[198] J. P. Sheets and A. Shah, "Techno-economic comparison of biogas cleaning for grid injection, compressed natural gas, and biogas-to-methanol conversion technologies," *Biofuels, Bioproducts and Biorefining*, vol. 12, no. 3, pp. 412–425, 2018.

[199] W. W. Tso, C. D. Demirhan, S. Lee, H. Song, J. B. Powell, and E. N. Pistikopoulos, "Energy carrier supply chain optimization: A texas case study," in *Computer Aided Chemical Engineering*, vol. 47, pp. 1–6, Elsevier, 2019.

[200] M. J. Palys, A. Kuznetsov, J. Tallaksen, M. Reese, and P. Daoutidis, "A novel system for ammonia-based sustainable energy and agriculture: Concept and design optimization," *Chemical Engineering and Processing-Process Intensification*, vol. 140, pp. 11–21, 2019.

[201] C. D. Demirhan, W. W. Tso, J. B. Powell, and E. N. Pistikopoulos, "Sustainable ammonia production through process synthesis and global optimization," *AIChE Journal*, vol. 65, no. 7, 2019.

[202] I. Dybkjaer, "Design of ammonia and methanol synthesis reactors," *Chemical Reactor Design and Technology*, pp. 795–819, 1986.

[203] J. Li, S. E. Demirel, and M. M. F. Hasan, "Process synthesis using block superstructure with automated flowsheet generation and optimization," *AIChE Journal*, vol. 64, no. 8, pp. 3082–3100, 2018.

[204] D. Dyson and J. Simon, "Kinetic expression with diffusion correction for ammonia synthesis on industrial catalyst," *Industrial & Engineering Chemistry Fundamentals*, vol. 7, no. 4, pp. 605–610, 1968.

[205] G. Graaf, H. Scholtens, E. Stamhuis, and A. Beenackers, "Intra-particle diffusion limitations in low-pressure methanol synthesis," *Chemical Engineering Science*, vol. 45, no. 4, pp. 773–783, 1990.

[206] D. P. Heiser, "Conversion of ammonia plants to methanol production," 1982.

[207] A. Soliman, "A new process for co-production of ammonia and methanol," *Prospects of Oil, Gas and Petrochemical Industries in the Arab Region: Opportunities and Challenges*, p. 1534, 2004.

[208] M. B. Lieberman, "The learning curve and pricing in the chemical processing industries," *The RAND Journal of Economics*, vol. 15, no. 2, pp. 213–228, 1984.

[209] A. D. Sagar and B. Van der Zwaan, "Technological innovation in the energy sector: R&d, deployment, and learning-by-doing," *Energy Policy*, vol. 34, no. 17, pp. 2601–2608, 2006.

[210] A. McDonald and L. Schrattenholzer, "Learning rates for energy technologies," *Energy Policy*, vol. 29, no. 4, pp. 255–261, 2001.

[211] J. M. Douglas, *Conceptual design of chemical processes*, vol. 1110. McGraw-Hill New York, 1988.

[212] K. Glinos and M. F. Malone, "Minimum reflux, product distribution, and lumping rules for multicomponent distillation," *Industrial & Engineering Chemistry Process Design and Development*, vol. 23, no. 4, pp. 764–768, 1984.

[213] M. L. McWilliams, "An equation to relate k-factors to pressure and temperature," *Chem. Eng*, vol. 80, no. 25, pp. 138–140, 1973.

[214] E. P. Schulz, M. S. Diaz, and J. A. Bandoni, "Supply chain optimization of large-scale continuous processes," *Computers & Chemical Engineering*, vol. 29, no. 6, pp. 1305–1316, 2005.

[215] M. S. Khan, Y. D. Chaniago, M. Getu, and M. Lee, "Energy saving opportunities in integrated ngl/lng schemes exploiting: Thermal-coupling common-utilities and process knowledge," *Chemical Engineering and Processing: Process Intensification*, vol. 82, pp. 54–64, 2014.

[216] D. Manley, "Thermodynamically efficient distillation: Ngl fractionation," *Latin American Applied Research*, vol. 28, no. 4, p. 212, 1998.

[217] N. V. D. Long, T. N. Pham, A. Bahadori, M. Lee, *et al.*, "Novel retrofit designs using a modified coordinate descent methodology for improving energy efficiency of natural gas liquid fractionation process," *Journal of Natural Gas Science and Engineering*, vol. 33, pp. 458–468, 2016.

[218] "Database of zeolite structures: http://www. iza-structure. org/databases," Last accessed on April 10, 2020.

[219] M. Xu and S. Deng, "Efficient screening of novel adsorbents for coalbed methane recovery," *Journal of Colloid and Interface Science*, 2020.

[220] D. Dubbeldam, S. Calero, D. E. Ellis, and R. Q. Snurr, "Raspa: molecular simulation software for adsorption and diffusion in flexible nanoporous materials," *Molecular Simulation*, vol. 42, no. 2, pp. 81–101, 2016.

[221] E. García-Pérez, J. Parra, C. Ania, A. García-Sánchez, J. Van Baten, R. Krishna, D. Dubbeldam, and S. Calero, "A computational study of CO_2, N_2, and CH_4 adsorption in zeolites," *Adsorption*, vol. 13, no. 5-6, pp. 469–476, 2007.

[222] A. Khajavirad and N. V. Sahinidis, "A hybrid LP/NLP paradigm for global optimization relaxations," *Mathematical Programming Computation*, vol. 10, no. 3, pp. 383–421, 2018.

[223] K. Hornik, M. Stinchcombe, and H. White, "Multilayer feedforward networks are universal approximators.," *Neural Networks*, vol. 2, no. 5, pp. 359–366, 1989.

[224] I. Fahmi and S. Cremaschi, "Process synthesis of biodiesel production plant using artificial neural networks as the surrogate models," *Computers & Chemical Engineering*, vol. 46, pp. 105–123, 2012.

[225] J. H. Lee, J. Shin, and M. J. Realff, "Machine learning: Overview of the recent progresses and implications for the process systems engineering field," *Computers & Chemical Engineering*, vol. 114, pp. 111–121, 2018.

[226] A. M. Schweidtmann, W. R. Huster, J. T. Lüthje, and A. Mitsos, "Deterministic global process optimization: Accurate (single-species) properties via artificial neural networks," *Computers & Chemical Engineering*, vol. 121, pp. 67–74, 2019.

[227] A. Gulli and S. Pal, *Deep learning with Keras*. Packt Publishing Ltd, 2017.

[228] D. P. Kingma and J. Ba, "Adam: A method for stochastic optimization," *arXiv preprint arXiv:1412.6980*, 2014.

[229] Z. Zhang, S. Xian, Q. Xia, H. Wang, Z. Li, and J. Li, "Enhancement of CO_2 adsorption and CO_2/N_2 selectivity on ZIF-8 via postsynthetic modification," *AIChE Journal*, vol. 59, no. 6, pp. 2195–2206, 2013.

[230] L. Zhen-shan, C. Ning-sheng, and E. Croiset, "Process analysis of CO_2 capture from flue gas using carbonation/calcination cycles," *AIChE Journal*, vol. 54, no. 7, pp. 1912–1925, 2008.

[231] X. Shao, Z. Feng, R. Xue, C. Ma, W. Wang, X. Peng, and D. Cao, "Adsorption of CO_2, CH_4, CO_2/N_2 and CO_2/CH_4 in novel activated carbon beads: Preparation, measurements and simulation," *AIChE Journal*, vol. 57, no. 11, pp. 3042–3051, 2011.

[232] S. Choi, J. H. Drese, and C. W. Jones, "Adsorbent materials for carbon dioxide capture from large anthropogenic point sources," *ChemSusChem: Chemistry & Sustainability Energy & Materials*, vol. 2, no. 9, pp. 796–854, 2009.

[233] M. F. Hasan, E. L. First, F. Boukouvala, and C. A. Floudas, "A multi-scale framework for CO_2 capture, utilization, and sequestration: CCUS and CCU," *Computers & Chemical Engineering*, vol. 81, pp. 2–21, 2015.

[234] L.-C. Lin, A. H. Berger, R. L. Martin, J. Kim, J. A. Swisher, K. Jariwala, C. H. Rycroft, A. S. Bhown, M. W. Deem, and M. Haranczyk, "In silico screening of carbon-capture materials," *Nature Materials*, vol. 11, no. 7, pp. 633–641, 2012.

[235] J. R. Bartels, "A feasibility study of implementing an ammonia economy," 2008.

[236] W. Davey and T. Wurzel, "Coproduction of methanol and ammonia from natural gas," Apr. 21 2009. US Patent 7,521,483.

[237] N. Yoshida and K. Hirotani, "Method of coproducing methanol and ammonia," Aug. 21 2012. US Patent 8,247,463.

[238] W. W. Tso, C. D. Demirhan, J. B. Powell, and E. N. Pistikopoulos, "Toward optimal synthesis of renewable ammonia and methanol processes (ramp)," in *Computer Aided Chemical Engineering*, vol. 44, pp. 1705–1710, Elsevier, 2018.

[239] W. W. Tso, C. D. Demirhan, C. A. Floudas, and E. N. Pistikopoulos, "Multi-scale energy systems engineering for optimal natural gas utilization," *Catalysis Today*, 2019.

[240] C. D. Demirhan, W. W. Tso, J. B. Powell, C. F. Heuberger, and E. N. Pistikopoulos, "A multi-scale energy systems engineering approach for renewable power generation and storage optimization," *Industrial & Engineering Chemistry Research*, 2020.

[241] A. Araújo and S. Skogestad, "Control structure design for the ammonia synthesis process," *Computers & Chemical Engineering*, vol. 32, no. 12, pp. 2920–2932, 2008.

[242] H. Kordabadi and A. Jahanmiri, "A pseudo-dynamic optimization of a dual-stage methanol synthesis reactor in the face of catalyst deactivation," *Chemical Engineering and Processing: Process Intensification*, vol. 46, no. 12, pp. 1299–1309, 2007.

[243] A. Dashti, K. Khorsand, M. A. Marvast, and M. Kakavand, "Modeling and simulation of ammonia synthesis reactor," *Petrol. Coal*, vol. 48, no. 2, pp. 15–23, 2006.

[244] A. Jinasena, B. Lie, and B. Glemmestad, "Dynamic model of an ammonia synthesis reactor based on open information," 2016.

[245] A. Cozad, N. V. Sahinidis, and D. C. Miller, "Learning surrogate models for simulation-based optimization," *AIChE Journal*, vol. 60, no. 6, pp. 2211–2227, 2014.

[246] Z. T. Wilson and N. V. Sahinidis, "The ALAMO approach to machine learning," *Computers & Chemical Engineering*, vol. 106, pp. 785–795, 2017.

[247] "Technical brief, ALAMO," *http://archimedes.cheme.cmu.edu/?q=alamoTechnicalBrief*.

[248] Y. Cui, X. Shi, C. Guang, Z. Zhang, C. Wang, and C. Wang, "Comparison of pressure-swing distillation and heterogeneous azeotropic distillation for recovering benzene and isopropanol from wastewater," *Process Safety and Environmental Protection*, vol. 122, pp. 1–12, 2019.

APPENDIX A

ADSORPTION MODEL AND ISOTHERM EXPRESSIONS

Linear Driving Force model for CO_2 adsorption on HTC

$$\frac{\partial \overline{q}_{\mathrm{CO_2}}}{\partial t} = k_{\mathrm{CO_2}} \left(q^*_{\mathrm{CO_2}} - \overline{q}_{\mathrm{CO_2}} \right) \tag{A.1}$$

$$k_{\mathrm{CO_2}} = \frac{15}{r_p^2} \frac{\varepsilon_p D_p}{\varepsilon_p + \rho_p RT \left(\dfrac{\partial q^*_{\mathrm{CO_2}}}{\partial P_{\mathrm{CO_2}}} \right)} \tag{A.2}$$

$$q^*_{\mathrm{CO_2}} = \frac{m_{\mathrm{CO_2}} b_{\mathrm{CO_2}} P_{\mathrm{CO_2}}}{1 + b_{\mathrm{CO_2}} P_{\mathrm{CO_2}}} \tag{A.3}$$

$$b_{\mathrm{CO_2}} = b_{o,\mathrm{CO_2}}\, exp\left[-\frac{\Delta U_{\mathrm{CO_2}}}{R} \left(\frac{1}{T} - \frac{1}{673} \right) \right] \tag{A.4}$$

Dual-site Langmuir model for CO_2 & N_2 adsorption on zeolite 13X-APG

$$q_i^* = \frac{m_{i,1} b_{i,1} P_i}{1 + b_{i,1} P_i} + \frac{m_{i,2} b_{i,2} P_i}{1 + b_{i,2} P_i} \tag{A.5}$$

$$b_{i,1} = b_{o,i,1}\ \exp\left[-\frac{\Delta U_{i,1}}{RT} \right] \tag{A.6}$$

$$b_{i,2} = b_{o,i,2}\ \exp\left[-\frac{\Delta U_{i,2}}{RT} \right] \tag{A.7}$$

APPENDIX B

BOUNDARY CONDITIONS

Pressurization from right end ($Z = 0$ closed, $Z = 1$ open)

$$\overline{v}_{0.5} = \overline{v}|_{Z=0} \ = 0 \tag{B.1}$$

$$\overline{P}_{0.5} = \overline{P}|_{Z=0} \ = \overline{P}_1 \tag{B.2}$$

$$\overline{T}_{0.5} = \overline{T}|_{Z=0} \ = \overline{T}_1 \tag{B.3}$$

$$y_{i,0.5} = y_i|_{Z=0} \ = y_{i,1} \tag{B.4}$$

$$\overline{T}_{w,0.5} = \overline{T_w}|_{z=0} \ = \overline{T}_a \tag{B.5}$$

$$\overline{v}_{N+0.5} = \overline{v}|_{Z=1} \ = -\frac{2}{\Delta Z}\left[\frac{4}{150}\left(\frac{\varepsilon_b}{1-\varepsilon_b}\right)^2\right]\frac{r_p^2 P_0}{\mu v_0 L}(\overline{P}_{N+0.5} - \overline{P}_N) \tag{B.6}$$

$$\overline{P}_{N+0.5} = \overline{P}|_{Z=1} \ = \frac{P\,(t)}{P_0} = \frac{1}{P_0}\left[P_L + \left(\frac{P_H - P_L}{t_{pres}}\right)t\right] \tag{B.7}$$

$$\overline{T}_{N+0.5} = \overline{T}|_{Z=1} \ = \frac{\overline{T}_N - \overline{v}|_{Z=1} Pe_h \overline{T_f}\left(\dfrac{\Delta Z}{2}\right)}{1 - \overline{v}|_{Z=1} Pe_h \left(\dfrac{\Delta Z}{2}\right)} \tag{B.8}$$

$$y_{i,N+0.5} = y_i|_{Z=1} \ = \frac{y_{i,N} - \overline{v}|_{Z=1} y_{fi} Pe\left(\dfrac{\Delta Z}{2}\right)}{1 - \overline{v}|_{Z=1} Pe\left(\dfrac{\Delta Z}{2}\right)} \tag{B.9}$$

$$\overline{T}_{w,N+0.5} = \overline{T_w}|_{z=1} \ = \overline{T}_a \tag{B.10}$$

Adsorption-reaction step ($Z = 0$ open, $Z = 1$ open)

$$\overline{v}_{0.5} = \overline{v}|_{z=0} \ = \frac{v_f}{v_0} \tag{B.11}$$

$$\overline{P}_{0.5} = \overline{P}|_{Z=0} = \overline{P}_1 + \frac{\overline{v}|_{z=0}\left(\frac{\Delta Z}{2}\right)}{\left[\frac{4}{150}\left(\frac{\varepsilon_b}{1-\varepsilon_b}\right)^2\right]\frac{r_p^2 P_0}{\mu v_0 L}} \tag{B.12}$$

$$\overline{T}_{0.5} = \overline{T}|_{z=0} = \frac{\overline{T}_1 + \overline{v}|_{Z=0} Pe_h \overline{T_f}\left(\frac{\Delta Z}{2}\right)}{1 + \overline{v}|_{Z=0} Pe_h \left(\frac{\Delta Z}{2}\right)} \tag{B.13}$$

$$y_{i,0.5} = y_i|_{z=0} = \frac{y_{i,1} + \overline{v}|_{z=0} y_{fi} Pe\left(\frac{\Delta Z}{2}\right)}{1 + \overline{v}|_{z=0} Pe\left(\frac{\Delta Z}{2}\right)} \tag{B.14}$$

$$\overline{T}_{w,0.5} = \overline{T_w}|_{z=0} = \overline{T}_a \tag{B.15}$$

$$\overline{P}_{N+0.5} = \overline{P}|_{Z=1} = \frac{P_H}{P_0} \tag{B.16}$$

$$\overline{v}_{N+0.5} = \overline{v}|_{Z=1} = -\frac{2}{\Delta Z}\left[\frac{4}{150}\left(\frac{\varepsilon_b}{1-\varepsilon_b}\right)^2\right]\frac{r_p^2 P_0}{\mu v_0 L}(\overline{P}_{N+0.5} - \overline{P}_N) \tag{B.17}$$

$$\overline{T}_{N+0.5} = \overline{T}|_{Z=1} = \overline{T}_N \tag{B.18}$$

$$y_{i,N+0.5} = y_i|_{z=L} = y_{i,N} \tag{B.19}$$

$$\overline{T}_{w\ N+0.5} = \overline{T_w}|_{z=1} = \overline{T}_a \tag{B.20}$$

Depressurization from right end ($Z = 0$ closed, $Z = 1$ open)

$$\overline{v}_{0.5} = \overline{v}|_{z=0} = 0 \tag{B.21}$$

$$\overline{P}_{0.5} = \overline{P}|_{z=0} = \overline{P}_1 \tag{B.22}$$

$$\overline{T}_{0.5} = \overline{T}|_{z=0} = \overline{T}_1 \tag{B.23}$$

$$y_{i,0.5} = y_i|_{z=0} = y_{i,1} \tag{B.24}$$

$$\overline{T}_{w,0.5} = \overline{T_w}|_{z=0} = \overline{T}_a \tag{B.25}$$

$$\overline{P}_{N+0.5} = \overline{P}|_{Z=1} = \frac{P(t)}{P_0} = \frac{1}{P_0}\left[P_H - \left(\frac{P_H - P_L}{t_{depres}}\right)t\right] \tag{B.26}$$

$$\overline{v}_{N+0.5} = \overline{v}|_{Z=1} = -\frac{2}{\Delta Z}\left[\frac{4}{150}\left(\frac{\varepsilon_b}{1-\varepsilon_b}\right)^2\right]\frac{r_p^2 P_0}{\mu v_0 L}(\overline{P}_{N+0.5} - \overline{P}_N) \tag{B.27}$$

$$\overline{T}_{N+0.5} = \overline{T}|_{Z=1} = \overline{T}_N \tag{B.28}$$

$$y_{i,N+0.5} = y_i|_{z=L} = y_{i,N} \tag{B.29}$$

$$\overline{T}_{w,N+0.5} = \overline{T_w}|_{z=1} = \overline{T}_a \tag{B.30}$$

APPENDIX C

REACTION RATE EXPRESSIONS

Steam Methane Reforming [128]

$$-R_{I,j} = \frac{1}{(DEN_j)^2} \frac{k_{1,j}}{\left(y_{\mathrm{H_2O},j}\overline{P}_j P_0\right)^{2.5}} \left(\frac{y_{\mathrm{H_2},j}^3 \, y_{\mathrm{CO},j} \, \overline{P}_j^4 P_0^4}{K_{I,j}} - y_{\mathrm{CH_4},j} \, y_{\mathrm{H_2O},j} \, \overline{P}_j^2 P_0^2 \right) \tag{C.1}$$

$$-R_{II,j} = \frac{1}{(DEN_j)^2} \frac{k_{2,j}}{\left(y_{\mathrm{H_2O},j}\overline{P}_j P_0\right)^{3.5}} \left(\frac{y_{\mathrm{H_2},j}^4 \, y_{\mathrm{CO_2},j} \, \overline{P}_j^5 P_0^5}{K_{II,j}} - y_{\mathrm{CH_4},j} \, y_{\mathrm{H_2O},j}^2 \, \overline{P}_j^3 P_0^3 \right) \tag{C.2}$$

$$-R_{III,j} = \frac{1}{(DEN_j)^2} \frac{k_{3,j}}{\left(y_{\mathrm{H_2},j}\overline{P}_j P_0\right)} \left(\frac{y_{\mathrm{H_2},j} \, y_{\mathrm{CO_2},j} \, \overline{P}_j^2 P_0^2}{K_{III,j}} - y_{\mathrm{CO},j} \, y_{\mathrm{H_2O},j} \, \overline{P}_j^2 P_0^2 \right) \tag{C.3}$$

$$DEN_j = 1 + (K_{\mathrm{CO},j} \, y_{\mathrm{CO},j} + K_{\mathrm{H_2},j} \, y_{\mathrm{H_2},j} + K_{\mathrm{CH_4},j} \, y_{\mathrm{CH_4},j})\overline{P}_j P_0 + \frac{K_{\mathrm{H_2O},j} \, y_{\mathrm{H_2O},j}}{y_{\mathrm{H_2},j}} \tag{C.4}$$

$$K_{I,j} = \frac{1}{\exp(0.2513Z_j^4 - 0.3665Z_j^3 - 0.58101Z_j^2 + 27.1337Z_j - 3.2770)} \ \mathrm{atm}^2 \tag{C.5}$$

$$K_{III,j} = \exp\left(-0.29353Z_j^3 + 0.63508Z_j^2 + 4.17782Z_j + 0.31688\right) \tag{C.6}$$

$$K_{II,j} = K_{I,j} \times K_{III,j} \tag{C.7}$$

$$k_{1,j} = 1.842 \times 10^{-4} \exp\left[-\frac{240,100}{R}\left(\frac{1}{\overline{T}_j T_0} - \frac{1}{648}\right)\right] \ \frac{\mathrm{kmol.bar}^{0.5}}{\mathrm{kg_{cat}.hr}} \tag{C.8}$$

$$Z_j = \frac{1000}{\overline{T}_j T_0} - 1 \tag{C.9}$$

$$k_{2,j} = 2.193 \times 10^{-5} \exp\left[-\frac{243,900}{R}\left(\frac{1}{\overline{T}_j T_0} - \frac{1}{648}\right)\right] \ \frac{\mathrm{kmol.bar}^{0.5}}{\mathrm{kg_{cat}.hr}} \tag{C.10}$$

$$k_{3,j} = 7.558 \exp\left[-\frac{67,130}{R}\left(\frac{1}{\overline{T}_j T_0} - \frac{1}{648}\right)\right] \ \frac{\mathrm{kmol}}{\mathrm{kg_{cat}.hr.bar}} \tag{C.11}$$

$$K_{\mathrm{CO},j} = 40.91 \exp\left[\frac{70,650}{R}\left(\frac{1}{\overline{T}_j T_0} - \frac{1}{648}\right)\right] \ \mathrm{bar}^{-1} \tag{C.12}$$

$$K_{\mathrm{H_2},j} = 0.0296 \exp\left[\frac{82,900}{R}\left(\frac{1}{\overline{T}_j T_0} - \frac{1}{648}\right)\right] \text{ bar}^{-1} \tag{C.13}$$

$$K_{\mathrm{CH_4},j} = 0.179 \exp\left[\frac{38,280}{R}\left(\frac{1}{\overline{T}_j T_0} - \frac{1}{823}\right)\right] \text{ bar}^{-1} \tag{C.14}$$

$$K_{\mathrm{H_2O},j} = 0.4152 \exp\left[-\frac{88,680}{R}\left(\frac{1}{\overline{T}_j T_0} - \frac{1}{823}\right)\right] \tag{C.15}$$

Water Gas Shift Reaction [131, 132]

$$R_{WGS,j} = k_0 \exp\left[\frac{-E_{WGS}}{R\overline{T}_j T_0}\right]\left(y_{\mathrm{CO}} y_{\mathrm{H_2O}} \overline{P}_j^2 P_0^2 - \frac{y_{\mathrm{CO_2}} y_{\mathrm{H_2}} \overline{P}_j^2 P_0^2}{K_{WGS,j}}\right) \times \frac{1}{101325^2} \frac{\text{mol}}{\text{gcat.hr}} \tag{C.16}$$

$$K_{WGS,j} = \exp\left[\frac{4577.8}{\overline{T}_j T_0} - 4.33\right] \tag{C.17}$$

where, k_0 = 2.96×10^5 mol/(gcat.hr.atm^2) and E_{WGS} = 47400 J/mol.

APPENDIX D

SIMULATION PARAMETERS

Table D.1: Parameters used for SE-SMR simulation [43, 146].

Parameter	Value
Reactor length, L	0.223 m
Reactor diameter, d_{in}	0.126 m
Bed porosity, ε_b	0.48
Particle porosity, ε_p	0.24
Total porosity, ε_t	0.64
Adsorbent pellet density, ρ_p	1300 kg/m^3
Gas phase density, ρ_g	74.147 mol/m^3
Gas phase viscosity, μ	2.87×10^{-5} Pa.s
Bed-wall heat transfer coefficient, h_{in}	71 W/(m^2.K)
Gas heat capacity, C_{pg}	42 J/(mol.K)
Solid heat capacity, C_{ps}	850 J/(kg.K)
Particle radius, r_p	2.5 $\times 10^{-4}$ m
Axial gas heat conductivity, K_z	0.29 J/(m.s.K)
Axial dispersion coefficient, D_L	1.6×10^{-5} m^2/s
$C_{p,a}$	42 J/(mol.K)
D_p	3.3×10^{-7} m^2/s
Scaling parameters	
T_0	723 K
P_0	445.7 kPa
v_0	0.2885 m/s
$q_{s,0}$	0.65 mol/kg
HTC sorbent isotherm parameters	
$m_{\mathrm{CO_2}}$	0.65 mol/kg
$b_{\mathrm{o,\,CO_2}}$	0.000236 Pa^{-1}
$\Delta U_{\mathrm{CO_2}}$	-17000 J/mol

Table D.2: Parameters used for SE-WGSR simulation [13].

Parameter	Value
Reactor diameter, d_{in}	0.0173 m
Reactor length, L	0.502 m
Bed porosity, ε_b	0.28
HTC sorbent isotherm parameters	
$m_{\mathrm{CO_2}}$	0.3033 mol/kg
$b_{\mathrm{o,\,CO_2}}$	0.000236 Pa^{-1}
$\Delta U_{\mathrm{CO_2}}$	-31475.6 J/mol

APPENDIX E

STATE VARIABLES' TRAJECTORIES AT CYCLIC STEADY STATE FOR INTENSIFIED METHANOL REACTOR

Here, the dynamic profiles of state variables inside the reactor are presented for the optimal SE-MeOH processes. In the following plots, the temperature is calculated at spatial distances relative to the inlet boundary. During a representative cycle, the inlet boundaries can change depending on the active operation mode. The exact spatial coordinate inside the reactor bed, at which temperature is obtained, would therefore be updated if there is a change in flow direction. This results in sudden temperature change in the following plots when the flow direction changes between two consecutive operation modes.

Typically, in the temperature plots, it was observed that the bed temperature during the first step of a process cycle (i.e., the process step during which CH_3OH is produced) has higher temperature due to exothermicity of methanol reaction and water adsorption. Furthermore, during the first step, the part of the reactor bed closer to the inlet boundary heats faster than the rest of the bed. This is again due to enhanced methanol reaction and water adsorption in the bed. The high overall heat transfer coefficient (284 W m^{-2} K^{-1}) ensures that the bed temperature does not increase to levels where catalyst deactivation may occur (Luyben et al., 2010). During regeneration, the bed temperature decreases due to a combination of bed purging and water desorption.

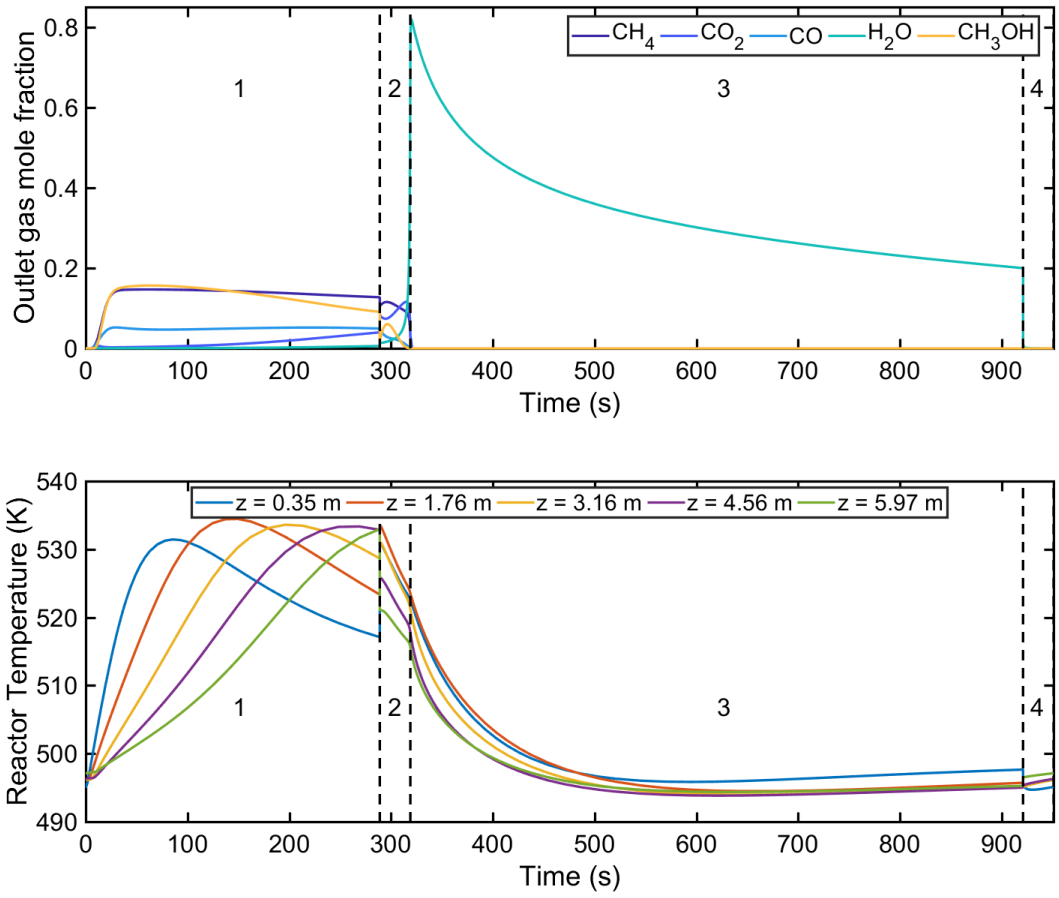

Figure E.1: Dynamic profiles of outlet gas mole fraction and reactor temperature at different bed length relative to the inlet boundary for case a.

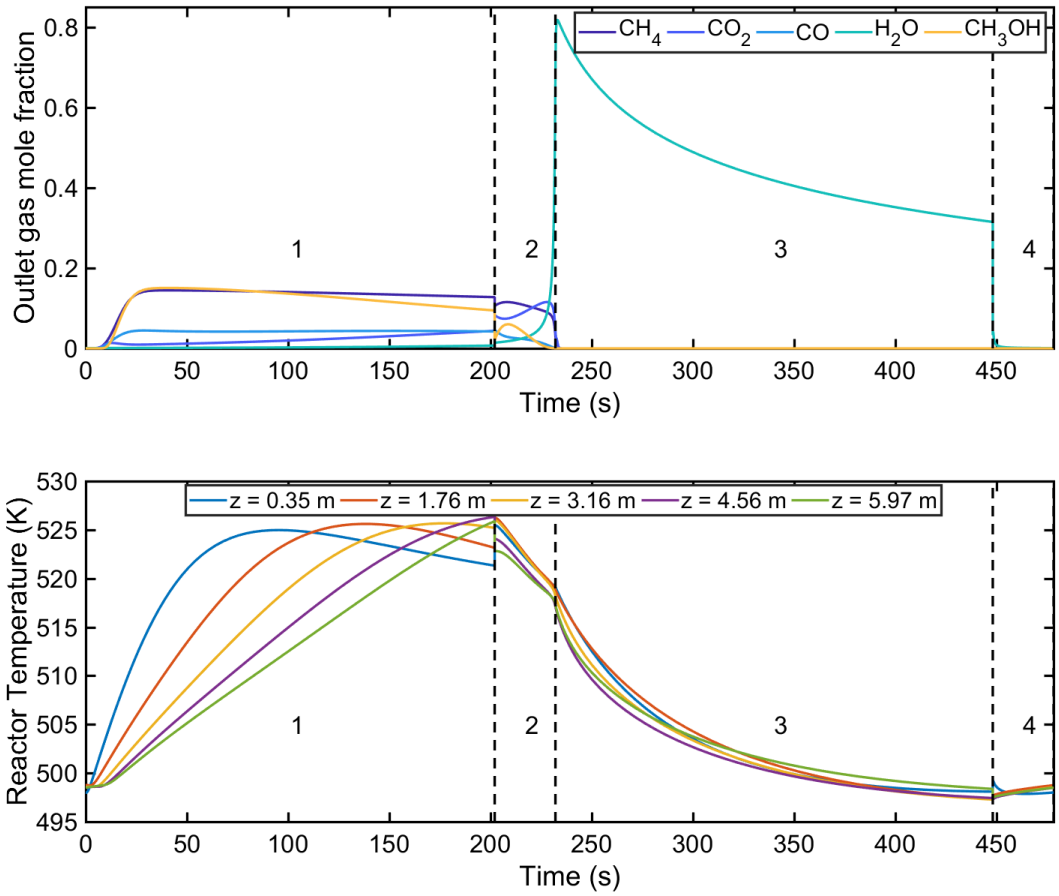

Figure E.2: Dynamic profiles of outlet gas mole fraction and reactor temperature at different bed length relative to the inlet boundary for case b.

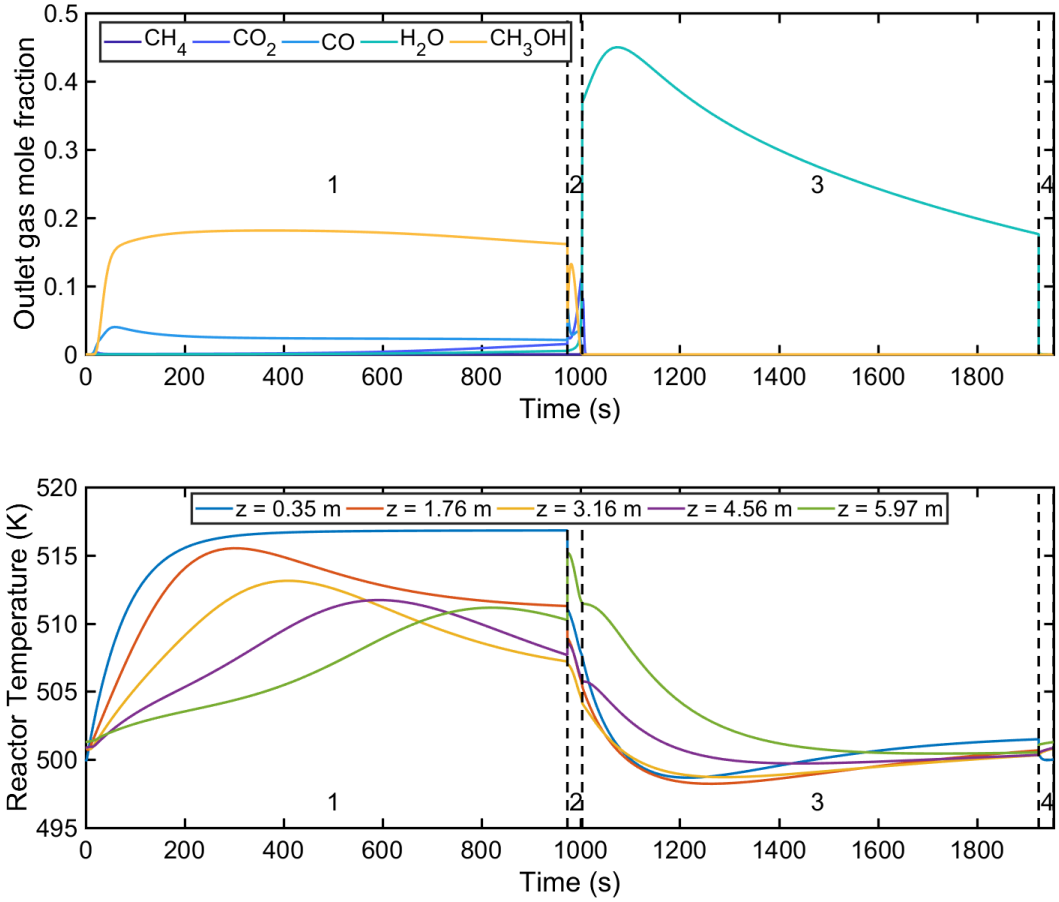

Figure E.3: Dynamic profiles of outlet gas mole fraction and reactor temperature at different bed length relative to the inlet boundary for case d.

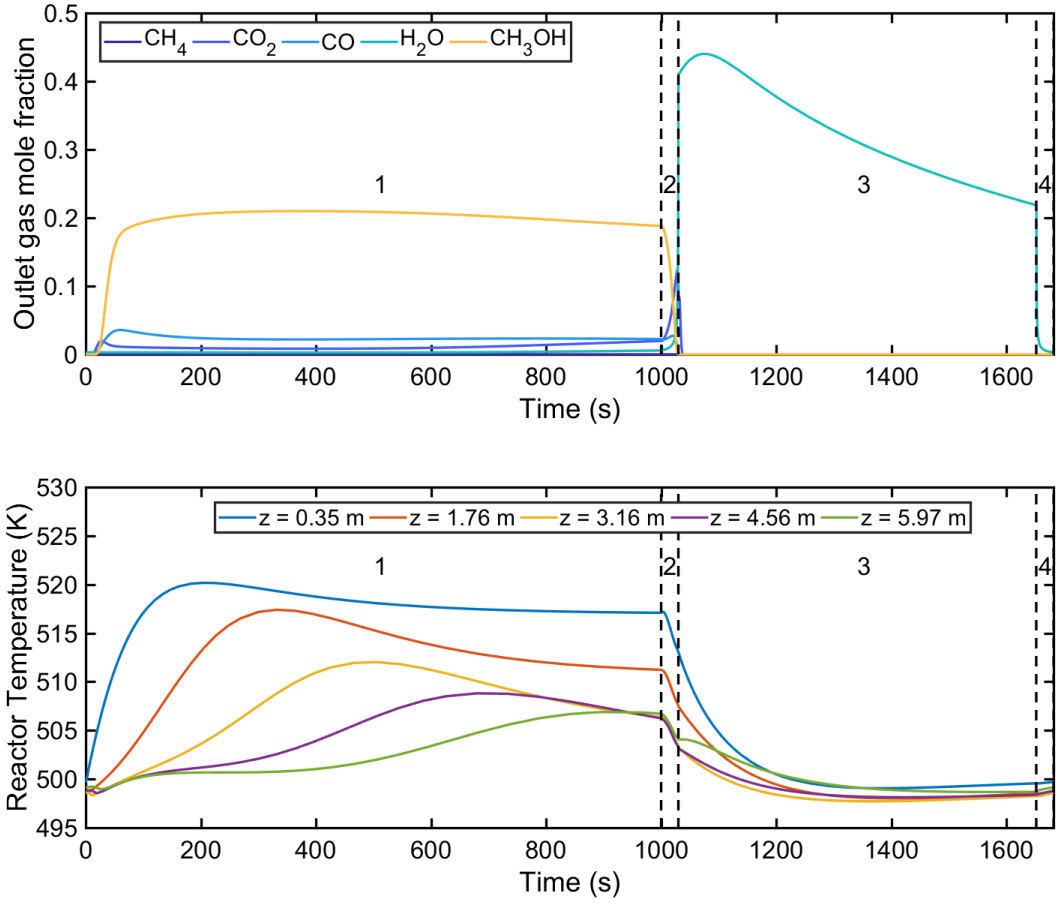

Figure E.4: Dynamic profiles of outlet gas mole fraction and reactor temperature at different bed length relative to the inlet boundary for case e.

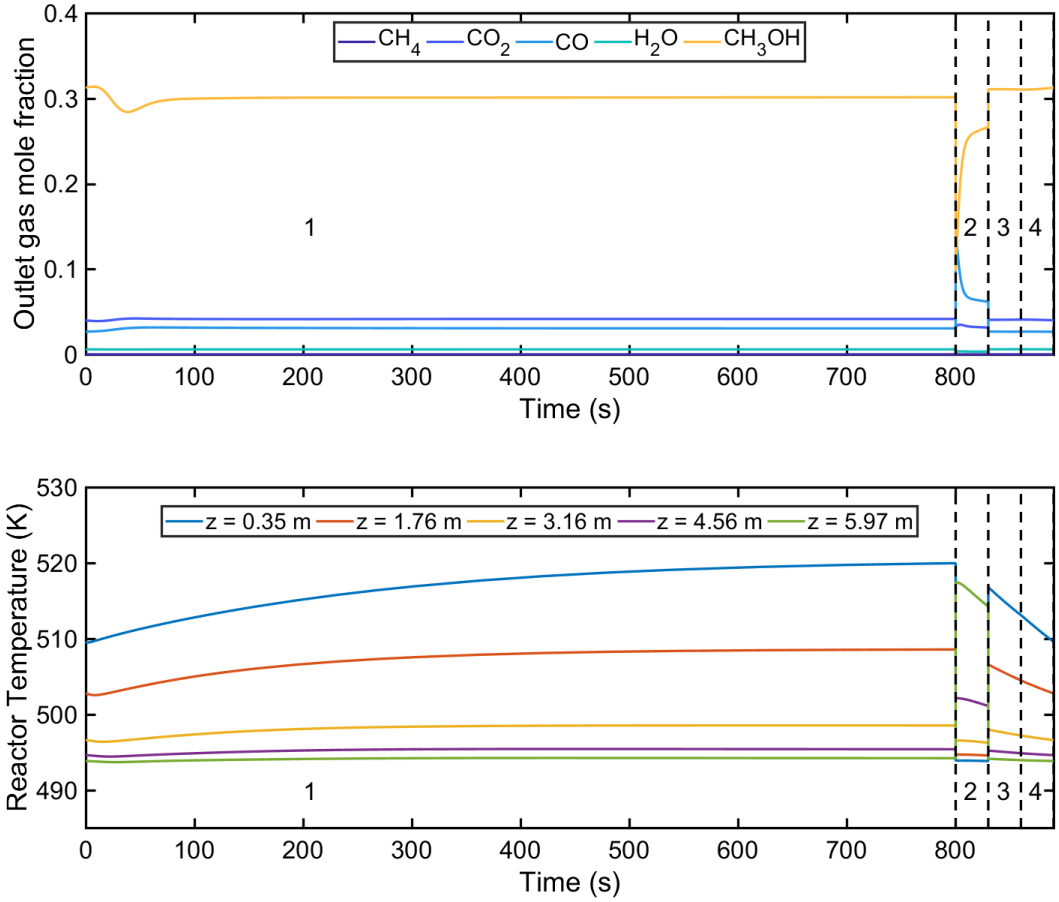

Figure E.5: Dynamic profiles of outlet gas mole fraction and reactor temperature at different bed length relative to the inlet boundary for case f.

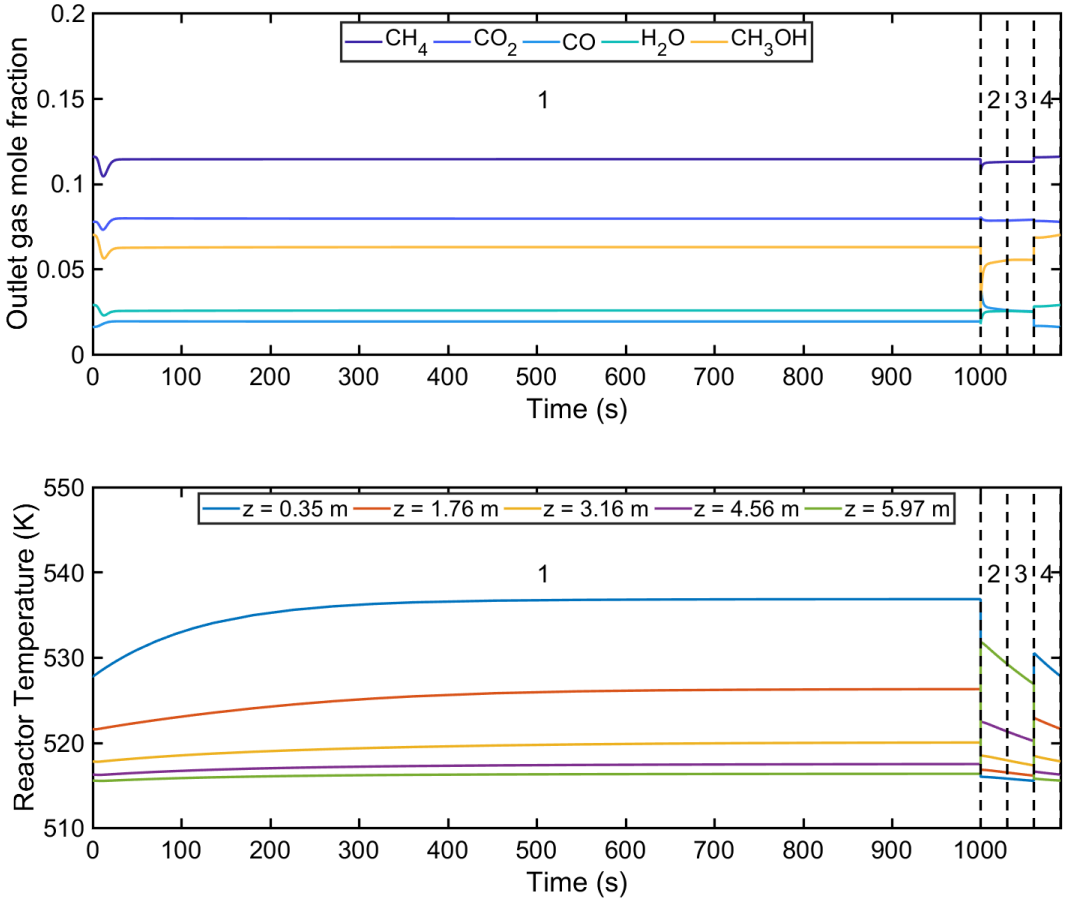

Figure E.6: Dynamic profiles of outlet gas mole fraction and reactor temperature at different bed length relative to the inlet boundary for case g.

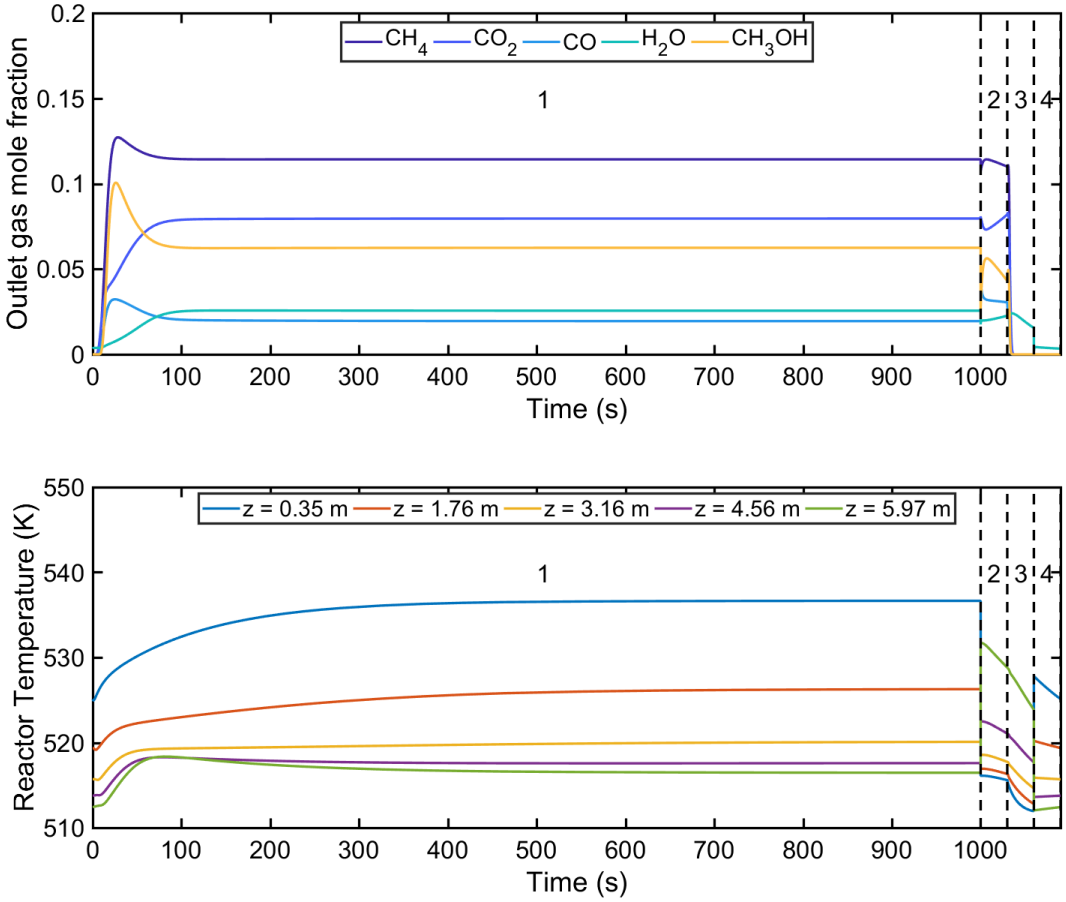

Figure E.7: Dynamic profiles of outlet gas mole fraction and reactor temperature at different bed length relative to the inlet boundary for case h.

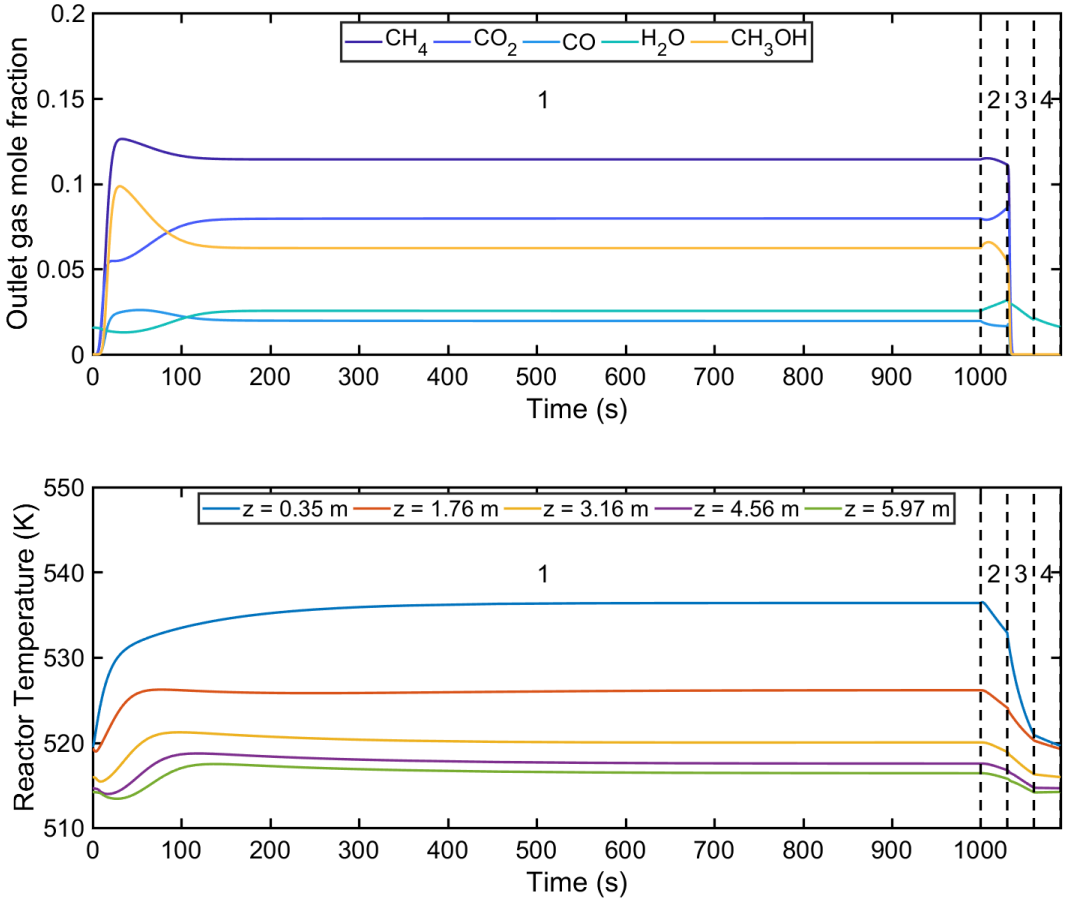

Figure E.8: Dynamic profiles of outlet gas mole fraction and reactor temperature at different bed length relative to the inlet boundary for case i.

APPENDIX F

INTENSIFIED METHANOL REACTOR DESIGN WITH VARYING NUMBER OF TUBES

The optimization studies were performed with total number of parallel tubes, in the Lurgi reactor, as a decision variable. The lower and upper bounds on the number of tubes were chosen as 2000 and 4000, respectively. The objective was to minimize the syngas-to-methanol production costs.

Table F.1: Optimization results obtained by minimizing CH_3OH production cost with fixed synthesis gas feed specifications and varying number of tubes.

Parameter	Unit	Productivity, $PC^{min}_{\mathrm{CH_3OH}}$	
		(300 tons per day)	(350 tons per day)
CH_3OH production cost	\$ per ton CH_3OH	**87.9**	**87.9**
number of tubes	-	4000	4000
CH_3OH production capacity	tons per day	371.36	371.33
CH_3OH yield	%	37.23	37.23
CO conversion	%	60.01	59.97
CO_2 conversion	%	27.66	27.68
cycle configuration	-	(i) sorption-reaction (ii) reverse purge (iii) reverse purge (iv) purge	(i) sorption-reaction (ii) reverse purge (iii) reverse purge (iv) purge
$y_{\mathrm{CO_2},fs_1}$	-	0.094	0.094
y_{CO,fs_1}	-	0.046	0.046
P_1	bar	76.98	76.98
P_2	bar	76.98	76.98
P_3	bar	76.98	76.98
t_1	s	1000	1000
t_2	s	30	30
t_3	s	30	30
t_4	s	30	30
$\dot{n}_{fs_1}$	mol s^{-1}	0.64	0.64
T_c	K	513.73	513.75
α_c	-	0.0756	0.077

APPENDIX G

METHANOL-AMMONIA CASE STUDY

Methanol production flowsheet

Figure G.1 shows the simplified process flowsheet for producing methanol from synthesis gas. The fresh inlet synthesis gas is assumed to consist of 65.9% hydrogen, 10.26% methane, 9.4% carbon dioxide, 9.3% nitrogen, 4.6% carbon monoxide, 0.5% methanol and 0.04% water. This proportion of gas species, in the synthesis gas feed, correspond to the feed composition typical in an industrial methanol plant [168]. Furthermore, the synthesis gas feed enters the process at 25 bar and 290 K. For increasing the pressure of incoming synthesis gas, a reciprocating compressor is used. The compressor compresses synthesis gas from 25 bar to 110 bar, which is the operating pressure of downstream methanol reactor.

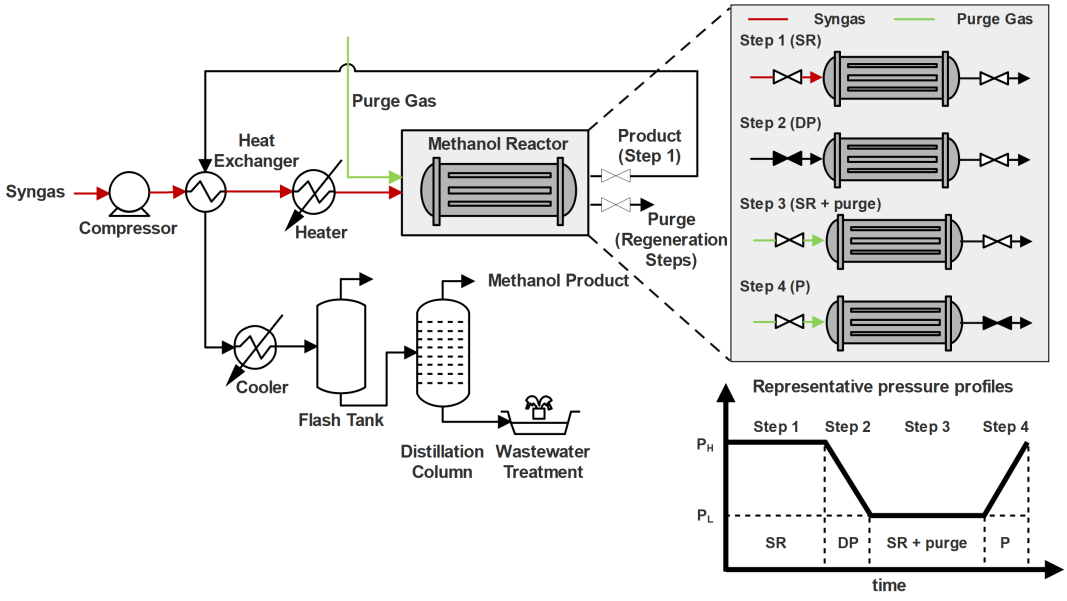

Figure G.1: Methanol process flowsheet for synthesizing methanol from syngas.

The methanol reactor operating temperature is taken as 550 K. To raise the inlet synthesis

gas feed temperature to the reactor temperature, enough heat is transferred from the heater unit. The outlet product stream from the reactor consists of methanol product, unconverted reactants, water and inert gas species. The reactor outlet stream is cooled to 311 K with the use of a cooler unit [169]. The cooled stream is then sent to the flash tank and distillation column for purifying product methanol.

The number of parallel tubes in the reactor is 2962 [168]. Furthermore, it is assumed that bed length varies linearly with the reactor feed rate design variable. As the base case, a design synthesis gas flow rate of 1834.41 ton per day is assumed to correspond to a bed length of 7.022 m [168]. The operating feed flow rate can, however, be different than the design flow rate for which the reactor length has been selected.

Ammonia production flowsheet

The simplified flowsheet considered for producing ammonia from hydrogen-nitrogen mixture has been adopted from Skogestad and coworkers [241], and is shown in Figure G.2. The molar composition of the feed is assumed to consist of 22.5% hydrogen, 67.5% nitrogen and 10% inert, and the inlet pressure and temperature are taken as 150 bar and 290 K, respectively. As the ammonia synthesis requires high pressure, the inlet feed is brought to the desired reactor pressure of 150 bar with the use of a compression train. Due to compressor work, the temperature of the feed increases. The rest of the heat is provided by a heater to raise feed temperature to 673 K, which is assumed to be the operating temperature of ammonia reactor. The hydrogen-nitrogen feed is then fed to the shell and tube-type reactor where it converts to form ammonia product. The downstream cooler cools the product stream to 313 K, which is the flash temperature for recovering ammonia from product stream [241].

Additional constraints

The following additional constraints have been included in the generalized model:

$$PC_1^{demand} \leq x_{1,7,4} \tag{G.1}$$

$$PC_2^{demand} \leq x_{2,7,7} \tag{G.2}$$

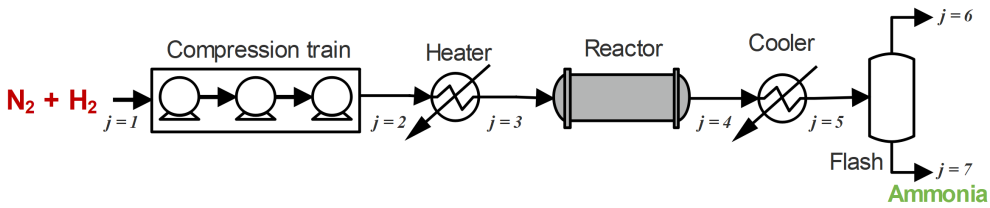

Figure G.2: Ammonia production flowsheet from hydrogen-nitrogen reactant feed.

Table G.1: Variables for the methanol-ammonia case study.

Variable	Unit	Significance
EP_p^{comp}	-	flexible compressor's performance efficiency in process p
EP_p^{c}	-	flexible cooler's performance efficiency in process p
EP_p^{h}	-	flexible heater's performance efficiency in process p
$\overline{F}_{in,p}$	-	normalized inlet feed flow rate in process p
$\overline{F}_{design,p}$	-	normalized reactor design flow rate in process p
F_p^{inlet}	ton per day	reactant feed flow rate in process p
$OC_{p,i}$	MM$ per yr	annualized operating cost for equipment i in process p
Q_p^{comp}	MW	compressor duty in process p
Q_p^{cool}	MW	cooling duty in process p
Q_p^{heat}	MW	heater duty in process p

$$x_{p,1,cs} = w_{cs,p} F_p^{inlet} \quad \forall p \in P, \forall cs \in CS \tag{G.3}$$

$$x_{p,1,9} = T_p^{inlet} \quad \forall p \in P \tag{G.4}$$

$$x_{p,1,10} = P_p^{inlet} \quad \forall p \in P \tag{G.5}$$

$$x_{p,2,cs} = x_{p,1,cs} \quad \forall p \in P, \forall cs \in CS \tag{G.6}$$

$$x_{p,2,9} = T_p^{inlet} + \frac{T_p^{inlet}}{\eta^{comp}} \left[\left(\frac{P_p^{reac}}{P_p^{inlet}} \right)^{\frac{\gamma-1}{\gamma}} - 1 \right] \quad \forall p \in P \tag{G.7}$$

$$x_{p,2,10} = P_p^{reac} \quad \forall p \in P \tag{G.8}$$

$$x_{p,3,cs} = x_{p,2,cs} \quad \forall p \in P, \forall cs \in CS \tag{G.9}$$

$$x_{p,3,9} = T_p^{reac} \quad \forall p \in P, \forall cs \in CS \tag{G.10}$$

$$x_{p,3,10} = x_{p,2,10} \quad \forall p \in P, \forall cs \in CS \tag{G.11}$$

$$\overline{F}_{in,p} = 1 + \left(\frac{2-1}{2500-10}\right)\left(F_p^{inlet} - 10\right) \quad \forall p \in P \tag{G.12}$$

$$\overline{F}_{design,p} = 1 + \left(\frac{2-1}{2374.6-500}\right)(d_{p,3} - 500) \quad \forall p \in P \tag{G.13}$$

$$x_{1,4,s} = x_{1,3,s} \quad \forall s \in \{6, 7, ..., 10\} \tag{G.14}$$

$$x_{2,4,s} = x_{2,3,s} \quad \forall s \in S \setminus \{2, 6, 7\} \tag{G.15}$$

$$x_{p,5,s} = x_{p,4,s} \quad \forall p \in P, \forall s \in S \setminus \{9\} \tag{G.16}$$

$$x_{p,5,9} = T_p^{flash} \quad \forall p \in P \tag{G.17}$$

$$x_{1,6,s} = x_{1,5,s} \quad \forall s \in \{4, 5, 9, 10\} \tag{G.18}$$

$$x_{2,7,s} = x_{2,5,s} \quad \forall s \in \{7, 9, 10\} \tag{G.19}$$

$$x_{1,7,s} = x_{1,6,s} \quad \forall s \in \{4, 9, 10\} \tag{G.20}$$

$$Q_p^{comp} = \frac{10^{-3}}{\eta^m \eta^{comp} EP_p^{comp}} \sum_{cs \in CS} \left(\frac{F_p^{inlet}}{86400 \times MW_{cs}}\right) RT_p^{inlet} \tag{G.21}$$

$$\times \left(\frac{\gamma}{\gamma - 1}\right) \left[\left(\frac{P_p^{reac}}{P_p^{inlet}}\right)^{\frac{\gamma-1}{\gamma}} - 1\right] \quad \forall p \in P$$

$$Q_p^{heat} = \frac{\sum_{cs \in CS} (x_{p,2,cs} Cp_{cs,p}) \times (x_{p,3,9} - x_{p,2,9})}{86400 \eta^h EP_p^h} \quad \forall p \in P \tag{G.22}$$

$$Q_p^{cool} = \frac{\sum_{cs \in CS} (x_{p,4,cs} Cp_{cs,p}) \times (x_{p,4,9} - x_{p,5,9})}{86400 \eta^c EP_p^c} \tag{G.23}$$

$$+ \frac{\sum_{cs \in CS} x_{p,4,cs} H_{cs}^{vap}}{86400 \eta^c EP_p^c} \quad \forall p \in P$$

$$OC_{p,1} = 70 \times 10^{-6} \times Q_p^{comp} T^{oper} \quad \forall p \in P \tag{G.24}$$

$$OC_{p,2} = 10^{-6} \times OC^{heat} Q_p^{heat} T^{oper} \quad \forall p \in P \tag{G.25}$$

$$OC_{p,4} = 10^{-6} \times \frac{3.6 \times 10^6 \times OC^{cold} Q_p^{cool} T^{oper}}{4.18 \times \Delta T^{cold}} \quad \forall p \in P \tag{G.26}$$

$$d_{p,5} \geq \frac{1000 \times \sum_{cs \in CS} x_{p,5,cs}}{24 \times 3600} \quad \forall p \in P \tag{G.27}$$

$$d_{1,6} = \frac{x_{1,6,4}}{24} \tag{G.28}$$

$$EP_p^{comp} \leq 1 - m_{p,1}(Q_p^{comp} - d_{p,1}) + (1 - z_{p,1}) \quad \forall p \in P \tag{G.29}$$

$$EP_p^{comp} \leq 1 + m'_{p,1}(Q_p^{comp} - d_{p,1}) + (1 - z_{p,1}) \quad \forall p \in P \tag{G.30}$$

$$EP_p^{h} \leq 1 - m_{p,2}(Q_p^{heat} - d_{p,2}) + (1 - z_{p,2}) \quad \forall p \in P \tag{G.31}$$

$$EP_p^{h} \leq 1 + m'_{p,2}(Q_p^{heat} - d_{p,2}) + (1 - z_{p,2}) \quad \forall p \in P \tag{G.32}$$

$$EP_p^{c} \leq 1 - m_{p,4}(Q_p^{cool} - d_{p,4}) + (1 - z_{p,4}) \quad \forall p \in P \tag{G.33}$$

$$EP_p^{c} \leq 1 + m'_{p,4}(Q_p^{cool} - d_{p,4}) + (1 - z_{p,4}) \quad \forall p \in P \tag{G.34}$$

The above equations, along with the input-output reactor relationships reported in Tables G.5 and G.6, constitute the extended model for methanol-ammonia case study. Eqs. G.1-G.2 denote the minimum production capacity constraints for methanol and ammonia processes, respectively.

Eqs. G.3- G.5 impose the inlet conditions of the feeds in each of the processes p to match the conditions of the inlet feeds available. The input-output relationships across the compressors for both involved processes are outlined in Eqs. G.6-G.8. The temperature of the feeds is appropriately raised to the desired levels using a heater, and the corresponding input-output relations are reported in Eqs. G.9-G.11. The input variables $\overline{F}_{in,p}$ and $\overline{F}_{design,p}$, which are used in reactor's surrogate models, are appropriately scaled using Eqs. G.12-G.13. The surrogate models are then used for predicting the reactor outlet flowrate of reactant and product species. For both processes, the rest of reactor outlet state variables, including inert species flowrate, temperature and pressure, are appropriately calculated using Eqs. G.14-G.15. Before product separation, the reactor outlet feed temperature is reduced to the desired flash temperature T_p^{flash}. The rest of the state variables for the cooler outlet are the same as of the inlet stream $j = 4$. These relations are imposed using Eqs.

G.16-G.17.

For the methanol process, the appropriate state variables for the flash bottom stream ($j = 6$) are computed using Eq. G.18. For methanol and ammonia processes, the appropriate state variables of the product streams are calculated through Eqs. G.19 and G.20, respectively. To obtain the required compressor, heating and cooling duties, Eqs G.21-G.23 are used. Eqs. G.24-G.26 calculate the operating cost incurred on the utilities. The additional design constraints for flash tank and distillation column are respectively reported in Eqs. G.27-G.28. Eq. G.27 further indicates that if the flash tank is commonly designed for both methanol and ammonia processes, the maximum required design variable among the two processes is selected as the common design. The set of constraints used for computing the operational performance of flexible equipment (i.e., compressor, heater and cooler) are outlined in Eqs. G.29-G.34.

Reactor simulation

Here, we report the steady-state, pseudo-homogeneous model which has been further used for simulating shell and heat exchanger-type methanol and ammonia synthesis reactors. The assumptions used for simplifying reactor modeling are listed below:

- There are no radial gradients of temperature, pressure and concentrations in the reactor [242].
- The ideal gas law is followed.
- The fluid on the shell side is not explicitly modeled, and it is assumed that it maintains the wall of the tubes at a constant temperature which is the same as of feed temperature.

In the formulated model, the component mass balance equation is as follows:

$$\frac{dF_c}{dZ} = A_c \rho_b \sum_{k \in K} \nu_{c,k}^{rxn} \eta_k R_k \quad \forall c \in C \tag{G.35}$$

where F_c is the flow rate of species c in moles per second per tube, and Z is the bed length coordinate. $A_c = \pi r_{in}^2$ denotes the inside tube cross section area in m^2, and ρ_b is the packing

Table G.2: Parameters used in the optimization model for ammonia-methanol case study.

Parameter	Unit	Significance	Value
$Cp_{cs,p}$	kJ kg^{-1} K^{-1}	heat capacity of species cs in process p	{1.12, 1.14; 14.64, 14.67; 1.18, 1.21; 6.41, 3.14; 6.19, 3.38; 1.11, 1.12; 3.13, 3.17; 3.24, 3.62}
H_{cs}^{vap}	kJ kg^{-1}	heat of vaporization for species cs	{0, 0, 0, 1200, 2256.42, 0, 1332.86, 0}
m	-	parameter dictating flexible equipment performance	66.67
MW^{cs}	kg mol^{-1}	molecular weight of chemical species cs	{0.028, 0.002, 0.044, 0.032, 0.018, 0.028, 0.017, 0.016}
OC^{cold}	\$ kg^{-1}	cold utility cost	0.001
OC^{heat}	\$ MWh^{-1}	heating utility cost	29.59
P_p^{inlet}	bar	inlet feed pressure in process p	{25, 25}
P_p^{reac}	bar	reactor pressure in process p	{110, 150}
P_p^{demand}	ton per day	methanol and ammonia demand	$\{\frac{3PC}{5}, PC\}$ where $PC = 1, 5, 10, 50, 100$
R	J K^{-1} mol^{-1}	universal gas constant	8.314
T^{oper}	hrs	annual operating time	8000
T_p^{inlet}	K	inlet feed temperature in process p	{290, 290}
T_p^{flash}	K	flash temperature in process p	{311, 313}
$w_{cs,p}$	-	inlet gas weight fraction of species cs in process p	$\frac{y_{cs,p}^f MW_{cs}}{\sum_{cs \in CS} y_{cs,p}^f MW_{cs}}$
$y_{cs,p}^f$	-	inlet gas mole fraction of species cs in process p	{0.046, 0; 0.659, 0.675; 0.094, 0; 0.005, 0; 0.0004, 0; 0.093, 0.225; 0, 0; 0.1026, 0.1}
ΔT^{cold}	K	temperature drop for cold utility	20
η^{comp}	%	compressor efficiency	75
η^{c}	%	cooler efficiency	80
η^{h}	%	heater efficiency	80
η^{m}	%	compressor's motor efficiency	95
γ	-	specific heat capacity ratio	1.40

Table G.3: Cost parameter values and design variable bounds for methanol-ammonia case study

i	equipment type	scaling parameter	AIC_i^{base} (MM$)	α_i	D_i^{base}	D_i^L	D_i^U
1	compressor	compressor power (MW)	2.941	0.67	10	0	10
2	heater	heat duty (MW)	8.279	1	355	0	100
3	reactor	feed flow rate (ton per day)	2.286	0.6	1834.41	500	1000
4	cooler	cooling duty (MW)	10.46	0.67	470	0	10
5	flash tank	feed flow rate (kg s^{-1})	3.44 $\times 10^{-4}$	0.8	1	0	10
6	distillation column	methanol flow rate (ton hr^{-1})	3.567	0.7	6.75	0	10

density of catalyst in the bed in terms of kg catalyst per m^3 bed volume. $\nu_{c,k}^{rxn}$ is the stoichiometric coefficient of species c in reaction k, and R_k is the forward rate of reaction k in mol kg. cat^{-1} s^{-1}.

The following equation states the steady-state momentum balance relationship. The Darcy's equation has been utilized to account for the pressure gradient along the axial direction.

$$\frac{dP}{dZ} = -\frac{150}{4r_p^2}\left(\frac{1-\epsilon}{\epsilon}\right)^2 \mu v_{int} \tag{G.36}$$

where P is the total gas phase pressure, r_p is the catalyst particle radius in m, μ is the gas phase mixture viscosity in Pa. s, ϵ is the bed void fraction and v_{int} is the gas-phase interstitial velocity in m s^{-1}. The viscosity of gas mixture is calculated using the following equation:

$$\mu = \frac{\sum_{c\in C} \mu_c y_c \sqrt{MW_c}}{y_c \sqrt{MW_c}} \tag{G.37}$$

where μ_c is the viscosity of component c, and y_c and MW_c are its gas-phase mole fraction and molecular weight, respectively.

The overall column energy balance can be written as below:

$$\frac{dT}{dZ} = \frac{\rho_b A_c \sum_{k\in K}(-\Delta H_k)\eta_k R_k}{\sum_{c\in C} F_c C_c^p} + \frac{2\pi r_{in} U (T^{shell} - T)}{\sum_{c\in C} F_c C_c^p} \tag{G.38}$$

where T is the gas phase temperature in K, ΔH_k is the heat of reaction k in J mol^{-1}, C_c^p is the specific heat capacity of component c in J mol^{-1} K^{-1}, U is the overall heat transfer coefficient in W m^{-2} K^{-1}, r_{in} is the inside tube radius in m, and T^{shell} is the shell-side temperature in degree kelvin. The specific heat capacity (C_c^p) is calculated using the Shomate equation as follows:

$$C_c^p = A_c + B_c\left(\frac{T}{1000}\right) + C_c\left(\frac{T}{1000}\right)^2 + D_c\left(\frac{T}{1000}\right)^3 + E_c\left(\frac{T}{1000}\right)^{-2} \quad \forall c \in C \qquad \text{(G.39)}$$

Methanol synthesis reaction model

The incoming synthesis gas mixture reacts on Cu-ZnO-Al_2O_3 catalyst to form methanol and water byproduct. Overall, the three reactions which occur are as follows [166]:

$$\mathrm{CO} + 2\,\mathrm{H_2} \rightleftharpoons \mathrm{CH_3OH}, \;\; \Delta H_{298} = \Delta H_{r,I} = -90.70\,\mathrm{kJ/mol} \qquad \text{(I)}$$

$$\mathrm{CO_2} + 3\,\mathrm{H_2} \rightleftharpoons \mathrm{CH_3OH} + \mathrm{H_2O}, \; \Delta H_{298} = \Delta H_{r,II} = -49.51\,\mathrm{kJ/mol} \qquad \text{(II)}$$

$$\mathrm{CO} + \mathrm{H_2O} \rightleftharpoons \mathrm{CO_2} + \mathrm{H_2}, \; \Delta H_{298} = \Delta H_{r,III} = -41.19\,\mathrm{kJ/mol} \qquad \text{(III)}$$

Reactions (I) and (II) denote CO and CO_2 hydrogenation for synthesizing methanol, and water gas shift is considered through reaction (III). The methanol synthesis reactions are favored at low temperatures due to exothermicity of the involved reactions. However, sufficiently high temperature needs to be maintained for appreciable reaction kinetics. Moreover, to achieve significant reaction conversions, high pressures are required.

The reaction kinetic model of Bussche and Froment [183] is used for simulating methanol synthesis reactions. In their model, the major source of carbon for producing methanol is assumed to be carbon dioxide which agrees with most of the previous studies in literature [167]. The model only considers CO_2 hydrogenation (reaction II) and water gas shift (reaction III) as the three reactions involved are linearly dependent. The rate expressions for these reactions can be found in Table G.4.

Ammonia synthesis reaction model

By passing a mixture of hydrogen and nitrogen in stoichiometric amounts over doubly pro-

Table G.4: Reaction kinetics model of Froment et al. for CH_3OH synthesis.

Expression	Unit
$R_{II} = \frac{K'_9 K'_{10}}{K'^3_8}$	$\mathrm{mol\ kg\ cat.^{-1}\ s^{-1}}$
$R_{II} = \frac{K'_9 K'_{10}}{K'^3_8}$	$\mathrm{mol\ kg\ cat.^{-1}\ s^{-1}}$
$R_{III} = \frac{K'_2}{K'_8}\left[P_{\mathrm{CO_2}} - \frac{K'_7 P_{\mathrm{H_2O}} P_{\mathrm{CO}}}{P_{\mathrm{H_2}}}\right]$	$\mathrm{mol\ kg\ cat.^{-1}\ s^{-1}}$
$K'_1 = 1.07 \exp\left(\frac{36696}{RT}\right)$	$\mathrm{mol\ kg\ cat.^{-1}\ s^{-1}\ bar^{-2}}$
$K'_2 = 1.22 \times 10^{10} \exp\left(\frac{-94765}{RT}\right)$	$\mathrm{mol\ kg\ cat.^{-1}\ s^{-1}\ bar^{-1}}$
$K'_3 = 3453.38$	$-$
$K'_4 = 6.62 \times 10^{-11} \exp\left(\frac{124119}{RT}\right)$	$\mathrm{bar^{-1}}$
$K'_5 = 0.499 \exp\left(\frac{17197}{RT}\right)$	$\mathrm{bar^{-0.5}}$
$K'_6 = \exp\left(\frac{3066}{T} - 10.592\right)$	$\mathrm{bar^{-2}}$
$K'_7 = \exp\left(\frac{2073}{T} - 2.029\right)$	$-$
$K'_8 = 1 + \frac{K'_3 P_{\mathrm{H_2O}}}{P_{\mathrm{H_2}}} + K'_4 P_{\mathrm{H_2O}} + K'_5 \sqrt{P_{\mathrm{H_2}}}$	$-$
$K'_9 = K'_1 P_{\mathrm{H_2}}$	$\mathrm{mol\ kg\ cat.^{-1}\ s^{-1}\ bar^{-1}}$
$K'_{10} = P_{\mathrm{CO_2}} - \frac{P_{\mathrm{H_2O}} P_{\mathrm{CH_3OH}}}{K'_6 P^3_{\mathrm{H_2}}}$	bar

moted iron, ammonia is synthesized. The following reaction occurs on the catalyst:

$$\mathrm{N_2 + 3\,H_2 \rightleftharpoons 2\,NH_3},\ \ \Delta H = -92.44\,\mathrm{kJ\,mol^{-1}} \tag{I}$$

The ammonia synthesis reaction is exothermic, and 92.44 kJ of energy is released per mole of nitrogen reacted. The rate of ammonia production can be obtained by the modified Temkin expression as follows [243]:

$$R_{\mathrm{NH_3}} = \frac{5}{18} \times \frac{2k}{\rho_{b,cat}} \left[K_a^2 f_{\mathrm{N_2}} \left(\frac{f^3_{\mathrm{H_2}}}{f^2_{\mathrm{NH_3}}} \right)^{\alpha} - \left(\frac{f^2_{\mathrm{NH_3}}}{f^3_{\mathrm{H_2}}} \right)^{1-\alpha} \right] \tag{G.40}$$

where $R_{\mathrm{NH_3}}$ is the rate of ammonia formation in mol NH_3 kg. cat.$^{-1}$ s^{-1}, $\rho_{b,cat} = 2200$ kg cat. m^{-3} bed is the bed packing density [244], k is the velocity constant for reverse reaction, K_a is the equilibrium constant of the following ammonia synthesis reaction:

$$\frac{1}{2}\mathrm{N_2} + \frac{3}{2}\mathrm{H_2} \rightleftharpoons \mathrm{NH_3}$$

In Eq. G.40, α is a parameter the value of which varies between 0.5-0.75 in literature depending on catalyst composition. We consider a value of 0.5. The unit of fugacities (i.e., $f_{\mathrm{H_2}}$, $f_{\mathrm{NH_3}}$ and $\mathrm{f_{N_2}}$) is atmospheres. The velocity constant (k) is calculated using an Arrhenius-type relation as follows:

$$k = k_o \exp\left(\frac{-E}{RT}\right) \tag{G.41}$$

where $k_o = 8.849 \times 10^{14}$, $E = 1.6381 \times 10^5$ J mol^{-1}, $R = 8.314$ J mol^{-1} K^{-1} and T is the gas phase temperature in K.

The relationship of Gillespie and Beattie has been employed for calculating the reaction equilibrium constant (K_a) as below:

$$\log_{10} K_a = -2.691122 \log_{10} T - 5.519265 \times 10^{-5} T + 1.848863 \times 10^{-7} T^2 + \frac{2001.6}{T} + 2.689 \tag{G.42}$$

where T is in kelvin.

The fugacities of hydrogen, nitrogen and ammonia can be obtained using the expression $f_c = \phi_c y_c P$, where ϕ_c is the fugacity coefficient of component c and can be calculated using the following expressions [204]:

$$\phi_{\mathrm{H_2}} = \exp\left\{ e^{(-3.8402 T^{0.125} + 0.541)} P - e^{(-0.1263 T^{0.5} - 15.98)} P^2 + 300 \left[e^{(-0.011901 T - 5.941)} \right] \times \left[e^{\left(-\frac{P}{300}\right)} - 1 \right] \right\} \tag{G.43}$$

$$\phi_{\mathrm{N_2}} = 0.93431737 + 0.3101804 \times 10^{-3}T + 0.295896 \times 10^{-3}P - 0.2707279 \times 10^{-6}T^2 + 0.4775207 \times 10^{-6}P^2 \tag{G.44}$$

$$\phi_{\mathrm{NH_3}} = 0.1438996 + 0.2028538 \times 10^{-2}T - 0.4487672 \times 10^{-3}P - 0.1142945 \times 10^{-5}T^2 + 0.2761216 \times 10^{-6}P^2 \tag{G.45}$$

In the above fugacity coefficient relations (Eqs. G.43-G.46), temperature is in degree kelvin and pressure in in atmospheres. The intra-particle mass transfer limitations are considered using the catalyst effectiveness factor as follows:

$$\eta = b_0 + b_1T + b_2X_{\mathrm{N_2}} + b_3T^2 + b_4X_{\mathrm{N_2}}^2 + b_5T^3 + b_6X_{\mathrm{N_2}}^3 \tag{G.46}$$

Input-output relations for methanol and ammonia reactor

Figures G.3 and G.4 depict the shell and tube-type reactors used for methanol and ammonia synthesis from syngas and nitrogen-hydrogen feed, respectively. The syngas feed mixture to methanol reactor majorly consists of hydrogen, carbon dioxide and carbon monoxide reactants mixed with inert methane and nitrogen. For ammonia reactor, the reactant feed consists of a stoichiometric ratio of nitrogen and hydrogen with small amounts of inert. In both of these cases, the input variables consist of reactant flow rate F_{in} and reactor design flow rate F_{design}. The methanol reactor has 5 outlet variables consisting of feed flow rates of carbon dioxide, water, hydrogen, methanol and carbon monoxide in ton per day. The ammonia reactor has 3 outlet variables including feed flow rates of ammonia, nitrogen and hydrogen.

The input variables to both methanol and ammonia reactors have been appropriately bounded as follows:

$$10 \leq F_{in}(\text{ton per day}) \leq 2500 \tag{G.47}$$

$$500 \leq F_{design}(\text{ton per day}) \leq 2374.6 \tag{G.48}$$

To obtain algebraic input-output surrogate models for both methanol and ammonia reactors,

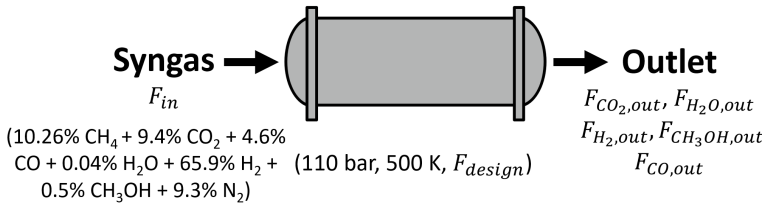

Figure G.3: Methanol reactor input-output variables.

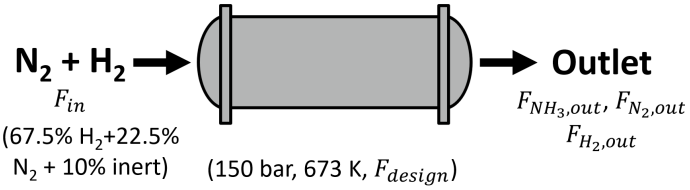

Figure G.4: Ammonia reactor input-output variables.

we utilize the ALAMO tool developed by Sahinidis and coworkers [245, 246] which balances the tradeoff between model complexity and prediction accuracy well. The workflow of ALAMO can further be explored on their webpage [247]. The input variables F_{in} and F_{design} are normalized between 1 and 2, and the resulting normalized variables are respectively denoted by $\overline{F}_{in}$ and $\overline{F}_{design}$. On the new scale for input variables, a lower bound of 1 is selected to preserve the logarithmic basis functions which ALAMO includes while developing reduced-order surrogate models.

The resulting surrogate models for methanol and ammonia reactor can be found in Tables G.5 and G.6, respectively. For a given normalized value of inlet flow rate $\overline{F}_{in}$ and design flow rate $\overline{F}_{design}$, these expressions are used for computing outlet flow rates of the involved species. It should be noted that the developed surrogate models should have a good balance between model complexity and accuracy as they constitute reactors' input-output constraints in the MINLP formulation. For establishing the accuracy of the generated surrogate models, cross-validation has been performed using 100 sampling points generated through lhsdesign subroutine in MATLAB. Figures G.5 and G.6 report the comparison between actual outlet variables obtained through simulations and predicted outlet variables obtained using developed surrogate models. It can be clearly observed that the surrogate-model predictions are in good agreement with the simulated values.

Table G.5: Input output relationships for methanol reactor.

$$F_{\mathrm{CO_2},out} = 1000 \times \left[0.7006\overline{F}_{in} + 0.0088\left(\frac{\overline{F}_{in}}{\overline{F}_{design}}\right)^2 - 0.7107\right]$$

$$F_{\mathrm{H_2O},out} = 1000 \times \left[0.0848\log(\overline{F}_{in}) + 0.0077\overline{F}_{in}^{2.5} - 0.0073\left(\frac{\overline{F}_{in}}{\overline{F}_{design}}\right)\right]$$

$$F_{\mathrm{H_2},out} = 1000 \times \Bigg[11.99 + 0.1938\overline{F}_{in} + 3.9309\overline{F}_{design} + 4.2941\log(\overline{F}_{in}) + 4.4167\log\left(\frac{\overline{F}_{design}}{\overline{F}_{in}}\right) + 0.0004\exp(\overline{F}_{in}) - 0.05233\exp(\overline{F}_{design}) + 0.3115\overline{F}_{in}^{0.5} - 16.2872\overline{F}_{design}^{0.5} - 0.0007\left(\frac{\overline{F}_{in}}{\overline{F}_{design}}\right)^5\Bigg]$$

$$F_{\mathrm{CH_3OH},out} = 1000 \times \Big[-5.6334\overline{F}_{in} + 7.8505\overline{F}_{design} - 8.2708\log(\overline{F}_{in}) + 8.3954\log(\overline{F}_{design}) - 1.3081\exp(\overline{F}_{in}) - 0.1152\exp(\overline{F}_{design}) + 32.9703\overline{F}_{in}^{0.5} - 31.7111\overline{F}_{design}^{0.5} + 0.4132\overline{F}_{in}^{3.5} - 0.02563\left(\frac{\overline{F}_{in}}{\overline{F}_{design}}\right)^2\Big]$$

$$F_{\mathrm{CO},out} = (F_{\mathrm{CO_2},in} + F_{\mathrm{CO},in} + F_{\mathrm{H_2},in} + F_{\mathrm{H_2O},in} + F_{\mathrm{CH_3OH},in}) - (F_{\mathrm{CO_2},out} + F_{\mathrm{H_2},out} + F_{\mathrm{H_2O},out} + F_{\mathrm{CH_3OH},out})$$

Table G.6: Input output relationships for ammonia reactor.

$$F_{\mathrm{NH_3},out} = 1000 \times \Big[66.020\overline{F}_{in} - 31.6736\overline{F}_{design} + 31.3680\log(\overline{F}_{in}) - 36\log(\overline{F}_{design}) + 0.1555\exp(\overline{F}_{in}) + 0.4122\exp(\overline{F}_{design}) - 155.1887\overline{F}_{in}^{0.5} + 132.7034\overline{F}_{design}^{0.5} - 13.0982\overline{F}_{in}^{1.5} - 0.285\left(\frac{\overline{F}_{design}}{\overline{F}_{in}}\right)\Big]$$

$$F_{\mathrm{N_2},out} = F_{\mathrm{N_2},in} - \left(\frac{28.01}{34.06}\right)F_{\mathrm{NH_3},out}$$

$$F_{\mathrm{H_2},out} = F_{\mathrm{H_2},in} - \left(\frac{6.045}{34.06}\right)F_{\mathrm{NH_3},out}$$

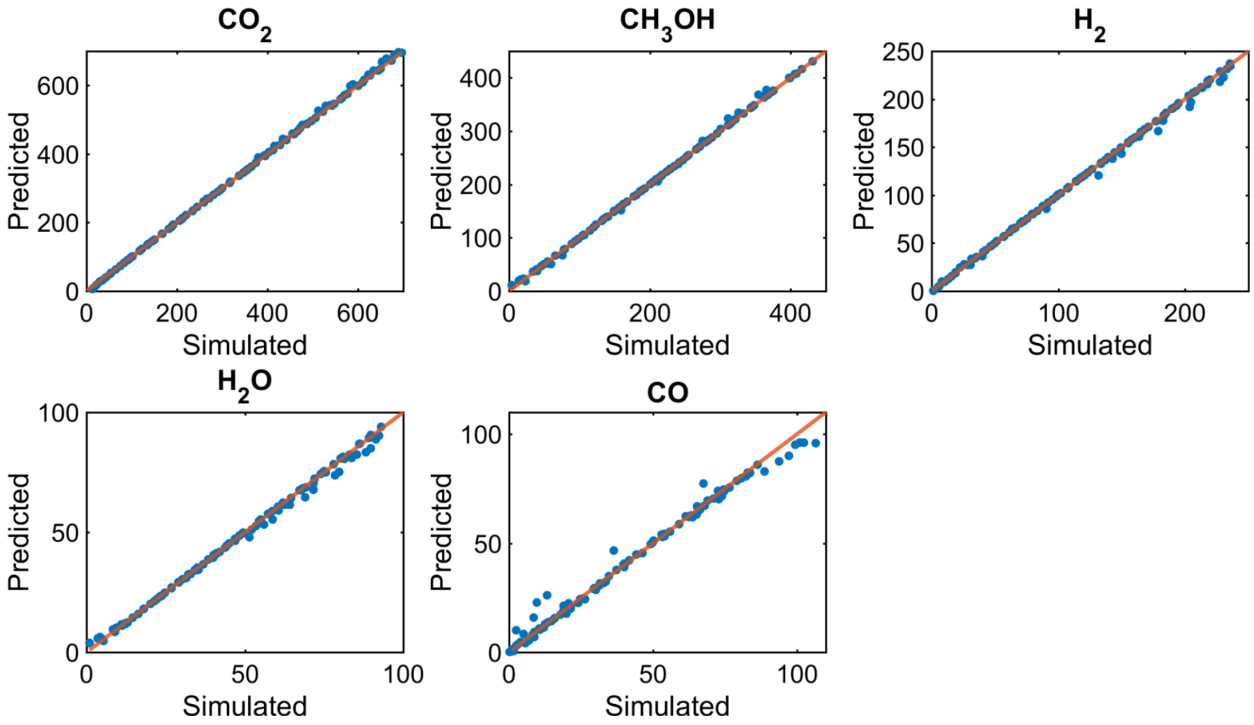

Figure G.5: Cross-validation of input-output surrogate models for methanol reactor using 100 sampling points.

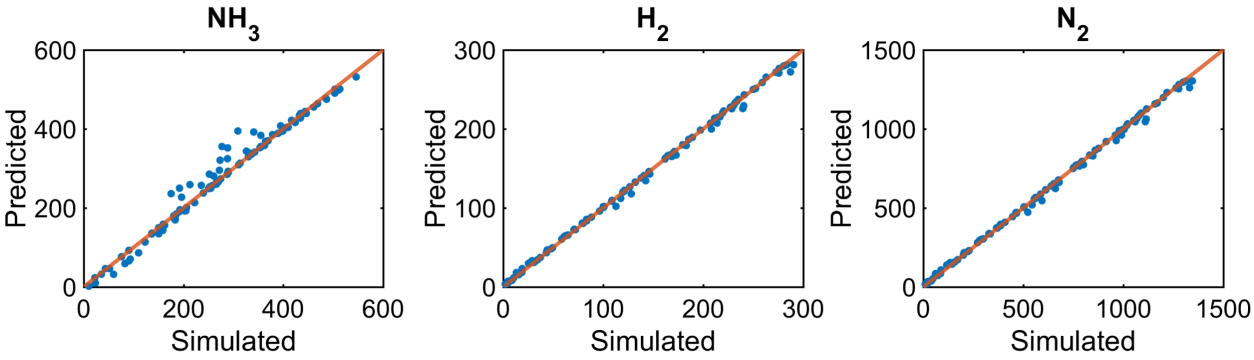

Figure G.6: Cross-validation of input-output surrogate models for ammonia reactor using 100 sampling points.

APPENDIX H

NGL FRACTIONATION CASE STUDY

Table H.1: Sets and indices used for NGL fractionation case study.

Index	Set	Set elements	Description
i	I	$\{1, 2\}$	unit operations: 1 - deethanizer and 2 - depropanizer
j	J	$\{1, 2, ..., 5\}$	process streams
p	P	$\{1, 2, 3, 4\}$	processes considered
s	S	$\{1, 2, 3, 4\}$	state variables: feed flow rate (kmol hr^{-1}) of 1 - C_2H_6, 2 - C_3H_8, 3 - iC_4H_{10} and 4 - nC_4H_{10}

Optimization model

Here, we report the overall optimization model with constraints which are specific to the NGL fractionation case study being investigated.

$$\min \sum_{p\in P}\sum_{i\in I}\left(AIC_{p,i}f_{p,i} + AIC^r_{p,i}f^r_{p,i} + AIC^c_{p,i}f^c_{p,i}\right) + \sum_{p\in P}\sum_{i\in I}\left(OC^r_{p,i} + OC^c_{p,i}\right) \tag{H.1}$$

$$\text{s.t.} f_{p,i} = (n_i)^{\beta_i}\,\frac{z_{p,i}}{n_i} + (1 - z_{p,i}) \quad \forall p, i \tag{H.2}$$

$$f^r_{p,i} = (n^r)^{\beta^r}\,\frac{z^r_{p,i}}{n^r} + (1 - z^r_{p,i}) \quad \forall p, i \tag{H.3}$$

$$f^c_{p,i} = (n^c)^{\beta^c}\,\frac{z^c_{p,i}}{n^c} + (1 - z^c_{p,i}) \quad \forall p, i \tag{H.4}$$

$$n_i = \sum_{p\in P} z_{p,i}NU_p \quad \forall i \tag{H.5}$$

$$n^r = \sum_{p\in P}\sum_{i\in I} z^r_{p,i}NU_p \quad \forall i \tag{H.6}$$

Table H.2: Variables used in the optimization model for NGL fractionation.

Variable	Unit	Significance
$AIC_{p,i}$	MM$ per yr	annualized installation cost for distillation column in unit operation i in process p
$AIC^{c}_{p,i}$	MM$ per yr	annualized installation cost for condenser in unit operation i in process p
$AIC^{r}_{p,i}$	MM$ per yr	annualized installation cost for reboiler in unit operation i in process p
$d_{p,i}$	ft	distillation column diameter for unit operation i in process p
$d^{r}_{p,i}$	MW	reboiler design duty for unit operation i in process p
$d^{c}_{p,i}$	MW	condenser design duty for unit operation i in process p
D_i	ft	column diameter for commonly designed distillation columns
D^{c}_{i}	MW	design duty for commonly designed condensers
D^{r}_{i}	MW	design duty for commonly designed reboilers
$EP^{c}_{p,i}$	-	flexible condenser's performance efficiency
$EP^{r}_{p,i}$	-	flexible reboiler's performance efficiency
$f_{p,i}$	-	economies of numbers factor for distillation column
$f^{c}_{p,i}$	-	economies of numbers factor for condenser
$f^{r}_{p,i}$	-	economies of numbers factor for reboiler
$H_{p,i}$	ft	column height
$K^{bot}_{p,i,s}$		species s vapor-liquid equilibrium ratio at bottom section for unit operation i in process p
$K^{top}_{p,i,s}$		species s vapor-liquid equilibrium ratio at top section for unit operation i in process p
n_i	-	number of distillation columns manufactured with common design for unit operation i
n^{c}	-	number of condensers produced with common design
n^{r}	-	number of reboilers produced with common design
$N_{p,i}$	-	minimum number of distillation stages for unit operation i in process p
N^{min}_{i}	-	minimum number of distillation stages for unit operation i in process p
N^{com}_{i}	-	number of trays for commonly designed distillation columns
$OC^{c}_{p,i}$	MM$ per yr	annualized condenser operating cost for unit operation i in process p
$OC^{r}_{p,i}$	MM$ per yr	annualized reboiler operating cost for unit operation i in process p
$Q^{c}_{p,i}$	MW	condenser operating duty for unit operation i in process p
$Q^{r}_{p,i}$	MW	reboiler operating duty for unit operation i in process p
$R_{p,i}$	-	reflux ratio for unit operation i in process p
$R^{min}_{p,i}$	-	minimum reflux ratio for unit operation i in process p
$T^{bot}_{p,i}$	R	distillation column bottom temperature for unit operation i in process p
$T^{top}_{p,i}$	R	distillation column top temperature for unit operation i in process p
$x_{p,j,s}$	kmol per hr	flow rate of species s present in stream j in process p
$y^{in}_{p,i,s}$	-	mole fraction of species s of inlet feed stream to column i in process p
$y^{top}_{p,i,s}$	-	mole fraction of species s of top stream from column i in process p
$y^{bot}_{p,i,s}$	-	mole fraction of species s of bottom stream from column i in process p
$z_{p,i}$	-	binary variable denoting whether distillation column i in process p is mass-produced
$z^{c}_{p,i}$	-	binary variable denoting whether condenser i in process p is mass-produced
$z^{r}_{p,i}$	-	binary variable denoting whether reboiler i in process p is mass-produced
$\alpha^{avg}_{p,i,s}$	-	average relative volatility for species s in unit operation i in process p

$$n^{c} = \sum_{p \in P} \sum_{i \in I} z^{c}_{p,i} NU_{p} \quad \forall i \tag{H.7}$$

$$z_{p,i} \leq \hat{z}_{p,i} \quad \forall p, i \tag{H.8}$$

$$z^{r}_{p,i} \leq \hat{z}^{r}_{p,i} \quad \forall p, i \tag{H.9}$$

Table H.3: Parameters used for NGL fractionation case study.

Parameter	Unit	Significance	Value
MS [248]	-	Marshall and Swift cost index	1431.7
E^t [211]	-	tray efficiency	0.5
F_m^v [211]	-	cost parameter for column vessel	1
$F_{p,i}^v$ [211]	-	cost parameter for column vessel	{1.45, 1.20}
F_s^t [211]	-	cost parameter for column tray	1
F_m^t [211]	-	cost parameter for column tray	1.7
F_t^t [211]	-	cost parameter for column tray	0
F_d^r [211]	-	cost parameter for reboiler	1.35
F_p^r [211]	-	cost parameter for reboiler	0.25
F_m^r [211]	-	cost parameter for reboiler	2.81
F_d^c [211]	-	cost parameter for condenser	1.35
F_p^c [211]	-	cost parameter for condenser	0.25
F_m^c [211]	-	cost parameter for condenser	2.81
T^{oper}	hrs	annual operating hours	8000
OC^{steam} [217]	\$ GJ^{-1}	steam operating cost	13.28
OC^r [217]	\$ GJ^{-1}	refrigerant operating cost	7.89
OC^{cw} [217]	\$ GJ^{-1}	cooling water operating cost	0.35
F_p^{in}	kmol hr^{-1}	inlet feed flow rate	varies
MW^s	g mol^{-1}	molecular weight	{30.07, 44.1, 58.12, 58.12}
NU_p	-	number of processes manufactured	{1, 1}
β_i	-	distillation column economies of mass production parameter	{0.7, 0.7}
β^r	-	reboiler economies of mass production parameter	0.7
β^c	-	condenser economies of mass production parameter	0.7
D_i^U	ft	maximum column design diameter	{10, 10}
N_i^U	-	maximum number of column stages	{200, 200}
D^{rU}	MW	maximum reboiler design duty	2
D^{cU}	MW	maximum condenser design duty	2
H_s^{vap}	kJ mol^{-1}	heat of vaporization	{8.65, 13.20, 22.6, 21.4}
$RC_{p,i}^{top}$	kJ mol^{-1}	light key recovery fraction	{0.99, 0.99; 0.99, 0.99}
$RC_{p,i}^{bot}$	kJ mol^{-1}	heavy key recovery fraction	{0.99, 0.99; 0.99, 0.99}
$\hat{z}_{p,i}$	-	whether column i is present in process p	{1, 1; 1, 1}
$\hat{z}_{p,i}^c$	-	whether condenser i is present in process p	{1, 1; 1, 1}
$\hat{z}_{p,i}^r$	-	whether reboiler i is present in process p	{1, 1; 1, 1}
$a_{i,s}$	-	K correlation parameter	{0.011, 0.007, 0.0035, 0.007; 0.019, 0.011, 0.006, 0.005}
$b_{i,s}$	-	K correlation parameter	{4.754, 3.268, 1.724, 1.45; 8.007, 5.145, 2.964, 2.555}

$$z_{p,i}^c \leq \hat{z}_{p,i}^c \quad \forall p, i \tag{H.10}$$

$$d_{p,i} \geq D_i - D_i^U(1 - z_{p,i}) \quad \forall p, i \tag{H.11}$$

$$d_{p,i} \leq D_i + D_i^U(1 - z_{p,i}) \quad \forall p, i \tag{H.12}$$

$$d_{p,i}^r \geq D^r - D^{rU}(1 - z_{p,i}^r) \quad \forall p, i \tag{H.13}$$

$$d_{p,i}^r \leq D^r + D^{rU}(1 - z_{p,i}^r) \quad \forall p, i \tag{H.14}$$

$$d_{p,i}^c \geq D^c - D^{cU}(1 - z_{p,i}^c) \quad \forall p, i \tag{H.15}$$

$$d_{p,i}^c \leq D^c + D^{cU}(1 - z_{p,i}^c) \quad \forall p, i \tag{H.16}$$

$$y_{p,i=1,s}^{in} = y_{p,s}^f \quad \forall p, s \tag{H.17}$$

$$x_{p,j,s} \leq y_{s,p}^{feed} PC_p \quad \forall p, j, s \tag{H.18}$$

$$K_{p,i,s}^{top} = a_{i,s} T_{p,i}^{top} - b_{i,s} \quad \forall p, i, s \tag{H.19}$$

$$K_{p,i,s}^{bot} = a_{i,s} T_{p,i}^{bot} - b_{i,s} \quad \forall p, i, s \tag{H.20}$$

$$\alpha_{p,i,s}^{avg} = \frac{K_{p,i,s}^{top}}{K_{p,i,s'=HK_i}^{top}} \quad \forall p, i, s \tag{H.21}$$

$$\sum_s K_{p,i,s}^{top} y_{p,i,s}^{top} = 1 \quad \forall p, i \tag{H.22}$$

$$\sum_s K_{p,i,s}^{bot} y_{p,i,s}^{bot} = 1 \quad \forall p, i \tag{H.23}$$

$$y_{p,i,s}^{in} = \frac{x_{p,j=IN_i,s}}{\sum_{s'} x_{p,j=IN_i,s'}} \quad \forall p, s, i = 2 \tag{H.24}$$

$$y_{p,i,s}^{top} = \frac{x_{p,j=IN_i,s}}{\sum_{s'} x_{p,j=IN_i,s'}} \quad \forall p, i \tag{H.25}$$

$$y_{p,i,s}^{bot} = \frac{x_{p,j=OU_i,s}}{\sum_{s'} x_{p,j=OU_i,s'}} \quad \forall p, i \tag{H.26}$$

$$\sum_s x_{p,j=1,s} = F_p^{in} y_{p,i=1,s}^{in} \quad \forall p, s \tag{H.27}$$

$$x_{p,j=IN_i,s} = x_{p,j=DT_i,s} + x_{p,j=BT_i,s} \quad \forall p, i, s \tag{H.28}$$

$$x_{p,j=IN_i,s=LLK_i} = x_{p,j=DT_i,s=LLK_i} \quad \forall p,i \tag{H.29}$$

$$x_{p,j=IN_i,s=HHK_i} = x_{p,j=BT_i,s=HHK_i} \quad \forall p,i \tag{H.30}$$

$$N_{p,i} \geq N_i^{com} - N_i^U(1-z_{p,i}) \quad \forall p,i \tag{H.31}$$

$$N_{p,i} \leq N_i^{com} + N_i^U(1-z_{p,i}) \quad \forall p,i \tag{H.32}$$

$$H_{p,i} = \frac{2.3N_{p,i}}{E^t} \quad \forall p,i \tag{H.33}$$

$$R_{p,i}^{min} = \frac{\alpha_{p,i,s+1}^{avg}(y_{p,i,s}^{in}+y_{p,i,s+1}^{in})}{y_{p,i,s}^{in}(\alpha_{p,i,s}^{avg}-\alpha_{p,i,s+1}^{avg})} + \frac{\alpha_{p,i,s+2}^{avg}y_{p,i,s+2}^{in}}{y_{p,i,s}^{in}(\alpha_{p,i,s}^{avg}-\alpha_{p,i,s+2}^{avg})} \quad \forall p,i=1,s=LK_i \tag{H.34}$$

$$+\frac{y_{p,i,s+3}^{in}}{y_{p,i,s}^{in}(\alpha_{p,i,s}^{avg}-1)}$$

$$R_{p,i}^{min} = \frac{\frac{\alpha_{p,i,s+1}^{avg}y_{p,i,s-1}^{in}}{\alpha_{p,i,s-1}^{avg}-\alpha_{p,i,s+1}^{avg}} + \frac{\alpha_{p,i,s+1}^{avg}(y_{p,i,s}^{in}+y_{p,i,s+1}^{in})}{\alpha_{p,i,s}^{avg}-\alpha_{p,i,s+1}^{avg}}}{(y_{p,i,s-1}^{in}+y_{p,i,s}^{in})(1+y_{p,i,s-1}^{in}(y_{p,i,s+1}^{in}+y_{p,i,s+2}^{in}))} \quad \forall p,i=2,s=LK_i \tag{H.35}$$

$$+y_{p,i,s+2}^{in}\frac{\frac{y_{p,i,s-1}^{in}}{\alpha_{p,i,s-1}^{avg}-1}+\frac{y_{p,i,s}^{in}}{\alpha_{p,i,s}^{avg}-1}}{(y_{p,i,s-1}^{in}+y_{p,i,s}^{in})^2} \quad \forall p,i=2,s=LK_i$$

$$\frac{N_{p,i}-N_{p,i}^{min}}{N_{p,i}+1} = 0.75\left[1-\left(\frac{R_{p,i}-R_{p,i}^{min}}{R_{p,i}+1}\right)^{0.5688}\right] \quad \forall p,i \tag{H.36}$$

$$N_{p,i}^{min} = \frac{\log\left[\left(\frac{y_{p,i,s=LK_i}^{top}}{1-y_{p,i,s=LK_i}^{top}}\right)\left(\frac{1-y_{p,i,s=LK_i}^{bot}}{y_{p,i,s=LK_i}^{bot}}\right)\right]}{\log(\alpha_{p,i,s=LK_i}^{avg})} \quad \forall p,i \tag{H.37}$$

$$d_{p,i} = 0.0164\left[2.2\left(\sum_s x_{p,j=DT_i,s}\right)(R_{p,i}+1)\right]^{0.5} \times \quad \forall p,i \tag{H.38}$$

$$\left[379MW_{s=HK_i}\left(\frac{T_{p,i}^{bot}}{520}\right)\left(\frac{14.7}{P_i^{col}}\right)\right]^{0.25}$$

$$x_{p,j=DT_i,s=LK_i} \geq RC_{p,i}^{top}x_{p,j=IN_i,s=LK_i} \quad \forall p,i \tag{H.39}$$

$$x_{p,j=BT_i,s=HK_i} \geq RC_{p,i}^{bot}x_{p,j=IN_i,s=HK_i} \quad \forall p,i \tag{H.40}$$

$$AIC_{p,i} = \frac{1}{3\times 10^6}\left[\left(\frac{MSd_{p,i}^{1.066}H_{p,i}^{0.82}F_m^v F_{p,i}^v}{2.75}\right) \quad \forall p,i \right. \tag{H.41}$$

$$\left. + \left(\frac{MSd_{p,i}^{1.55}H_{p,i}(F_s^t + F_m^t + F_t^t)}{59.57}\right)\right]]$$

$$AIC_{p,i}^r = \frac{1}{3\times 10^6}\left[\frac{MS}{2.76}\left(262.47Q_{p,i}^r\right)^{0.65}\left(2.29 + (F_d^r + F_p^r)F_m^r\right)\right] \quad \forall p,i \tag{H.42}$$

$$AIC_{p,i}^c = \frac{1}{3\times 10^6}\left[\frac{MS}{2.76}\left(341.21Q_{p,i}^c\right)^{0.65}\left(2.29 + (F_d^c + F_p^c)F_m^c\right)\right] \quad \forall p,i \tag{H.43}$$

$$OC_{p,i}^r = 3.6\times 10^{-6}T^{oper}Q_{p,i}^r OC^{steam} \quad \forall p,i \tag{H.44}$$

$$OC_{p,i}^c = 3.6\times 10^{-6}T^{oper}Q_{p,i}^c OC^{refr} \quad \forall p, i=1 \tag{H.45}$$

$$OC_{p,i}^c = 3.6\times 10^{-6}T^{oper}Q_{p,i}^c OC^{cw} \quad \forall p, i=2 \tag{H.46}$$

$$Q_{p,i}^c = \frac{\sum_s x_{p,j=DT_i,s}H_s^{vap}(1+R_{p,i})}{EP_{p,i}^c} \quad \forall p,i \tag{H.47}$$

$$Q_{p,i}^r = \frac{\sum_s x_{p,j=DT_i,s}H_s^{vap}(1+R_{p,i})}{EP_{p,i}^r} \quad \forall p,i \tag{H.48}$$

$$EP_{p,i}^c \le 1 - m_{p,i}^c(Q_{p,i}^c - d_{p,i}^c) + (1 - z_{p,i}^c) \quad \forall p,i \tag{H.49}$$

$$EP_{p,i}^c \le 1 + m_{p,i}^{\prime c}(Q_{p,i}^c - d_{p,i}^c) + (1 - z_{p,i}^c) \quad \forall p,i \tag{H.50}$$

$$EP_{p,i}^r \le 1 - m_{p,i}^r(Q_{p,i}^r - d_{p,i}^r) + (1 - z_{p,i}^r) \quad \forall p,i \tag{H.51}$$

$$EP_{p,i}^r \le 1 + m_{p,i}^{\prime r}(Q_{p,i}^r - d_{p,i}^r) + (1 - z_{p,i}^r) \quad \forall p,i \tag{H.52}$$

$$0 \le y_{p,i,s}^{in}, y_{p,i,s}^{top}, y_{p,i,s}^{bot} \le 1; 0.01 \le EP_{p,i}^c, EP_{p,i}^r \le 1;$$

$$460 \le T_{p,i}^{top}, T_{p,i}^{bot} \le 760; 0 \le x_{p,j,s}; R_{p,i}^{min} \le 3$$

APPENDIX I

EFFECT OF ADSORBENT PROPERTIES ON BREAKTHROUGH DYNAMICS

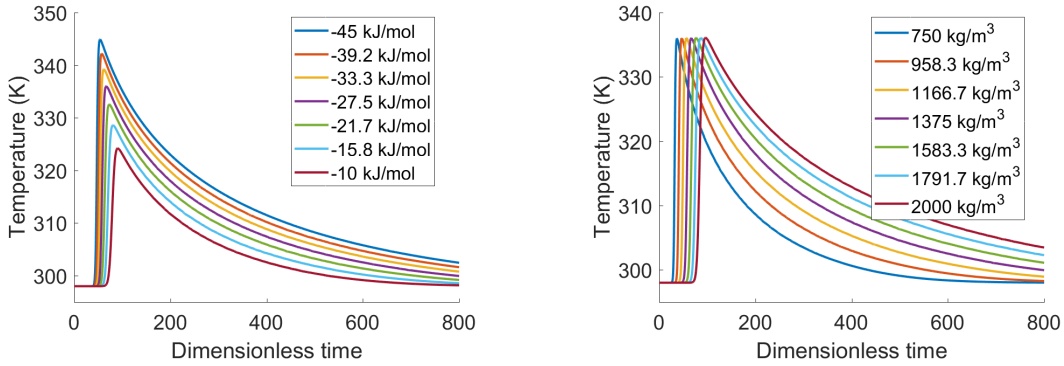

(a) (b)

Figure I.1: Effect of (a) heat of adsorption and (b) adsorbent framework density on outlet temperature.

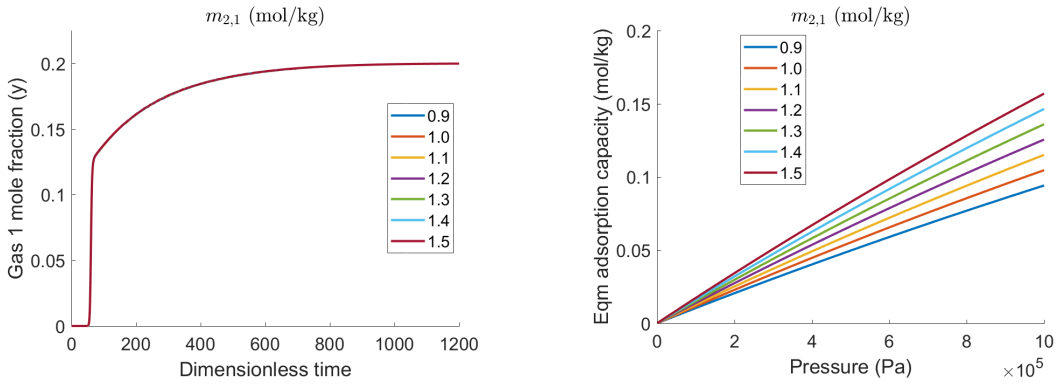

(a) (b)

Figure I.2: Effect of saturation adsorption capacity of gas species 2 on (a) breakthrough dynamics and (b) equilibrium adsorption isotherms. Fixed material parameters: $m_{1,1} = m_{1,2}$ = 4 mol kg^{-1}, $b_{1,1} = b_{1,2} = b_{2,1} = 10^{-10}$ Pa^{-1}, $\Delta U_{1,1} = \Delta U_{1,2} = \Delta H_1$ = -27.5 kJ mol^{-1}, $\Delta U_{2,1} = \Delta H_2$ = -17.5 kJ mol^{-1}, $\rho_b = 1375$ kg ads. m^{-3} bed.

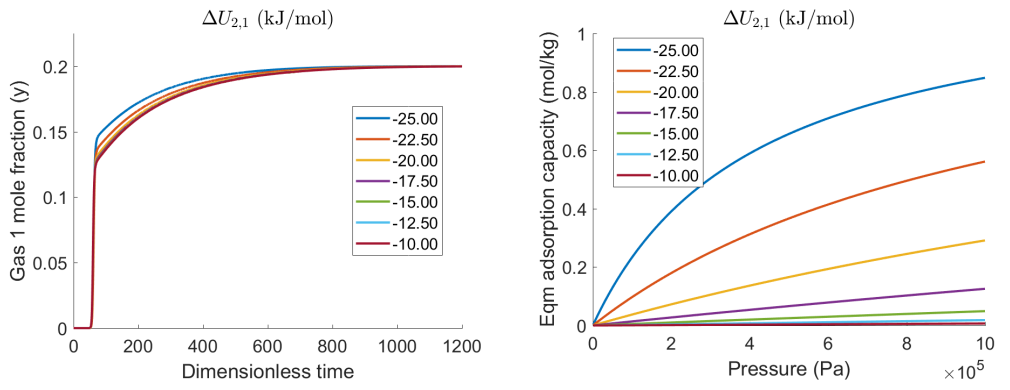

(a) (b)

Figure I.3: Effect of adsorption energy of gas 2 on (a) breakthrough dynamics and (b) equilibrium adsorption isotherms. Fixed material parameters: $m_{1,1} = m_{1,2}$ = 4 mol kg^{-1}, $b_{1,1} = b_{1,2} = b_{2,1} = 10^{-10}$ Pa^{-1}, $m_{2,1}$ = 1.2 mol kg^{-1}, $\Delta U_{1,1} = \Delta U_{1,2} = \Delta H_1$ = -27.5 kJ mol^{-1}, ΔH_2 = -17.5 kJ mol^{-1}, $\rho_b = 1375$ kg ads. m^{-3} bed.

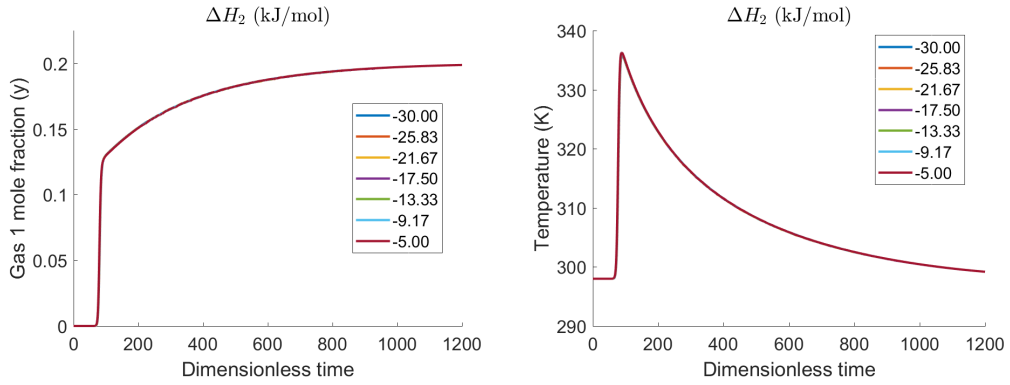

(a) (b)

Figure I.4: Effect of heat of adsorption of gas 2 on outlet (a) concentration and (b) temperature profiles. Fixed material parameters: $m_{1,1} = m_{1,2}$ = 4 mol kg^{-1}, $b_{1,1} = b_{1,2} = b_{2,1} = 10^{-10}$ Pa^{-1}, $m_{2,1}$ = 1.2 mol kg^{-1}, $\Delta U_{1,1} = \Delta U_{1,2} = \Delta H_1$ = -27.5 kJ mol^{-1}, $\Delta U_{2,1} = \Delta H_2$ = -17.5 kJ mol^{-1}, $\rho_b = 1375$ kg ads. m^{-3} bed.